ABSTRACT

Title of Dissertation: AN EXPERIMENTAL AND THEORETICAL INVESTIGATION OF THE LOW TEMPERATURE CREEP DEFORMATION BEHAVIOR OF SINGLE-PHASE TITANIUM ALLOYS

Paul Gregory Oberson, Doctor of Philosophy, 2006

Dissertation Directed by: Professor Sreeramamurthy Ankem
Department of Materials Science and Engineering

Titanium alloys are used for many applications due to their desirable properties, including its high strength-to-weight ratio, corrosion resistance, and biocompatibility. Titanium alloys are used extensively for aerospace, chemical, nuclear, industrial, biomedical, and consumer applications. In many applications, titanium components may be subject to stresses for extended periods of time. It has long been known that single-phase hexagonally close-packed (HCP) α and body-centered cubic (BCC) β titanium alloys deform over time, or creep, at low temperatures ($<0.25*T_m$). As such, creep is an important factor to consider when assessing the structural reliability of titanium components. However, the factors that affect creep behavior such as grain size and alloy chemistry and the deformation mechanisms associated with creep such as slip and twinning are not well understood. The aim of this investigation is to experimentally and theoretically study the creep deformation behavior of single-phase α and β titanium alloys.

The first part of the investigation concerns α-Ti alloys. The low temperature creep behavior was studied experimentally, using α-Ti-1.6wt.%V as the model alloy. Creep testing was performed at a range of temperatures and slip and twinning were identified as creep deformation mechanisms by optical, SEM and TEM microscopy. The activation energy for creep was measured for the first time for an α-Ti than deforms by twinning. The activation energy was found to increase as a function of creep strain, suggesting that there is a change in the predominant deformation mechanism from slip at low strain to twinning at high strain. The reason for this change is explained by a model for twin nucleation caused by dislocation pileups. The theoretical aspect of the study of α-Ti, concerns the phenomenon of slow twin growth (time-dependent twinning) during low temperature creep. This phenomenon is unusual and poorly understood as twins in bulk, polycrystalline metals are expected to grow very fast. It was suggested that interstitial atoms, particularly oxygen could be responsible for time-dependent twinning but there were no models to explain this. As such, crystallographic models were developed for the HCP lattice of α-Ti to show how the octahedral interstitial sites where atoms such as oxygen can reside are eliminated by the atomic movements associated with twinning. As such, the rate of twin growth, and in turn the creep strain rate is controlled by the diffusion of oxygen away from these eliminated sites.

The second part of the investigation builds on experimental work from a previous investigation to extend the theoretical model for time-dependent twinning to the BCC lattice of β-Ti. Similar to the case for α-Ti alloys, twin growth is rate limited by the diffusion of oxygen atoms away from eliminated interstitial sites.

The results of these findings are very valuable when designing Ti alloys for improved creep resistance and mechanical reliability. This is critical because creep can directly alter dimensional tolerances and creep deformation products can contribute to crack nucleation leading to catastrophic failure.

This work was supported by the National Science Foundation under Grant Number DMR-0513751.

AN EXPERIMENTAL AND THEORETICAL INVESTIGATION OF THE LOW TEMPERATURE CREEP DEFORMATION BEHAVIOR OF SINGLE PHASE TITANIUM ALLOYS

By

P. Gregory Oberson

Dissertation submitted to the Faculty of the Graduate School of the
University of Maryland, College Park in partial fulfillment
of the requirements for the degree of
Doctor of Philosophy.
2006

Advisory Committee:

Professor Sreeramamurthy Ankem, Advisor/Chair
Professor Mohammad Al-Sheikhly
Professor Aris Christou
Professor Lourdes Salamanca-Riba
Associate Professor Evanghelos Zafiriou, Dean's Representative

Acknowledgements

I first want to thank my fiancée, Amy, for your love, support, and encouragement. You've been an amazing motivator and you always know whether I need a hug or a kick in the pants. Thank you for sticking with me through all the highs and lows. I would also like to thank my family and friends for their thoughts, cares, and prayers.

I would like to thank my advisor, Dr. Ankem, for guiding my research project and for challenging me to achieve my very best. We have had many conversations and shared many laughs. Thank you for your advice, assistance, and mostly for your friendship. I would like to thank the entire faculty and staff of the Department of Materials Science and Engineering and the University of Maryland for welcoming me here all their efforts on my behalf over the last four years. I sincerely appreciate the time and effort of my Dissertation Committee to review this work. Many thanks are also due to Tim Zhang, manager of the microscopy facilities for his assistance with SEM and TEM, and Phil Piccoli for his help with the electron microprobe for beam writing.

Thanks to my co-workers, particularly Allan Jaworski and Brett Neuberger, for their teaching, conversations, jokes, and friendship. You did great work and set a high standard for me to live up to.

Finally, I am extremely grateful for the financial support that has allowed me to complete this work, including support of Dr. Briber and the Department of Materials Science and Engineering. This work was funded by the National Science Foundation under Grant Number DMR-0513751.

Table of Contents

List of Tables

List of Figures

Chapter 1

Introduction and Project Aims

Titanium alloys are technologically important. There are numerous properties of titanium alloys that make them desirable for many applications. Among these properties are high strength-to-weight ratio, excellent corrosion resistance, good formability, and biocompatibility. As such, titanium alloys find application in many fields and industries. Aerospace applications currently present the largest market for titanium alloys and they are used in jet engines and in the airframe. Titanium alloys make up the largest fraction by weight of any material in the new F-22 Raptor military fighter plane [1]. Titanium alloys are also used extensively in the biomedical field, as the biocompatibility of the materials makes them ideal for applications such as knee and hip joint implants, dental implants, and pacemaker cases. Further, titanium alloys have many uses in chemical and nuclear industries. Their high temperature performance and corrosion resistance make them ideal for heat exchangers, reactor vessels, and for piping systems. Finally, titanium alloys are increasingly finding application in consumer goods such as jewelry, bicycles, and golf clubs. The applications for titanium alloys are certain to grow in the 21st century, making it critical to understand the microstructure and mechanical behavior of these alloys.

In many applications, titanium alloys may be subject to significant loads or stresses for long periods of time at low temperatures. For the purposes of this investigation, low temperature will be defined as less than $0.25*T_m$, where T_m is the melting temperature of the material in question (1941 K for Ti). It has long been known

that titanium alloys may plastically deform over time, or creep, at low temperature, which may compromise the mechanical reliability of titanium components. For instance, consider the case of the Yucca Mountain nuclear waste storage project. The United States Department of Energy has proposed to bury nuclear waste under Yucca Mountain in Nevada. The radioactive material would be housed within a titanium drip shield, which is a garage-like structure which would protect the material from rockfalls caused by earthquakes and other geological activity. This is illustrated in Figure 1.1 [2]. The titanium drip shield must be able to sustain the weight of any rocks that fall on it for thousands of years at temperatures in the range of 100-150^{o}C.

Other examples where creep of titanium alloys at ambient temperature is an important consideration include pressure vessels, aircraft components, including landing gear, and weight-bearing biomedical implants, such as artificial hip and knee joints. Given the importance of mechanical reliability in these cases, it is critical to understand the low temperature creep deformation mechanisms of titanium alloys so as to design alloys for improved creep resistance.

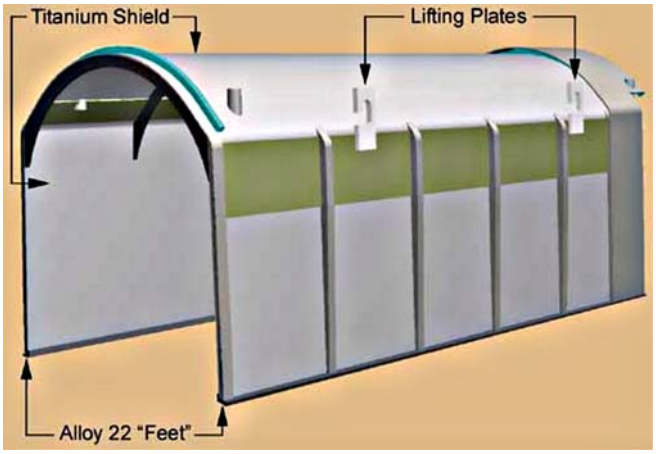

Figure 1.1: Illustration of proposed drip shield for Yucca Mountain nuclear waste storage project [2].

There is currently a lack of understanding regarding some of the fundamental aspects of low temperature creep of Ti alloys, which will be addressed in this investigation. Of particular interest in this investigation is creep by deformation twinning. Slow twin growth (time-dependent twinning) has been identified as a low temperature creep deformation mechanism in coarse-grained (>200 μm) single-phase α and β-Ti alloys. Twinning is limited in fine-grained alloys and hence these alloys show less creep, though it was not clear why. Moreover, the phenomenon of time-dependent twinning is unusual as twinning is typically considered to be a high strain-rate or low (cryogenic) temperature deformation mechanism and twins are expected to grow at the speed of sound in bulk, polycrystalline metals, many orders of magnitude faster than that recorded during low-temperature creep. The activation energy for creep of an α-Ti alloy that deforms by time-dependent twinning was never measured and it was not clear what is the rate-limiting process or how creep deformation products such as dislocations and twins interact. Further, it was suggested in previous investigations that interstitial impurities, particularly oxygen, may be responsible for slow twin growth during creep of Ti alloys, but no models were available to explain this conjecture. To address some of these issues, a systematic investigation has been undertaken. The specific aims of this investigation are as follows:

1. Determine why and how a decrease in the grain size of a Ti alloy reduces the twinning activity and hence, the extent of creep deformation.
2. Determine why twins are growing at speeds much lower than the speed of sound in BCC β-Ti alloys by atomistic modeling of the twin growth process and determining the activation energy for twinning.

3. Similarly for HCP α-Ti alloys, determine why twins are growing at speeds much lower than the speed by atomistic modeling of the twin growth process and determining the activation energy for twinning.
4. Experimentally measure the activation energy for low temperature creep of an α-Ti alloy, namely α-Ti-1.6wt.%V, and compare this value to the theoretical value for time-dependent twinning.
5. Further, in the creep deformed α-Ti-1.6V, systematically identify and characterize the deformation products by optical, SEM, and TEM microscopy, with the particular focus on interactions between dislocations and twins and how the microstructure, i.e. grain size may affect the creep behavior.

A thorough literature review and technical background is given in Chapter 2. Chapter 3 gives an outline of the experimental and theoretical procedures. The results and discussion are included in Chapter 4. Chapter 5 gives the main conclusions and Chapter 6 gives some potential avenues for future work.

Chapter 2

Technical Background

This chapter consists of a brief review of titanium alloys phases, creep deformation behavior, and previous studies which are most relevant to the present investigation.

2.1 Titanium Alloy Phases

Single phase titanium alloys may be characterized by one of two microstructures. The hexagonal close-packed, HCP (α) phase is the stable phase at room temperature. At 1155 K (882^{o}C), titanium undergoes an allotropic phase transition to the body-centered cubic, BCC (β) phase [3].

2.1.1 α-Titanium Alloys

Unalloyed titanium and alloys of it with α stabilizing elements are in the HCP α-phase at room temperature. Elements which increase the allotropic transformation temperature, typically simple metals or interstitial elements, such as Al, Ga, Sn, or O, are known as α stabilizers [3]. These alloys have good strength, toughness, and weldability. Further, they have no ductile-to-brittle transition, making them suitable for cryogenic applications. A phase diagram for a typical α-titanium alloy is seen in Figure 2.1.

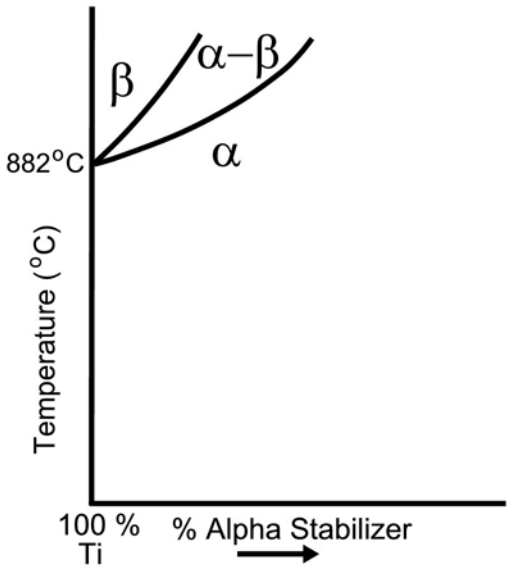

Figure 2.1: Phase diagram of a typical α-Ti alloy.

2.1.2 β-Titanium Alloys

β-titanium alloys are metastable at room temperature and β-stabilizing elements decrease the allotropic transformation temperature of titanium. β-stabilizers are generally transitions metals such as Mo, V, Nb, and Ta [3]. Advantages of β-Ti alloys include their cold workability and their hardenability. The stability of the β-phase is an important consideration in these alloys. The lower the phase transformation, the more β phase will remain after quenching. To quantify stability, the molybdenum equivalency (MoE) is given for any β–alloy with any number and concentration of α and β stabilizers [4]. Molybdenum is the reference β-stabilizing element and the MoE of an alloy is the volume percent of Mo in a Ti-Mo alloy with the same stability. A MoE of about 10 is required to stabilize the β phase [4]. A phase diagram for a typical β-titanium alloy is shown in Figure 2.2.

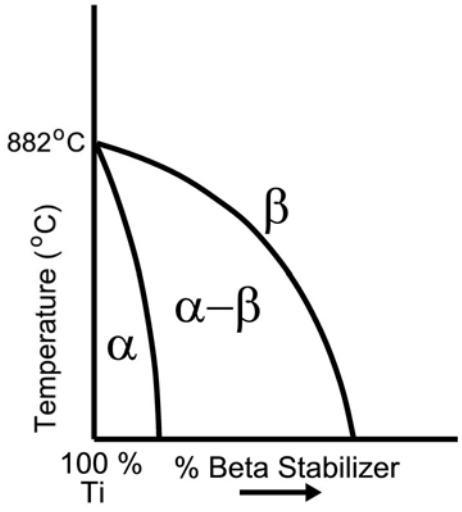

Figure 2.1: Phase diagram of a typical β-Ti alloy.

2.2 Creep

The subject of this investigation is the low temperature ($<0.25*T_m$) creep behavior of single phase α and β titanium alloys. The term *creep* refers to the time-dependent deformation of a material under an applied load [5]. Creep is generally considered to be a high-temperature phenomenon, where high-temperature would be defined as greater than $0.25*T_m$, where T_m is the melting temperature of the material in question. Titanium alloys, and other alloys such as high strength steel, however, are known to creep at room temperature, which is much less than $0.25*T_m$. As such, creep in these materials is considered to be a low-temperature phenomenon.

Creep behavior is divided into three stages. After an initial, instantaneous elastic strain, ε_0, the creep strain increases with time while the creep *rate* decreases. This region

is called stage I or primary creep and the deformation is described by a power law of the type given in Equation 2-1:

$$\varepsilon = A^* t^a \tag{2-1}$$

where t is the time and A^* and a are constants. The constant a is a measure of the creep exhaustion rate and smaller values of a correspond to a more rapid exhaustion. The value of a is often taken to be 1/3, but generally varies from a value of between 0.03 and 1 [5]. When dynamic equilibrium is reached between the applied load and the microstructure, a minimum creep rate is obtained and there is a linear relationship between creep strain and time. This is referred to as stage II or secondary creep. Finally, after extensive deformation, large defects cause the creep rate to increase dramatically, during stage III, or tertiary creep. Mechanisms for high-temperature creep include vacancy diffusion through the bulk (Nabarro-Herring creep) or along the grain boundaries (Coble creep), dislocation climb, or grain boundary sliding [5]. Given the low-temperature creep seen in titanium alloys, it is unlikely that these mechanisms will be at work in the given temperature range. The three stages of creep are shown in the strain (ε) vs. time curve in Figure 2.3.

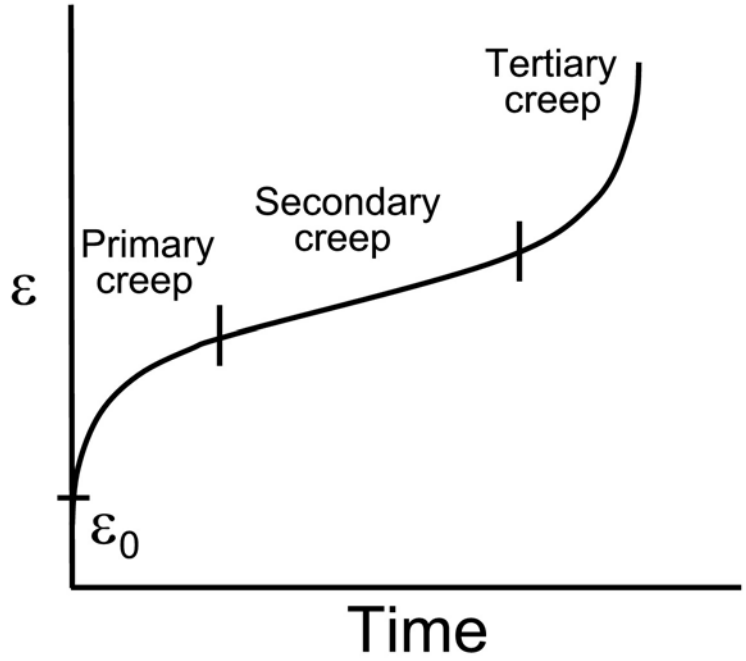

Figure 2.2: Typical strain vs. time curve illustrating the three stages of creep.

2.3 Ambient Temperature Creep of Single Phase Titanium Alloys

In many of the applications of single phase titanium alloys, the components may be subject to significant stresses at ambient temperatures for long periods of time. It has long been known that titanium alloys show primary creep at low temperatures ($<0.25*T_m$) [6-17], so creep at these temperatures becomes an important factor. Given the difference in microstructure and chemistry of single phase α and β titanium alloys, the low temperature creep behavior of the respective phases will be reviewed separately below.

2.3.1 Ambient Temperature Creep of α Titanium Alloys

Creep of commercially pure titanium at room temperature was first reported by Adenstedt in 1949 [6]. He identified creep at stresses from 60 to 90% of the yield stress. A more thorough analysis by Zeyfang, *et al* [12] in 1971 suggests that the rate controlling process during low temperature creep of α titanium alloys is the thermally activated overcoming of interstitial atoms by dislocation glide. More recent studies, however, have incorporated TEM microscopy and modeling to identify creep deformation mechanisms and more systematically characterize the effect of microstructure on creep deformation behavior [18-22].

Neeraj, *et al,* [18] have analyzed creep deformation of α-Ti-6Al, and several phenomena are of particular interest. It is suggested that low strain hardening exponents in the alloy may be responsible for significant room temperature creep. The low strain hardening is attributed to the very planar nature of slip in the alloy. Dislocations are generally found in groups or arrays, possibly due to short-range ordering of Ti and Al atoms in the alloy [21]. The heterogeneity of the dislocation structure means that interaction between slip systems will occur infrequently and will not present a significant barrier to dislocation motion.

One aspect of the microstructure that is particularly important in HCP materials is the crystal orientation, as the orientation is known to have a large effect on the deformation behavior. In particular, the resistance to slip, or critical resolved shear stress (CRSS), is highly anisotropic in HCP materials [21]. This means that for a given applied stress orientation, there will be grains that are more or less favorably oriented for slip. Hasija, *et al*, [21] suggest that during primary creep of α-Ti-6Al, slip will first occur on

grains most favorably oriented for slip. To maintain compatibility, load will be distributed to neighboring grains which are not as favorably oriented for slip, leading to significant local stress concentrations.

The α-Ti-6Al alloy described above is a fine-grained (20 μm) alloy and is highly stabilized by the presence of a significant quantity of Al and slip is the only identified creep deformation mechanism. The work by Ankem and co-workers [23-26], however, has suggested another potentially significant creep deformation mechanism, namely twinning. Twinning is a deformation mechanism in which the atoms in the twinned part of the material are sheared to positions which form a mirror with that of the untwinned part of the materials [5]. Similar to slip, twins grow on particular crystalline planes in definite crystalline directions. Twinning has long been associated with rapid (shock) loading [5] and it is expected that deformation twins in bulk, polycrystalline metals grow at a very high rate of speed, i.e. the speed of sound [27]. Ankem and co-workers [23], however, were the first to observe that during room temperature creep deformation of α-Ti-0.4Mn, twins grow at speeds that are many orders of magnitude lower than the speed of sound, as illustrated in Figure 2.4. This unexpected phenomenon, referred to as time-dependent twinning, was subsequently observed in the α-Ti-1.6V alloy as well, as seen in Figure 2.5 [26].

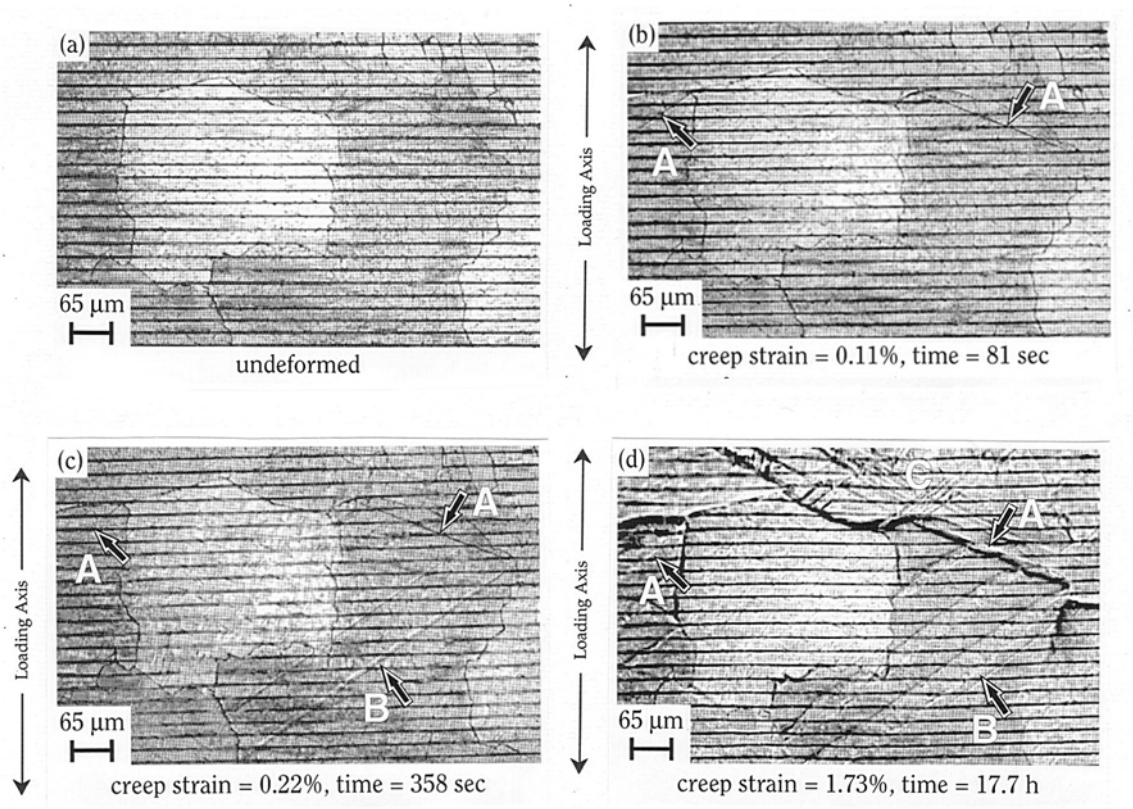

Figure 2.4: Creep tested α-Ti-0.4 Mn, grain size = 500 μm, stress level = 95% YS, T ~ 300 K. Optical micrographs of (a) undeformed, (b), (c), and (d) deformed α-Ti-0.4 Mn alloy. Horizontal lines are gold fiducial lines. (b) shows instantaneous twins at "A", (c) shows nucleation of new twins at "B", and (d) shows the growth of twins at "A" and "B" and the formation of new twins at "C" [23].

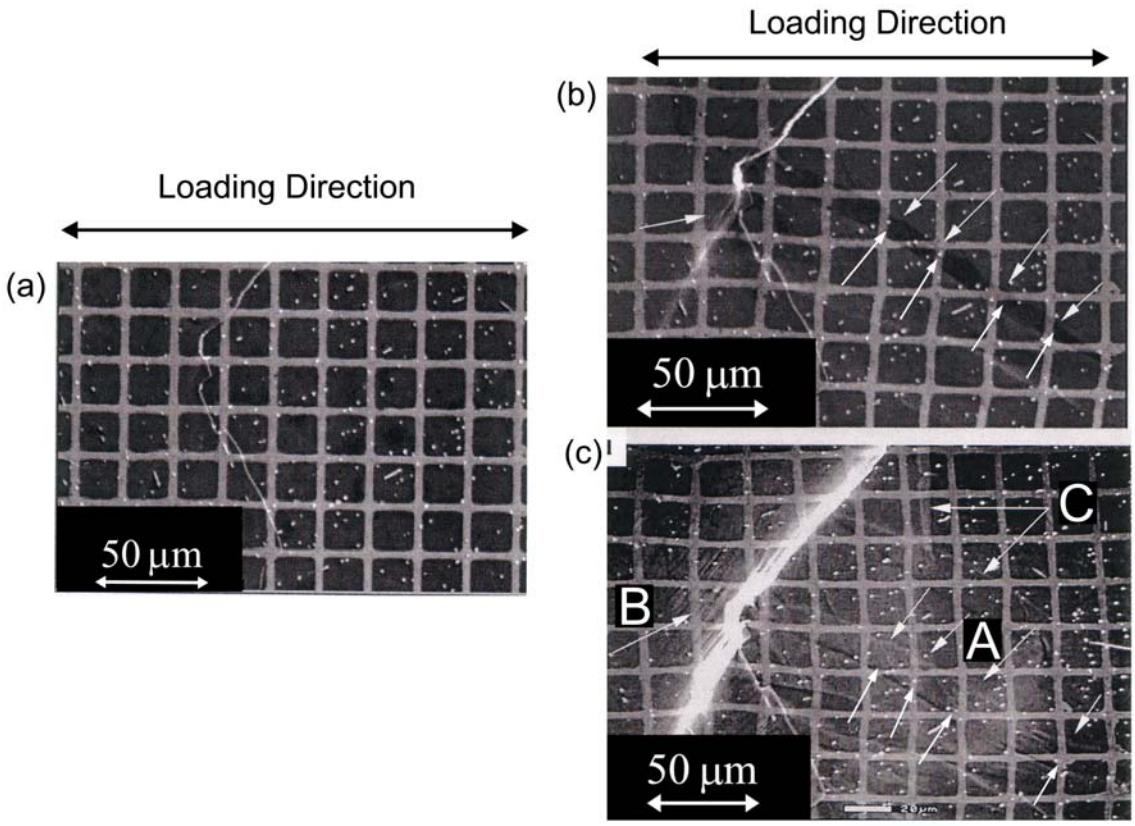

Figure 2.5: Creep tested α-Ti-1.6 V alloy, grain size = 226 μm, stress level = 95% YS, T ~ 300 K. Secondary SEM images of specimen after (a) 3 minutes, (b) 10 hours with arrows indicating twin (right side) and slip lines (left side), and (c) 200 hours with arrows at "A" indicating growth of twin, arrow at "B" indicating coarse slip lines, and arrow at "C" indicating growth of new twins [26].

Given the complex ambient temperature creep deformation behavior of α-Ti alloys, Ankem and co-workers have done extensive work to characterize the effect of parameters such as grain size and applied stress level on creep deformation. Regarding the effect of grain size, Ankem, *et al* [23], and Aiyangar, *et al* [26], have observed that in the α-Ti-0.4Mn and α-Ti-1.6V alloys, respectively, the extent of twinning and hence the amount of ambient temperature creep strain increases with increasing grain size. Large grained alloys (>200 μm) show extensive slip and time-dependent twinning, whereas fine

grained alloys (<100 μm) deform solely by slip [23, 26]. Ambient temperature creep curves for the alloys are shown in Figure 2.6. This observation is opposite that expected for high temperature creep where fine grained alloys show increased creep due to grain

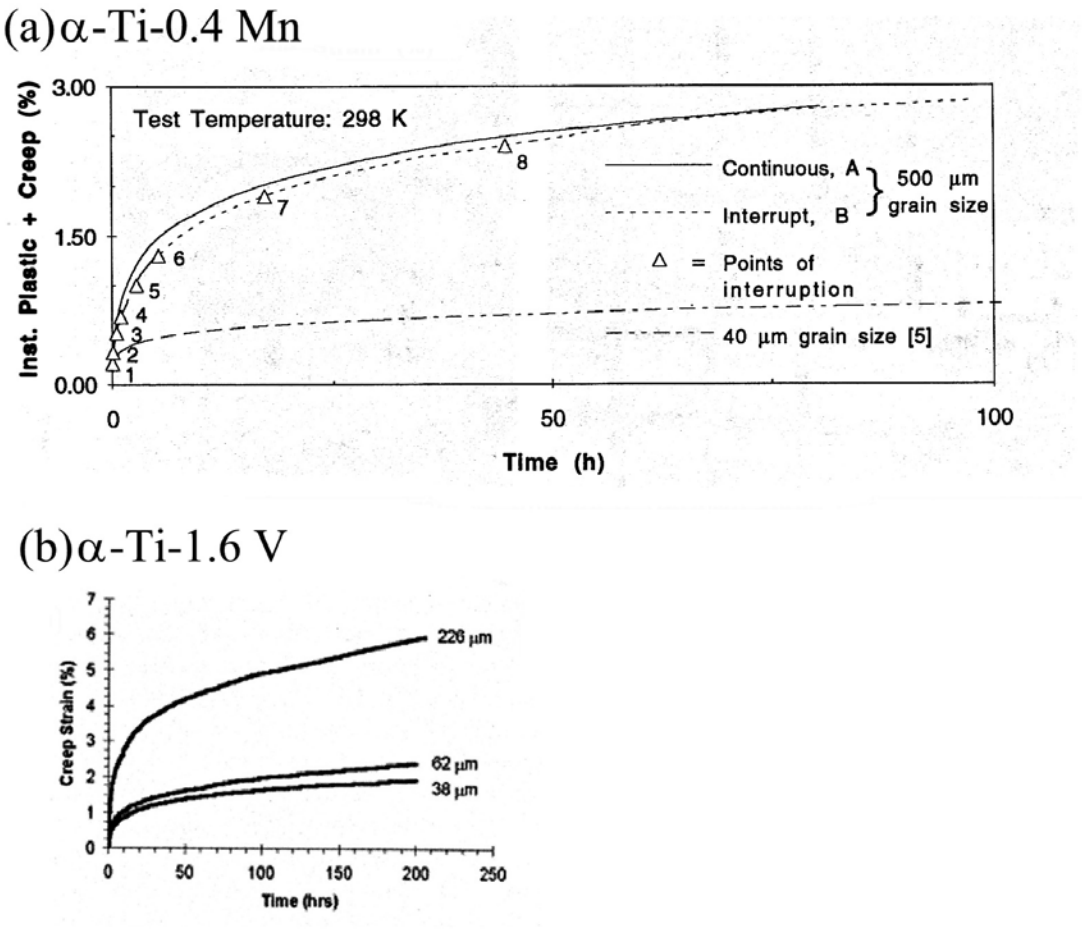

Figure 2.6: Ambient temperature creep curves for different grain sizes of (a) α-Ti-0.4 Mn [23] and (b) α-Ti-1.6 V [26]. For (a), stress level is 95% YS. For (b), stress level is 90% YS.

boundary sliding. The amount of creep strain, ε, is related to the time of testing, *t*, by a power law relation of the type given in Equation 2-1. The creep constant, A^*, varies with grain size, *d*, according to an equation of the type given in Equation 2-2:

$$A^* = A' d^m \tag{2-2}$$

where A' and m are constants. Moreover, when the α-Ti-1.6V was creep tested with constant grain size (226 μm) at varying stress levels [26], it was found that the amount of creep strain decreased with decreasing stress level and would be negligible at stresses less than approximately 60% YS, as seen in Figure 2.7. At varying stress levels, the creep strain, ε, is best related to time of testing by a logarithmic fit of the type given in Equation 2-3:

$$\varepsilon = A' + B \ln t \tag{2-3}$$

where A' and B are constants (A' represents a different constant than that given in Equation 2-2).

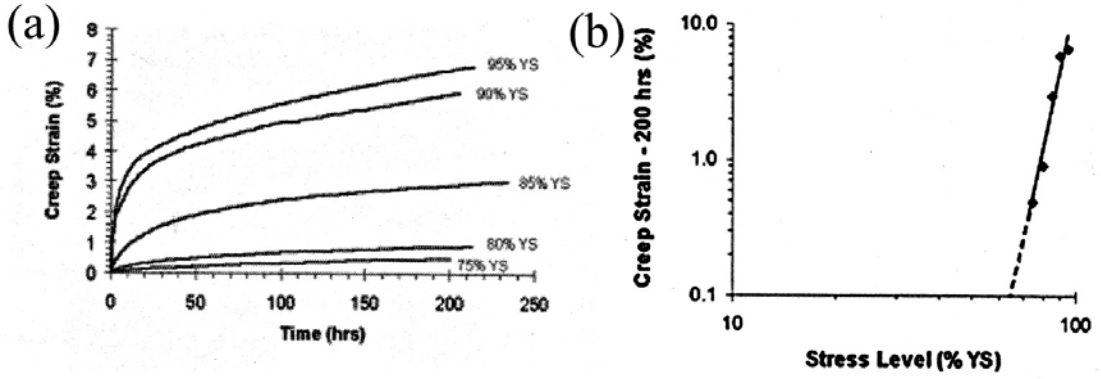

Figure 2.7: Effect of stress level on ambient temperature creep of α-Ti-1.6V. (a) Creep curves of coarse grained (226 μm) alloy tested at various stress levels. (b) Log-log plot of creep strain vs. stress level [26].

2.3.2 Ambient Temperature Creep Deformation of β-Titanium Alloys

The ambient temperature creep deformation of β-titanium alloys has been studied less extensively than that of α titanium alloys. Factors that must be considered include the grain size and stability of the β phase. Ankem and co-workers [28, 29] examined the effect of grain size on the ambient temperature creep deformation of the β-Ti-14.8V and β-Ti-9.4Mn alloys. As is the case for α-titanium alloys, specimens with large grain size showed more creep deformation than fine-grained alloys. The creep deformation mechanisms for β-Ti-14.8V were identified as slip and time-dependent twinning [28] whereas β-Ti-9.4Mn deformed solely by slip [29]. Examination of twin growth by interrupt creep testing, seen in Figures 2.8 and 2.9 [30], shows that the twins grow slowly, as described for α-titanium alloys. Twinning in Ti-14.8V is less extensive in fine-grained alloys, suggesting that the smaller grain size impedes the formation and growth of twins [28]. The extent of creep deformation is again best related to time of testing, t, by a power law of the type described for α-titanium alloys in Equation 2-1. Again, as for α-titanium alloys, the creep constant, A^*, varies with grain size, d, according to an equation of the type given in Equation 2-2.

The stability of the β phase must also be considered when describing the ambient temperature creep deformation behavior of β titanium alloys. Ankem and co-workers [28, 29] have examined creep behavior in β-titanium alloys of varying stability, namely Ti-14.8V, Ti-9.4Mn, and Ti-13Mn, with MoE of 9.9, 14.3, and 19.9, respectively. It was shown that for coarse grained alloys, the amount of creep strain increases with decreasing stability of the β-phase. β-Ti-13Mn, the most stable β alloy, shows almost no creep

strain at room temperature whereas β-Ti-14.8V, the least stable β alloy, shows the greatest creep strain. It is known that in lower stability β-titanium alloys, i.e. Ti-14.8V and Ti-9.4Mn, there exists a second metastable (ω) phase in the β matrix that is not present in higher stability alloys such as Ti-13Mn. This suggests that the presence of the ω-phase may be a factor in decreasing creep resistance in lower stability β alloys.

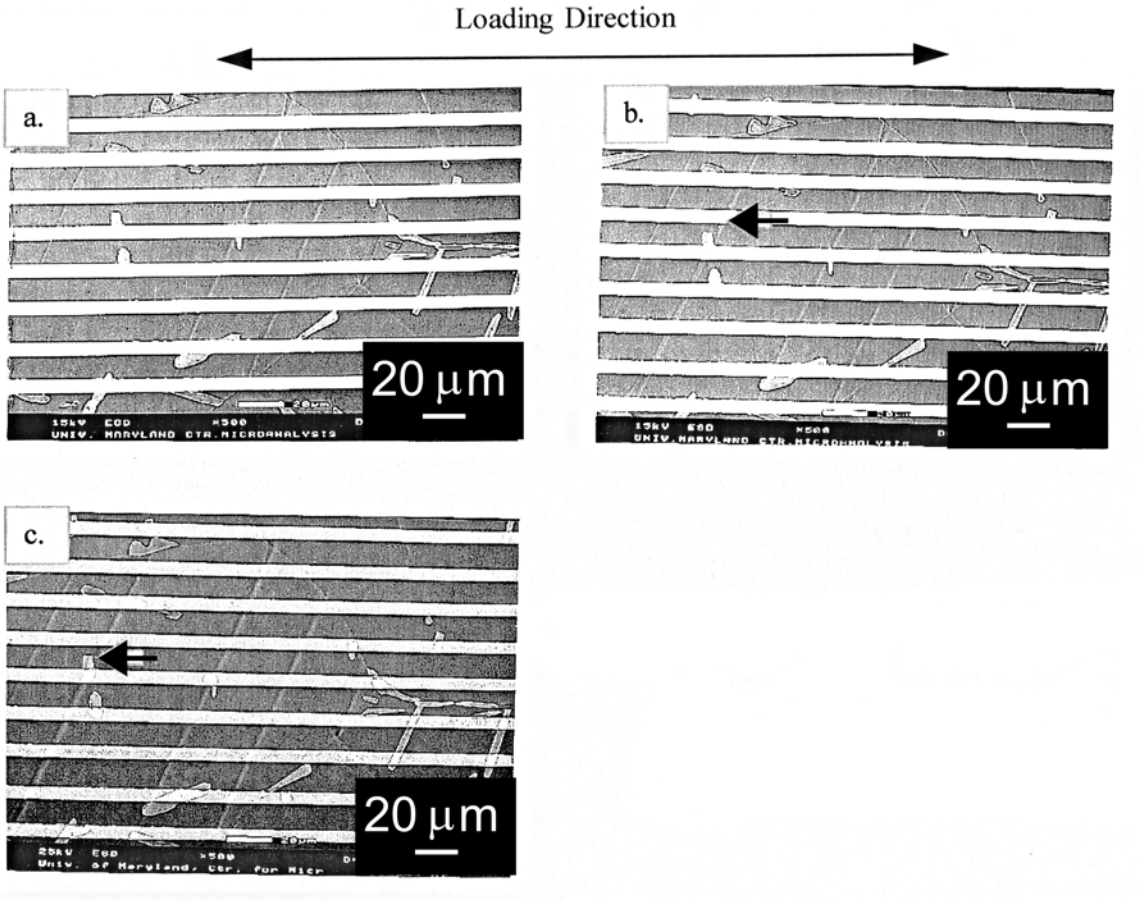

Figure 2.8: SEM micrographs from interrupt creep test of β-Ti-14.8V. Stress level is 95%YS. Grain size is 350 μm. (a) After 3.62 minutes. Strain = 0.056%. (b) After 1.68 hours. Strain = 0.07%. Note formation of twin indicated by arrow. (c) After 8.13 hours. Strain = 0.075%. Note thickening of twin at arrow [30].

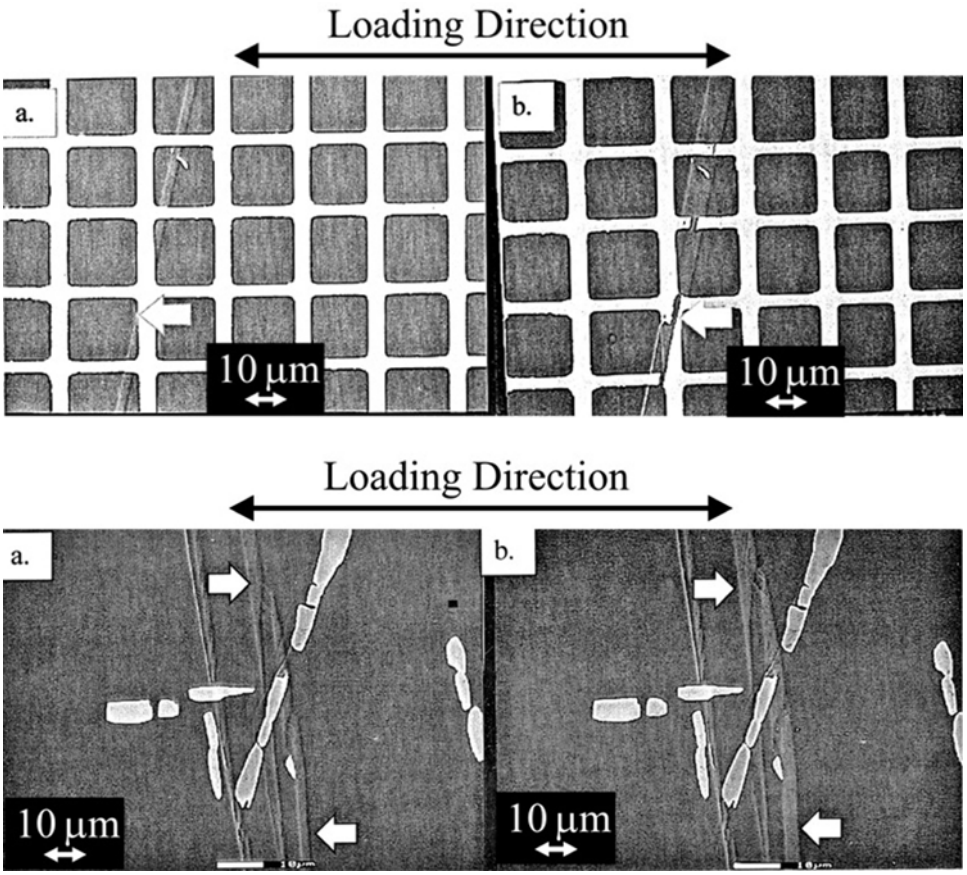

Figure 2.9: SEM micrographs from interrupt creep test of β-Ti-14.8V. Stress level is 95%YS. Grain size is 350 μm. Figures are taken from two areas of the same specimen. Figures labeled (a) are after 3.62 minutes where strain = 0.056%. Arrows indicate twins. Figures labeled (b) are after 1.68 hours where strain = 0.07%. Note thickening of twins at arrows [30].

Moreover, in β titanium alloys which do show ambient temperature creep, the stability will affect the creep deformation mechanisms. Interrupt creep testing on coarse-grained Ti-9.4Mn [29] shows that slip is the predominant creep deformation mechanism, and no twinning is observed. Further, most of the slip lines are generated in the first 10 minutes of the creep test. Recall that in the lower stability Ti-14.8V alloy, time-dependent twinning was seen to be a significant deformation mechanism [28]. This suggests that there is a critical stability above which twinning will not occur in β titanium alloys. The effect of grain size and stability on ambient temperature creep of β titanium alloys is shown in Figure 2.10.

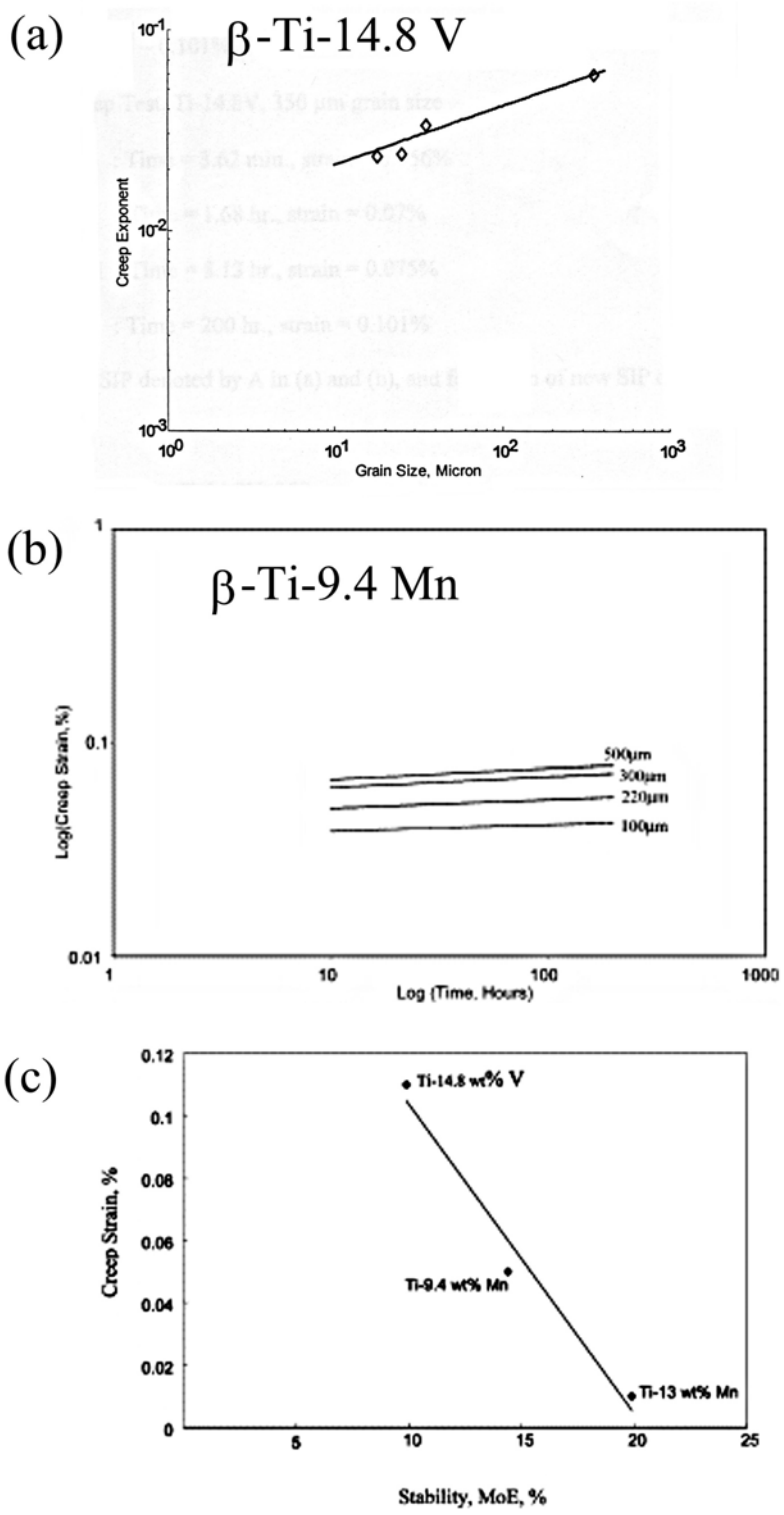

Figure 2.10: Effect of grain size and stability on ambient temperature creep of β-Ti alloys. (a) Variation of creep exponent, *a*, (from Equation 2-1) with grain size for Ti-14.8 V [28]. (b) Log-log plot of creep strain vs. time for various grain sizes of Ti-9.4 Mn [29]. (c) Creep strain vs. stability for three β-Ti alloys [29].

2.4 Elements of Twinning

As mentioned above, twinning is the predominant deformation mechanism during low temperature creep of large-grained α and β titanium alloys. As twinning will be the focus of the majority of this investigation, the elements of twinning will be reviewed here. According to the classical theory of deformation, the original untwinned (matrix) lattice is transformed by displacements which are equivalent to, or an integral fraction of, a simple shear of the lattice points [31]. There are two planes which are not distorted by the shear of the lattice. One of these, denoted $\mathbf{K_1}$, is referred to as the twinning plane and the shear direction is given by $\boldsymbol{\eta_1}$. The second undistorted, or conjugate plane is denoted $\mathbf{K_2}$ and the plane of shear, **P**, contains $\boldsymbol{\eta_1}$ and the normals to $\mathbf{K_1}$ and $\mathbf{K_2}$. The intersection of $\mathbf{K_2}$ and **P** gives the conjugate or reciprocal shear direction, $\boldsymbol{\eta_2}$. When describing a twin, it is typical to identify the twin by the shear plane, $\mathbf{K_1}$ and the shear direction, $\boldsymbol{\eta_1}$, i.e. $\{hkl\}\langle uvw\rangle$. Twins are typically classified as Type I or Type II depending on the nature of the twinning elements [31]. For Type I twins, $\mathbf{K_1}$ and $\boldsymbol{\eta_2}$ have rational indices and the orientation change may be described as a reflection in $\mathbf{K_1}$ or a rotation of 180^o about the normal to $\mathbf{K_1}$. For Type II twins $\mathbf{K_2}$ and $\boldsymbol{\eta_1}$ have rational indices and the orientation relation may be described as a rotation of 180^o around $\boldsymbol{\eta_1}$ or a reflection in the plane normal to $\boldsymbol{\eta_1}$. The planes and directions associated with twinning are schematically illustrated in Figure 2.11.

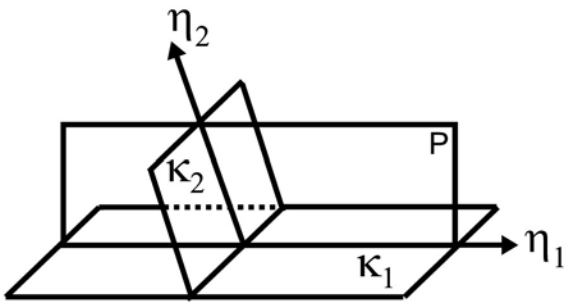

Figure 2.11: Schematic illustration of planes and directions associated with twinning.

Consider the case of a simple twin in the BCC lattice, the $\{112\}\langle 11\bar{1}\rangle$ twin. This means that atoms lying on the $\mathbf{K_1} = \{112\}$ planes of the BCC lattice will be sheared in the $\boldsymbol{\eta_1} = \langle 11\bar{1}\rangle$ direction from the untwinned matrix to the twinned position such that they are symmetric to an untwinned atom on the other side of the twin-matrix interface. Consider the illustration in Figure 2.12. The BCC lattice is projected onto a $\{110\}$ type plane. The lower half of the figure shows the atoms in the untwinned position. The arrows in the upper part of the figure show the shear required to move the atoms from the untwinned (solid blue) to the twinned (dashed blue) positions. Note that the magnitude of shear is proportional to the distance from the twin-matrix interface. After twinning, there is mirror symmetry across the (112) twinning plane.

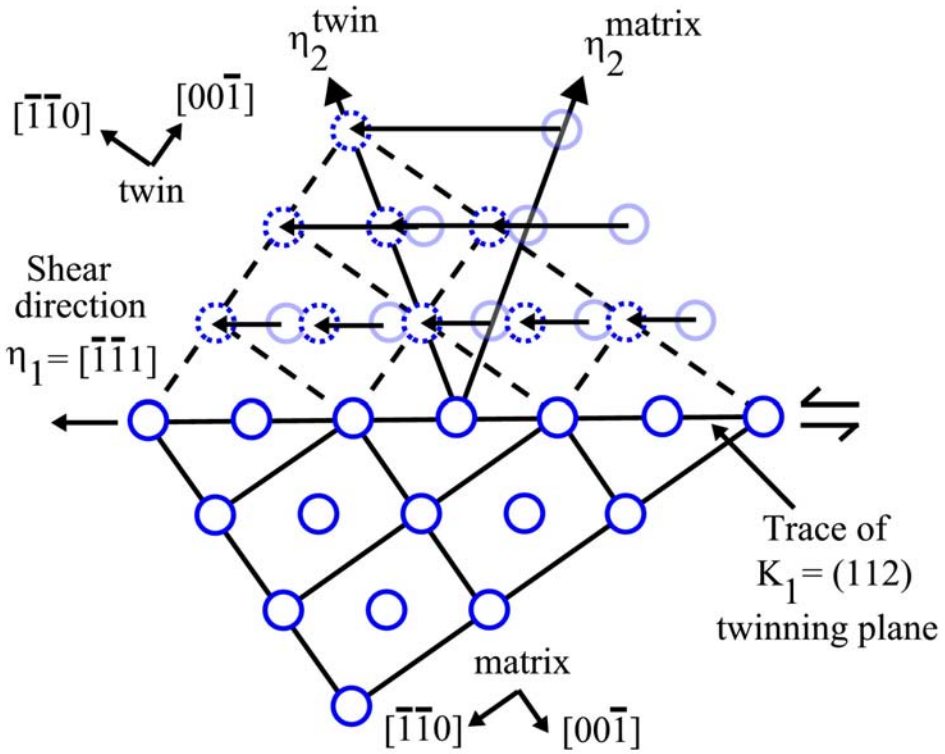

Figure 2.12: Schematic illustration of $\{112\}\langle 11\bar{1}\rangle$ twinning in the BCC lattice. Lattice is projected onto a $\{110\}$ plane. Arrows indicate shear of atoms from untwinned (solid blue) to twinned (dashed blue) position.

Chapter 3

Experimental and Theoretical Procedures

3.1 Materials, Processing, and Heat Treatments

3.1.1 Materials

The alloy used in this investigation in an α-Ti-1.6 wt.%V alloy. The chemical composition of the alloy is given in Table 3.1. The chemical compositions are actual chemical compositions of the alloys after fabrication as determined by the wet chemistry method. This alloy has a hexagonal close packed (HCP) crystal structure. The Ti-V phase diagram is shown in Figure 3.1.

Table 3.1 – Chemical Composition of α-Ti-1.6wt.%V Alloy

Vanadium (wt.%)	Carbon (wt.%)	Nitrogen (wt.%)	Oxygen (wt.%)	Iron (wt.%)	Hydrogen (ppm)
1.62	0.01	0.012	0.069	0.02	50

3.1.2 Processing

The alloy was melted as 13.6 kg ingots and processed to 1.74 cm diameter bars at RMI Co. in Niles, Ohio (now RTI International Metals, Inc.). The final step (rolling) was carried out in the α−β phase field at 973 K. A 60% reduction in area was given for the alloys.

3.1.3 Heat Treatments

The rods were sectioned to the required length and encapsulated in quartz tubes. The tubes were vacuum-sealed at a pressure of 10^{-5} Pa. To obtain the desired

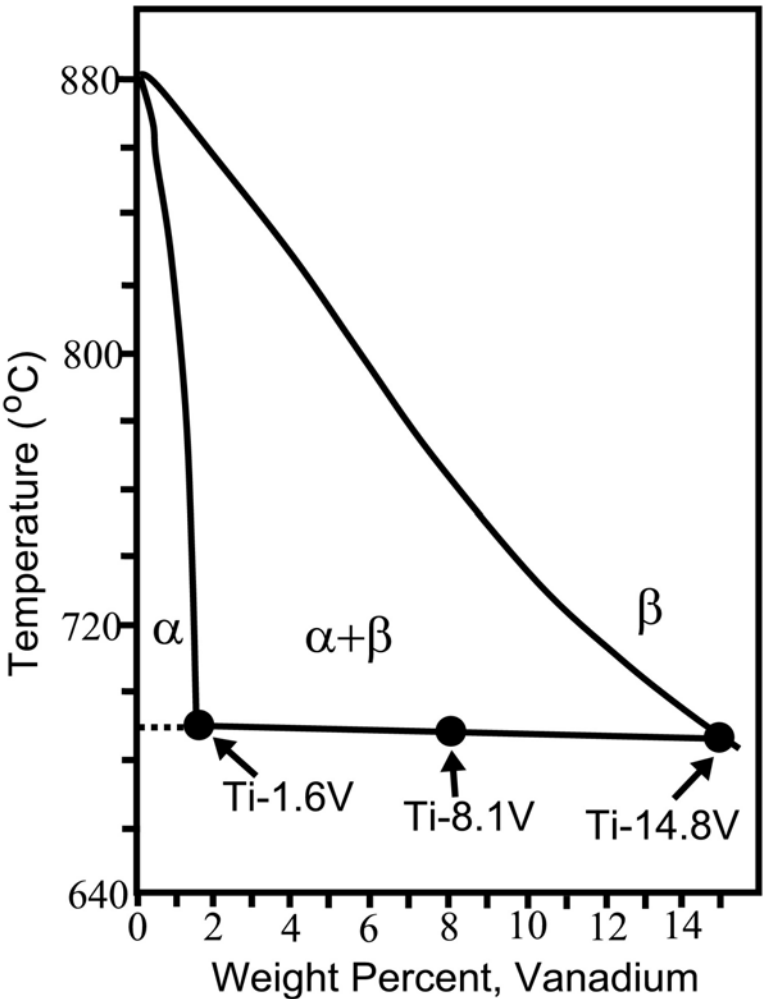

Figure 3.1: Ti-V phase diagram.

microstructure, the alloy was annealed at 900°C for 2 hours, furnace cooled to 690°C, annealed at 690°C for 200 hours, and water quenched to room temperature. The quartz tubes were broken before quenching to ensure a fast quench.

3.2 Machining

Creep specimens were machined from the quenched bars. Multiple passes and small cut depths were used to minimize the amount of strain induced. The samples were threaded with 1.23 cm (0.485") diameter ends to fit threaded grips. The length of the gage section was maintained at 1.13". The diameter of the gage section was machined to 0.25". Flats were then made on the cylindrical gage section using the Electron Discharge Machine (EDM) to minimize any possible deformation that may be induced by conventional milling. The thickness across the flats was maintained at 0.15". A schematic of the test specimens is shown in Figure 3.2.

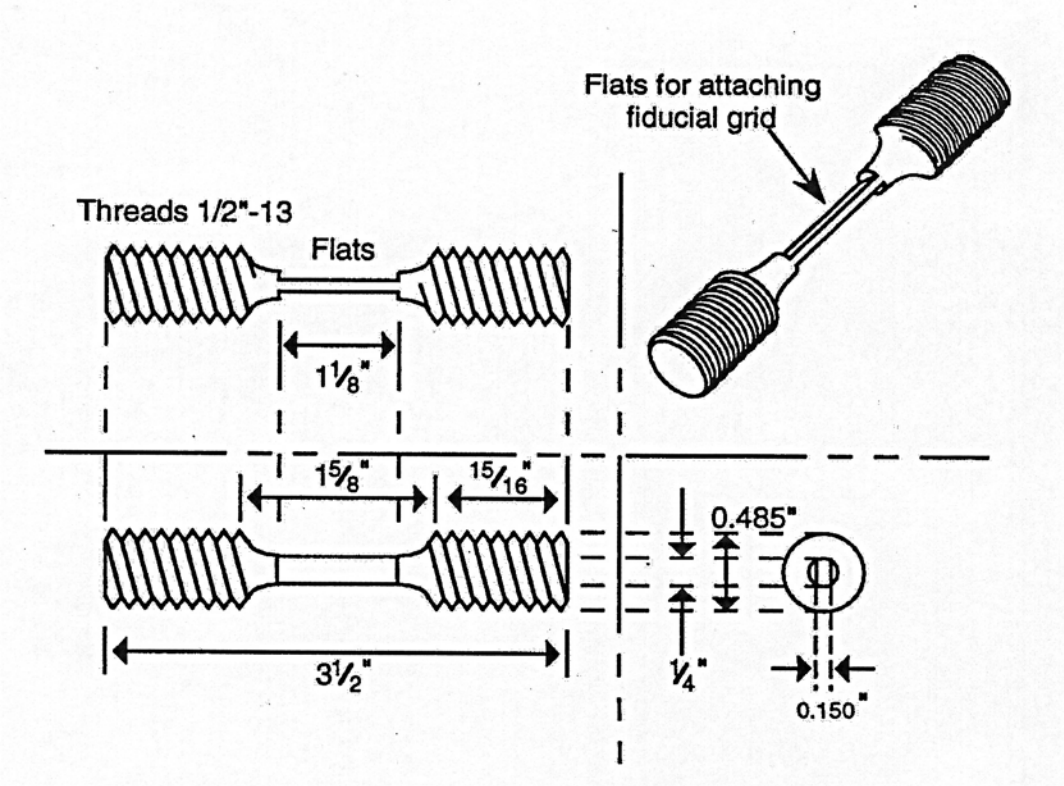

Figure 3.2: Schematic illustration of creep test specimens.

3.3 Sample Preparation

The procedure for the preparation of the samples for creep testing consists of the following steps:

1. Hand polishing
2. Etching

3.3.1 Hand Polishing

The aim of polishing is to obtain a smooth and scratch free surface with no deformation products such as twins. The first step is to hand polish the surfaces of the specimen with silicon carbide grit paper. Relatively coarse 600 grit paper is used first followed by 800 then 1200 grit paper. With each successively finer grit, polish in a direction perpendicular to that of the previous grit until no scratches are visible to the naked eye in that direction. The specimen is rinsed with water and dried with compressed air every few minutes to reduce abrasion by residual particles. The 600 grit paper was used for approximately 10 minutes per side followed by 30 minutes per side for the 800 and 1200 grit.

In previous experimental works, electropolishing was used as a final finish on the specimens to produce a mirror surface. This process, however, comes with a risk of heavily pitted specimens and a low success rate. Given the limited number of Ti-1.6V test specimens available for creep testing, an alternative final polishing step was used. Buehler Mastermet® colloidal silica polishing suspension on a Chemomet® pad was used for the final polishing of the creep specimens. The specimen was polished for

approximately 20 minutes on each side to achieve a mirror finish and until no scratches or surface features were visible under an optical microscope.

3.3.2 Etching

Chemical etching is done in order to reveal the grain boundaries. Two different etchants are used. Previous experimental works have used what is known as A-etch to reveal the grain boundaries. This etchant includes glycerin, nitric acid, and hydrofluoric acid and is highly reactive. It carries the risk of explosion if stored in closed bottles over a long period. To minimize this risk, a different etchant, commonly known as Kroll's reagent was used to reveal the grain boundaries. The composition of this etchant is given in Appendix A. The specimen flat surface is etched very lightly with Kroll's reagent for approximately 20 seconds per side with a cotton swab. Kroll's reagent is a low-contrast etchant so the specimen is rinsed and next etched with R-etch which stains the surface of the specimen. The composition of this etchant is given in Appendix A. The surface is etched for approximately 10 seconds with R-etch.

3.4 Attachment of Fiducial Grids

Gold-palladium fiducial lines were deposited on the polished specimen surfaces following the method of Attwood and Hazzledine [32] to allow easy identification of the same area for pre- and post-testing microscopy. Shipley Microposit 950 C6 PMMA positive electron resist (about 5 to 6 drops) was spun onto the specimen surface at 3300 PPM for 50 seconds in a UV free clean room and pre-baked at 170^{o}C for 30 minutes. The specimens were transported in aluminum foil inside a sealed box to guard the resist

from light. A JEOL 840 microprobe was used to expose the resist. The specimen is placed into the microprobe with the lights off though the resist should not be sensitive to normal light for a short period of time. The grid line spacing was set for 50 μm. Beam writing conditions were 25 kV, 25x magnification, aperture size 4, beam current 100 nA, and exposure time 1 second. Following beam writing, the specimen was transported in a dark box to the dark room where the resist was developed for one minute with agitation in Shipley MIBK:IPA 1:3 Developer. At this point, the specimen can be taken into light and the grid was examined on an optical microscope to verify that the line drawing process was a success. If the grid is acceptable, the specimen surface is lightly etched for about 15 seconds with dilute titanium etch (given in Appendix A) to facilitate the removal of the resist. The specimen is rinsed with water and air dried. Next, a layer of gold-palladium was sputter deposited onto the specimen to a thickness of 50 nm by an Anatech LTD Hummer X sputtering system. To remove the remaining photoresist, the specimen was sonicated in acetone for 10 minutes.

3.5 Creep Testing

3.5.1 Creep Test Apparatus

Creep testing was conducted on an Applied Test Systems (ATS) Series 2330 creep tester with a lever arm ratio of 20:1 rated at 20,000 lbs. To enable elevated temperature testing, an ATS Series 3210 split tube furnace with a Series 3910 retort assembly for controlled gas environment is installed in the center of the creep tester frame. Testing was performed in an argon atmosphere. After the specimen is loaded and the furnace is sealed, argon is run through the furnace for 3 to 4 hours to purge the system

of oxygen. Following this step, the furnace is turned on and about 5 to 6 hours before testing starts so that the temperature of the creep specimen will reach equilibrium. The creep test apparatus is shown in Figures 3.3-3.6 [33]. Prior to testing, the equipment was inspected and calibrated by a technician from ATS. The equipment should be calibrated once per year. Instructions for loading and unloading specimens from the creep tester are included in Appendix B.

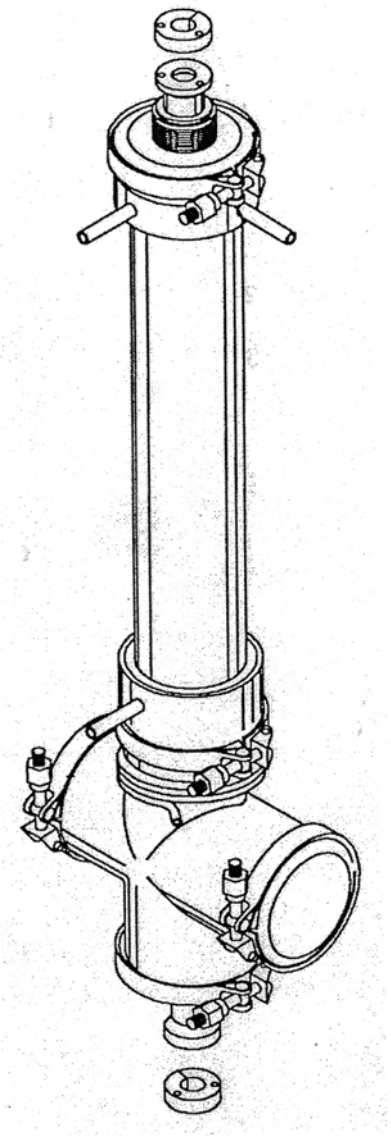

Figure 3.3: Applied Test System Series 3910 retort chamber assembly design. For controlled gas contained atmospheric conditions [33].

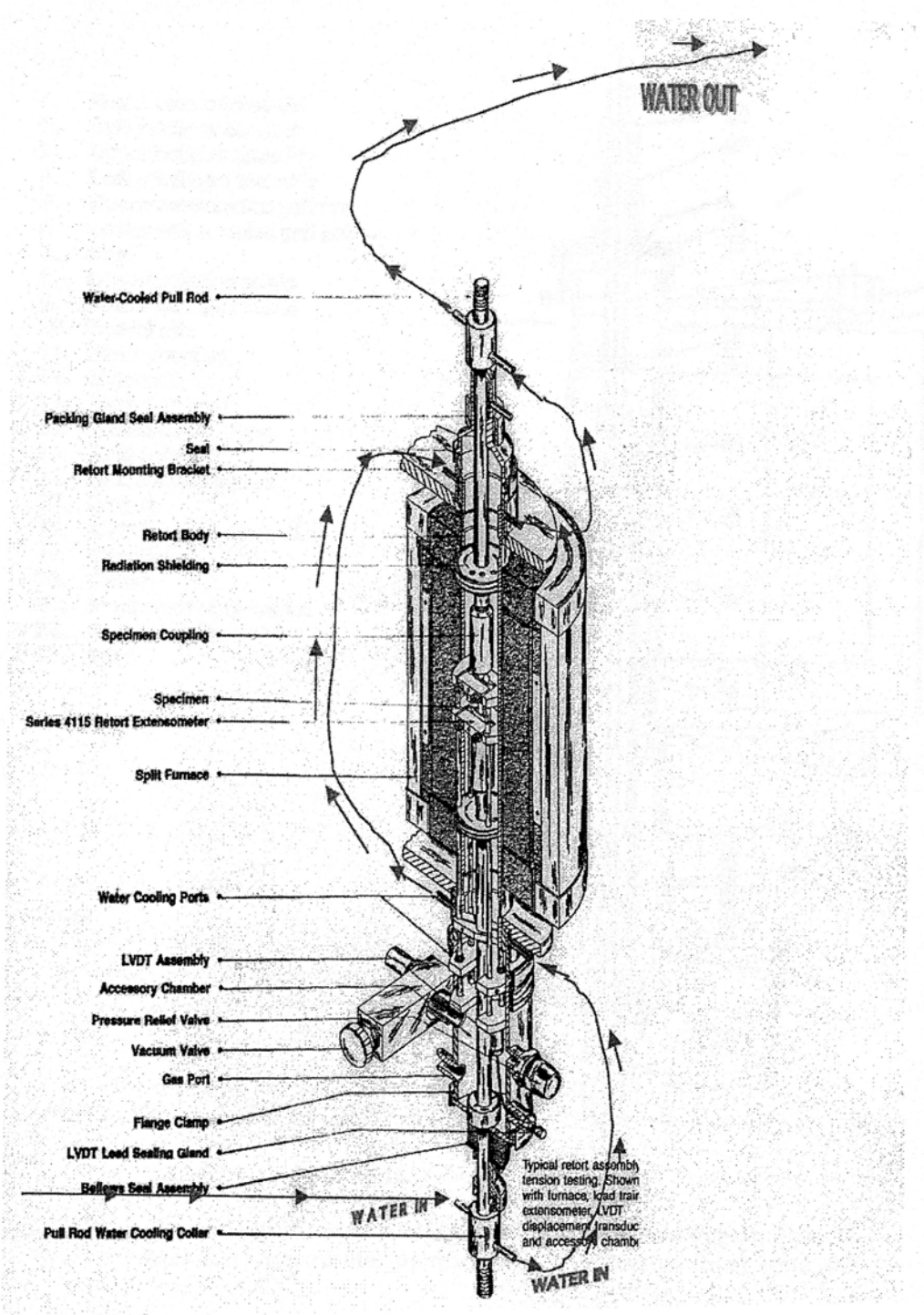

Figure 3.4: Creep furnace assembly [33].

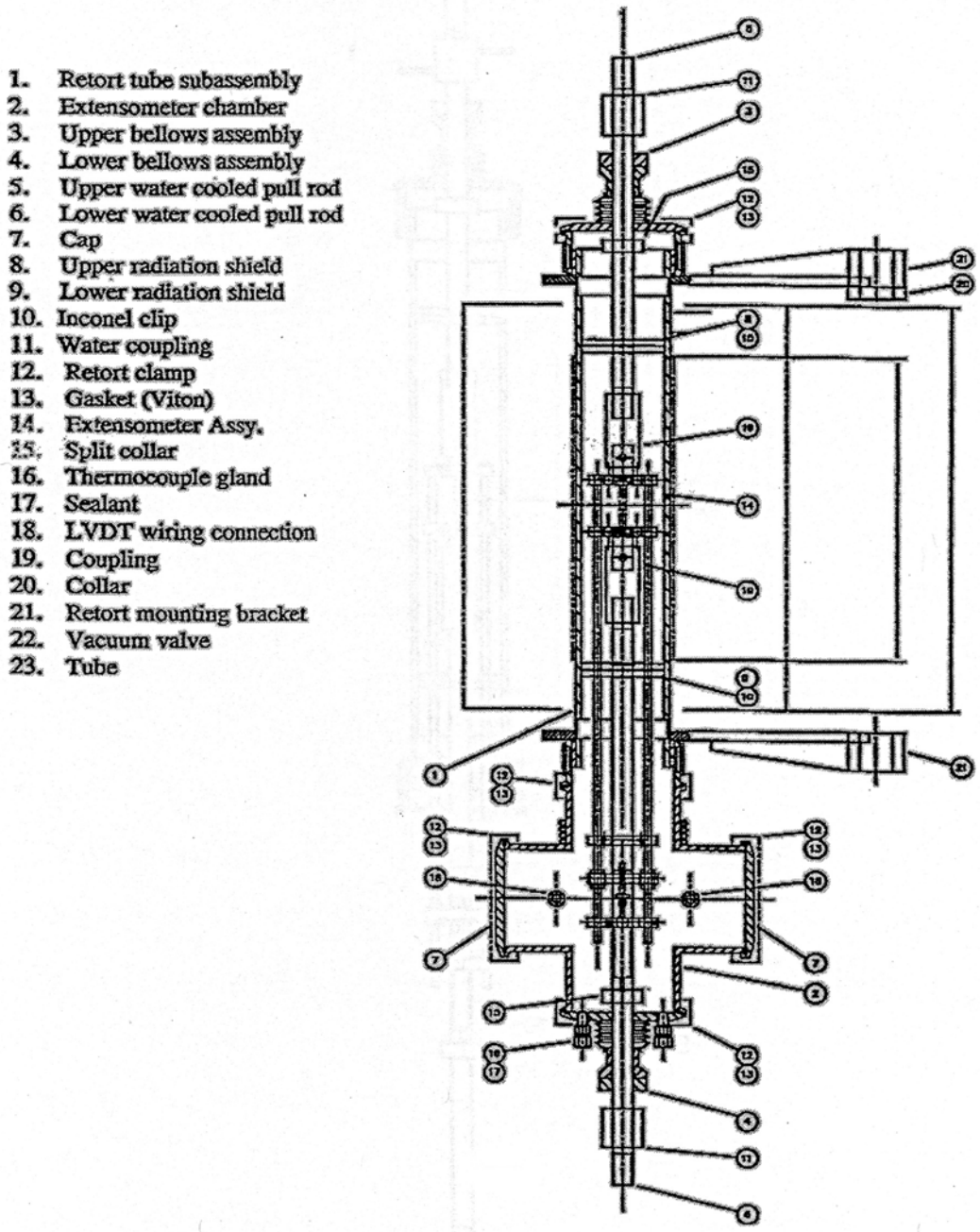

Figure 3.5: Schematic of retort assembly, creep furnace, and specimen with attached extensometer positioned inside furnace heat zone [33].

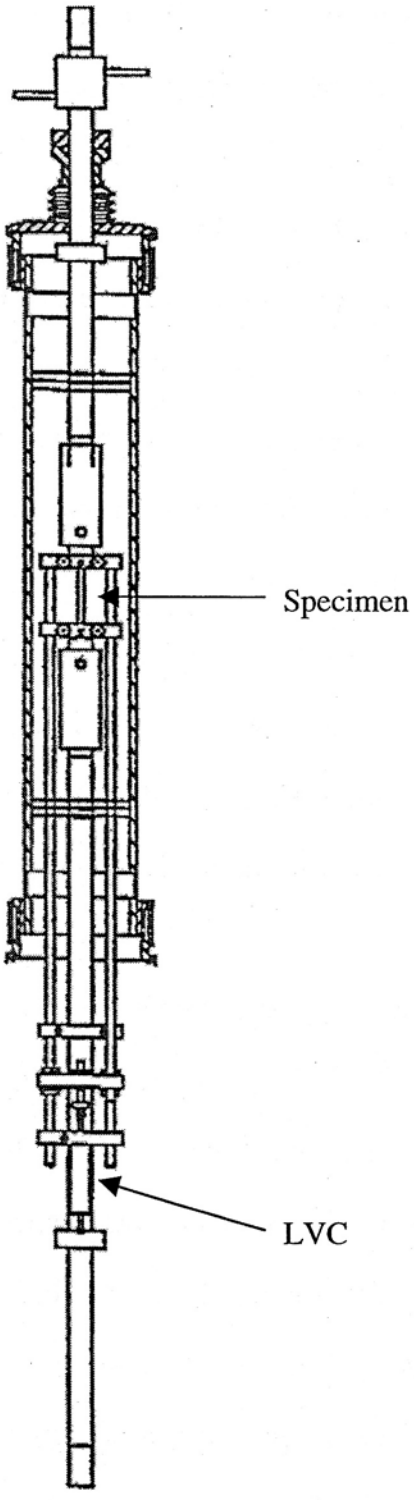

Figure 3.6: Schematic of extensometer and water cool pull rod assembly for specimen positioning [33].

3.5.2 Data Acquisition

A new data acquisition system was purchased and set up for this work. Strain is measured by a linear voltage capacitor (LVC) transducer supplied by ATS. The LVC is connected to a module which supplies a voltage to a data acquisition unit (DAQ) depending on the strain. The DAQ is a National Instruments NI USB-9221 portable USB-based DAQ for high voltage (±60V), high speed (800 kS/s) signals. At the start of the test, the measured voltage corresponds to zero strain. Once testing starts, the measured voltage will increase at a rate of 10V per 0.5" extensometer displacement.

Test data is recorded using Labview Version 7.1 Student Edition. A new VI was written to log the data, the details of which are given in Appendix C. Data acquisition rates are as follows:

1. 10 per second for 3 minutes (loading)
2. 1 per second for 30 minutes
3. 1 per 10 seconds for 2 hours
4. 1 per minute for 5 hours
5. 1 per hour for the remainder of the test
6. 10 per second for 3 minutes (unloading)

3.6 Optical and SEM Microscopy

Optical and scanning electron microscope (SEM) micrographs were taken of the polished specimen surfaces before and after creep deformation. This procedure is useful for separating deformation products that arise during tensile and creep testing from those that may be present prior to testing. A Zeiss ICM 405 inverted metallographic light

microscope was used for optical microscopy and an Electroscan Environmental SEM (ESEM) was used for SEM. Instructions for using the ESEM are given in Appendix D.

3.7 Transmission Electron Microscopy (TEM)

3.7.1 TEM Sample Preparation

The success of TEM depends on the careful preparation of specimens which must remain unaltered and be sufficiently thin for electron transparency. The first step is removal of a specimen from the bulk material. A Buehler Isomet Low Speed Saw with diamond wafering blade was used to slice sections of material from the deformed portions of the tensile and creep specimens. Buehler Isocut® fluid was used to lubricate and cool the wafering blade while removing debris, as a saw speed of 5 was selected. Cutting speeds were kept slow to prevent sample damage due to cutting forces. One slice was made initially to reveal the interior of the specimen of interest, then subsequent slices were made by moving the sample holder a set distance in relation to the blade. This is accomplished by dialing in the attached micrometer to the desired displacement. 18 divisions of the micrometer yielded specimens of approximately 120 μm thick. A Gatan Model 659 disc punch was then used to produce 3 mm diameter discs from the cut slices. The Gatan punch is designed so than no additional deformation is introduced into the specimen.

The next step involves pre-thinning the TEM disks by mechanical polishing. Dimpling was performed on a South Bay Technologies Model 515 Precision Dimpling Instrument. The specimen stage is heated on a hot plate and a small amount of Crystalbond adhesive is melted onto the top of the stage to adhere the specimen to the

stage. The TEM specimen disc is placed as close as possible to the center of the stage inside the centering ring and the stage is removed from the hot plate and allowed to cool for about 10 minutes. Once cooled, the stage is placed onto the dimpling apparatus underneath the polishing wheel. A small amount of South Bay Technologies 6 μm diamond paste is placed on top of the specimen and on the polishing wheel. The specimen is then dimpled at a wheel speed of 4 until the diameter of the dimple is approximately 2 mm. This corresponds to a dimple depth of approximately 40 μm. The stage is then removed from the instrument and heated on the hot plate to release the specimen. The specimen is flipped over and the process is repeated on the other side, leaving the center of the specimen approximately 40 μm thick (120 μm starting thickness minus two dimples of 40 μm depth).

Following dimpling, the final thinning was performed by jet polishing. Jet polishing is a chemical process that uses a combination of an acid containing electrolyte and electric current to remove material from the sample. Specimens were prepared in a Fischione 120 twin-jet polishing unit. The polishing solution used was 3% hydrochloric acid, 3% sulfuric acid, and 94% methanol. The samples were polished in the range of -60 to -70^{o}C at a voltage of 20V. Full details of this procedure are included in Appendix E.

3.7.2 TEM Operations

TEM was used in this investigation to image and characterize the creep deformation products for α-Ti-1.6V. A JEOL 2100F Field Emission Transmission Electron Microscope operating at 200 KeV was used. A combination of techniques was required to understand the deformation mechanisms of Ti-1.6V, including Selected Area

Diffraction (SAD), bright fiend imaging, dark field imaging, and high resolution microscopy. A brief outline of operating procedures is given in Appendix F.

In order to obtain high quality TEM images, the following factors must be considered. First, the TEM must be well aligned. The alignment process is too lengthy to include here, but may be found in the JEOL 2100F operations manual. Next, tilting of the specimen should be kept to a minimum. In order to orient the specimen to the proper zone axis, the specimen may be tilted up to 25^{o} tilt and azimuth. However, increasing the tilt will increase the cross section of the specimen that electrons must pass through and will decrease image quality. Therefore, images are best taken from a very well-thinned area of the specimen. Third, the best bright-field images are taken with an exposure time of approximately 1.5-2 seconds. The TEM has an auto-exposure function and the brightness can be adjusted to bring the exposure time into this range. The ideal exposure time for diffraction patterns is usually in the range of 0.2-0.5 seconds.

The various deformation mechanisms were identified in several ways. Slip was identified by dark field imaging using three different g vectors, and $g \bullet b$ analysis. To determine if slip involving screw dislocations with a Burgers vector $\vec{b} = \frac{1}{3}\langle 11\bar{2}0 \rangle$ were gliding on basal or prism planes, bright and dark field images were taken along both $\langle 11\bar{2}0 \rangle$ and $[0001]$ zone axes and tilted slightly to determine if the dislocation lines visible were single dislocations or stacks of dislocations on single planes in projection. This was necessary because *a*-type screw dislocations in hexagonal crystals can glide on basal or prism slip planes.

To identify twins, selected area diffraction patterns (SADPs) were taken from the matrix and across the twin matrix interface. To identify a twin, the specimen must be tilted along a zone axis that contains the *g* vector for the twin plane common to both the twin and the matrix. The twin identification process is described in Section 4.1.1.3.4. Note that there is a rotation between the bright-field TEM images and SADPs taken from the same area that changes at different magnifications. These rotations are given in Appendix G.

3.8 Theoretical Procedures

3.8.1 Projections for Modeling the Lattice

The theoretical portion of this investigation involves developing a crystallographic model for twin growth in single phase α and β titanium alloys, including octahedral interstitial sites and from this model, calculating the activation energy for time-dependent twinning. The schematics and figures which are used to illustrate the model were drawn with Microsoft PhotoDraw Version 2.0.0.1129. The crystallographic models are used to describe the atomic movements associated with deformation twinning. To show these movements the three dimensional lattices of hexagonal close-packed (HCP) α-Ti and body-centered cubic (BCC) β-Ti will be projected onto two-dimensional planes which contain all the atomic movements associated with twinning. For the purposes of clarity, these projections will be described below.

3.8.1.1 Projections for Modeling HCP Lattice

First, consider the HCP unit cell of α-Ti to define the various important directions and planes, shown in Figure 3.7

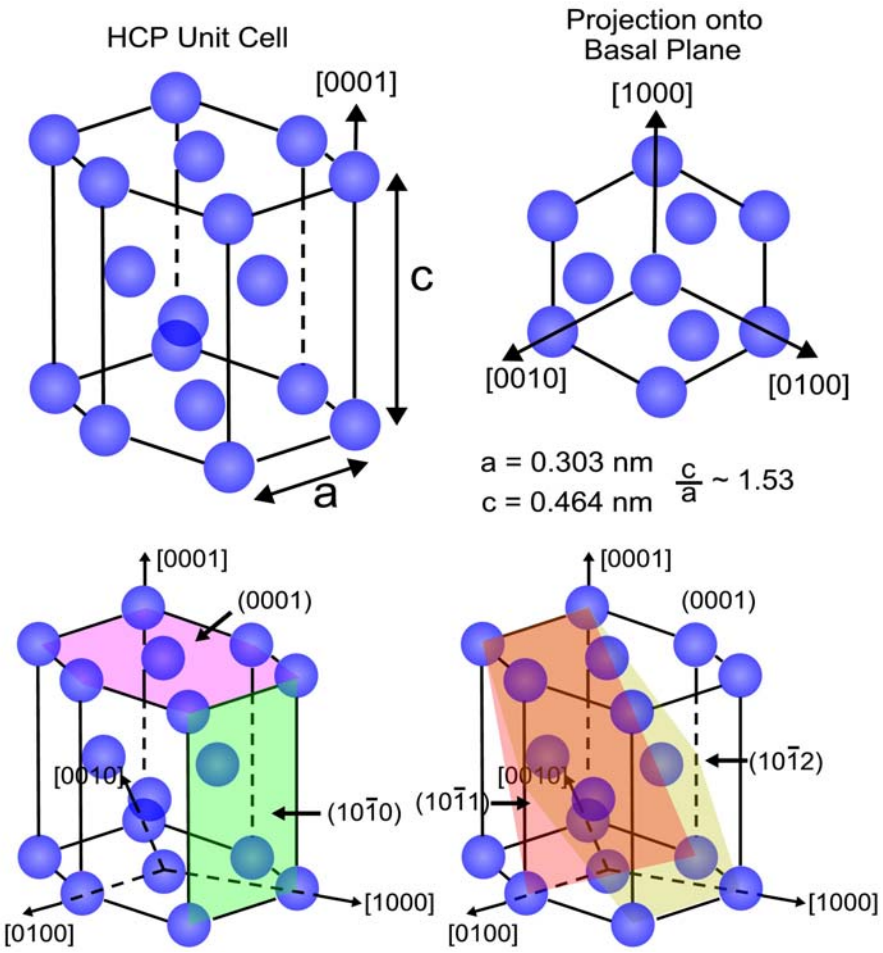

Figure 3.7: Schematic illustration of the HCP unit cell of α-Ti illustrating the various directions and planes.

Now, for the models, the HCP lattice will be projected onto a $\{11\bar{2}0\}$ type plane, as shown in Figure 3.8. The $(11\bar{2}0)$ plane of projection is shaded in Figure 3.8(a). Ti atoms located on the plane of the projection are given in blue, while those in the $\{11\bar{2}0\}$ type plane above (or alternatively below) the plane of projection are given in red. Other atoms are given in gray. Figure 3.8(b) shows that the interplanar spacing for the $\{11\bar{2}0\}$ planes is $\frac{a}{2}$, where *a* is the lattice constant. Figure 3.8(c) shows the HCP lattice projected onto the 2-D $(11\bar{2}0)$ plane of projection including atoms in and above or below the plane of projection. This will be the basis for the crystallographic models presented in this investigation.

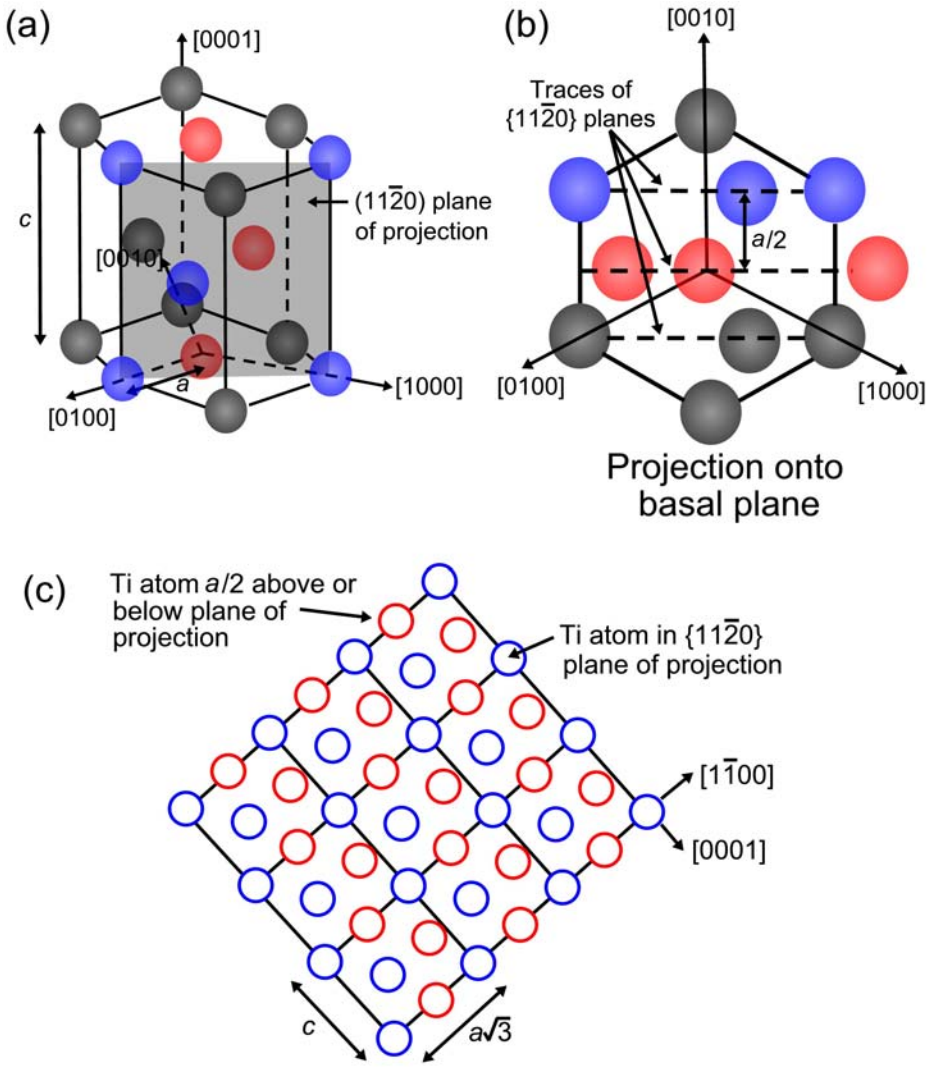

Figure 3.8: (a) HCP lattice of α-Ti. $\{11\bar{2}0\}$ plane of projection is shaded. Atoms in the plane of the projection are given in blue. Those above (or below) the plane of the projection are red. (b) Projection of the HCP lattice onto the basal plane. $\{11\bar{2}0\}$ planes are separated by a distance of *a*/2. (c) Projection of the HCP lattice onto a $\{11\bar{2}0\}$ plane.

As will become apparent, it is necessary to include in the projections the location of octahedral interstitial sites where atoms such as oxygen can reside. An octahedral interstitial atom resides at the center of an octahedron defined by six host atoms. An octahedral interstitial is shown in Figure 3.9. Figure 3.10 is similar to Figure 3.8 above, but now includes the octahedral interstitial sites. As for Ti matrix atoms, the octahedral interstitial sites can lie in (green) and above or below (orange) the $(1\bar{1}20)$ plane of projection.

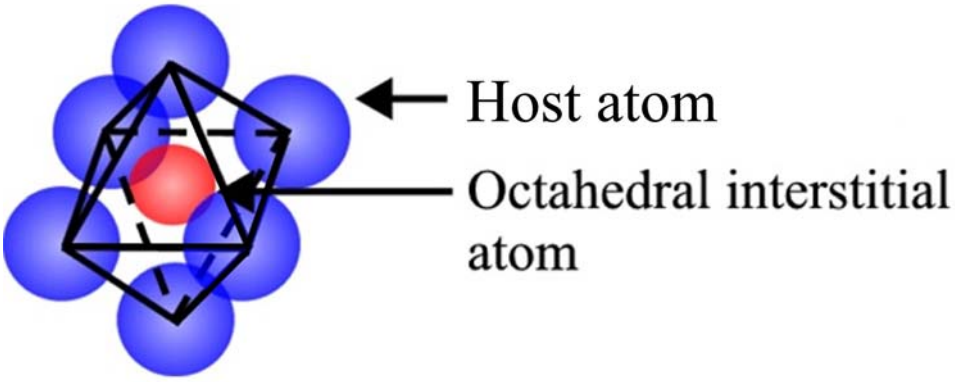

Figure 3.9: Illustration of an octahedral interstitial atom residing in an octahedron defined by six host atoms.

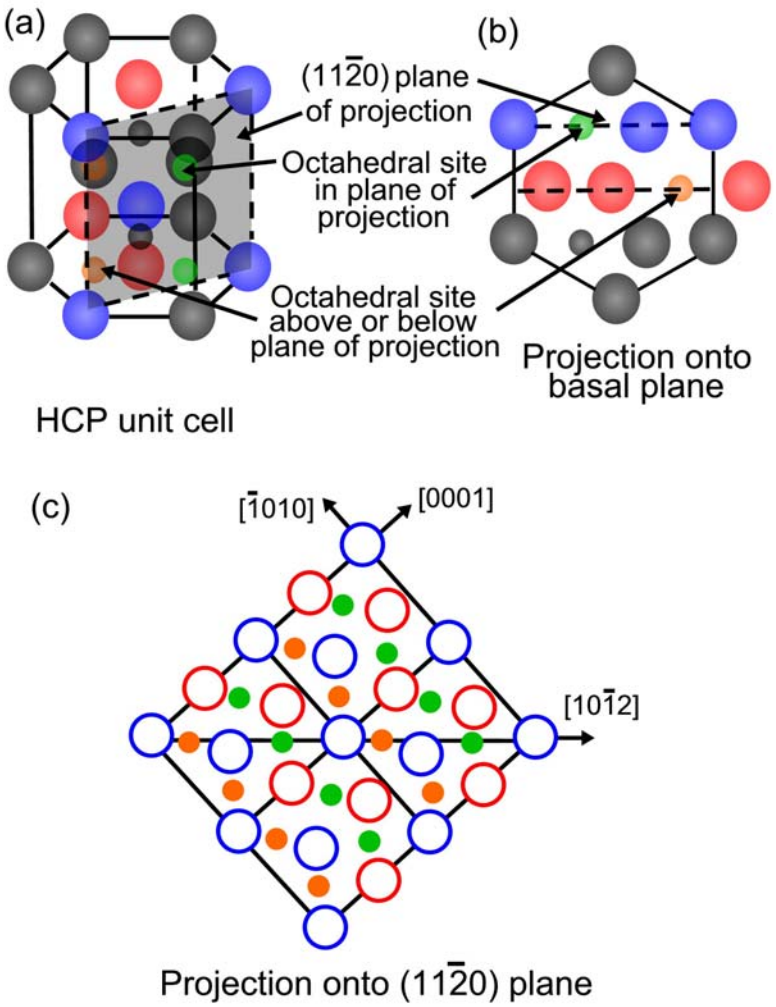

Figure 3.10: (a) HCP lattice of α-Ti including octahedral interstitial sites $\{11\bar{2}0\}$ plane of projection is shaded. Octahedral interstitial sites in the plane of the projection are given in green. Those above (or below) the plane of the projection are orange. (b) Projection of the lattice onto the basal plane. $\{11\bar{2}0\}$ planes are separated by a distance of *a*/2. (c) Projection of the HCP lattice onto a $\{11\bar{2}0\}$ plane including matrix atoms and octahedral interstitial sites in and above (or below) $\{11\bar{2}0\}$ plane of projection.

3.8.1.2 Projections for Modeling BCC Lattice

In this investigation, a model will also be developed for twinning of the BCC lattice of β-Ti, as was described by Oberson and Ankem [34]. Consider the BCC unit cell to define the important directions and planes, illustrated in Figure 3.11.

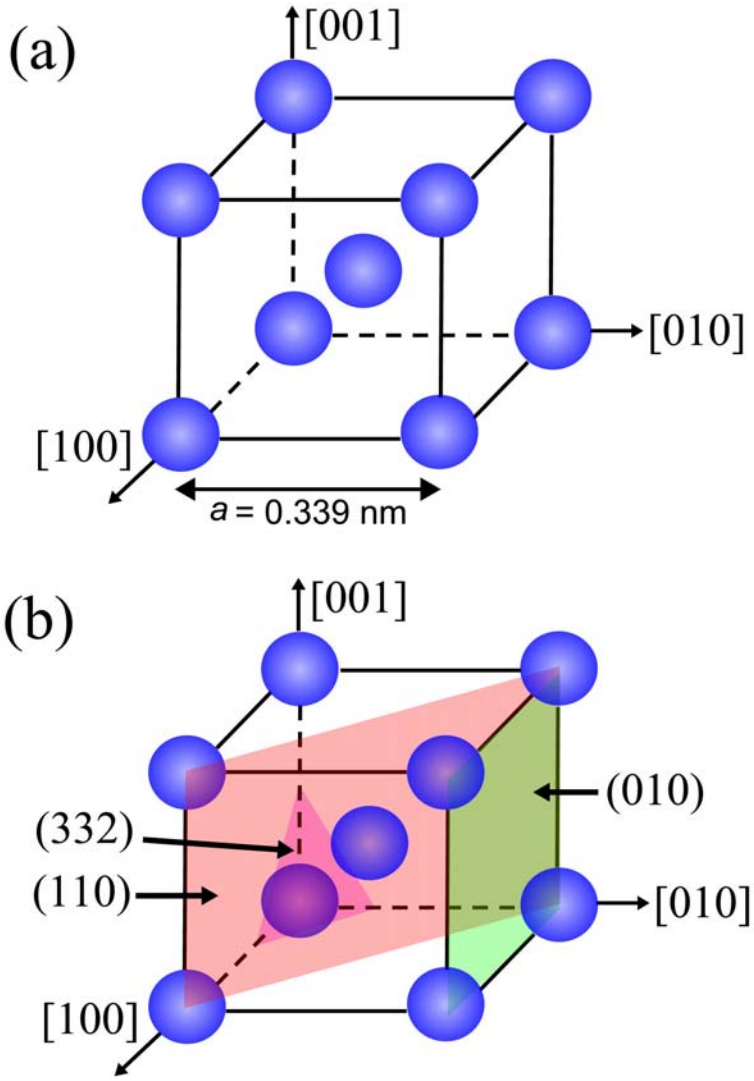

Figure 3.11: Schematic illustration of BCC lattice of β-Ti including important (a) directions and (b) planes.

Now, for the models, the BCC lattice will be projected onto a $\{110\}$ type plane, as shown in Figure 3.12. The (110) plane of projection is shaded in Figure 3.12(a). Ti atoms located on the plane of the projection are given in blue, while those in the $\{110\}$ type plane above (or alternatively below) the plane of projection are given in red. Other atoms are given in gray. Figure 3.12(b) shows that the interplanar spacing for the $\{11\bar{2}0\}$ planes is $a\sqrt{2}/2$, where a is the lattice constant. Figure 3.12(c) shows the BCC lattice projected onto the 2-D (110) plane of projection including atoms in (blue) and above or below (red) the plane of projection. This will be the basis for the models presented in this investigation.

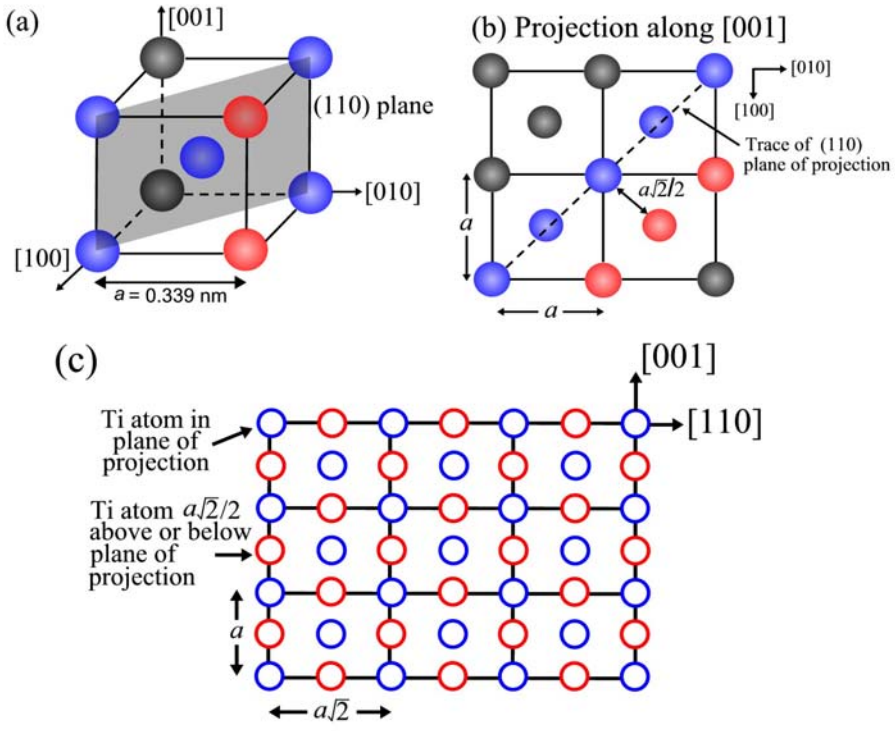

Figure 3.12: (a) BCC unit cell of β-Ti. (110) plane of projection is shaded. Atoms in the plane of the projection are given in blue. Those above (or below) the plane of projection are given in red. Projection of lattice onto (001) plane. {110} planes are separated by a distance of $\frac{a\sqrt{2}}{2}$. (c) Projection of BCC lattice onto (110) plane.

As is the case for α-Ti alloys, it is necessary to include in the projections the location of octahedral interstitial sites where atoms such as oxygen can reside. Figure 3.13 is similar to Figure 3.12 above, but now includes the octahedral interstitial sites. As for Ti matrix atoms, the octahedral interstitial sites can lie in (green) and above or below (orange) the $(11\bar{2}0)$ plane of projection.

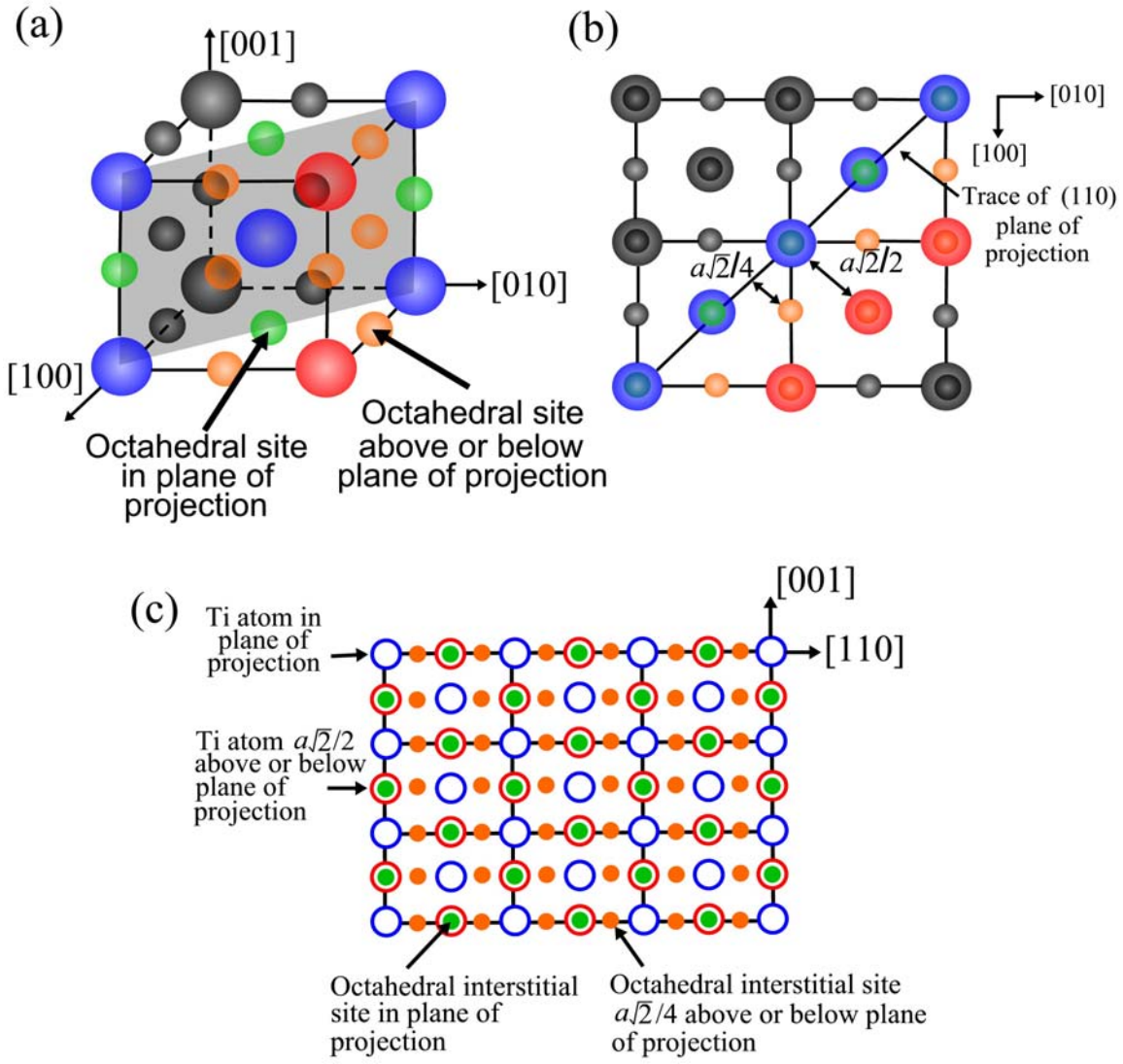

Figure 3.13: (a) BCC lattice of β-Ti, including octahedral interstitial sites in (green) and above or below (orange) the shaded (110) plane of projection. (b) Projection of lattice onto [110] planes. (c) Projection of lattice onto (110) plane showing matrix atoms and octahedral interstitial sites in and above (or below) plane of projection.

3.8.2 Modeling the Advancing Twin Front

In the models presented in this investigation, the plane that defines the twin-matrix interface is assumed to advance in one dimension (in opposite directions) away from the start plane where the twin is nucleated. This is schematically illustrated in Figure 3.14. The length of the twin (in the direction parallel to the twin start plane) is considered to be much greater than the thickness (normal to the twin start plane). The part of the twin-matrix interface that is parallel to the twinning start plane is a coherent boundary, and that in the vicinity of the twin tips is semi-coherent. The lenticular shape of the twin minimizes the area of the high-energy semi-coherent boundary. For instance, see the lenticular twins in Figure 2.4.

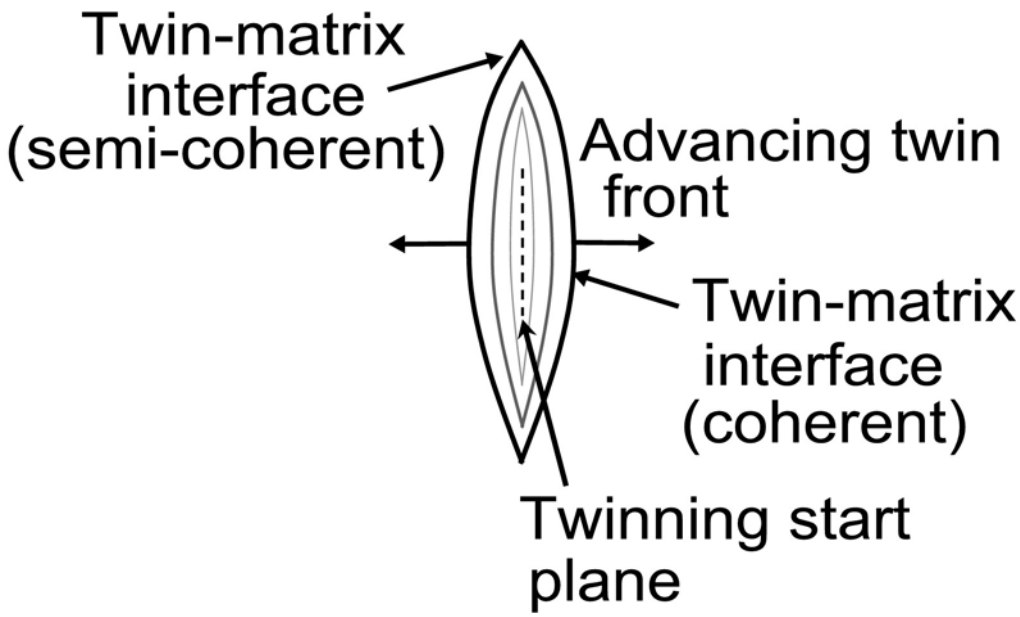

Figure 3.14: Schematic illustrating the growth of a lenticular twin. The twin nucleates at the twin start plane, indicated by a dashed line and the twin-matrix interface will advance in one dimension (normal to the twin start plane), in opposite directions.

Chapter 4

Results and Discussion

This chapter gives the experimental and theoretical results and discussion for the investigation of the low temperature (<0.25 T_m) creep deformation behavior of single-phase α and β titanium alloys. The chapter will be divided into two parts. The first part of the investigation concerns α-Ti alloys. The low temperature creep behavior was studied experimentally, using α-Ti-1.6wt.%V as the model alloy. Creep tests were performed at various temperatures and the activation energy for creep deformation was calculated as a function of the amount of strain. The activation energy was found to increase as the strain level increases, suggesting a change in deformation mechanism from predominantly slip in the lower strains, to slip + twinning at higher strains. Creep deformation products were identified characterized by SEM and TEM.

The theoretical aspect of the study of α-Ti, concerns the phenomenon of slow twin growth (time-dependent twinning) during low temperature creep. This phenomenon is unusual and poorly understood as twins in bulk, polycrystalline metals are expected to grow very fast. It was suggested that interstitial atoms, particularly oxygen could be responsible for time-dependent twinning but there were no models to explain this. As such, crystallographic models were developed for the HCP lattice of α-Ti to show how the octahedral interstitial sites where atoms such as oxygen can reside are eliminated by the atomic movements associated with twinning.

The second part of the chapter, concerning β-Ti alloys, builds on previous experimental work [35] and the crystallographic model for time-dependent twinning is extended to the BCC lattice of β–Ti. Similar to the case for α-Ti alloys, the slow growth of twins is attributed to the diffusion of interstitial oxygen atoms away from octahedral interstitial sites ahead of the advancing twin boundary.

4.1 α-Titanium Alloys

4.1.1 Experimental Investigation

As discussed in Section 2.3.1, α-titanium alloys are known to creep at low temperature [6-26]. Time-dependent twinning has been identified as a creep deformation mechanism in coarse-grained α-Ti-0.4wt.%Mn [26] and α-Ti-1.6wt.%V [26], but this phenomenon is not well understood. The experimental part of this investigation involved creep testing of the α-Ti-1.6wt.%V at various temperatures to determine the activation energy for creep as a function of the strain level. Deformation products were characterized by SEM and TEM. The effect of the microstructure on the creep deformation products and defect interactions is discussed.

4.1.1.1 Background

For single-phase materials, a number of equations are available to describe the creep behavior of each stage. Recall from Chapter 2.2 that primary or transient creep is often described by the following empirical power function equation [5] for a given uni-axial stress σ, normalized with respect to yield stress:

$$\varepsilon = A^* t^a \tag{4-1}$$

where ε is the creep strain, A^* is a constant, reportedly dependent on microstructure and temperature and a is the time exponent. Alternatively, creep deformation may follow a logarithmic fit of the type [26]:

$$\varepsilon = A' + B \ln t \tag{4-2}$$

where ε is the creep strain, A' and B are constants. When the time, t, is set to 1 hour, the constants A^* from Equation 4-1 and A' from Equation 4-2 will be the same.

The activation energy for non-steady state creep at constant stresses for a Ti alloy was first determined by Thompson and Odegard [13] for α–β Ti-2.5 Sn by using Equation 4-1. They utilized the time derivative of the above Equation 4-1 to eliminate the time dependence of the strain rate in order to obtain an equation for strain rate as a function of strain:

$$\dot{\varepsilon}(\varepsilon) = aA^{*1/a}(\varepsilon)^{1-1/a} \tag{4-3}$$

They also calculated the activation energy, $Q(\varepsilon)$,at a given uni-axial stress σ, from the equation:

$$Q(\varepsilon) = -R\left[\frac{\Delta \ln \dot{\varepsilon}(\varepsilon)}{\Delta(1/T)}\right]_{const.\sigma} \tag{4-4}$$

where, σ is the constant uni-axial normalized (with respect to the corresponding yield stress at a given temperature) stress and ε is the selected strain level at which $Q(\varepsilon)$ is calculated. A similar analysis was performed by Miller, Chen, and Starke, Jr. for α–β Ti-6Al-2Nb-1Ta-0.8 Mo [16]. They show that the activation energy for creep may change if the deformation mechanism responsible for creep changes. For instance, the creep mechanism may change from slip at low temperatures to self-diffusion at high

temperatures. A more recent investigation by Hudson and Ankem [35] determined the activation energy for low temperature creep of the β-Ti-14.8V alloy using Equation 4-4. It was found that the activation energy increases as the strain level increases. It is suggested that the deformation mechanism changes from predominantly slip at low strain to time-dependent twinning at higher strains. This alloy will be discussed in more detail later. Thus, the activation energy is important for determining the deformation mechanisms associated with creep.

4.1.1.2 Procedures

Alpha-Ti-1.6 V was thermomechanically processed according to the procedure given in Section 3.1. This treatment resulted in an equiaxed microstructure with an average grain size of approximately 226 μm. Creep test specimens were prepared by the method described in Section 3.3. Gold-palladium fiducial lines with a 50 μm spacing were deposited the polished gage surface of two of the specimens by the process described in Section 3.4. The lines are useful for measuring local strain and for finding the same specimen area for microscopy prior to and following testing. The surfaces of the creep specimens with the grid lines were imaged extensively in several areas prior to and following testing using an Electroscan ESEM.

Constant-load creep testing was conducted on an Applied Test Systems (ATS) Series 2330 creep tester with a lever arm ratio of 20:1 rated at 20,000 lbs. To enable elevated temperature testing, an ATS Series 3210 split tube furnace with a Series 3910 retort assembly for controlled gas environment is installed in the center of the creep tester frame. In a previous investigation [26], Ti-1.6V has been creep tested at room

temperature (298 K) at 95% YS. In the present investigation, it was creep tested at 95% YS at four higher temperatures: 338 K, 358 K, 378 K, and 478 K. In order to determine the yield stress of Ti-1.6V at these respective temperatures, elevated temperature tensile tests were conducted on the same alloy with the same microstructure by a previous investigator. Tensile tests were performed in vacuum at four test temperatures: 338 K, 378 K, 418 K, and 458 K. A Materials Research Furnace (MRF) furnace is mounted to a floor model Instron 8562 servo-hydraulic testing machine. Specimens were strained to 3%. A plot of 0.2% yield stress as a function of temperature is shown in Figure 4.1.

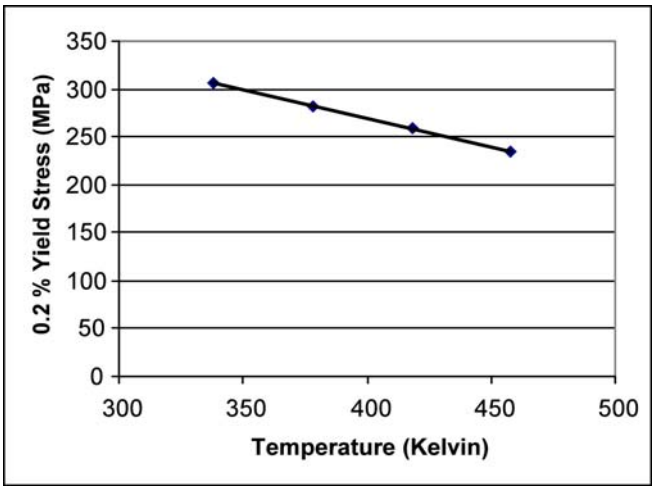

Figure 4.1: 0.2% yield stress as a function of temperature for coarse-grained (226 μm) α-Ti-1.6V.

The duration of the creep test was intended to be 192 hours, as was the case in previous investigations [23, 26]. It was found, however, that at temperatures of 358 K and above, the strain rate was such that significant strains were reached in a fraction of this time. As such, creep tests were stopped when specimens reached a strain of approximately 10%. The reduction in specimen area beyond this point means that given a constant load, the stress level is significantly higher than at the beginning of the test.

4.1.1.3 Results

4.1.1.3.1 Creep Test Results

Creep curves for α-Ti-1.6V at the temperatures of 298 K [26], 338 K, 358 K, 378 K, and 478 K are shown in Figures 4.2 – 4.6, respectively. An overlay of all the curves on the same axis is shown in Figure 4.7.

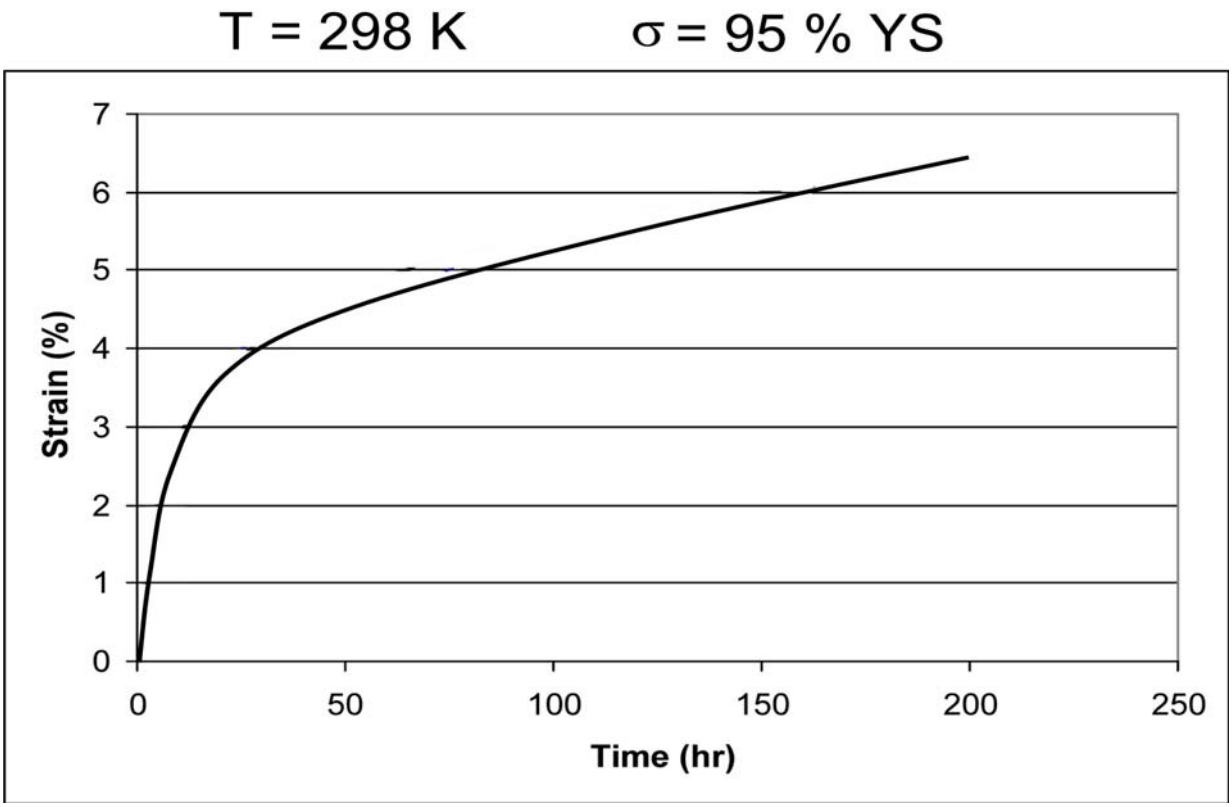

Figure 4.2: Creep curve for α-Ti-1.6V alloy with 226 μm grain size tested at room temperature (298K) at 95% YS [26].

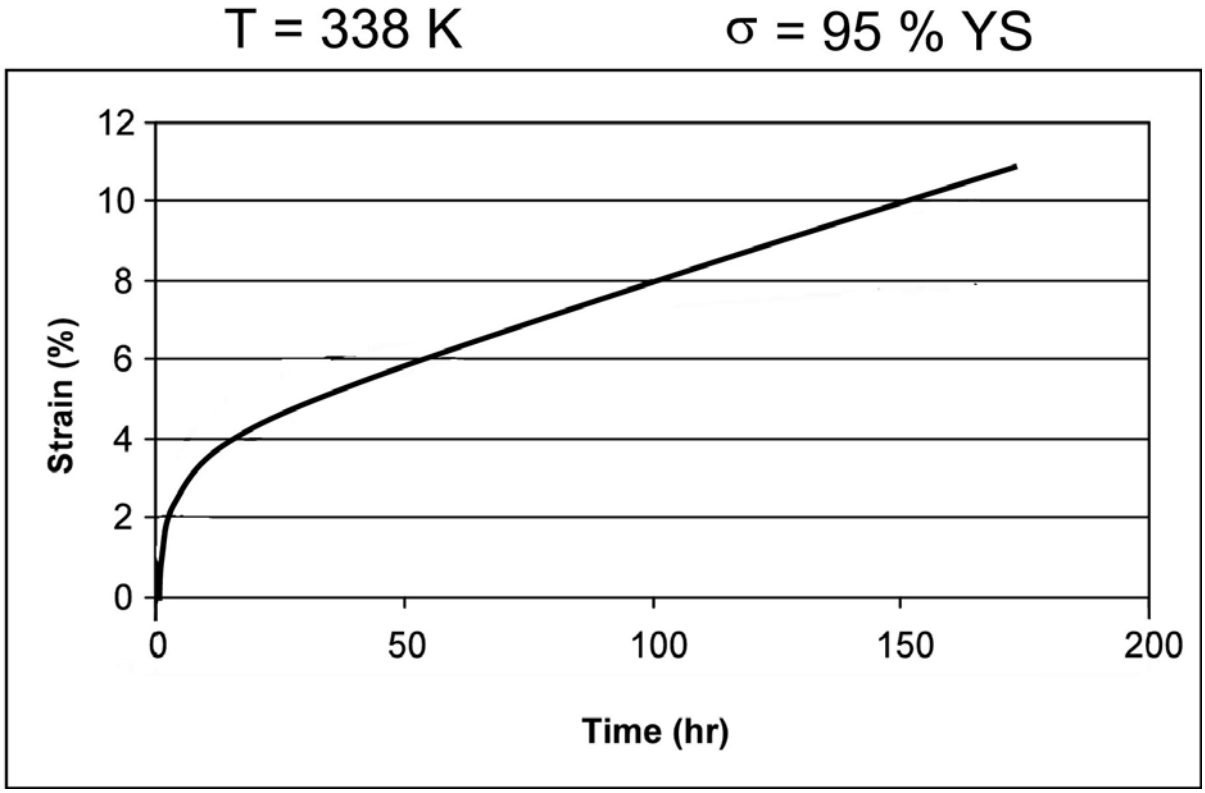

Figure 4.3: Creep curve for α-Ti-1.6V alloy with 226 μm grain size tested at 338 K at 95% YS.

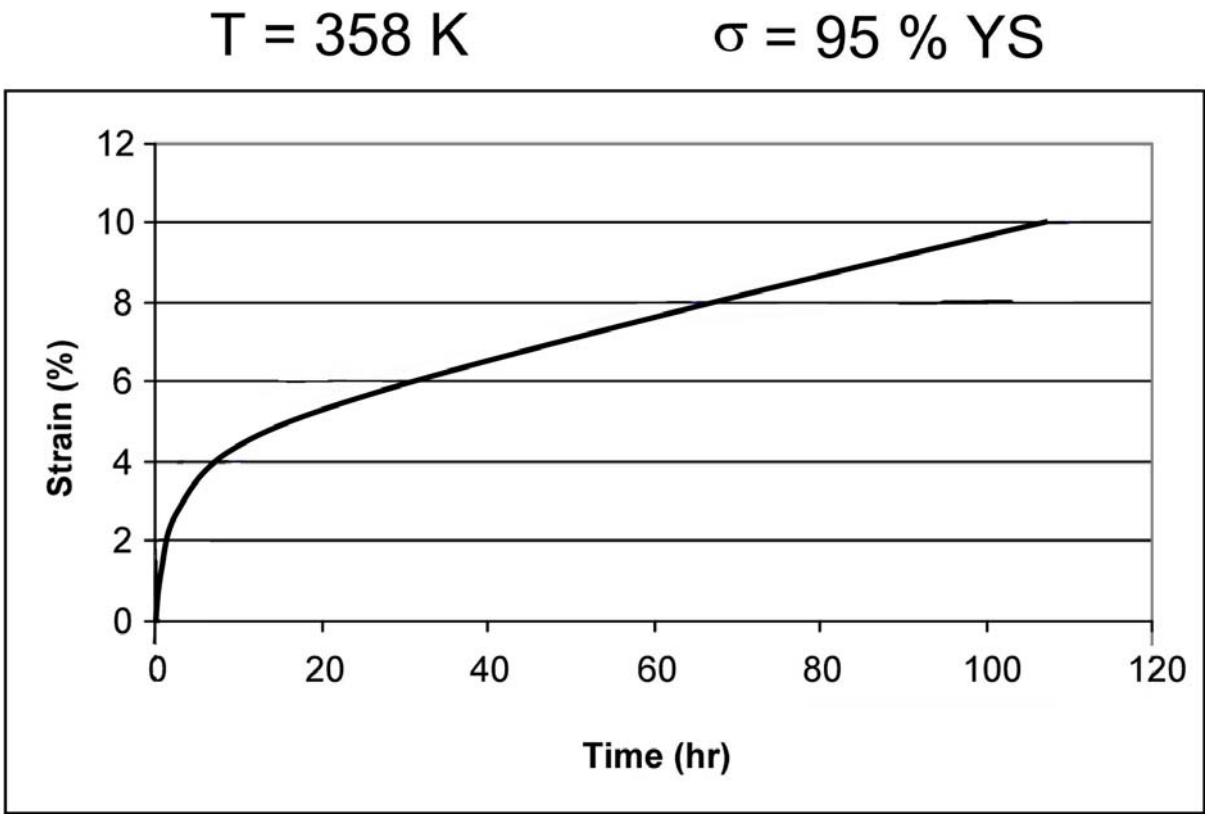

Figure 4.4: Creep curve for α-Ti-1.6V alloy with 226 μm grain size tested at 358 K at 95% YS.

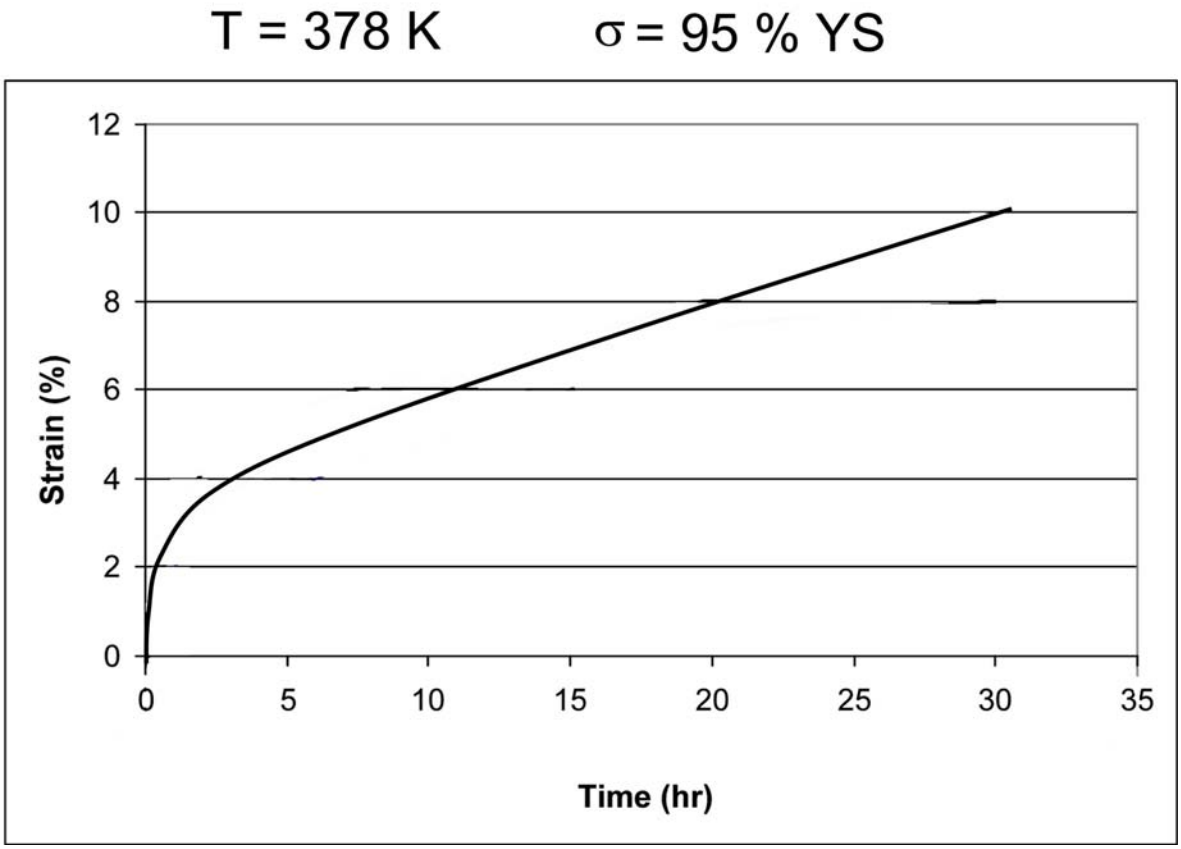

Figure 4.5: Creep curve for α-Ti-1.6V alloy with 226 μm grain size tested at 378 K at 95% YS.

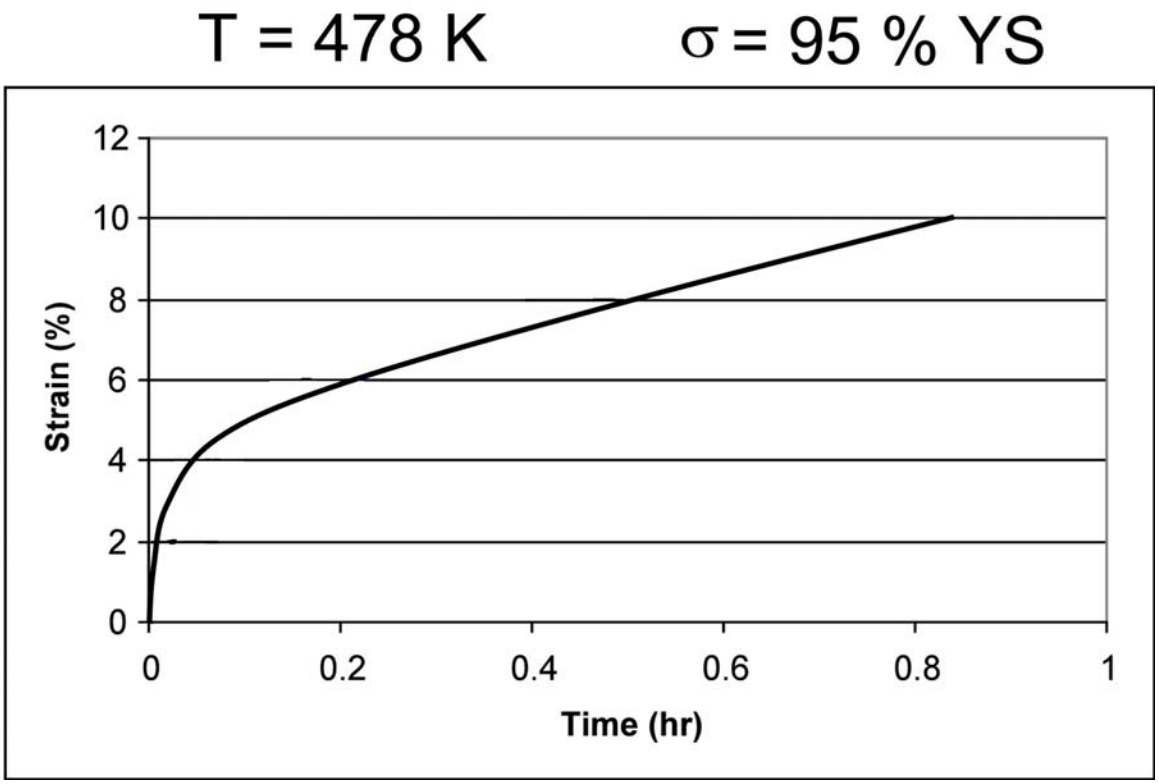

Figure 4.6: Creep curve for α-Ti-1.6V alloy with 226 μm grain size tested at 478 K at 95% YS.

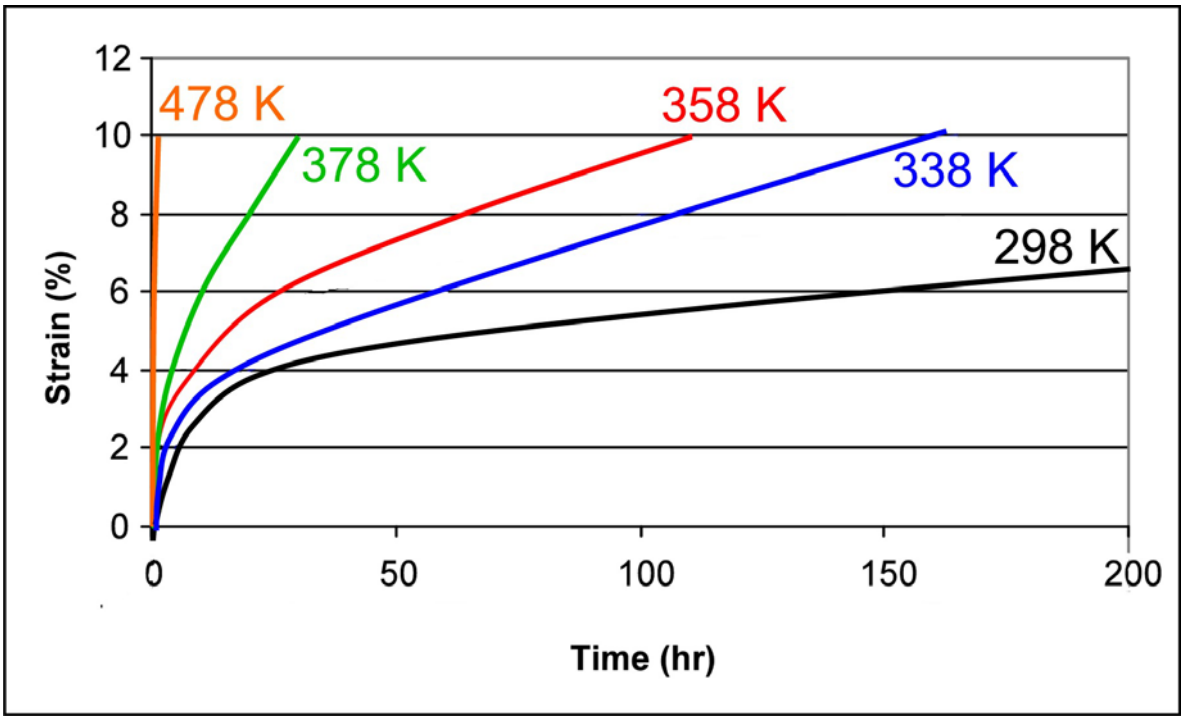

Figure 4.7: Creep curves for α-Ti-1.6V alloy with 226 μm grain size tested at 95% YS at various temperatures.

4.1.1.3.2 Calculation of Activation Energy for Creep

Recall from Section 4.1.1.1 of this chapter that the activation energy for creep, $Q(\varepsilon)$,at a constant uni-axial stress σ, is given by the equation:

$$Q(\varepsilon) = -R\left[\frac{\Delta \ln \dot{\varepsilon}(\varepsilon)}{\Delta(1/T)}\right]_{const.\sigma} \tag{4-4}$$

where, σ is the constant uni-axial normalized (with respect to the corresponding yield stress at a given temperature) stress and ε is the selected strain level at which $Q(\varepsilon)$ is calculated. Thus, from the above creep curves, the instantaneous strain rate, $\dot{\varepsilon}$, is measured at particular strain levels for the respective temperatures. When $ln\,\dot{\varepsilon}$ at a

particular strain is plotted versus 1/T, a line is given whose slope is proportional (by a factor of $-R$) to the activation energy for creep deformation at that strain level. For the five temperatures 298 K, 338 K, 358 K, 378 K, and 478 K, the instantaneous strain rate was measured at strain levels in the region of primary creep: 0.5%, 1%, 2%, 2.5%, 3%, 3.5%, 4%, and 5%. An Arrhenius plot of $\ln \dot{\varepsilon}$ vs. 1/T is shown in Figure 4.8. The best fit lines along with corresponding equations for the respective strain levels are shown.

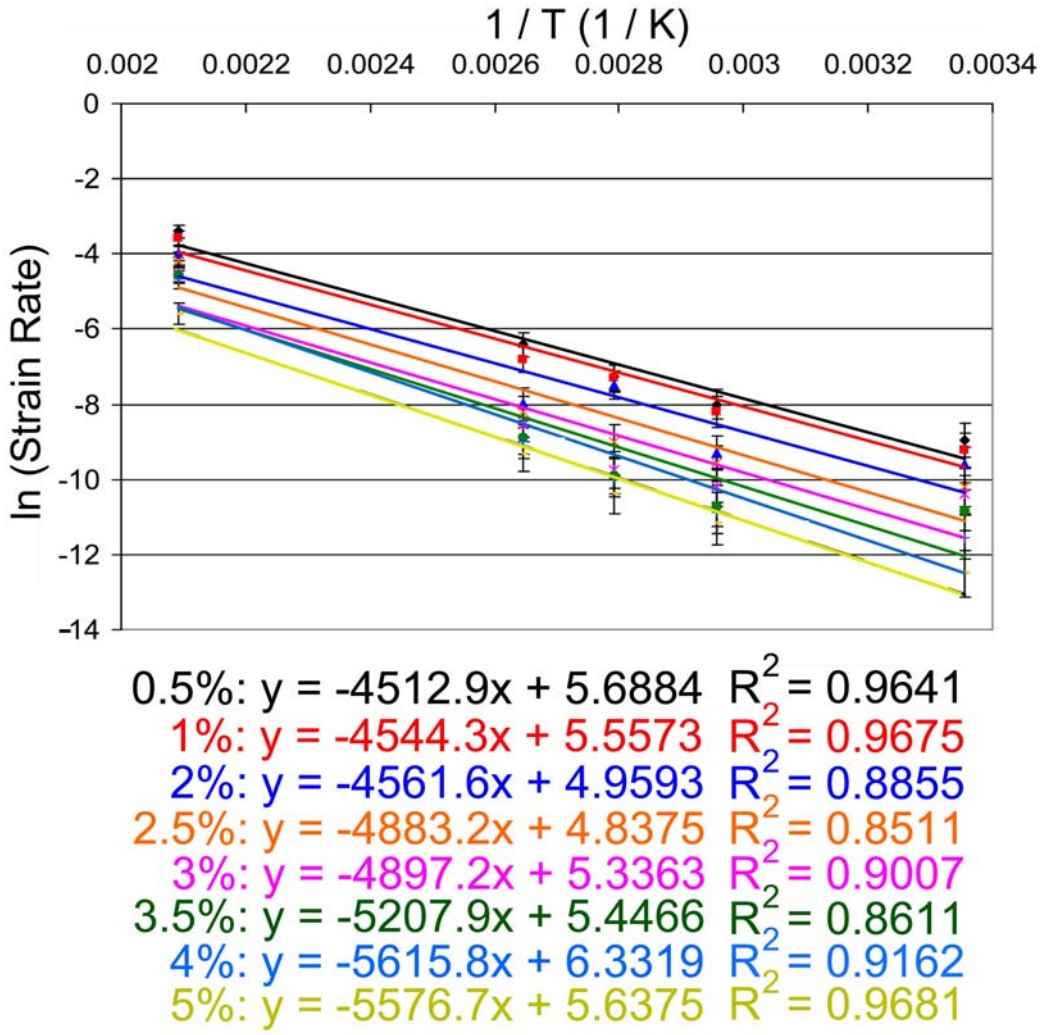

Figure 4.8: Arrhenius plot of $\ln \dot{\varepsilon}$ vs. 1/T for the creep of α-Ti-1.6V at the temperatures of 298 K, 338 K, 358 K, 378 K, and 478 K for the strain levels of 0.5%, 1%, 2%, 2.5%, 3%, 3.5%, 4%, and 5%. Equations for best-fit lines at the respective strain levels are shown, along with R^2 values.

When the slopes of the best-fit lines for the respective strain levels are multiplied by the negative of the constant R (8.31 J/mol/K), this gives the value for the activation energy, Q, for creep at that particular strain level. A plot of Q vs. strain is shown in Figure 4.9. From the plot, it is seen that the activation increases from a value of approximately 37 KJ/mol at low strains ($\leq 2\%$) to approximately 47 KJ/mol at higher strains ($\geq 4\%$).

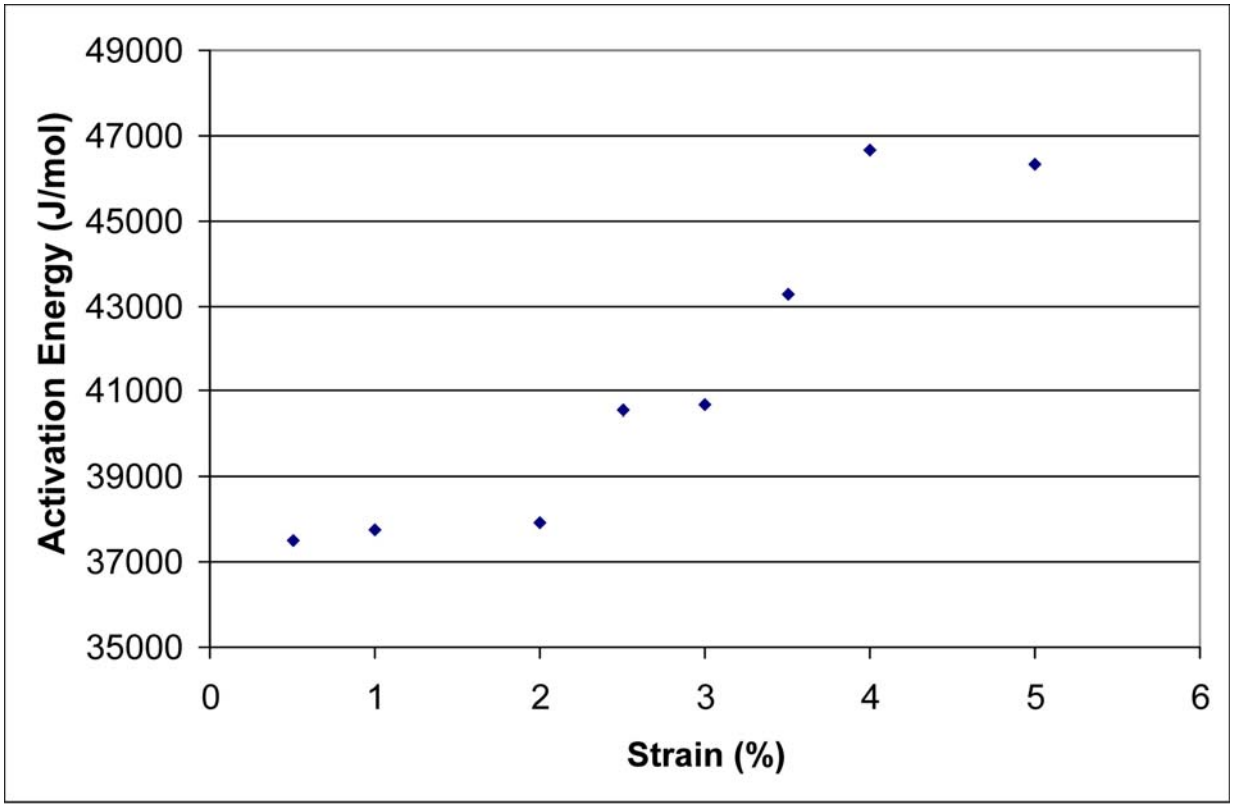

Figure 4.9: Plot of activation energy for creep of coarse-grained α-Ti-1.6V at various strain levels, as calculated by Equation 4-4.

4.1.1.3.3 Optical and SEM Microscopy

Creep specimens were examined before and after testing by optical and SEM to look for evidence of deformation mechanisms such as slip and twinning. Grid lines were placed on the creep specimens to be tested at the lowest and highest of the elevated temperatures, 65°C (338 K) and 205°C (478 K), respectively, to determine if the behavior is similar to a previous investigation of the alloy when creep tested at 25°C [26]. The grid serves as a reference to identify the same area of the specimen before and after testing. The micrographs show similar behavior as that seen at 25°C. Namely, slip and twinning are creep deformation mechanisms across the temperature range of this investigation. Figures 4.10 and 4.11 are optical micrographs of creep specimens at 65°C and 205°C, respectively, showing extensively twinned regions. Figures 4.12 and 4.13 are optical micrographs of regions showing coarse slip. Figures 4.14-4.16 are bright field SEM images of α-Ti-1.6V before and after creep testing at 65°C. The total creep strain is approximately 11%. Figures 4.17-4.20 are bright field SEM images of α-Ti-1.6V before and after creep testing at 205°C. The total creep strain is approximately 10%.

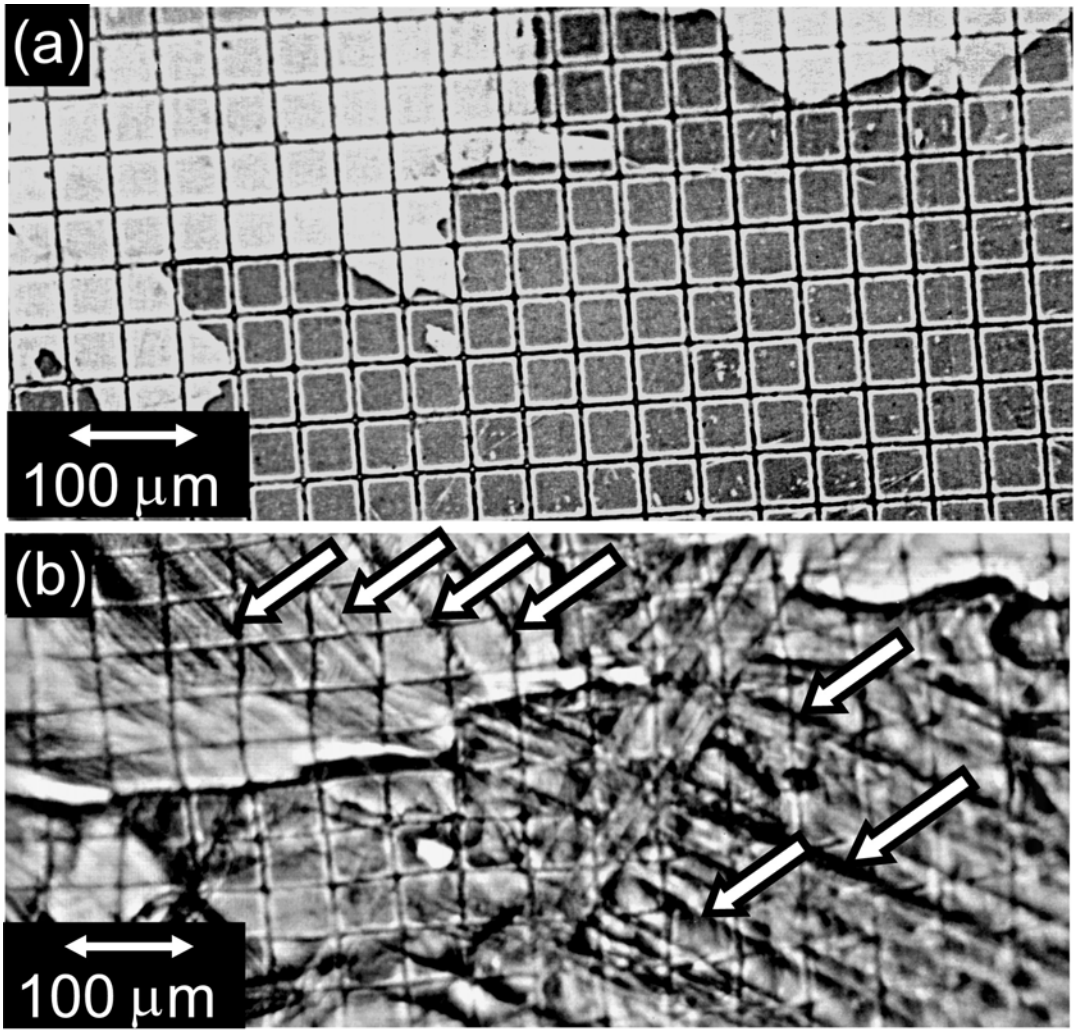

Figure 4.10: Optical micrograph of α-Ti-1.6V, (a) before, and (b) after creep testing at 95% YS at 65°C. Total strain is approximately 10%. Specimen shows extensive twinning in (b), some of which are indicated by arrows.

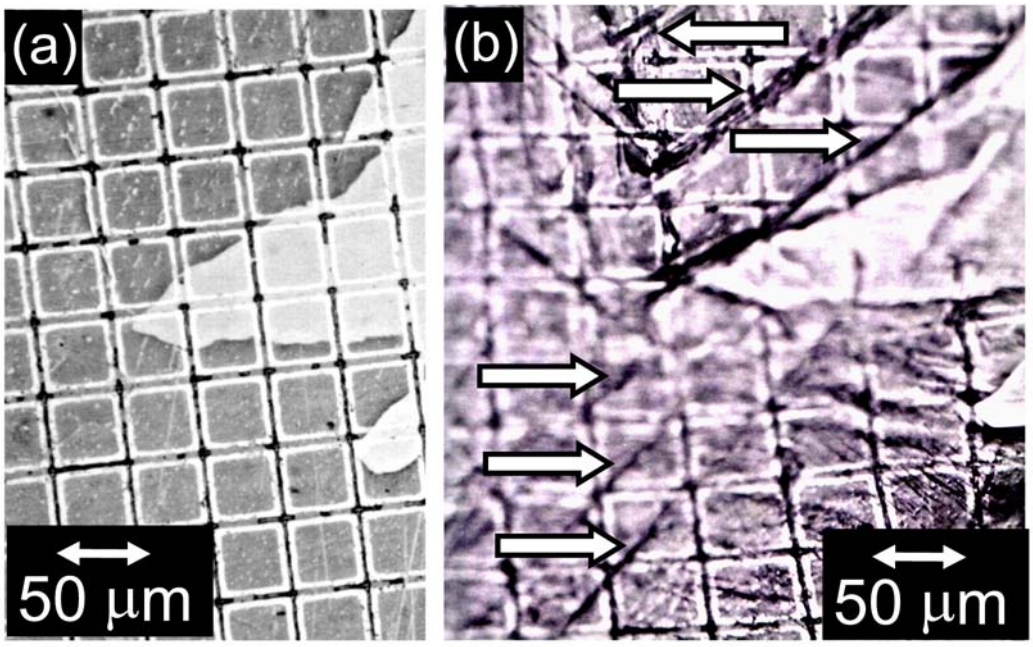

Figure 4.11: Optical micrograph of α-Ti-1.6V, (a) before, and (b) after creep testing at 95% YS at 205°C. Total strain is approximately 11%. Twins in (b) are indicated by arrows.

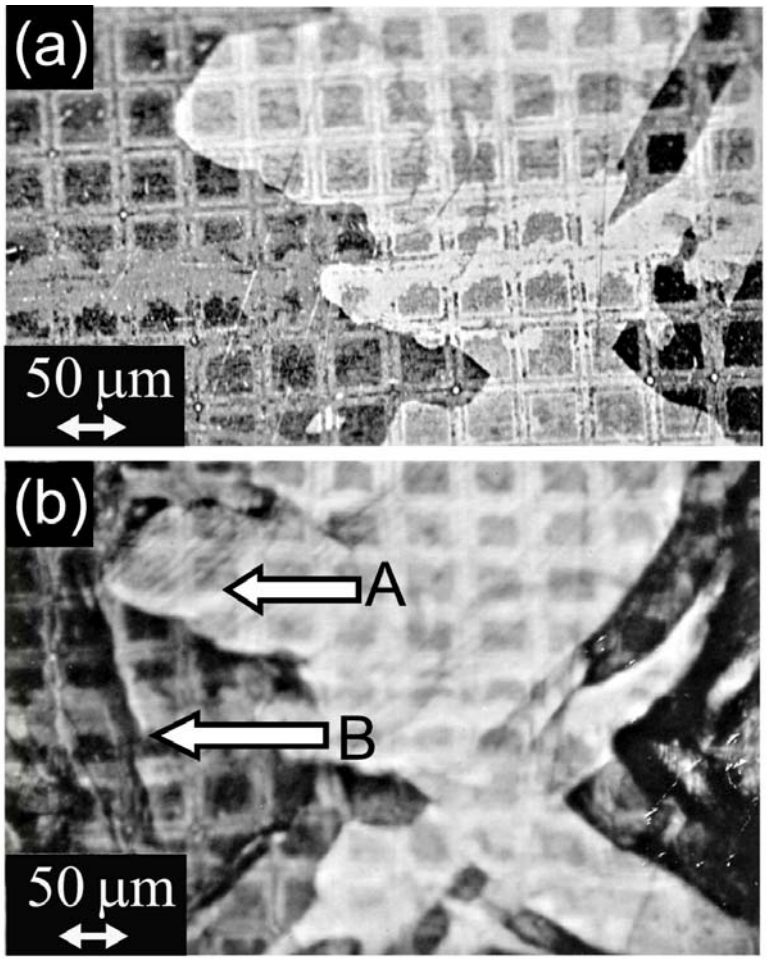

Figure 4.12: Optical micrograph of α-Ti-1.6V, (a) before, and (b) after creep testing at 95% YS at 65°C. Total strain is approximately 10%. In (b), note coarse slip lines at 'A' and twin at 'B'.

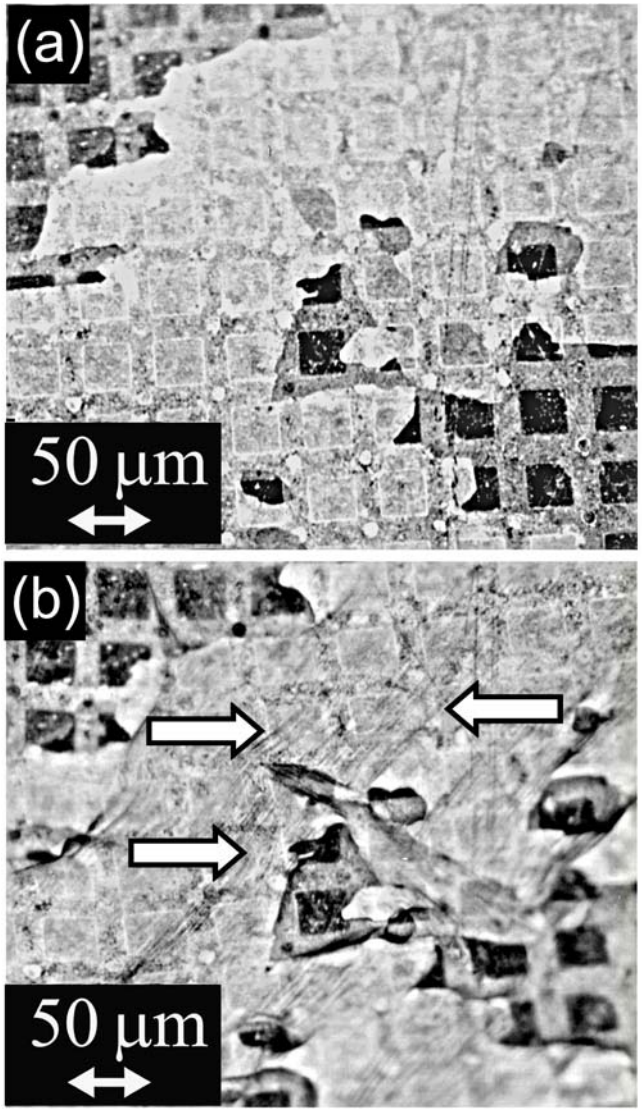

Figure 4.13: Optical micrograph of α-Ti-1.6V, (a) before, and (b) after creep testing at 95% YS at 205°C. Total strain is approximately 11%. Note coarse slip lines in (b) indicated by arrows.

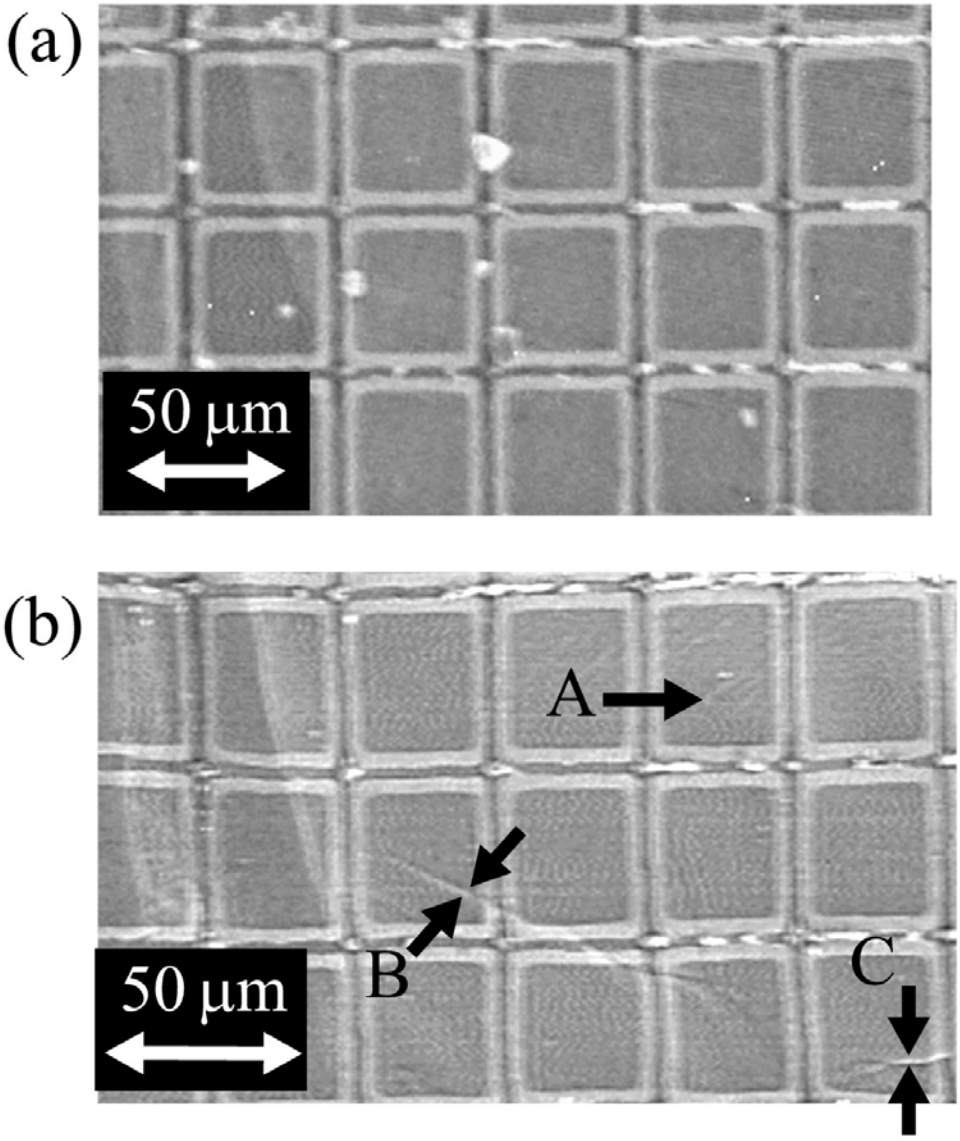

Figure 4.34: Secondary SEM micrograph of α-Ti-1.6V (a) before and (b) after creep at 65°C. Total creep strain is approximately 11%. In (b) note coarse slip lines at 'A' and twins at 'B' and 'C'.

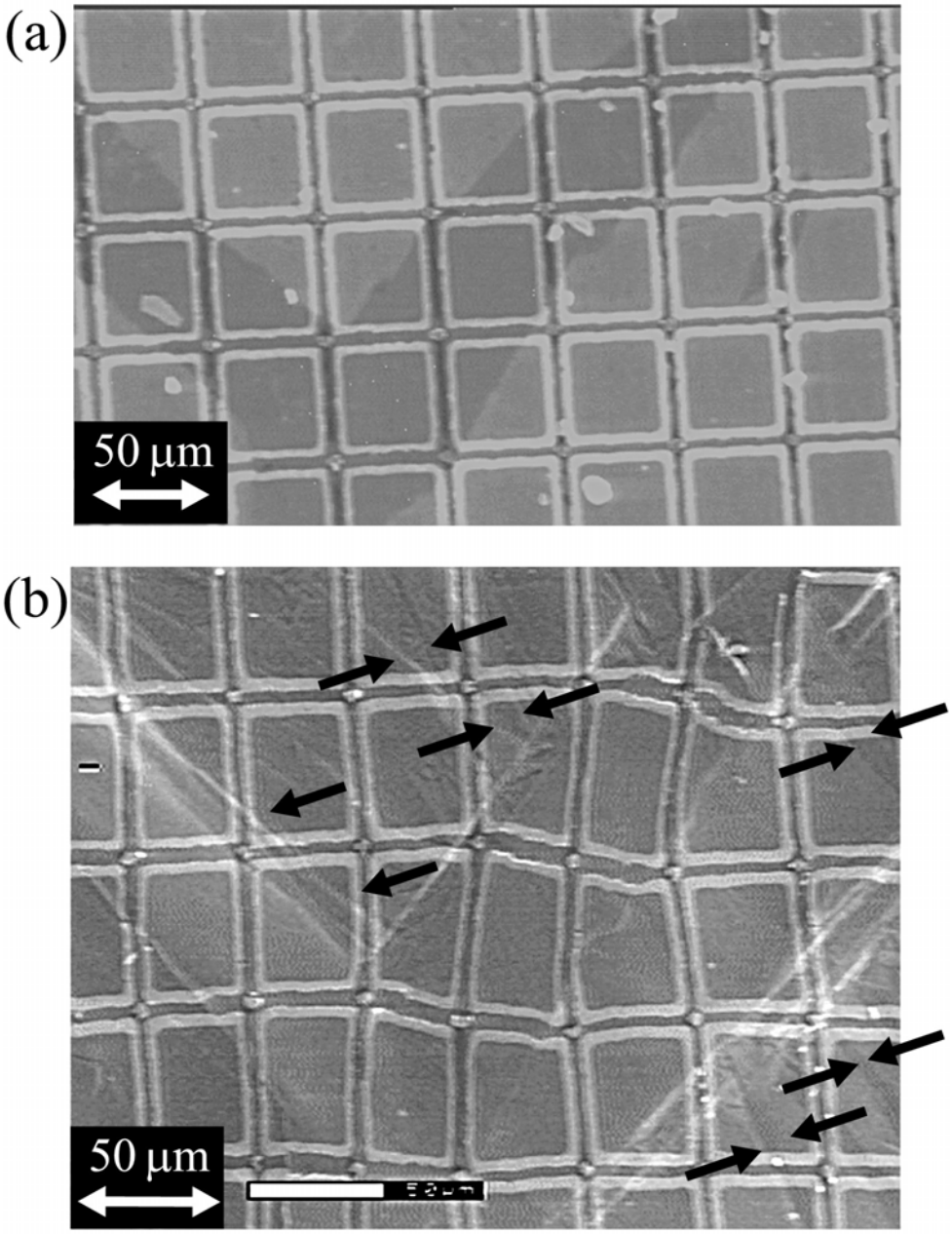

Figure 4.15: Secondary SEM micrograph of α-Ti-1.6V (a) before and (b) after creep at 65°C. Total creep strain is approximately 11%. Note profuse twinning indicated by arrows in (b).

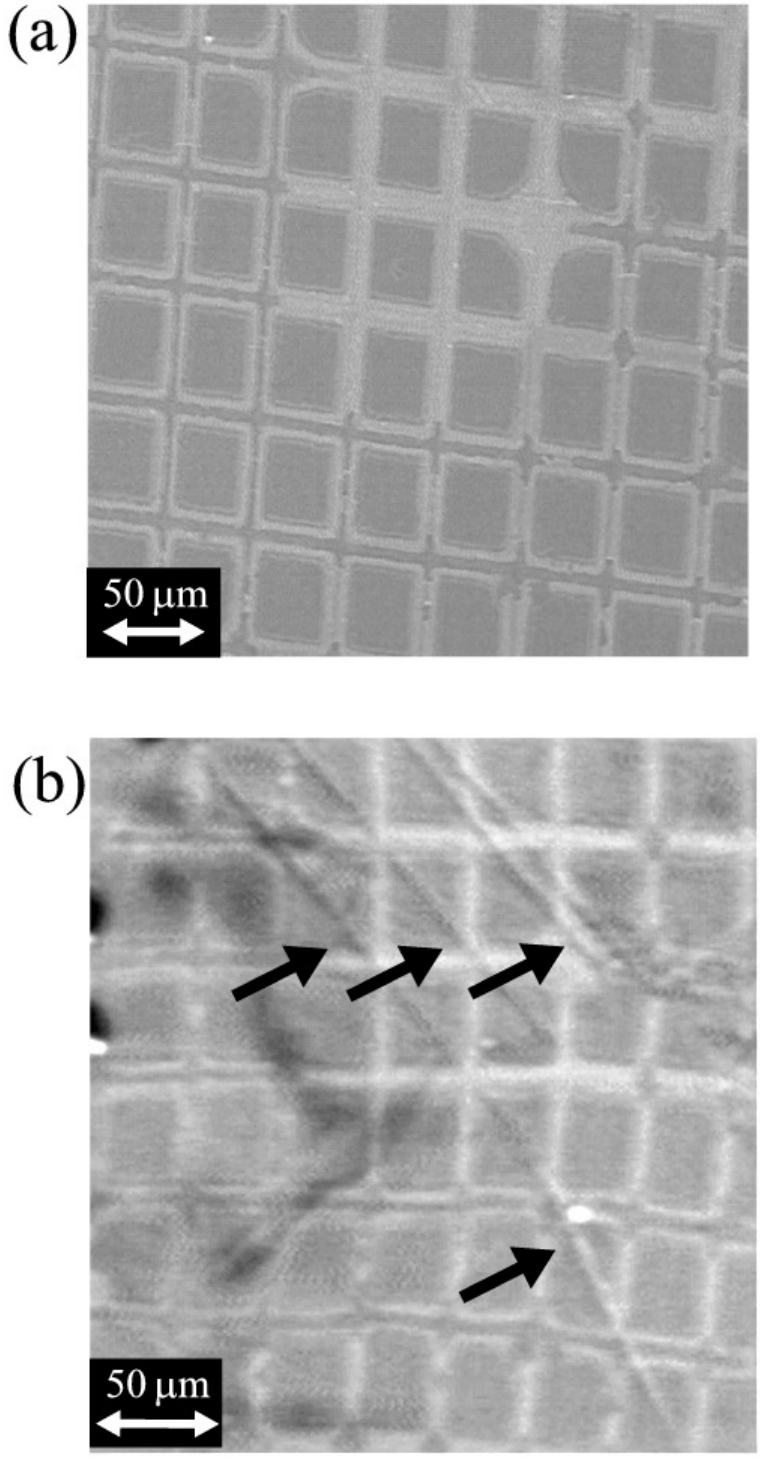

Figure 4.16: Secondary SEM micrograph of α-Ti-1.6V (a) before and (b) after creep at 65°C. Total creep strain is approximately 11%. Note profuse twinning indicated by arrows in (b).

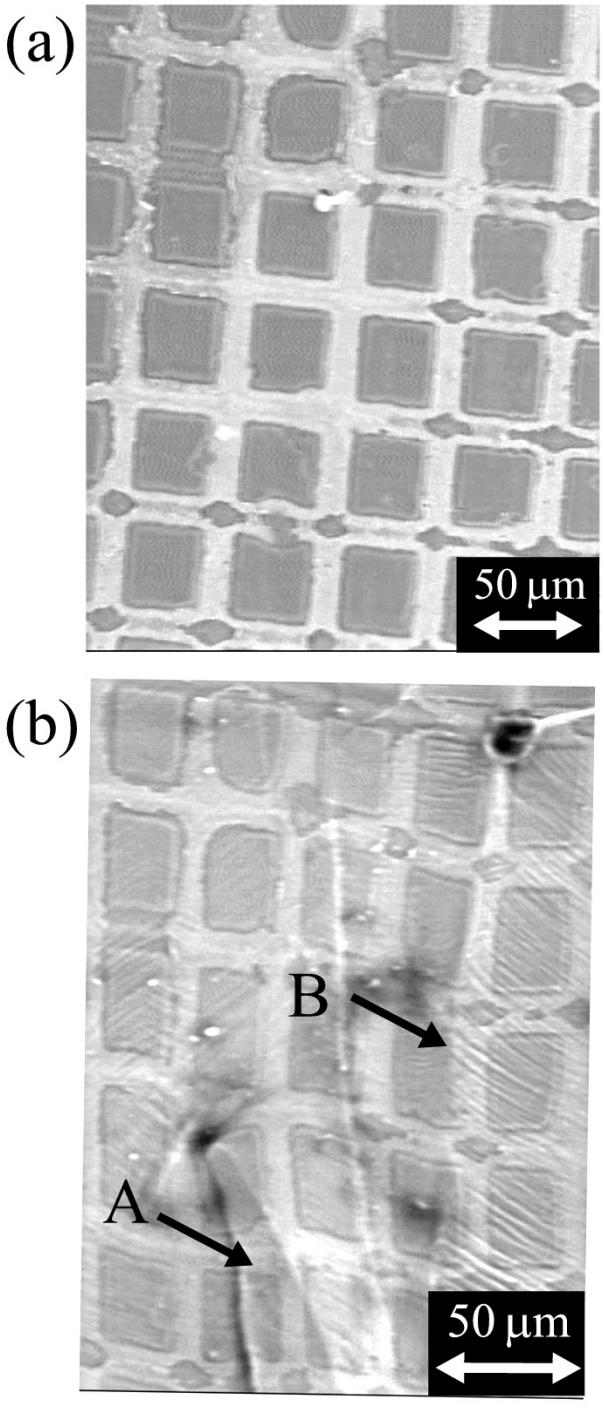

Figure 4.17: Secondary SEM micrograph of α-Ti-1.6V (a) before and (b) after creep at 205^{o}C. Total creep strain is approximately 10%. In (b) note twinning at 'A' and coarse slip lines at 'B'.

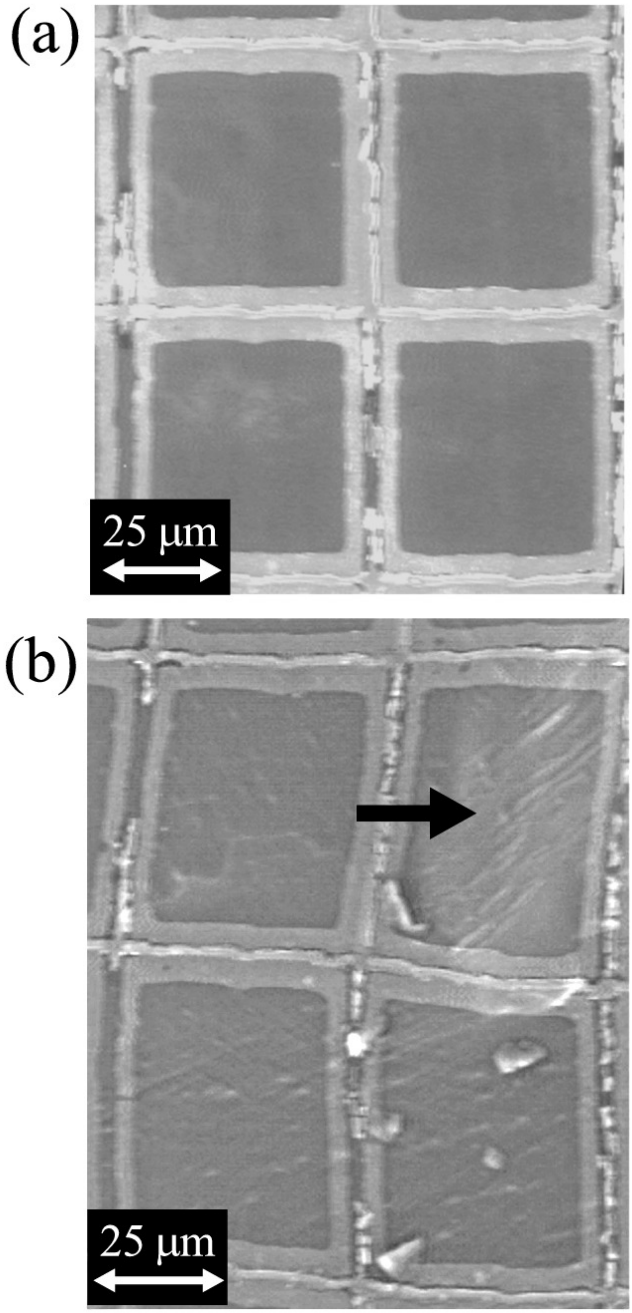

Figure 4.18: Secondary SEM micrograph of α-Ti-1.6V (a) before and (b) after creep at 205°C. Total creep strain is approximately 10%. Note coarse slip in (b) indicated by arrows.

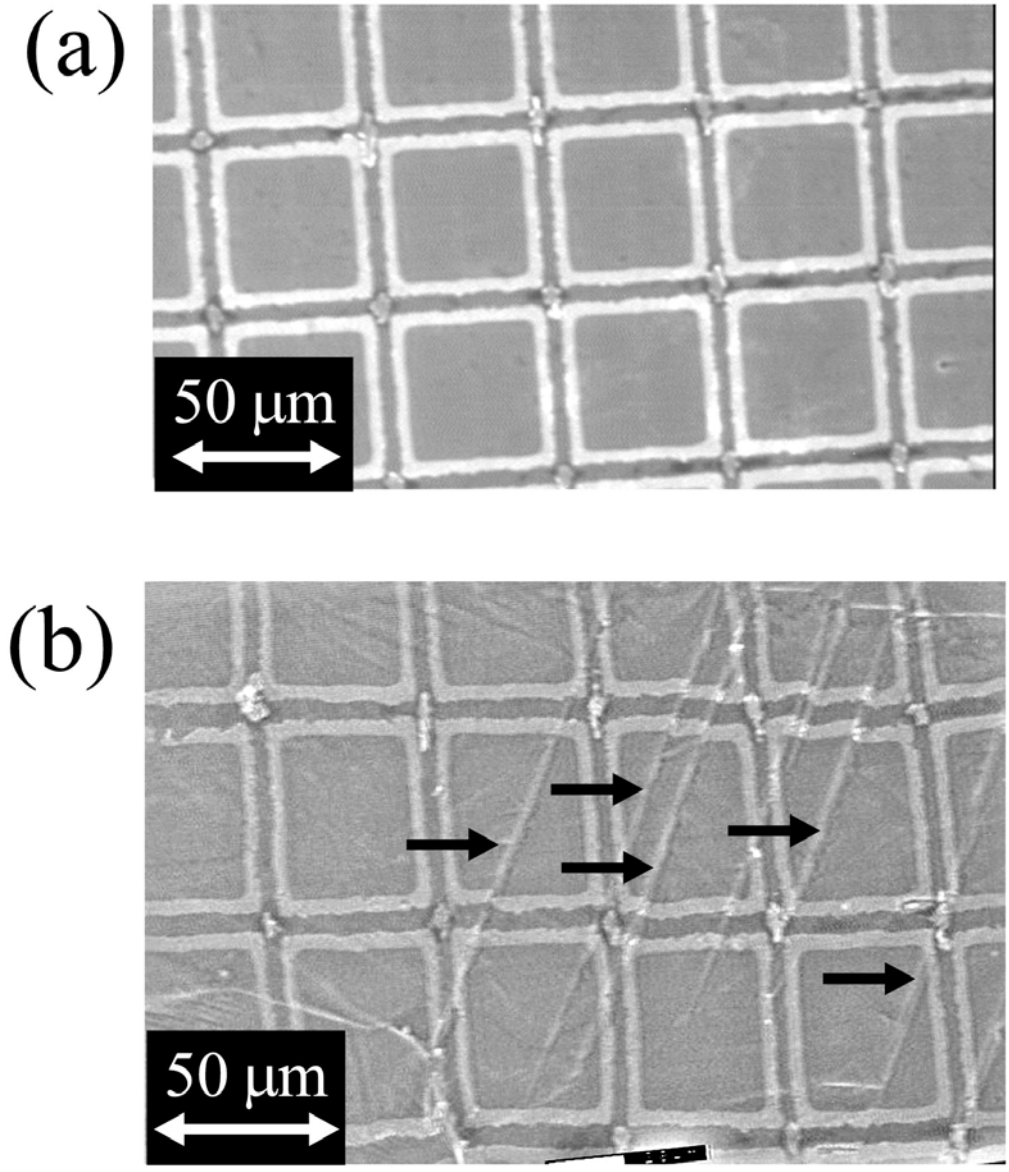

Figure 4.19: Secondary SEM micrograph of α-Ti-1.6V (a) before and (b) after creep at 205°C. Total creep strain is approximately 10%. Note profuse twinning in (b) indicated by arrows.

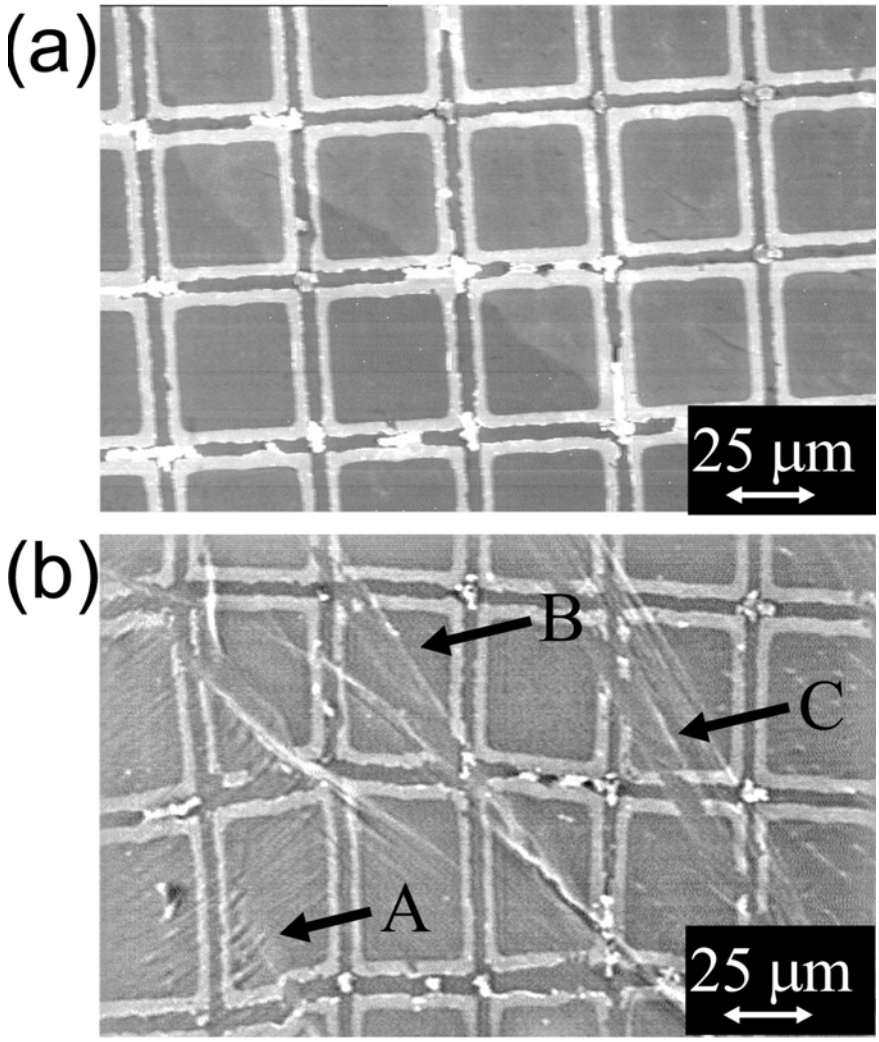

Figure 4.20: Secondary SEM micrograph of α-Ti-1.6V (a) before and (b) after creep at 205°C. Total creep strain is approximately 10%. In (b) note coarse slip lines at 'A' and twinning at 'B' and 'C'.

4.1.1.3.4 TEM Analysis of Creep Deformation Products

The following section presents the results of a TEM study of the deformation products associated with creep of the α–Ti-1.6V alloy. TEM foils were prepared from specimens which were creep tested at the temperatures of 298 K [26], 358 K, and 478 K to determine if the deformation products were similar over the entire temperature range of this investigation. Results from a TEM investigation of the creep deformation mechanisms of α–Ti-1.6V tested at 298 K have previously been published in *Metallurgical and Materials Transactions A* by Aiyangar, Neuberger, Oberson, and Ankem [26], but the same foils were re-examined in this investigation with a higher resolution microscope.

One of the reasons that twinning is an active deformation mechanism in HCP materials is that there are only two types of dislocations that are active during plastic deformation [36]. The first is referred to as an *a*-type dislocation and has a Burgers vector of the type $\frac{1}{3}\langle 11\bar{2}0\rangle$. The other type, less common, is called a *c*+*a*-type dislocation and has a Burgers vector of the type $\frac{1}{3}\langle 11\bar{2}3\rangle$. *a*-type dislocations can glide on either $\{1\,\bar{1}\,00\}$ planes (prism slip) or less frequently on the (0001) plane (basal slip). *c*-type dislocations, with Burgers vector of the type $\langle 0001\rangle$ are not seen in the matrix during plastic deformation. The Burgers vectors of the various dislocations in the HCP structure and the common slip planes are schematically illustrated in Figure 4.21.

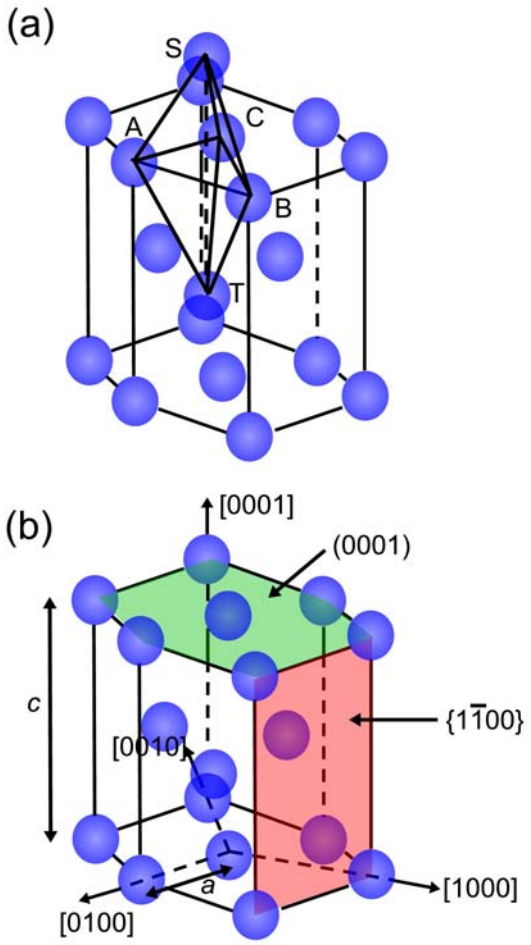

Figure 4.21: (a) Schematic illustration of the Burgers vectors of the dislocations in the HCP lattice of α-Ti. *a*-type dislocations have a Burgers vector given by *AB*, *BC*, or *AC* (or the reverse, i.e. *BA*). *c*-type dislocations have a Burgers vector given by *ST* or *TS*. *c*+*a* type dislocations have a Burgers vector given by the type *ST* + *AB*, etc. (b) The most common slip planes for α-Ti. Basal slip refers to slip on the (0001) basal plane. Prism slip refers to slip on the $\{1\bar{1}00\}$ type prism planes.

Figure 4.22 are bright-field TEM micrographs showing planar arrays of *a*-type screw dislocations with $\vec{b} = \frac{1}{3}\langle 11\bar{2}0\rangle$ in the matrix of creep deformed α-Ti-1.6V at various temperatures.

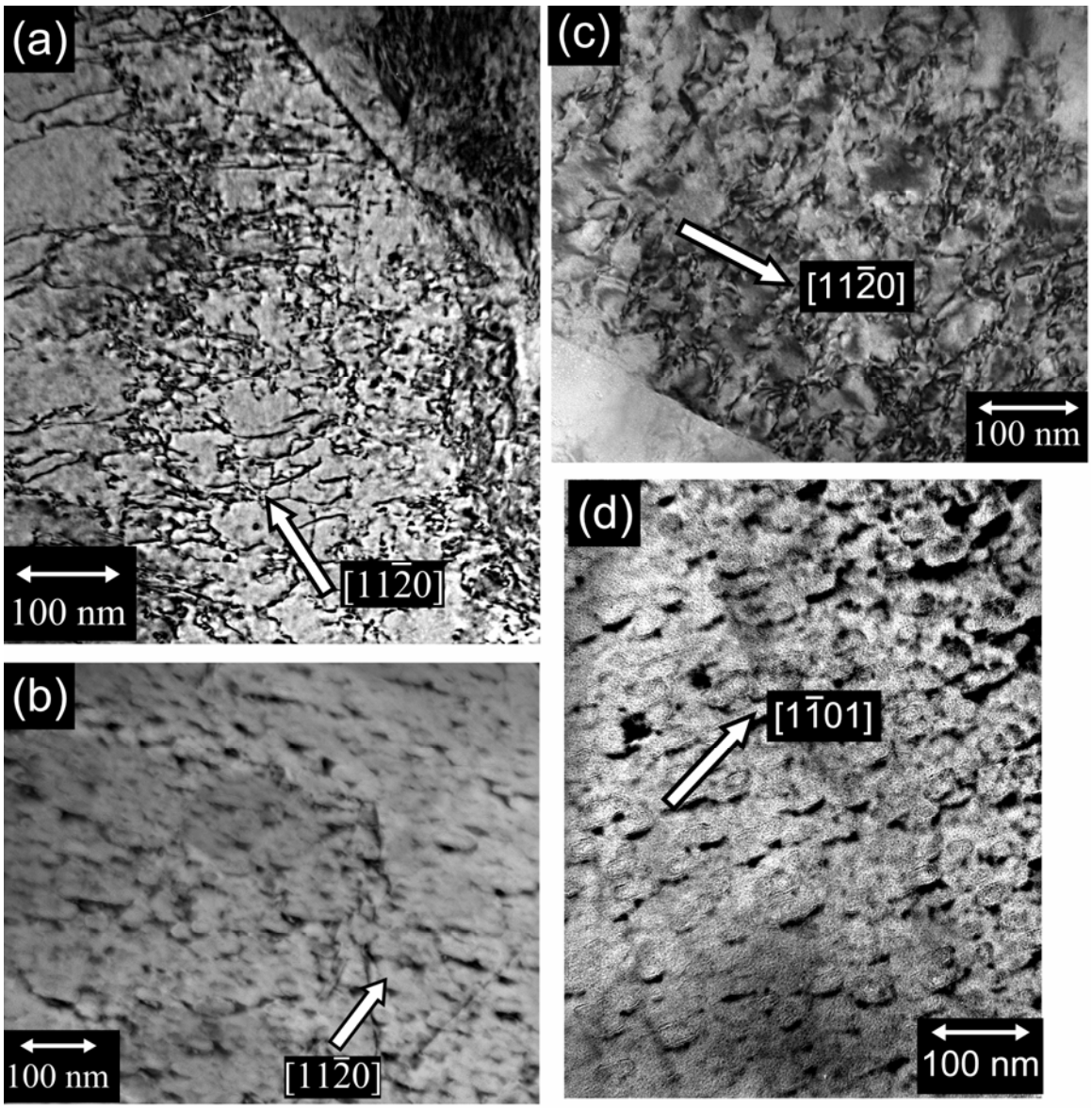

Figure 4.22: Bright-field TEM micrographs of *a*-type dislocations ($\vec{b} = \frac{1}{3}\langle 11\bar{2}0\rangle$) in matrix of α-Ti-1.6 V creep deformed at 95% YS. (a), (b), and (c) show prism slip on $\{1\,\bar{1}\,00\}$ planes at 298 K, 358 K, and 478 K, respectively. (d) shows basal slip on (0001) plane at 298 K.

As will be described later, creep deformation causes dislocation pileups at grain boundaries that generate the stress concentration necessary for twin nucleation and growth. The TEM micrographs of Figure 4.23 show twins at grain boundaries in various stages of growth. In Figure 4.23(a), in particular, the dislocations are clearly visible on the other side of the grain boundary from the growing twins. Similar behavior is seen in Figure 4.24. Figure 4.24(a) shows a more extensive network of dislocations in the pileup than 4.24(b), corresponding to a larger twin thickness. Note that it is also possible for the stress concentration caused by a twin in a grain to initiate twinning in the neighboring grain, as seen in Figure 4.25.

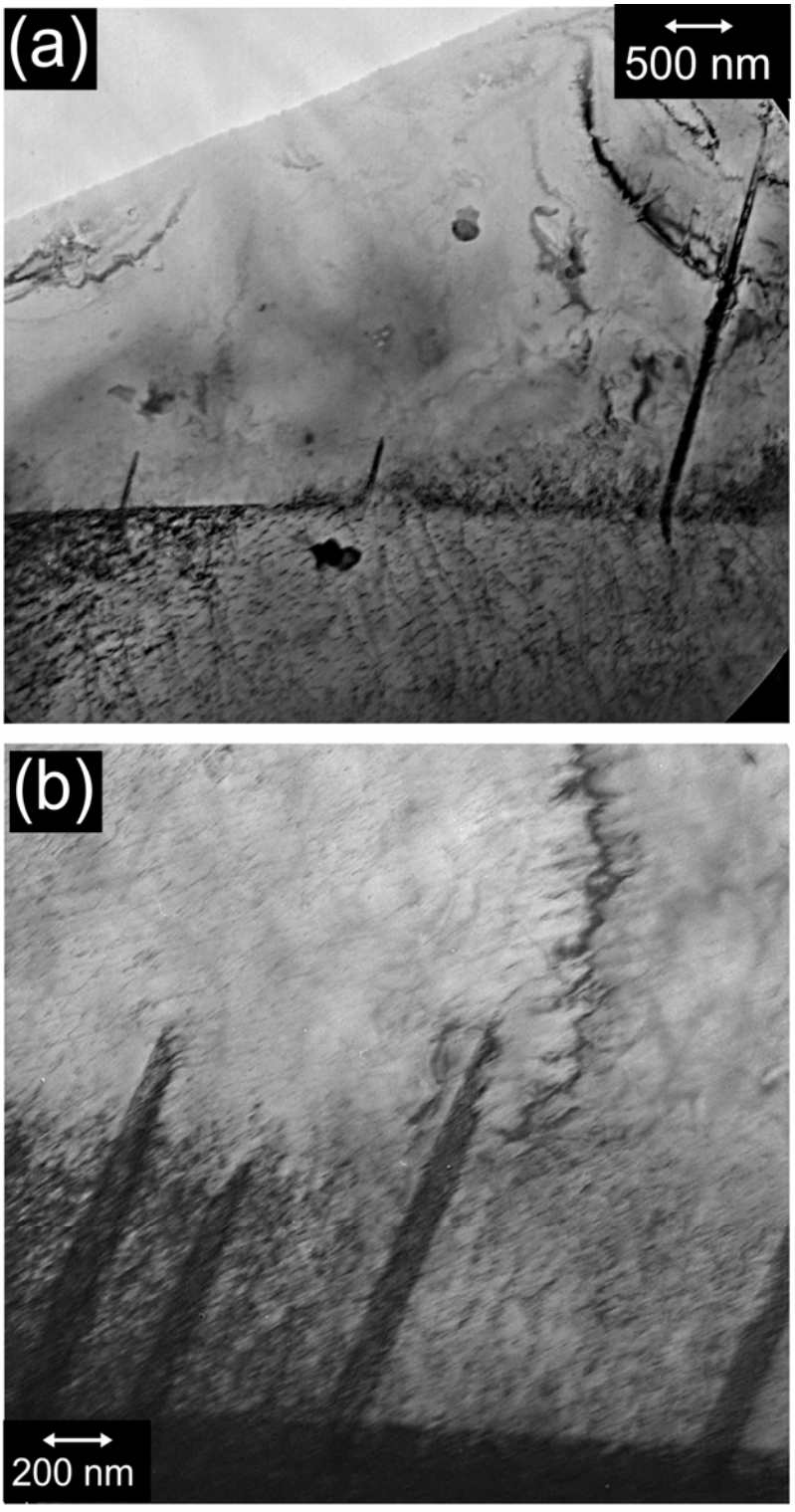

Figure 4.23: Bright field TEM micrographs of $\{1\bar{1}02\}\langle 10\bar{1}\bar{1}\rangle$ twins growing from the grain boundary in α-Ti-1.6V creep deformed at 95% YS at (a) 298 K and (b) 358 K. In (a) note numerous dislocation on the other side of the grain boundary from the twin.

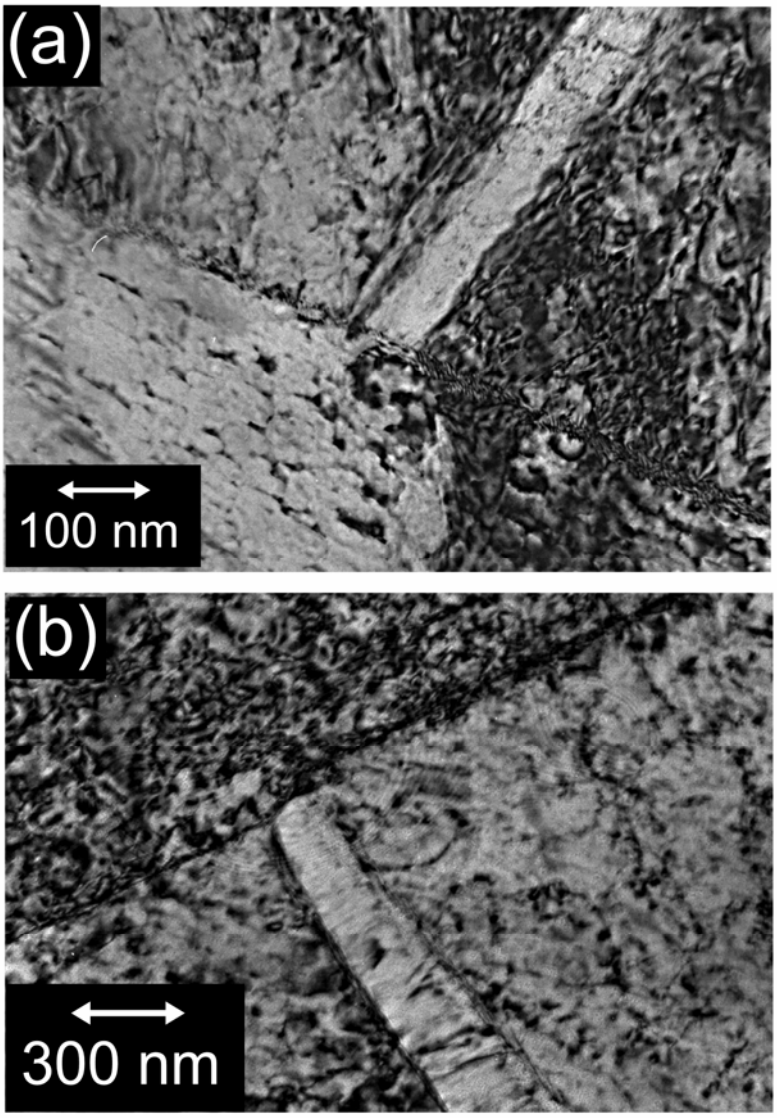

Figure 4.24: Bright field TEM micrographs of $\{1\bar{1}02\}\langle 10\bar{1}\bar{1}\rangle$ twins growing from the grain boundary in α-Ti-1.6V creep deformed at 95% YS at (a) 298 K and (b) 478 K.

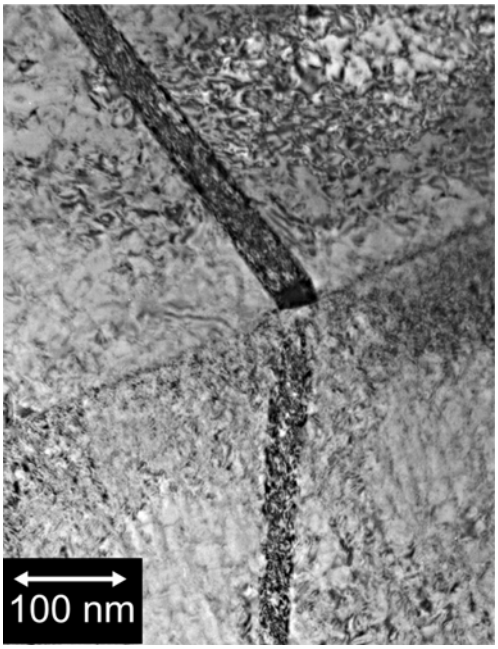

Figure 4.25: Bright field TEM micrograph of two $\{1\bar{1}02\}\langle 10\bar{1}\bar{1}\rangle$ twins intersecting at a grain boundary in creep deformed α-Ti-1.6V, suggesting that the stress concentration from a twin can serve to nucleate twinning in the neighboring grain.

As mentioned in Section 2.4, the lattice of a twin is a mirror reflection of the lattice of the untwinned matrix across the $\mathbf{K_1}$ twinning plane. Alternatively, the twinned lattice can be related to the untwinned lattice by a rotation around a pole perpendicular to the twin plane normal and the twinning direction [35]. As such, when using the TEM, twins are identified by obtaining selected area diffraction patterns (SADPs) of the matrix and the twin where the zone axis is the direction of the pole of rotation. The matrix and twin will have the same SADP but they will be rotated with respect to one another at an angle which is characteristic of the twinning mode. As will be discussed later, there are four main twinning modes which have been identified in HCP materials. The modes are characterized by a particular twinning plane ($\mathbf{K_1}$) and direction ($\boldsymbol{\eta_1}$) which are defined in Section 2.4. In the case of creep deformed α-Ti-1.6V in this investigation, two types of

twins were identified. The first and most common is the $\{1\bar{1}02\}\langle 10\bar{1}\bar{1}\rangle$ twin, hereafter to be referred to as the $\{1\bar{1}02\}$ twin. In this case, the twin and the matrix are related by a rotation of approximately 85° along the shear plane normal, as schematically illustrated in Figure 4.26. Figure 4.28 shows the SADPs of the $\{\bar{1}\bar{1}20\}$ foil plane taken from the area shown in Figure 4.27, including the untwinned matrix, a $\{1\bar{1}02\}$ twin, and across the twin-matrix interface, respectively. Note that the diffraction pattern of the twin-matrix interface in Figure 4.28(c) is symmetric with respect to the line that passes through the shared $\{1\bar{1}02\}$ spots, which is indicated by the dashed line. The second and less common is the $\{10\bar{1}1\}\langle 10\bar{1}\bar{2}\rangle$ twin, hereafter to be referred to as the $\{10\bar{1}1\}$ twin. In this case, the twin and matrix are related by a rotation of approximately 58° along the shear plane normal, as illustrated in Figure 4.29. Diffraction patterns taken from the area shown in Figure 4.30 are shown in Figure 4.31.

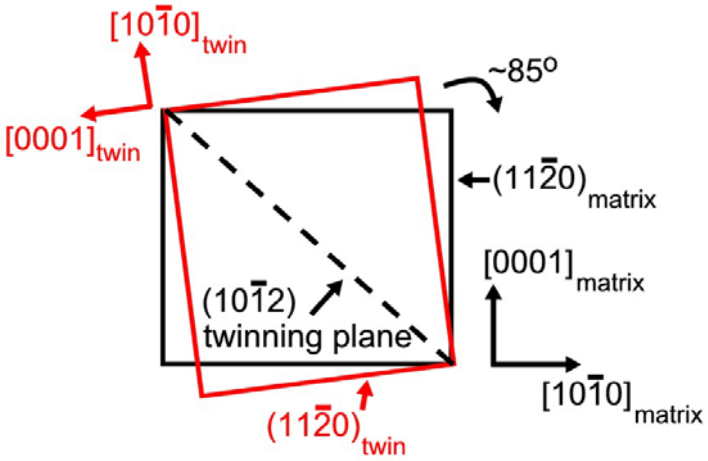

Figure 4.26: Schematic illustration of $\{1\bar{1}20\}$ planes of the matrix (black) and twin (red), respectively. In the case of the $\{1\bar{1}02\}$ twin, the $\{1\bar{1}20\}$ plane of the twin is rotated by a rotation of 85° (clockwise) with respect to the $\{1\bar{1}20\}$ plane of the matrix.

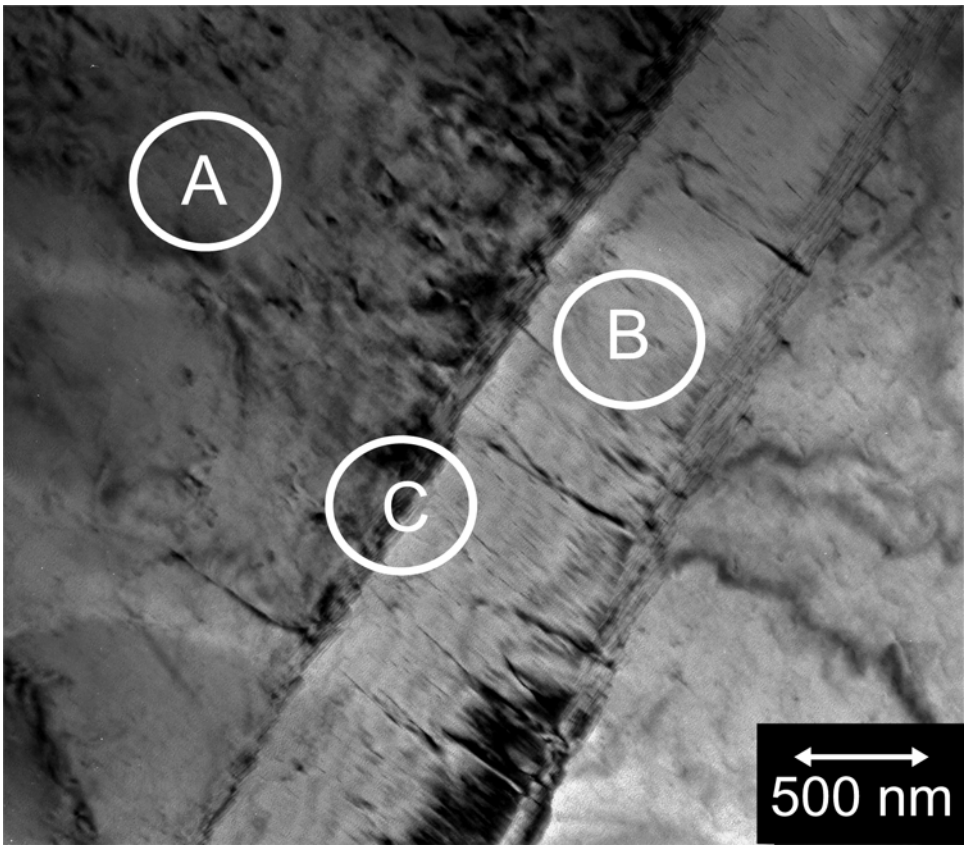

Figure 4.27: Bright field TEM micrograph of $\{1\bar{1}02\}$ twin showing the areas from which the SADPs in Figure 4.28 were taken. 'A' is the untwinned matrix, 'B' is inside the twin, and 'C' is across the twin-matrix interface.

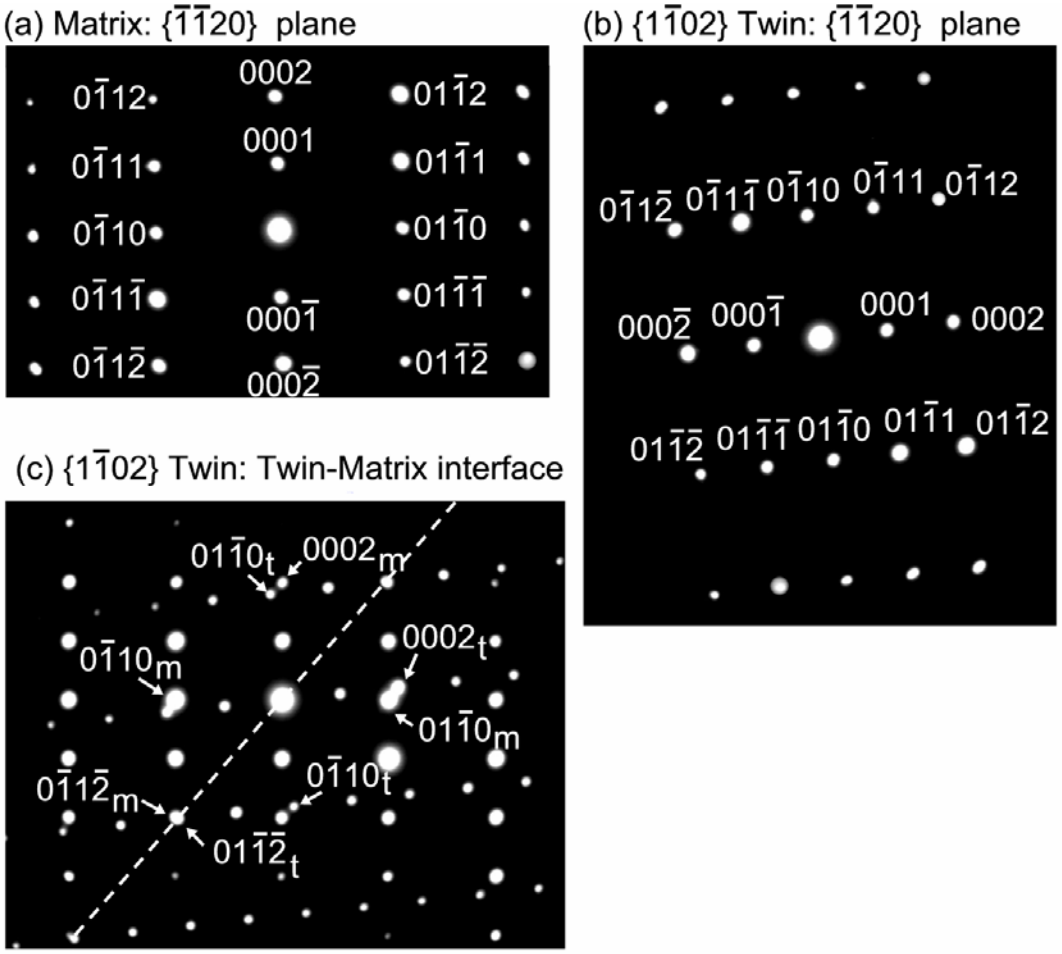

Figure 4.28: Selected Area Diffraction Patterns (SADPs) along the $\{\bar{1}\,\bar{1}\,20\}$ zone axis taken from creep deformed α-Ti-1.6V shown in Figure 4.27 above. (a) Untwinned matrix. (b) $\{1\,\bar{1}\,02\}$ twin. Diffraction pattern of the twin is rotated approximately 85^o clockwise with respect to the untwinned matrix. (c) Across twin-matrix interface. Diffraction pattern is symmetric with respect to the dashed line that passes through the shared $\{1\,\bar{1}\,02\}$ spots. Spots with the subscript 'm' refer to matrix spots and spots with the subscript 't' refer to twin spots.

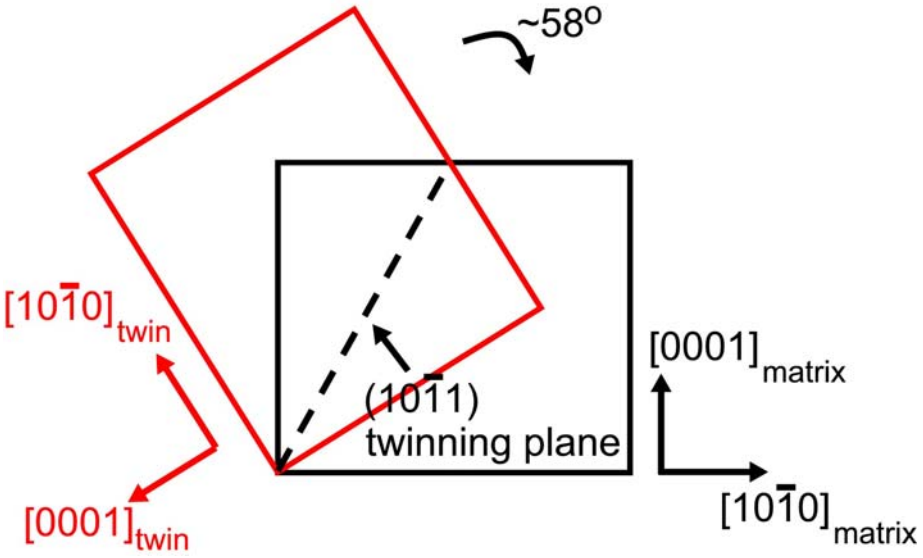

Figure 4.29: Schematic illustration of $\{11\bar{2}0\}$ planes of the matrix (black) and twin (red), respectively. In the case of the $\{1\bar{1}01\}$ twin, the $\{11\bar{2}0\}$ plane of the twin is rotated by a rotation of 58° (clockwise) with respect to the $\{11\bar{2}0\}$ plane of the matrix.

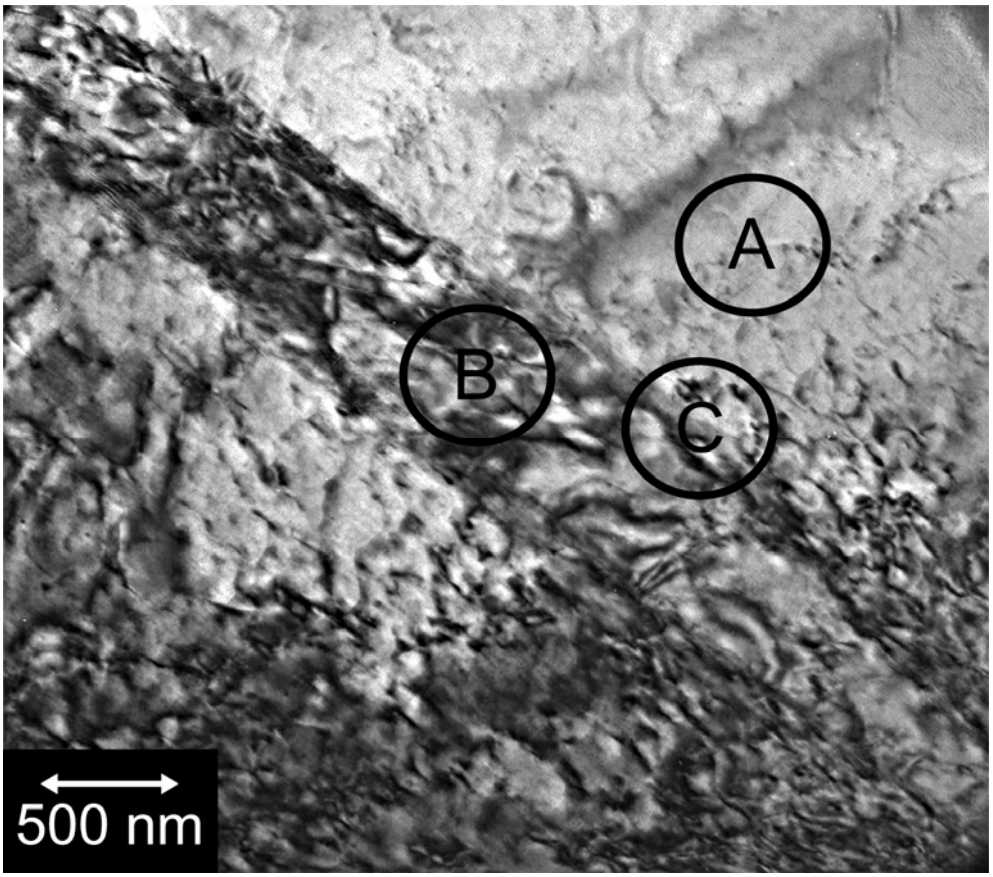

Figure 4.30: Bright field TEM micrograph of $\{1\bar{1}01\}$ twin showing the areas from which the SADPs in Figure 4.31 were taken. 'A' is the untwinned matrix, 'B' is inside the twin, and 'C' is across the twin-matrix interface.

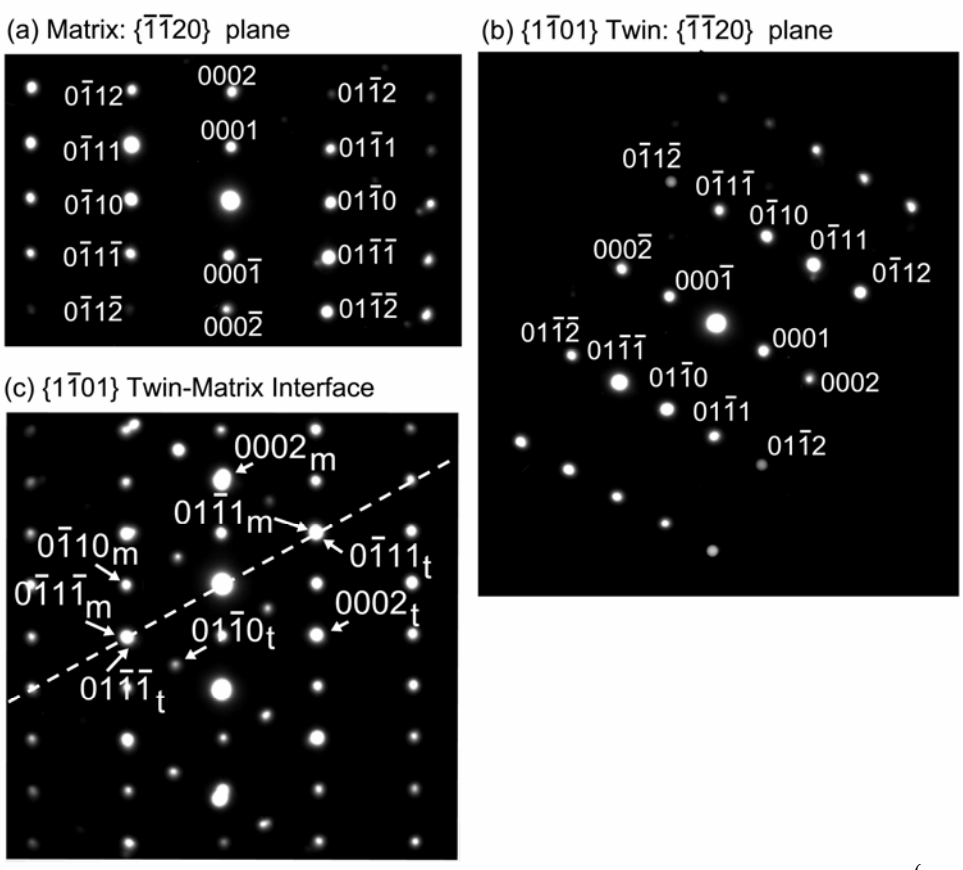

Figure 4.31: Selected Area Diffraction Patterns (SADPs) along the $\{\bar{1}\,\bar{1}\,20\}$ zone axis taken from creep deformed α-Ti-1.6V. (a) Untwinned matrix. (b) $\{1\,\bar{1}\,01\}$ twin. Diffraction pattern of the twin is rotated approximately 58° clockwise with respect to the untwinned matrix. (c) Across twin-matrix interface. Diffraction pattern is symmetric with respect to the dashed line that passes through the shared $\{1\,\bar{1}\,01\}$ spots. Spots with the subscript 'm' refer to matrix spots and spots with the subscript 't' refer to twin spots.

Bright-field TEM micrographs of $\{1\bar{1}02\}$ twins from specimens creep tested at 298 K, 358 K, and 478 K are shown in Figures 4.32, 4.33, and 4.34, respectively. The thickness of the twins ranges from less than 100 nm to in excess of 500 nm, indicating twins in various stages of growth. The coherent nature of the twin-matrix interface is shown in the high-resolution micrograph of Figure 4.35. Twins are often found in close proximity and it is not uncommon for twins to touch or intersect one another. Figure 4.36 shows bright field TEM micrographs of the less common $\{10\bar{1}1\}$ twin in the specimens tested at the various temperatures. They appear identical to $\{1\bar{1}02\}$ twins, suggesting that nucleation and growth mechanisms are similar. As $\{1\bar{1}02\}$ twins are the predominant twin observed during creep of α-Ti-1.6V, they will be the focus of the remainder of this investigation.

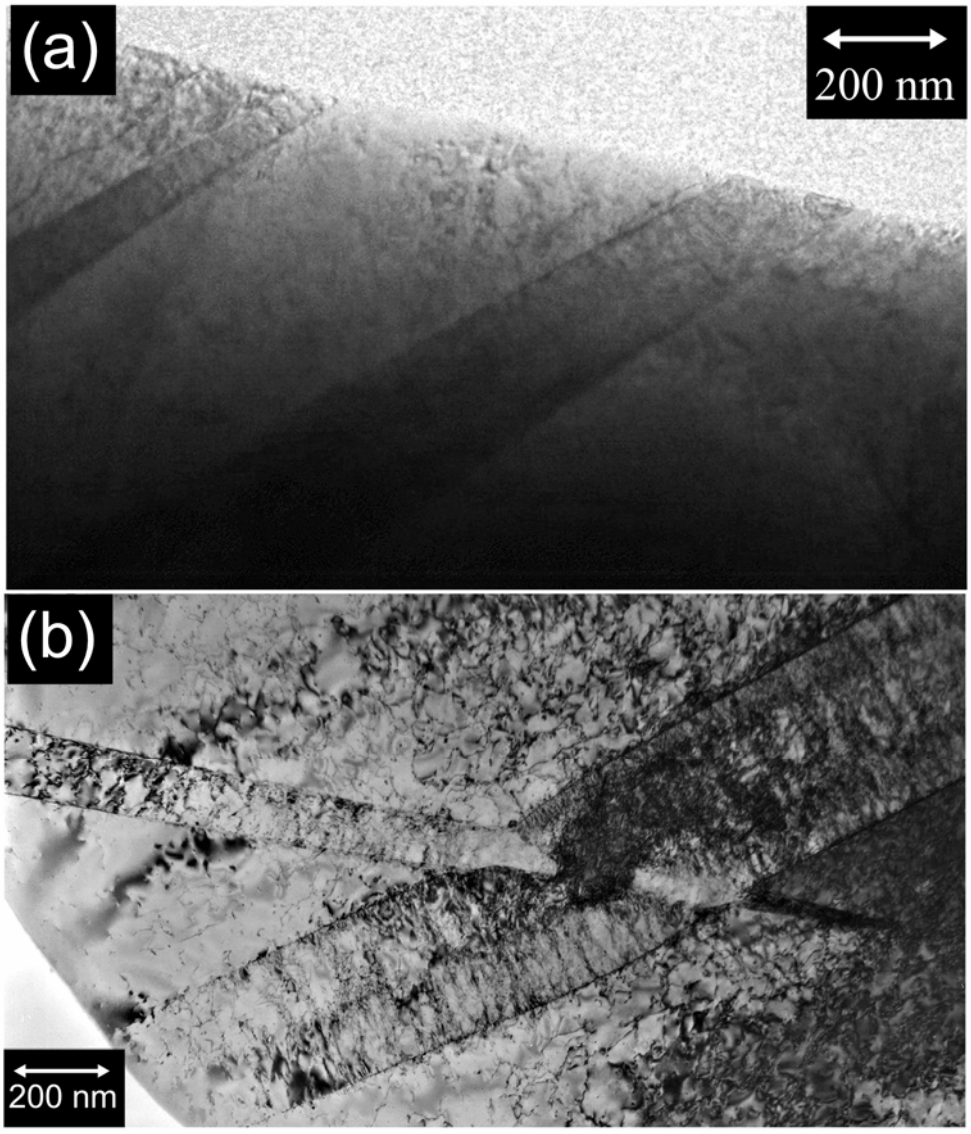

Figure 4.32: Bright field TEM micrograph of $\{1\bar{1}02\}$ twins in α-Ti-1.6V creep deformed at 95% YS at 298 K.

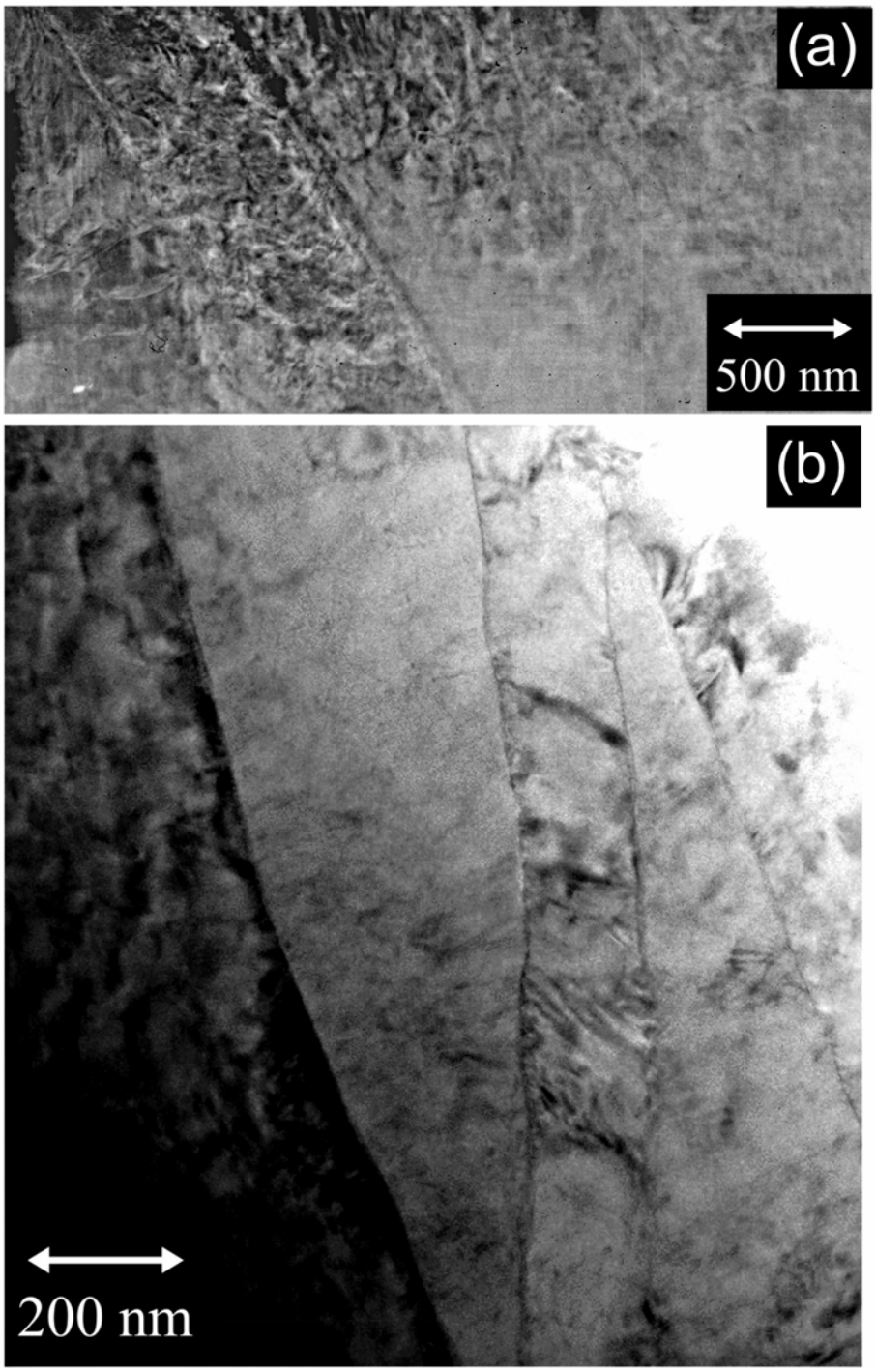

Figure 4.33: Bright field TEM micrograph of $\{1\bar{1}02\}$ twins in α-Ti-1.6V creep deformed at 95% YS at 358 K.

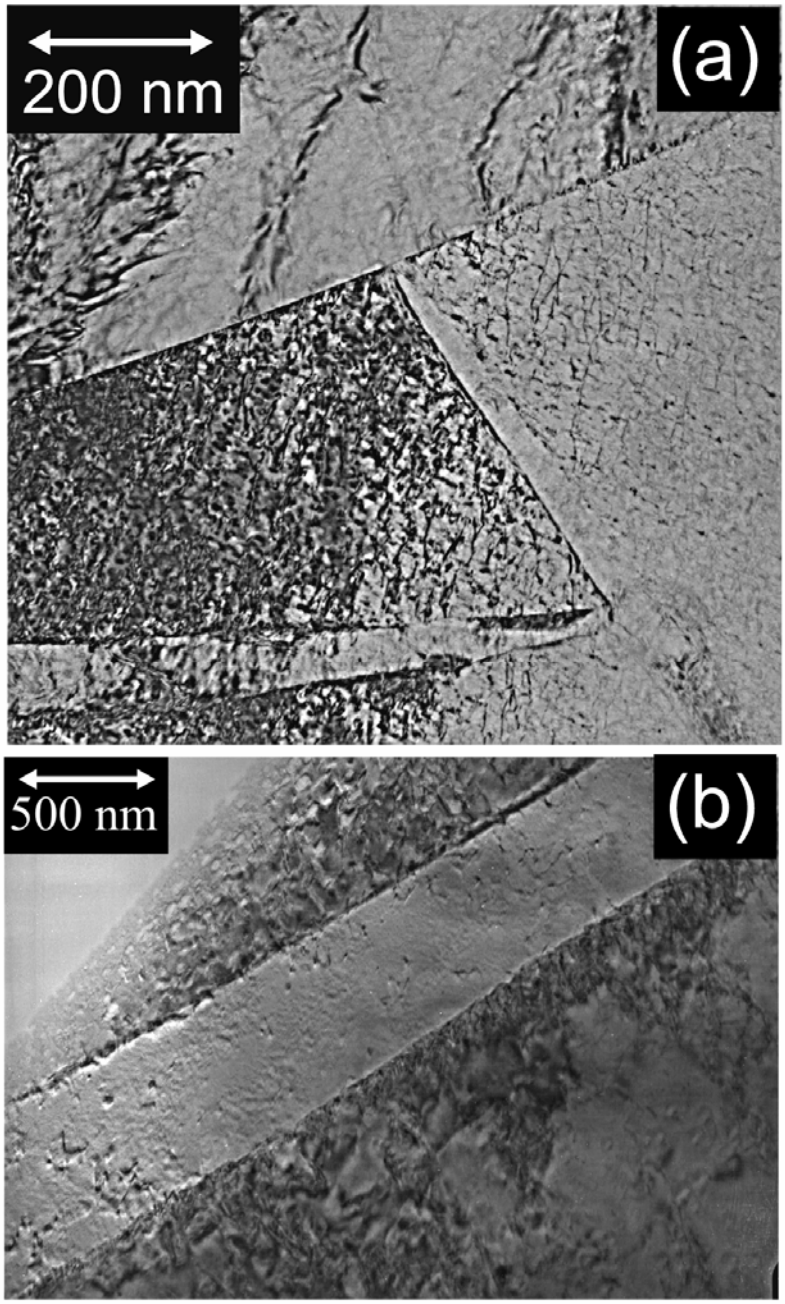

Figure 4.34: Bright field TEM micrograph of $\{1\bar{1}02\}$ twins in α-Ti-1.6V creep deformed at 95% YS at 478 K.

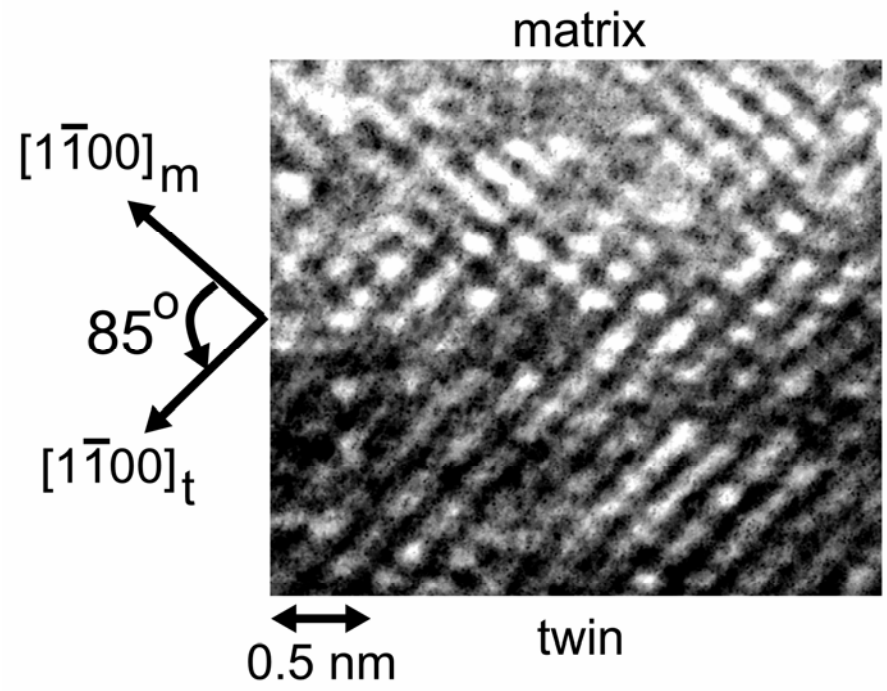

Figure 4.35: High-resolution image of $\{1\bar{1}02\}$ twin-matrix interface in creep deformed α-Ti-1.6V. Note 85° angle between $[1\bar{1}00]$ directions in the twin and matrix, respectively.

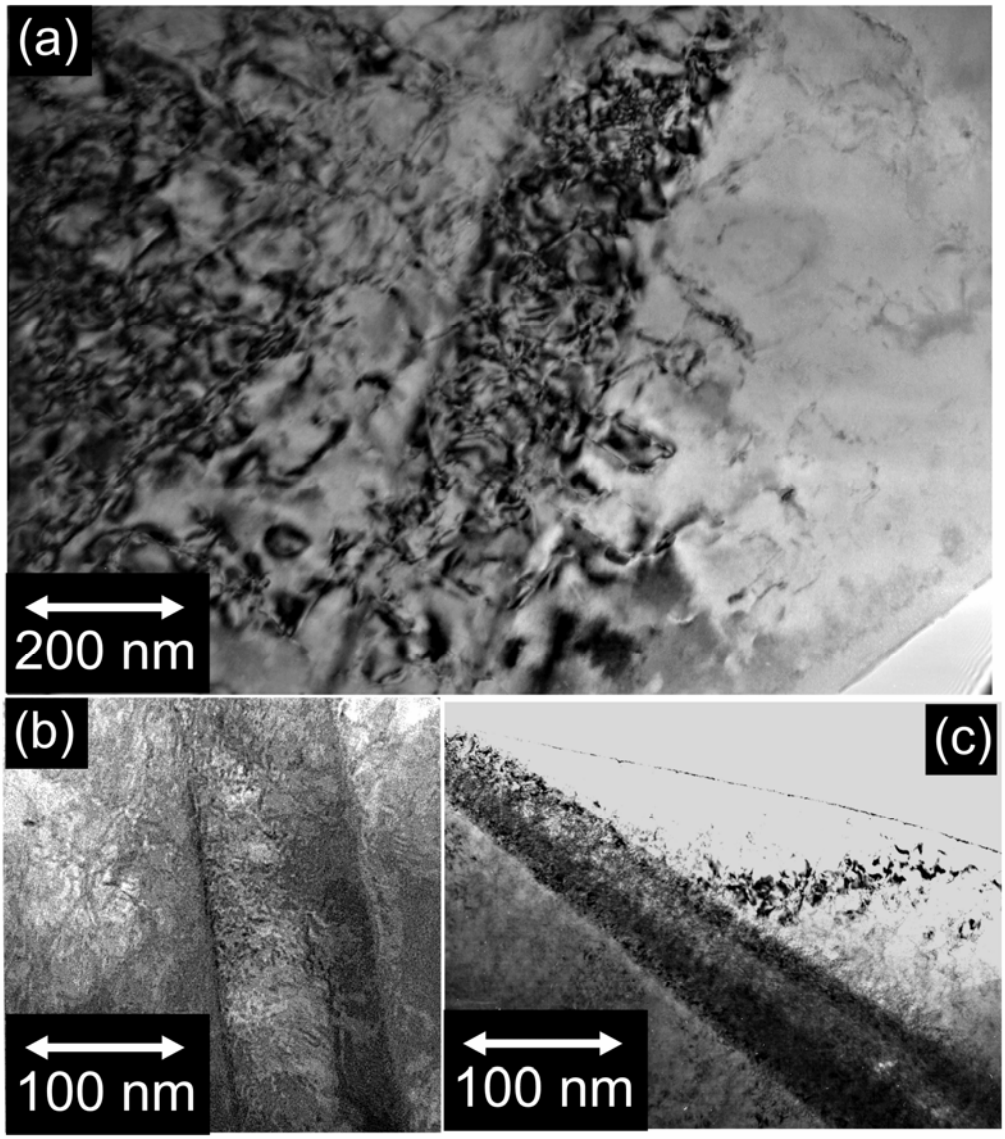

Figure 4.36: Bright-field TEM micrographs of the less common $\{10\bar{1}1\}$ twins in α-Ti-1.6V creep deformed at 95% YS at (a) 298 K, (b) 358 K, and (c) 478 K.

From the TEM analysis, it is clear that there is an interaction between twins and dislocations, suggesting that these dislocations are involved in the twin growth process. First, *a*-type dislocations are found in the untwinned matrix in the vicinity of twin boundaries and twin tips, as illustrated in Figure 4.37. Next, *c*-type dislocations with Burgers vector $\langle 0001 \rangle$ with are found inside twins. Recall that these dislocations are not found in the untwinned matrix.

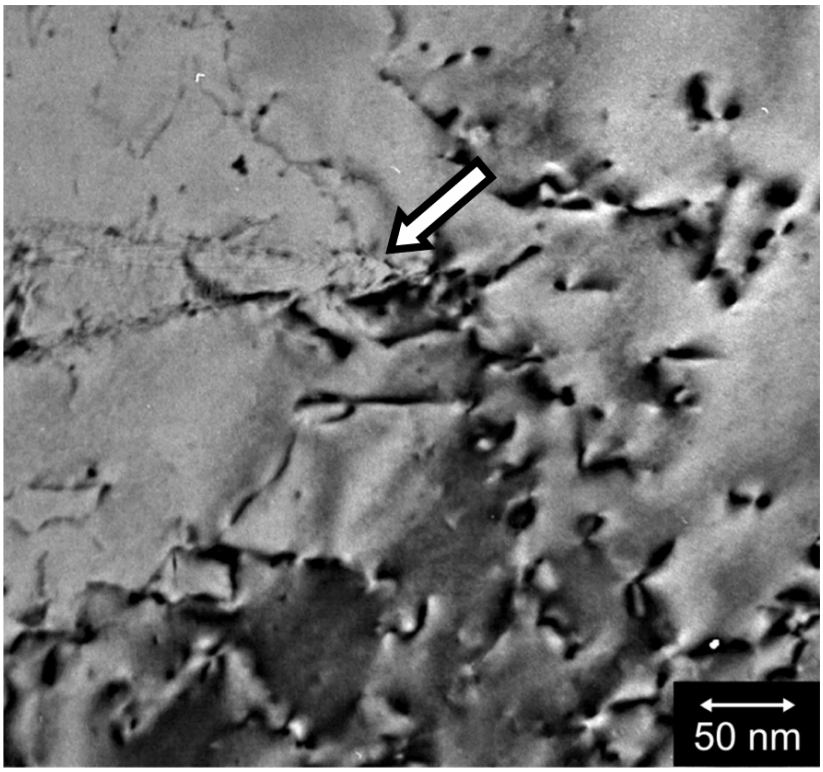

Figure 4.37: Bright-field TEM micrograph of *a*-type dislocations interacting with a growing twin-tip, indicated by arrow, in creep deformed α-Ti-1.6V.

c-type dislocations that are located within $\{1\bar{1}02\}$ twins are illustrated in Figure 4.38. One interesting characteristic of *c*-type dislocations in twins is that they have a 'U' shape with the bottom of the 'U' parallel to the twin boundary and the legs of the 'U' perpendicular to the twin-boundary. This is usually difficult to see because it is common for the legs to be cut off by the foil surface. Figure 4.39 shows a number of 'U' shaped dislocations from Figure 4.38 at a higher magnification. The density of the *c*-type dislocations generally increases as the twin thickness increases. Particularly, note Figure 4.38(b), where the twin thickness is greater than 500 μm. The extensive network of dislocations and compare to Figure 4.38(c) where the twin thickness is only about 100 nm and there are significantly fewer dislocations. Because the *c*-type dislocations originate at varying distances from the center of the twin, and the legs terminate at the twin boundary, the highest density of dislocations will be at the twin-matrix interface.

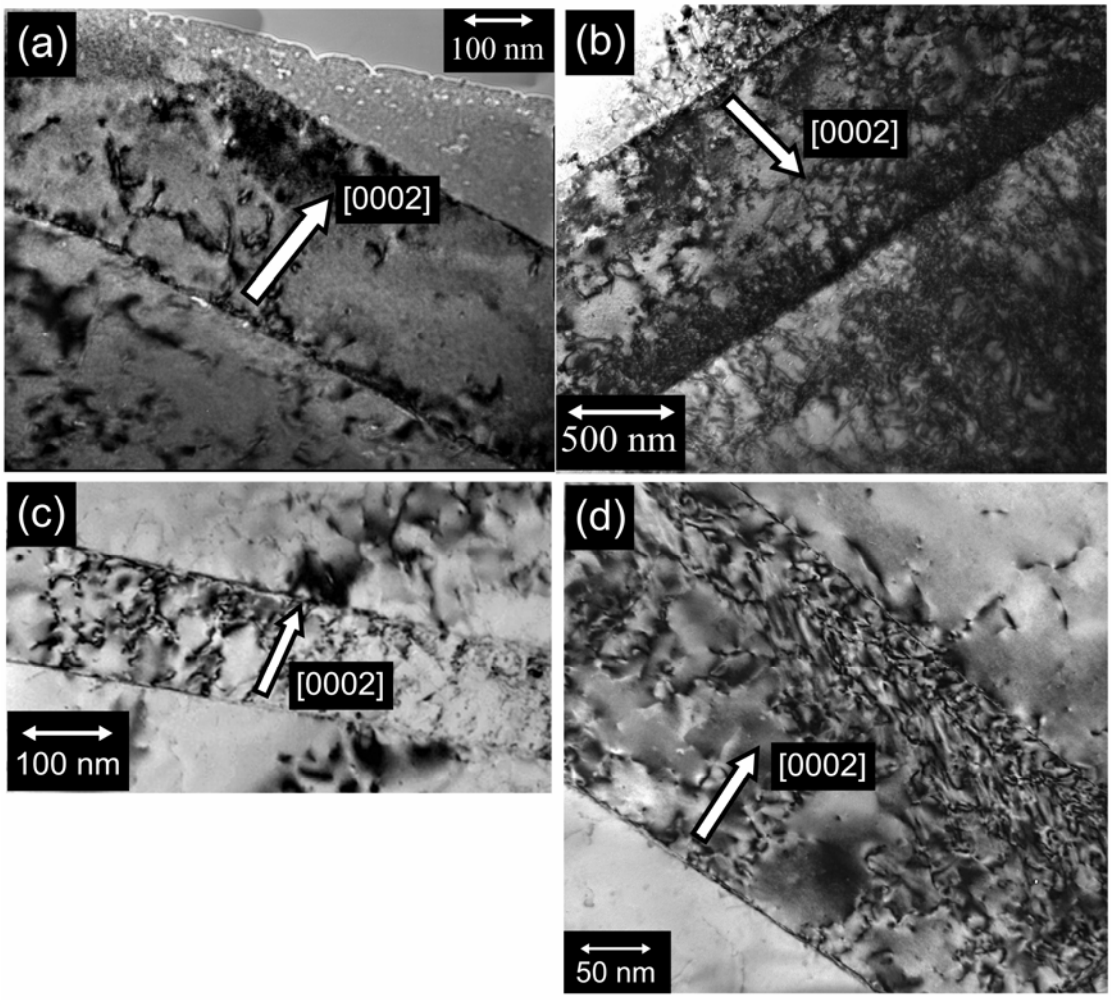

Figure 4.38: Bright field TEM micrograph of *c*-type dislocations in the $\{1\bar{1}02\}$ type twins in α-Ti-1.6V creep deformed at 95% YS at (a) 298 K, (b) 358 K, (c) and (d) 478 K.

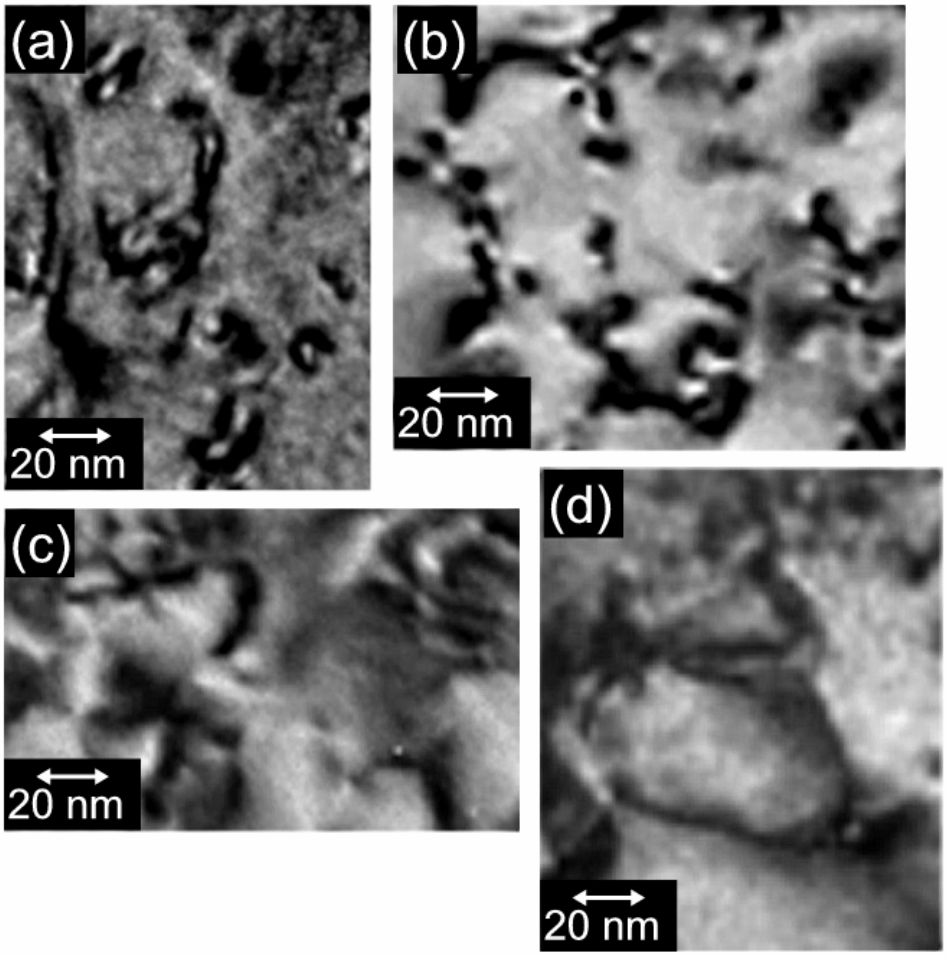

Figure 4.39: Bright field TEM micrograph of 'U' shaped *c*-type dislocations in the $\{1\bar{1}02\}$ type twins in α-Ti-1.6V creep deformed at 95% YS at (a) 298 K, (b) and (c) 478 K, and (d) 358 K.

As will be discussed later, the presence of the *a*-type dislocations in the matrix and the *c*-type dislocations in the $\{1\bar{1}02\}$twins can be explained by a model for twin growth based on the sideways motion of twin-boundary ledges. Such ledges are seen in the TEM micrographs of Figure 4.40.

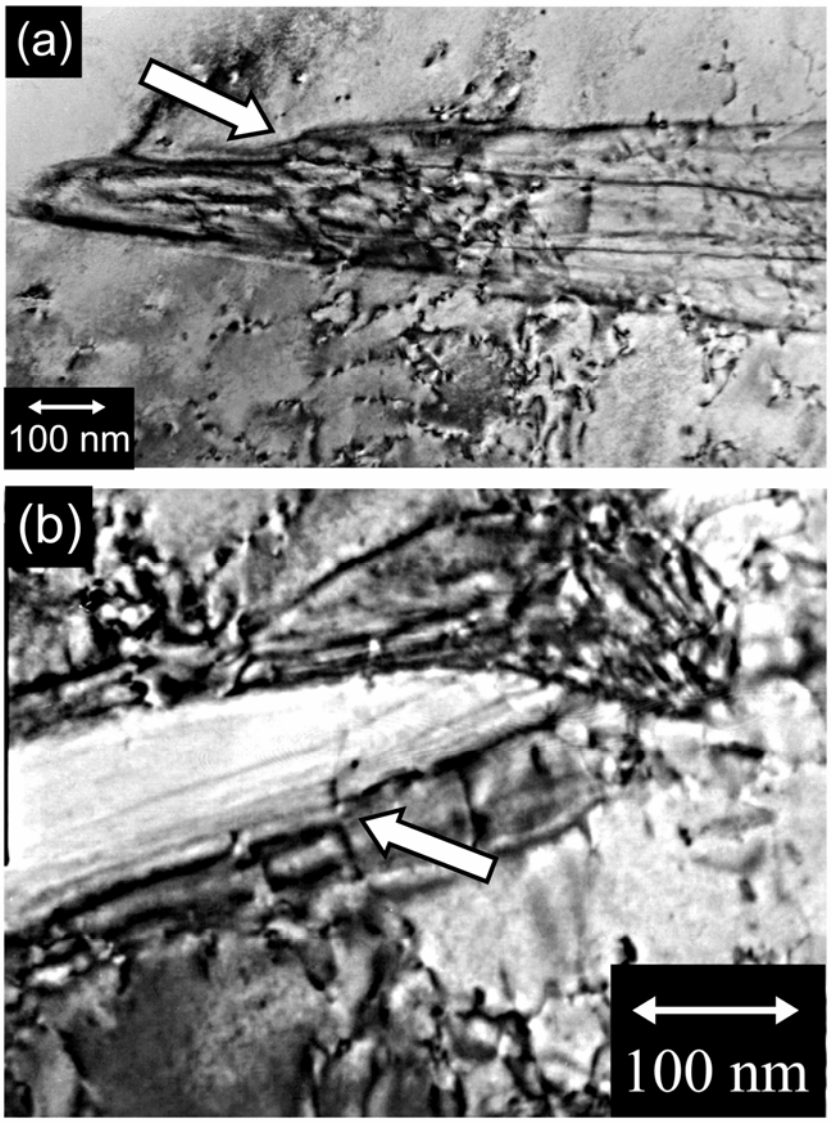

Figure 4.40: Bright field TEM micrographs showing steps (indicated by arrows) on the $\{1\bar{1}02\}$ twin-matrix interface of α-Ti-1.6V creep deformed at (a) 298 K, and (b) 358 K.

The last interesting feature of the $\{1\bar{1}02\}$ twins in α-Ti-1.6V is the presence of stacking faults within the twins, seen in Figures 4.41 and 4.42. The stacking faults are different from those typically observed in HCP materials, namely the I_1 fault (intrinsic vacancy collapse), the I_2 fault (intrinsic dislocation dissociation), and the E fault (extrinsic, inserting *C* plane in *ABAB…* sequence). The origins of the stacking faults in the twins will be discussed in the following sections, but for now it is sufficient to note that in these stacking faults, only half the atoms on one side of the fault shift their positions with respect to those on the other side during twinning. As such, the faults are referred to as partial stacking faults (PSFs). The stacking sequence across the faulting plane for the PSFs is given as …ABAB||ACAC....

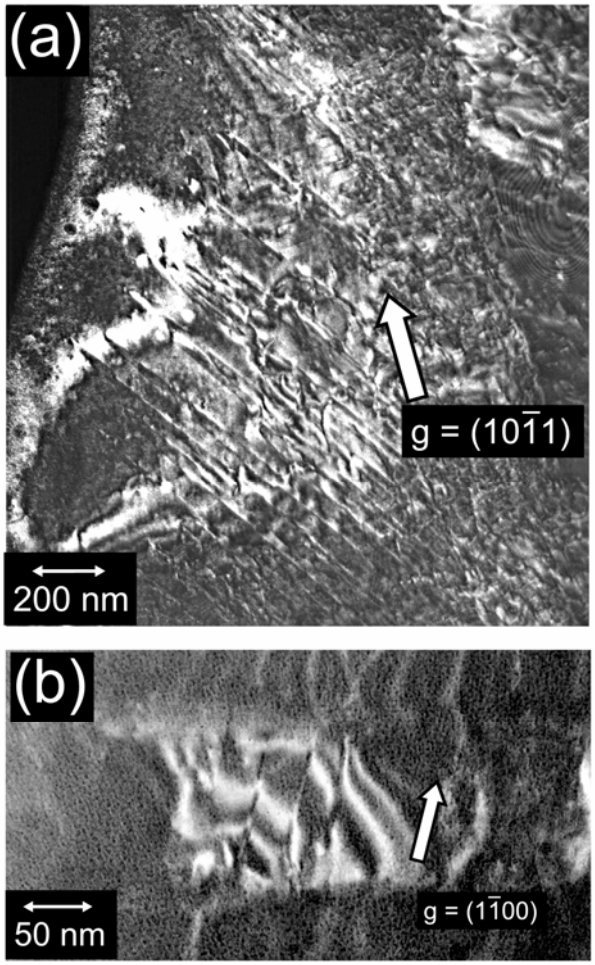

Figure 4.41: Dark-field TEM images of stacking faults in $\{1\bar{1}02\}$twins in creep deformed α-Ti-1.6V. (a) Specimen deformed at 298 K using $g = (10\bar{1}1)$ vector. (b) Specimen deformed at 478 K using $g = (1\bar{1}00)$ vector.

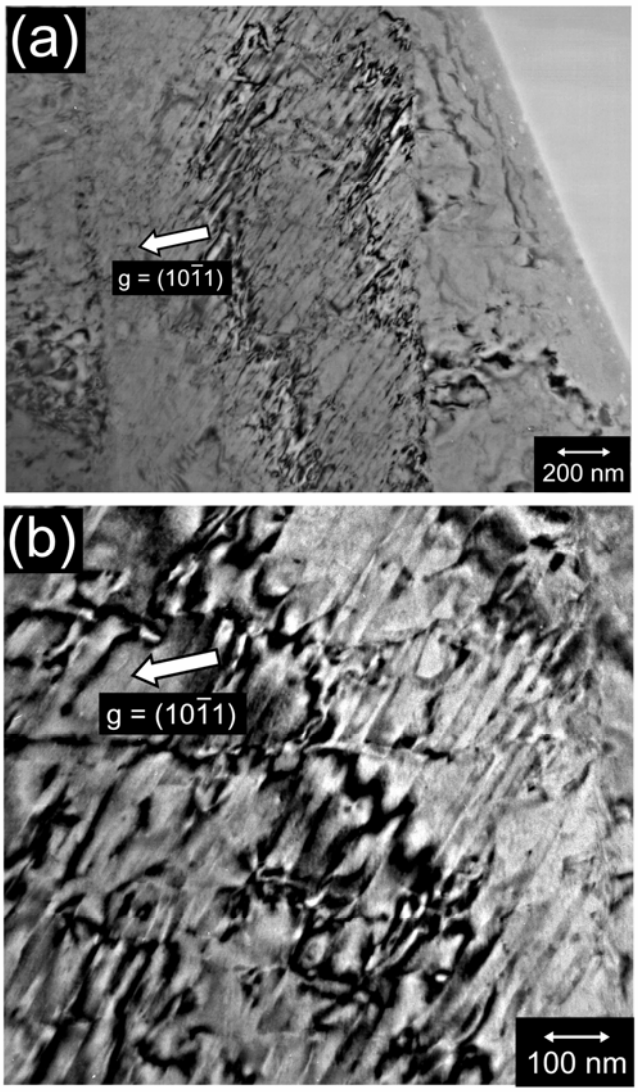

Figure 4.42: Bright-field TEM images of stacking faults in $\{1\bar{1}02\}$twins in α-Ti-1.6V creep deformed at 298 K. (b) shows an area from (a) at higher magnification.

4.1.1.4 Discussion

4.1.1.4.1 Variation of Activation Energy with Creep Strain

As seen in Figure 3.9, the measured activation energy for creep deformation of α-Ti-1.6V increases from a value of approximately 37 KJ/mol at low strains ($\leq 2\%$) to approximately 47 KJ/mol at higher strains ($\geq 4\%$). This is a similar pattern to that seen in β-Ti-14.8V, where the activation energy increases with increasing strain [35]. Moreover, it has been observed in previous investigations involving interrupt creep testing of Ti-0.4Mn [23] and Ti-1.6V [26], that at low strains, slip is the predominant deformation mechanism and few twins are observed. As creep continues to higher strains, twinning becomes more common although slip does continue. This behavior was described in Section 2.3.1 and is seen for α-Ti-0.4Mn in the optical micrograph of Figure 4.43 [37]. Thus, the question arises as to whether the change in activation energy corresponds to a change in the predominant deformation mechanism from slip at low strains to slip + twinning at higher strains.

Previous investigations in which the activation energy for deformation of α-titanium alloys has been calculated have focused on alloy systems in which slip is the predominant deformation mechanism. Activation energy for tensile deformation of α-titanium at temperatures less than $0.4*T_m$ was first measured by Conrad [38]. It was suggested that the rate-controlling process during plastic deformation is the thermally activated overcoming of interstitial solute atoms by dislocations gliding on first order prism planes. Tung and Sommer [39] describe dislocation energetics in commercially pure α-titanium with a grain size of 25 μm during tensile deformation over the range of 300 to 500 K. They calculate a value for the activation energy to be approximately 30

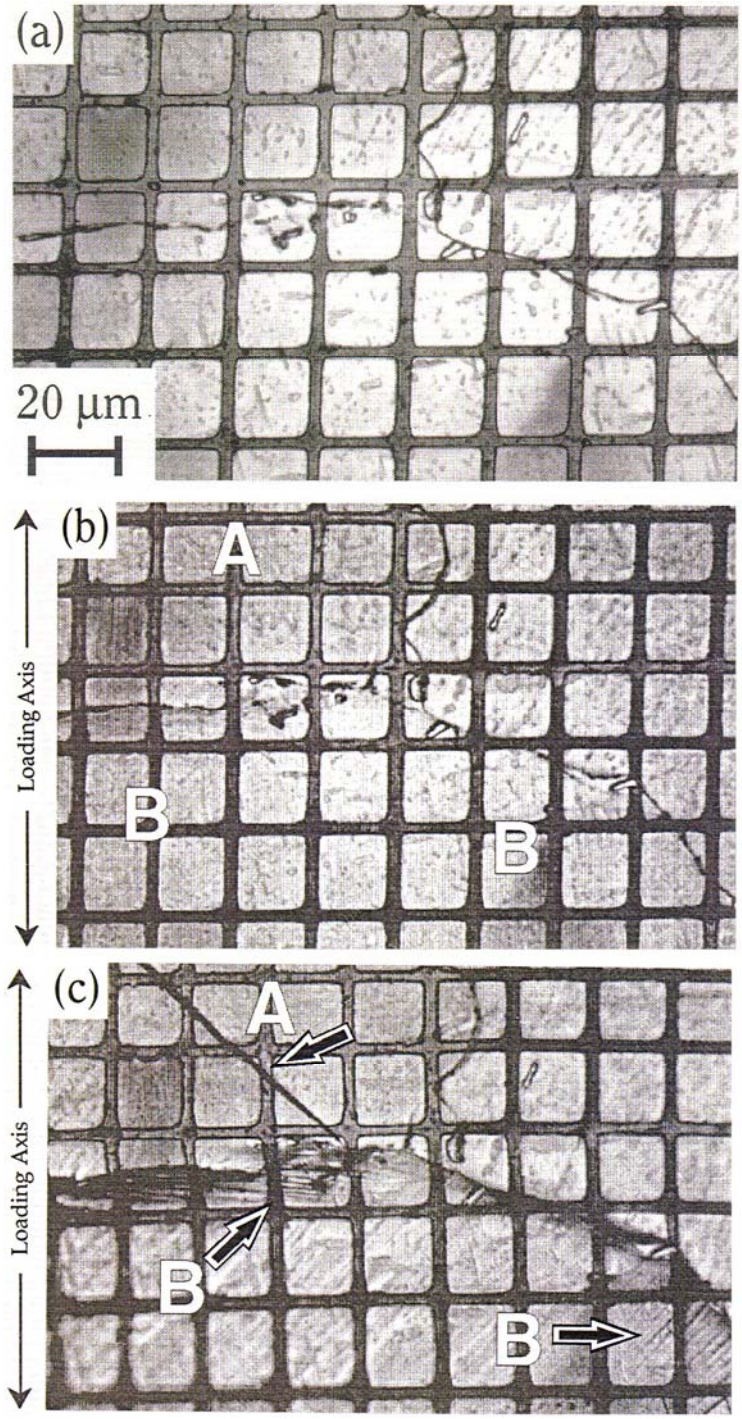

Figure 4.43: Optical micrographs of coarse grained (500 μm) α-Ti-0.4Mn creep deformed at room temperature at 95% YS. (a) Undeformed, (b) creep strain = 0.61%, time = 0.96 hours, and (c) creep strain = 2.82%, time = 115 hours. Note distortion of grid lines at 'A' and 'B' in (b), indicative of fine slip. In (c), 'A' indicates a twin and 'B' indicates coarse slip lines [37].

KJ/mol. Moreover, in another study [40], basal slip has been shown to have higher activation energy than prism slip. Another systematic study was undertaken by Yongning, *et al* [41]. They performed tensile tests on an α-Ti-3Al alloy at temperatures from 77 K to 373 K and at strain rates from 10^{-4} to 10^{2} per second. The results show that activation energy increases slightly with temperature but is independent of strain rate. In regard to creep deformation, Zeyfang, Martin, and Conrad [12] determined the activation energy as a function of temperature for creep of commercially pure titanium (0.2% O, 2.5 μm grain size). The activation energy was found to increase with increasing temperature. In the range of interest for this investigation, the value ranges from approximately 48 KJ/mol at 300 K to 77 KJ/mol at 450 K. Similarly, Miller, Chen, and Starke, Jr. [16] determined the activation energy for creep deformation of the near-alpha Ti-6Al-2Nb-1Ta-0.8Mo alloy. It was found that at temperature less than 778 K, the activation energy for deformation is approximately 53 KJ/mol. It is suggested that creep may be related to the diffusion of oxygen in α-titanium given that the activation energy for diffusion of oxygen in this material has a similar value. Again, the alloy is one where slip will be the predominant deformation mechanism. Moreover, they propose that dislocations with the lowest activation energy will move first upon initial loading and creep continues by the movement of dislocations of higher activation energies. A review of the literature shows that there are no studies to determine the activation energy of tensile or creep deformation of α-Ti alloys when twinning is the predominant deformation mechanism.

The measured value for activation energy for deformation of α-titanium alloys by slip in previous investigations (30-50 KJ/mol) corresponds well with the experimentally

measured activation energy for creep of α-Ti-1.6V in the low strain region in the present investigation (~37 KJ/mol), suggesting that slip is the predominant deformation mechanism during the early stages of creep of Ti-1.6V. This is supported by observations from interrupt creep tests where slip is observed much more frequently than twinning at low strains. It is proposed, however, that twinning will become a predominant creep deformation mechanism at higher strains, which is responsible for the increase in activation energy. The next section will discuss the slip-to-twinning transition in these alloys.

4.1.1.4.2 Slip-to-Twinning Transition

Excellent overviews of the slip-to-twinning transition for metals in general [42], and HCP alloys [43], in particular, are very relevant to the current investigation. As described in the previous sections, there seems to be a transition in the predominant creep-deformation mechanism from slip to slip + twinning at about 2% strain. This results is consistent with previous studies involving tensile and fatigue testing of α-Ti alloys [44] and HCP Zr [43], that there is a particular strain below which slip is the predominant deformation mechanism and above which twinning is the predominant deformation mechanism. The reasons for this transition and the factors that affect this transition will next be discussed.

The reason that slip is the predominant deformation mechanism during the early stages of creep is that the critical stress for dislocation glide is less than the critical stress to initiate twinning [42]. The stress required to initiate twinning is largely independent of temperature, while the stress for slip decreases as temperature increases. Thus, at room

temperature and above, the first result of the applied stress will be to initiate dislocation glide in grains that are favorably oriented for slip. One particular aspect of plastic deformation in HCP alloys is that it is highly dependent on crystal orientation [43]. Thus, it is likely that a grain which is favorably oriented for slip will be adjacent to a grain which is not favorably oriented for slip. The most favorably oriented grains for slip are those in which the basal plane of the HCP unit cell is parallel to the loading axis [23]. Those which are least favorably oriented for slip are those in which the basal plane of the HCP unit cell is normal to the loading axis. When dislocations on the favorably oriented planes encounter a grain boundary with a non-favorably oriented plane, energy is required for the dislocations to overcome such a barrier. At elevated temperatures, the energy barrier may be low enough for dislocations to cross the grain boundary and deformation could continue solely by slip [43]. At low temperatures ($<0.25*T_m$), however, it is likely that dislocations will not be able to cross the grain boundary and will instead pile up there, limiting the amount of strain that is possible due solely to slip. If, in fact, the energy for twin nucleation is less than that required for dislocations to overcome the grain boundary, this dislocation pileup will provide the energy necessary for twin nucleation in the adjacent grain. Thus, twinning will become the predominant deformation mechanism even though the critical stress for slip is less than that for twinning. Indeed, Song and Gray have observed for HCP Zr that there is a critical strain where the predominant deformation mechanism transitions from slip to twinning and this strain level decreases with decreasing temperature [43].

Meyers, Vöhringer, and Lubarda [42] have reviewed the onset of twinning in metals and developed a model for the nucleation of twinning as a result of dislocation

pileups. It is based on the stress concentration generated by a pile-up due to activation of a Frank-Read or Köhler source. The dislocation pileup is illustrated in Figure 4.44. The number of dislocations piled up is determined by the distance, l_b, between the source and the barrier. The local stress in front of the barrier is equal to the product of the applied stress and the number of dislocations in the pileup. The macroscopically measured twinning stress will depend strongly on the microstructure of the sample because the distance, l_b, is microstructure dependent. The velocity, v, of the dislocations traveling from the source to the barrier is given by the Johnston-Gilman equation [45]:

$$v = A_o \tau^m \exp\left(-\frac{Q}{RT}\right) \tag{4-5}$$

where τ is the stress acting on the dislocation, Q is the activation energy, T is the

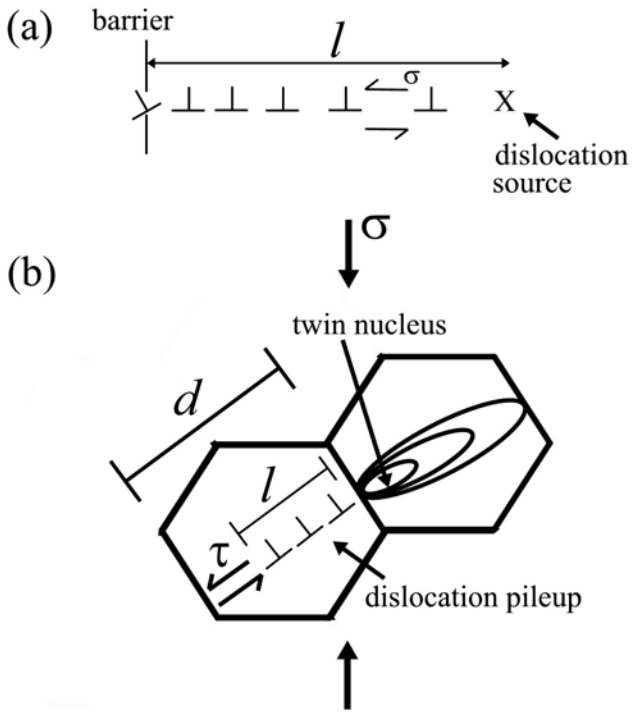

Figure 4.44: (a) Schematic of edge dislocations piled up at a barrier. (b) Dislocation source creating a pileup at a grain boundary and nucleating a twin in a neighboring grain. (After Meyers, *et al* [45]).

temperature, and A_o and m are constants. The time for an individual dislocation to travel from the source to the obstacle is $\frac{l_b}{v}$. A reasonable approximation is that all the dislocations will travel from the source to the pileup in the same time, thus the total time, t, required to build up a pileup of n dislocations is given by:

$$t = n\frac{l_b}{v} \tag{4-6}$$

assuming that no two dislocations are traveling simultaneously to the obstacle. Combining equations 4-5 and 4-6 gives:

$$t = \frac{nl_b}{A_o \tau^m} \exp\left(\frac{Q}{RT}\right) \tag{4-7}$$

Based on the model of Meyers, *et al* [42], the induced stress acting on a barrier to dislocation motion will generate an elastic distortion which has to supply the energy required to create a twin-matrix interface and the energy needed for the formation of the twin as an Eshelby's inclusion [46]. Eshelby showed how to calculate the stress, strain, and elastic-strain energy arising when a region (inclusion) within a matrix changes shape or size. The full details of the calculations of Meyers, *et al* [42] are beyond the scope of this work, but essentially, the total change in free energy, $\Delta\Phi$, can be written as:

$$\Delta\Phi = \Delta W + \gamma_{TB} A \tag{4-8}$$

where ΔW is the energy of the Eshelby's inclusion, γ_{TB} is the energy required to create the twin boundary, and A is the interface area of the twin embryo. Meyers, *et al* [42] go on to calculate a critical radius size, r_c, for a twin embryo as a function of the driving stress for twin formation, σ_T, which is the stress at the tip of the dislocation pileup at the grain boundary of the neighboring grain:

$$r_c = \frac{5\pi}{4}\frac{G\gamma_{TB}}{(\sigma_T)^2} \tag{4-9}$$

where G is the shear modulus of the matrix.

The twin-boundary energy, γ_{TB}, is given as the sum of the coherent twin-boundary energy and the energy of the dislocations necessary for the twin-dislocation reactions, which will be described later [43]:

$$\gamma_{TB} = CG\delta^2 + \frac{\sum n_i E_i \beta_i}{\rho l} \tag{4-10}$$

where C is a constant, δ is the twin boundary mismatch, n_i, E_i, and β_i are the number, energy of formation, and geometric factor, respectively of the dislocations involved in the twin-dislocation reactions, ρ is the twinning shear, and l is the length of the interface. For α-Ti, γ_{TB} has been calculated as approximately 0.3 J/m^2, and the critical radius of a twin embryo, r_c, as 47 nm.

Now, the length of the dislocation pile-up necessary to initiate twinning can be calculated, using the analysis of Meyers, *et al* [42]. To relate the local stress driving twin formation, σ_T, to the externally applied stress, τ, they consider the number of dislocations at the pileup and use the analysis developed by Eshelby, *et al* [47]. The shear stress σ_T is created by the pileup of equivalent dislocations with Burgers vector nb and the shear stress $n\tau$ at a distance $\frac{l_p}{4}$ from the tip of the pileup of length l_p. Essentially, the presence of n dislocations concentrates the applied stress acting upon the lead dislocation by a factor of n. The externally applied stress, τ, is related to the number of dislocations in the pileup by:

$$n = \frac{\beta \pi l_p \tau}{Gb} \tag{4-11}$$

where β is a parameter that depends on the dislocation character (β = 1 for edge dislocations, 1.5 for screw dislocations), and b is the Burgers vector. The relation between the local stress σ_T and the globally applied stress τ is:

$$\sigma_T = n\tau = \frac{\beta \pi l_p \tau^2}{Gb} \tag{4-12}$$

Now, solving Equation (4-9) for σ_T, and equating with Equation (4-12) gives an expression for the length of the pile-up required for the twinning nucleation:

$$l_p = \frac{1}{\beta}\frac{G}{\tau^2}\left(\frac{5}{4\pi}\frac{G\gamma_{TB}}{r_c}\right)^{1/2} b \tag{4-13}$$

Using this analysis, the length of the dislocation pileup required to initiate twinning in α-Ti with a grain size of approximately 250 μm at a stress level of 95% YS can be calculated. The following values are taken from literature [42]: β = 1, G = 40 GPa, γ_{TB} = 0.3 J/m, r_c = 47 nm, b = 0.3 nm. The externally applied stress, τ, is 95% YS, which at room temperature is 328 MPa [3]. Inserting the values in to Equation 3-14 and solving for length l_p gives a value of approximately 36 nm, which is much smaller than the grain size, confirming that such pileups can be responsible for the onset of twinning.

An additional factor that must be considered when discussing the slip-to-twinning transition in titanium alloys is the grain size. The grain size dependence of twinning stress is larger compared to slip stress [48]. In both cases, a Hall-Petch type relationship is followed where:

$$\sigma = \sigma_o + kd^{-1/2} \tag{4-14}$$

where σ is the onset stress for slip or twinning, σ_o is a friction stress opposing slip or twinning, k is the Hall-Petch constant, and d is the grain size. The values of the Hall-Petch slope for titanium for slip (k_s) and twinning (k_t) have been measured as 6 and 18 MPa*mm$^{1/2}$ respectively [49]. It has been observed in many cases [3, 25, 50] that under similar loading conditions, twinning is favored in coarse-grained Ti alloys compared with fine-grained alloys. It is assumed that the onset of twinning occurs when the slip stress, σ_S becomes equal to the twinning stress, σ_T. Zerilli and Armstrong [51] have developed an equation for the slip stress in HCP metals such as α-Ti:

$$\sigma_s = \sigma_G + C_1\left(\frac{\dot{\varepsilon}}{\dot{\varepsilon}_0}\right)^{C_3T} + C_2\varepsilon^n \exp\left(C_4T\right) + k_s d^{-1/2} \tag{4-15}$$

where σ_G is the athermal component of stress, $C_1 - C_4$ are the Zerilli-Armstrong parameters, $\dot{\varepsilon}_o$ is the reference strain rate, n is a constant, k_s is the Hall-Petch constant for slip, and d is the grain size. For HCP Ti, the following values are given: $\sigma_G = 0$, $C_1 = 990$, $C_2 = 700$ MPa, $C_3 = 1.06\text{x}10^{-3}$ K^{-1}, $C_4 = 6.8\text{x}10^{-4}$ K^{-1}, $n = 0.5$, $k_s = 6$ MPa*mm$^{1/2}$. The twinning stress, σ_T is given by:

$$\sigma_T = \sigma_{T0} + k_T d^{-1/2} \tag{4-16}$$

Setting Equations 4-15 and 4-16 equal and solving for grain size will give the grain size, d_{crit}, where the slip and twinning stress are equal under given loading conditions:

$$d_{crit} = \left(\frac{k_T - k_s}{\sigma_G + C_1\left(\frac{\dot{\varepsilon}}{\dot{\varepsilon}_0}\right)^{C_3T} + C_2\varepsilon^n \exp\left(C_4T\right) - \sigma_{T0}}\right)^2 \tag{4-17}$$

Thus, in the case of HCP Ti, d_{crit} will be function of strain rate, strain, and temperature. If the grain size is larger than d_{crit}, twinning will be favored under those loading conditions. If the grain size is smaller than d_{crit}, slip will be favored under those loading conditions. At small grain sizes, the twin nucleation stress will be very high and the length of the dislocation pileups which would be required to achieve this stress will not be accommodated in the finite size of the grain.

4.1.1.4.3 Discussion of TEM Analysis

As was discussed in the previous sections, it is proposed that creep deformation is attributable primarily to slip in the low strain regions. Eventually, dislocation pileups provide the stress concentration necessary to nucleate twins, which then become a predominant deformation mechanism (see Figures 4.23 and 4.24). It cannot be assumed, however, that the slip and twinning processes are otherwise independent. In fact, slip and twins interact frequently and they must be considered together.

Song and Gray have developed a model for twin growth by the sideways (normal to the direction of the advancing interface) motion of twin boundary ledges such as those seen in Figure 4.40. Consider Figure 3.14. The increase in boundary energy is the main barrier for twin nucleation. The energy of twin boundaries parallel to the $\mathbf{K_1}$ twinning plane is coherent, while that at the tips of the twin embryo are initially non-coherent because the twinning shear produces a volume excess at one tip and a volume deficit at the other. The local strain caused by the volume excess and deficit can be significantly reduced by generating or attracting dislocations to the vicinity of the tips (see Figure 4.37). However, the resulting boundaries at these regions are still semicoherent and these

are the main fraction of the nucleation energy for the twin embryo. The boundary energy of a twin embryo can be reduced by quite a bit if the twin tip is in contact with a grain boundary

For the lattice shift associated with twinning, dislocations are needed to remove the volume excess or deficit at the tips of the twins caused by the unit step movement of a twin boundary ledge in a direction normal to the coherent interface. For reasons that will be explained later, the unit step distance of a boundary ledge in a $\{1\,\bar{1}\,02\}$ type twin is the interatomic distance for atoms $\boldsymbol{\eta}_1 = \langle 10\,\bar{1}\,1 \rangle$ direction. Thus, for $\{1\,\bar{1}\,02\}$ type twinning, two different *a*-type and one *c*-type dislocation are required for the dislocation reaction, i.e. $a + a' + c$. For instance:

$$\frac{1}{3}[1\bar{2}10] + \frac{1}{3}[2\,\bar{1}\,\bar{1}\,0] + [0001] \rightarrow [1\,\bar{1}\,01]$$

Recall that there should be many *a*-type dislocations in the lattice due to prior slip (see Figure 4.22). In this sense, prior slip may aid the twin growth process. These dislocations will be attracted to the boundaries and tips of growing twins to give the necessary amount of displacement for the twinning (see Figure 4.37). However, *c*-type dislocations are absent from the lattice. As such, dislocation reactions will be required to generate *c*-type dislocations which are subsequently emitted into the matrix or left inside the twins [52, 53] (see Figures 4.38 and 4.39). Such reactions would, of necessity, involve *c*+*a* type dislocations with Burgers vector of the type $\frac{1}{3}\langle 11\bar{2}3 \rangle$, i.e. $(c + a) + a' \rightarrow c$. For instance:

$$\frac{1}{3}[11\bar{2}3] + \frac{1}{3}[\bar{1}\,\bar{1}\,20] \rightarrow [0001]$$

Note that the reaction to generate a *c*-type dislocation will annihilate a corresponding number of *a*-type dislocations.

Consider a schematic illustration of the twin-matrix boundary, following the work of Song and Gray [53], given in Figure 4.45. The sideways propagation of the boundary steps does not need to be uniform; hence the front of the steps is not straight. Further, the height of each step need not be the same as long as it is a multiple of the unit step height. For every sideways jump of the twin-boundary step, dislocation reactions have to take place at the initial and final positions of the ledge. As such, *c*-dislocations are formed during twinning and are either emitted into the matrix or trapped in the twins, while *a*-type dislocations are attracted to the boundary ledges to give the necessary dislocation reaction for the displacement which offsets the strain caused by twinning shear at the ledges.

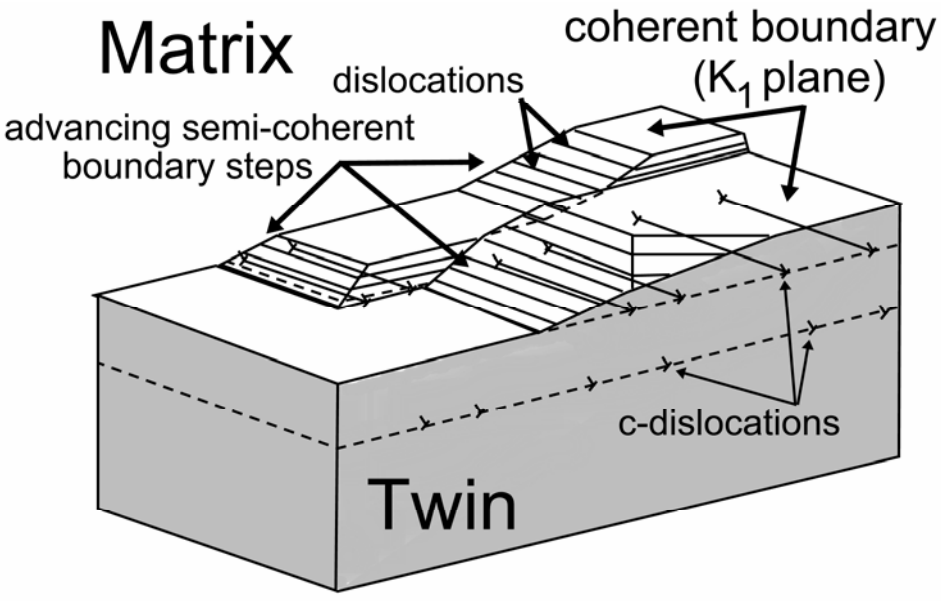

Figure 4.45: Schematic illustration of twin-boundary steps, misfit dislocations on the semicoherent boundaries, and *c*-dislocations in the twin, after Song and Gray [53].

According to Song and Gray [53], *c*-type dislocations are formed during the sideways movement of twin-boundary steps in prism slip planes, $\{1\,\bar{1}\,00\}$. The trapped *c*-dislocations will be perpendicular to the shear plane since the displacement from the matrix to the twinned lattice caused by twinning shear is parallel to the shear plane. Therefore, the trapped *c*-dislocations will be parallel to the line of intersection of the prism plane with the semicoherent plane, as seen in Figure 4.45.

During the early stages of twin growth, the coherent twin boundaries are flat and smooth. The jump distance of the boundary steps is large because of the small thickness of the twin. As such, there is infrequent interaction with dislocations in this stage and there is a low density of *c*-dislocations in the middle of twins. As the twin thickness increases, the boundary step splits because there is an upper limit to the number of atoms that can be transformed from the matrix to the twin position in the sideways jump at a given applied stress. The twin boundary will thus become rougher as the twin thickens. The sideways movement of the boundary steps is not uniform so that the *c*-dislocations formed in a twin step terminate at the twin boundary on both sides of the step, as shown in Figure 4.45. When the neighboring boundary step moves to, and passes by, the positions of these *c*-dislocations, the dislocations turn around between the two steps and lie in non-slip planes, becoming sessile. The turned-around portions of the *c*-dislocations (the legs of the 'U') in the twins are nearly perpendicular to, and are terminated at, the twin boundary. Since they are sessile and unable to slip out of the twin, they accumulate as the twin thickness increases. Moreover, the density of the *c*-dislocations in the twin is proportional to the frequency of the sideways jump or inversely proportional to the jump distance. As such, it is dependent on the local stress level. As the stress level increases,

fewer *c*-dislocations will be needed for twinning because the sideways jump distance increases with local stress level.

To offset the strain produced by the twinning shear at the tips of a twin or the ledges of semicoherent boundary steps following the sideways jump, *a*-dislocations in the matrix are attracted to the semicoherent boundaries where they interact with the tips and ledges. If the access of the *a*-dislocations to the tips or ledges is blocked, twin growth will be hindered. If two twins meet in a grain, the *a*-dislocations in the matrix are attracted to the tips but they cannot reach the inner surfaces of the two tips so a strip of the matrix between the two twins remains which cannot be converted to the twinned structure, as seen in Figure 4.33(b). The collision of the twin tips will slow the advance of the twins.

4.1.2 Theoretical Investigation of Time-Dependent Twinning in α-Titanium Alloys

As discussed in Section 2.3.1, some α-titanium alloys, namely Ti-0.4 Mn [23] and Ti-1.6V [26] have been shown to deform by the slow growth of deformation twins (time-dependent twinning) during ambient temperature creep. This is an unusual phenomenon, as twins are expected to grow at the speed of sound in bulk, polycrystalline metals. It has long been known that interstitial atoms, particularly oxygen, can make twinning more difficult in α-Ti alloys, but Ankem, *et al* [23] were the first to suggest that these interstitial atoms could be responsible for time-dependent twinning. There were, however, no models to support this idea as the existing crystallographic models for twinning only considered the host atoms. This part of the investigation expands existing crystallographic models for twinning in HCP materials to include the presence of interstitial sites where atoms such as oxygen can reside. It was shown that the slow growth of twins can attributed to the time necessary for diffusion of interstitial oxygen atoms away from the advancing twin boundary. This model is similar to one for the BCC lattice of β-Ti which was published by Oberson and Ankem in *Physical Review Letters* [34] and which will be described later.

4.1.2.1 Theoretical Background

Twinning has long been recognized as an important deformation mechanism in hexagonal close packed metals and alloys [31, 36, 54-58]. There are four predominant twinning modes which have been identified in such materials, and they are given in Table 4.1

Table 4.1 – Common Twinning Modes in HCP Materials

K_1	η_1	K_2	η_2
$(10\bar{1}2)$	$[10\bar{1}\,\bar{1}]$	$(10\bar{1}\bar{2})$	$[10\bar{1}1]$
$(10\bar{1}1)$	$[10\bar{1}\bar{2}]$	$(10\bar{1}\bar{3})$	$[30\bar{3}2]$
$(11\bar{2}2)$	$\frac{1}{3}[11\bar{2}\bar{3}]$	$(11\bar{2}\bar{4})$	$\frac{1}{3}[22\bar{4}3]$
$(11\bar{2}1)$	$\frac{1}{3}[\bar{1}\,\bar{1}26]$	(0002)	$\frac{1}{3}[11\bar{2}0]$

Moreover, the above twins can be characterized as 'tension' or 'compression' twins. A 'tension' twin will cause expansion along the **c** axis, whereas the 'compression' twin will cause contraction along the **c** axis [57]. A particular twinning mode may be a 'tension' twin or a 'compression' twin depending on the *c/a* ratio of the metal or alloy. For instance, when *c/a* is less than $\sqrt{3}$, the $\{1\,\bar{1}02\}$ type twin is a compression twin and when *c/a* is greater than $\sqrt{3}$ it is considered a tension twin. Generally speaking, while all the twinning modes described above are possible, $\{1\,\bar{1}02\}$ is the predominant deformation twinning mode in α-titanium alloys at room temperature, for reasons that will be given later.

4.1.2.2 Twinning Mechanisms in α-Titanium Alloys

As will be discussed in Section 4.3, it has been suggested that rather than twinning by homogeneous shear of atoms from the untwinned to the twinned position, twinning in cubic materials, such as BCC β-titanium, can occur by the repeated sideways

glide of so-called twinning dislocations on the planes parallel to the $\mathbf{K_1}$ twinning plane. This is attributed to a mobile dislocation coiling itself around a pole dislocation. In fact, a pole mechanism was proposed to describe $\{1\bar{1}02\}$ twinning in HCP materials [59]. This mechanism will not be described in detail but it involves a reaction of the type:

$$[000\bar{1}] \rightarrow \alpha[10\bar{1}\,\bar{1}] + \textit{sessile}$$

where α is approximately $\frac{1}{12}$. This is called a ratchet pole because the glissile partial dislocation recombines with the sessile partial dislocation after one revolution, and the recombined perfect $[000\bar{1}]$ dislocation must cross slip before twin propagation can occur. This dislocation is illustrated in Figure 4.46. Such a model, however, does not seem

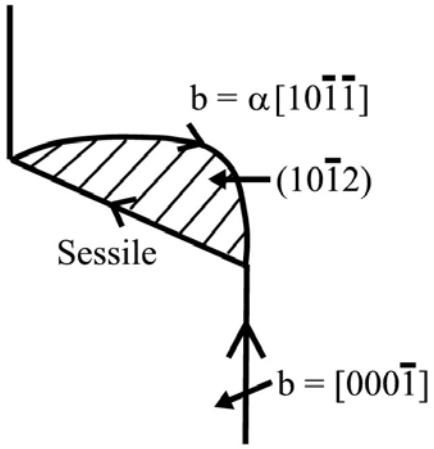

Figure 4.46: Schematic illustration of $\{1\bar{1}02\}$ twinning by the ratchet dislocation mechanism in the HCP lattice.

likely in non-cubic materials such as HCP, α-titanium. Twinning partial dislocations are only stable in cubic structures where the Burgers vectors are rational fractions of the lattice constant [52]. Twinning dislocations proposed for low symmetry structures such as HCP alloys have irrational Burgers vectors. This type of twinning dislocation does not

exist in the matrix, but are formed by a step in a coherent twin boundary. There is, however, no evidence to link the twinning process in HCP materials to twinning dislocations.

Indeed, Song and Gray [52] propose that maintaining a coherent interface after the passage of a twinning dislocation would have one of two consequences. First, the untwinned lattice outside of the interface region stays in position but the lattice is bent near the interface to account for the displacement caused by the passage of the twinning dislocation. Alternatively, the entire untwinned lattice outside the region of the interface is shifted by an amount equal to the Burgers vector of the twinning dislocation. In the former case, the energy caused by such a bending near the boundary would be sufficient to prevent the movement of the twinning dislocation. The latter was thus assumed to be the case [54, 59]. However, the models used to describe dislocation twinning in HCP materials were focused on the region near the boundary and neglected to consider the larger scale implications that follow.

Consider the case of a growing twin embryo [52]. The twin-matrix interface parallel to the twinning plane can be assumed to be a low-energy coherent boundary, whereas at the tips of the lamella, it is semicoherent. If the twin grows by sideways glide of twinning dislocations, the parent lattice outside of the interface region would be shifted by the distance of its Burgers vector to maintain interface coherency. Because the entire twin embryo is imbedded in the grain, the matrix lattice has to homogeneously twist as a result of the movement of a dislocation with an irrational Burgers vector. Only when the twin boundaries contact free surfaces at both tips, can the matrix move freely by an irrational distance. By focusing twinning dislocation models on the twin-matrix interface

region, it was incorrectly assumed that the parent lattice on either side of the twin lamella could be displaced parallel to the twinning boundary by an arbitrary amount. Given that twinning via dissociation of a unit lattice vector into partial twinning dislocations is unlikely in α-titanium, classical shear mechanisms for deformation twinning will be discussed.

4.1.2.3 Simple Models for Twinning in the HCP Lattice

In this section, reference will be made to the projections for the HCP lattice given in Section 3.8.1 (Figures 3.7-3.10). In the simplest cases for twinning in a cubic lattice, as illustrated in Figure 2.12, the shear of the matrix moves all of the atoms directly from the untwinned to the twinned position. There are some instances, however, when the magnitude of the shear does not carry all of the atoms to the proper twinned position such that they are symmetric to a corresponding atom on the other side of the twin-matrix interface. In this a case, an additional atomic translation, called a shuffle, is required to move the sheared atom to the proper twinned position. This is true of the HCP lattice, where there are two atoms in the primitive unit cell (double lattice structures). A rigorous treatment of the crystallography of twinning involving shears and shuffles was developed by Bilby and Crocker [60].

The shear/shuffle concept can be illustrated for the case of $\{1\bar{1}02\}$ twinning in the HCP lattice, following Crocker and Bevis [61]. Figure 4.47(a) shows a projection of the untwinned HCP lattice onto two adjacent $\{11\bar{2}0\}$ planes separated by a distance of $\frac{a}{2}$. The $\mathbf{K_1}$ twinning plane and the directions $\boldsymbol{\eta_1}$ and $\boldsymbol{\eta_2}$ are also identified. Figure 4.47(b) shows the sheared lattice. The magnitude of the shear is given by the distance between

the η_2 directions in the matrix and twin, respectively. However, none of the parent atoms are sheared to the correct twin positions which are shown as dashed circles in Figure 4.47(c). As such, the shuffles, which are indicated by arrows in Figure 4.47(d), are required to move the Ti atoms to the correct twin position.

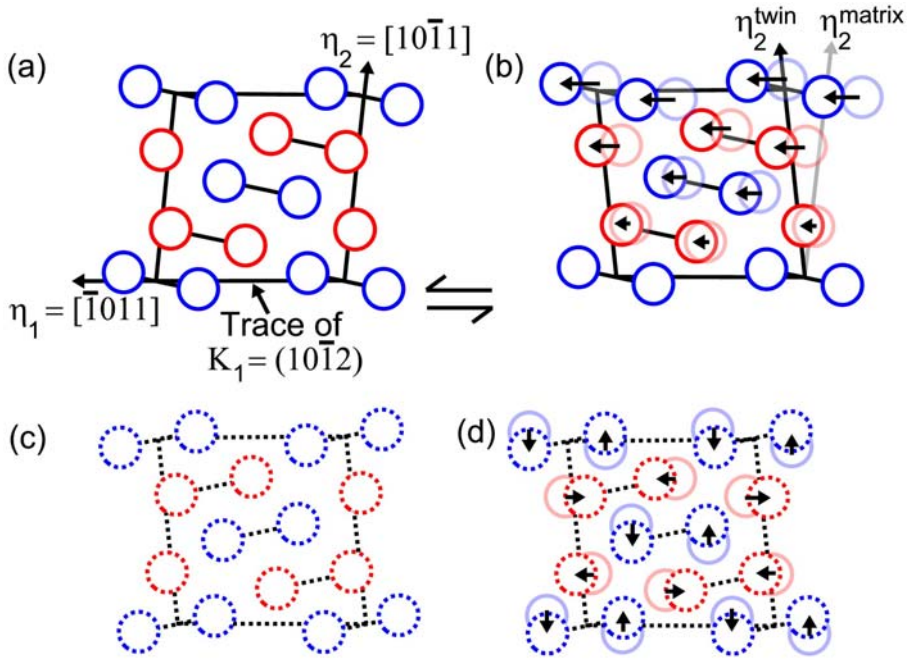

Figure 4.47: Crystallographic model for $\{1\bar{1}02\}$ twinning given by Crocker [68]. (a) Untwinned HCP lattice projected onto $\{11\bar{2}0\}$ plane including atoms in plane of projection (blue) and $\frac{a}{2}$ above or below plane of projection (red). (b) Shear of lattice does not move atoms to twinned positions, which are shown by dashed circles in (c). (d) Shuffles indicated by arrows move atoms from sheared position to twinned position. After Crocker and Bevis [61].

Bilby and Crocker give four criteria for evaluating the operative shear/shuffle mechanism. First, the shear magnitude should be small. Second, the shuffle mechanism should be simple. Third, the shuffle magnitude should be small. Fourth, shuffles parallel to the shear direction are favorable to those perpendicular to the shear direction.

While the twinning scheme illustrated in Figure 4.47 is useful for showing the concept of shears and shuffles, it should not be considered to reflect the actual $\{1\bar{1}02\}$twinning mechanism operative during deformation in α-Ti. The motif lattice is arbitrarily defined by the center of gravity between pairs of atoms in the plane of the projection. The $\mathbf{K_1}$ twinning plane does not correspond to a plane of Ti atoms. As such, the shuffles in the pair of atoms, as illustrated, are of equal magnitude in opposite direction. In reality, however, the twin-matrix interface is likely to be defined by a physical plane of Ti atoms, as was the case for the cubic lattice of Figure 2.12. Given the asymmetry of the HCP lattice, the shuffles will by asymmetric as well.

An alternative model for $\{1\bar{1}02\}$ twinning in HCP alloys in general, and α-Ti alloys in particular was developed by Kronberg [62]. He notes that the octahedral interstitial sites in the HCP lattice themselves define a hexagonal lattice. Consider the location of octahedral interstitial sites in the HCP lattice (see Figure 3.9). Note that the origin of the lattice can be moved such that it is centered on the octahedral lattice sites. Figure 4.48(a) shows a projection of the HCP lattice onto $\{1\bar{2}10\}$ planes, including octahedral sites. Figure 4.48(b) illustrates the lattice as centered on the octahedral sites. Figure 4.48(c) shows that when lattice of octahedral lattice is sheared so as to create a mirror reflection across the $(10\bar{1}2)$ plane, half of the octahedral lattice sites undergo simple homogeneous shear. The other half must, in addition to the shear, undergo a shuffle of $\pm\frac{a}{2}$. Kronberg notes that structurally, such motion is not possible because the octahedral interstices must be moved and reformed in the twin position. Thus, Kronberg developed a model in which twinning occurs by cooperative movement of close packed

rows of atoms surrounding the interstices, as illustrated in Figure 4.48(d). No single atom can move to its twinned position unless all move in sync at the instant of nucleation.

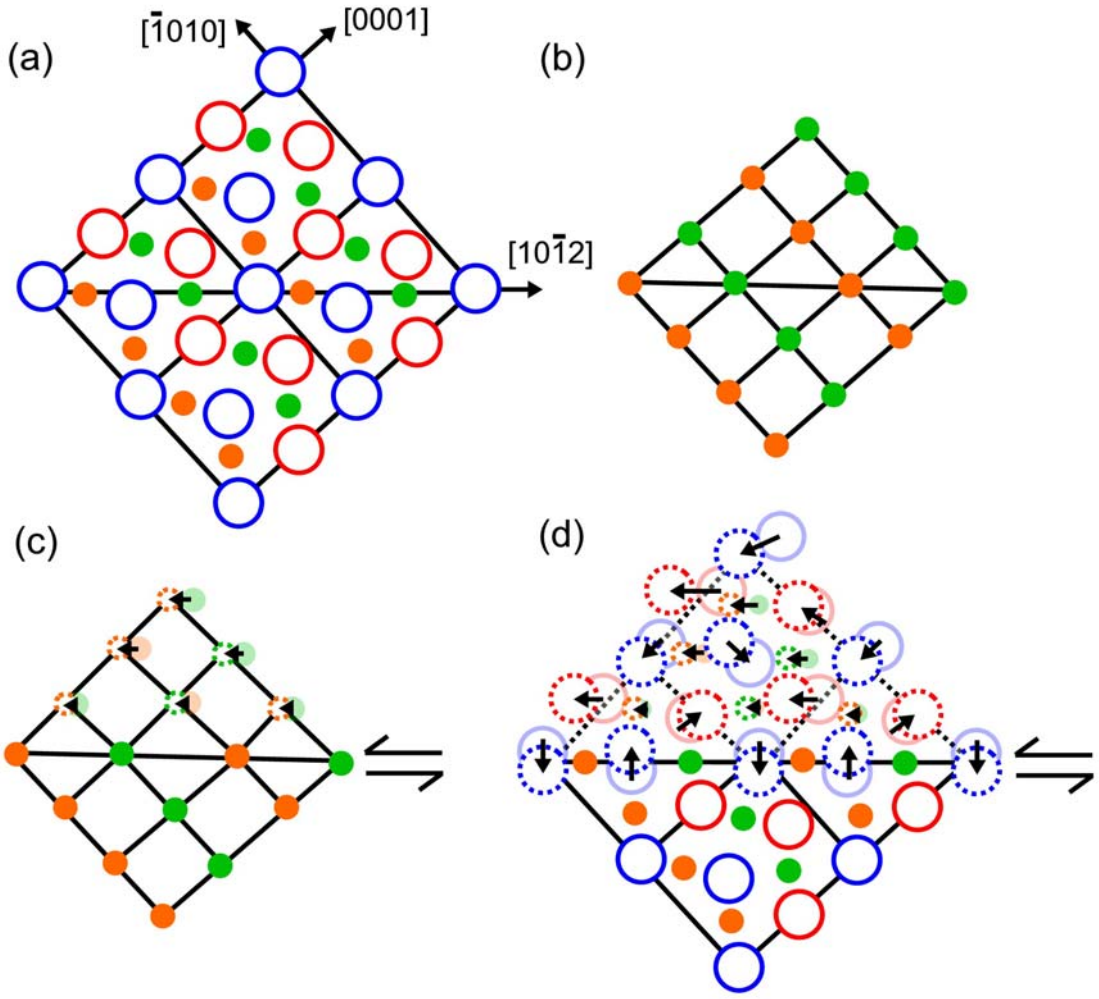

Figure 4.48: Crystallographic model for $\{1\bar{1}02\}$ twinning, after Kronberg [62]. (a) Untwinned HCP lattice of α-Ti projected onto $\{11\bar{2}0\}$ plane including Ti atoms (blue) and octahedral interstitial sites (green) in the plane of projection and Ti atoms (red) and octahedral interstitial sites (orange) $\frac{a}{2}$ above or below the plane of projection. (b) Projection of lattice now centered on octahedral interstitial sites. (c) Shear of octahedral interstitial sites to form twin moves half of the interstitial sites to twinned position. Other half must shuffle $\pm\frac{a}{2}$ to the adjacent $\{11\bar{2}0\}$ type plane. (d) Schematic for cooperative movement of Ti and octahedral interstitial sites to twinned position.

As was the case for the proposed dislocation twinning mechanism, however, this model only considers the atoms near the twin-matrix interface and neglects the macroscopic implications. Song and Gray [52] note that the relative movement of the twin lattice with respect to the parent lattice on a stable twin boundary has to be a rational lattice vector so as not to disturb the matrix lattice during twinning. Furthermore, the twin-matrix interface must be maintained during twin nucleation. As such, they suggest that only well-matched planes between the two lattices can be used as boundaries in order to reduce the energy necessary for twinning. Thus, the Coincident Site Lattice (CSL) theory is used to understand the nucleation and growth of twins in α titanium.

4.1.2.4 Coincident Site Lattice (CSL) Theory

The idea of the CSL theory is to minimize the interfacial energy between two phases or two variants of the same phase [63]. Consider all possible orientations of two grains with respect to one another. For some angles, lattice points of the first lattice will coincide with lattice points of the second. A type of superstructure or Coincident Site Lattice develops. This is illustrated for the FCC lattice in Figure 4.49. The unit cells of two FCC lattices are indicated in green and yellow, respectively. Coinciding lattice points are marked in red, as is the two dimensional elementary cell of the CSL. Extending the idea of the CSL to three dimensions, the relation between the number of lattice points in the unit cell of a CSL and the number of lattice points in the unit cell of the generating lattice is called Σ. It is the unit cell volume of the CSL in units of the unit cell volume of the elementary cells of the crystal.

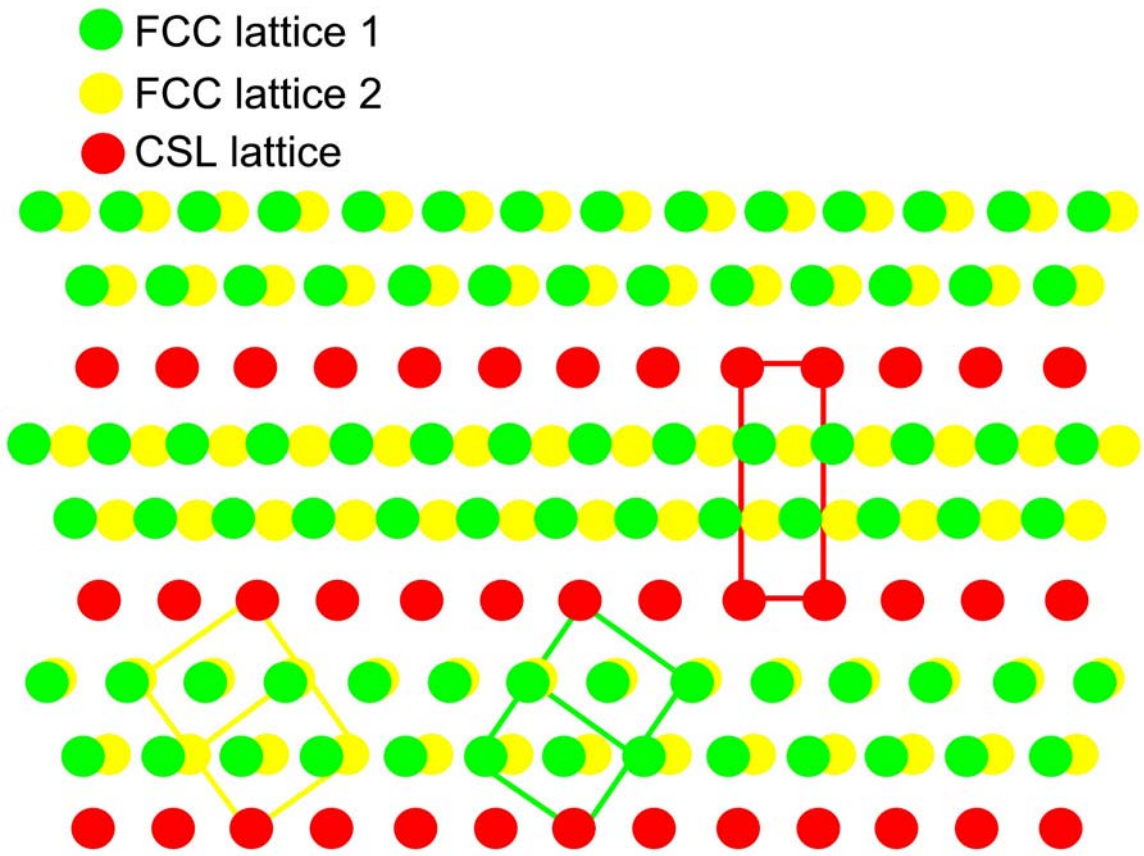

Figure 4.49: Schematic representation of Coincident Site Lattice (CSL) drawn in red formed by two FCC lattices, green and yellow, rotated with respect to one another.

Interfacial energy is one of the most important factors that determine the kinetics of a lattice transformation, as in that of twinning. This energy is the main barrier to nucleation of a twin. Song and Gray [52] show that the energy barrier, γ, is proportional to the square of the lattice mismatch on the boundary:

$$\gamma = C\mu\sigma^2$$

where C is a constant, μ is the shear modulus, and σ is the lattice mismatch on the boundary.

4.1.2.4.1 Application of the CSL Theory to Twinning in α-Titanium Alloys

Song and Gray [52] have applied the CSL theory to the problem of describing $\{1\bar{1}02\}$ twinning in HCP materials. To understand their analysis, first consider that the stacking sequence of atomic planes for HCP materials is ABABAB… Thus, Ti atoms may be designated at lying on an **A**-plane, in what is called an **A**-type site, or lying on a **B**-plane, in what is called a **B**-type site. However, the stacking sequence of atomic planes for the HCP lattice could also be ACACAC… where the atoms in **C**-type sites are rotated 60° with respect to **B**. Otherwise, they are structurally equivalent. These sites are illustrated in Figure 4.50.

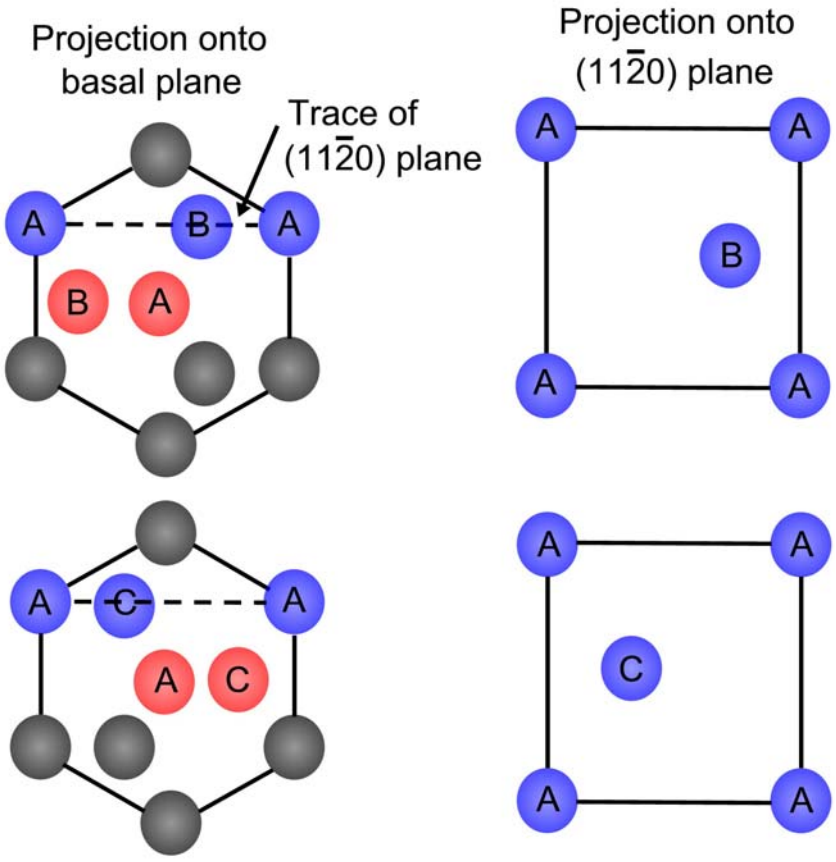

Figure 4.50: Schematic illustration of *A*, *B*, and *C* type sites in HCP lattice of α-Ti. *B* and *C* type sites are structurally equivalent.

Now, consider the atomic movements involved in $\{1\bar{1}02\}$ twinning given by Song and Gray [52], seen in Figure 4.51. The untwinned matrix has ABAB… type stacking (atoms in **A** and **B** type sites). Twinning occurs about a $\{1\bar{1}02\}$ twinning plane defined by **A** type atoms in the figure. Atoms in **A** type sites are homogeneously sheared from the untwinned to the twinned position with no shuffle required (as a consequence of the assumption that the twinning plane consists of **A** type atoms). There are two possible sites in the twin lattice into which the **B** atoms from the matrix can be shifted: the **B** or **C** type site in the twinned lattice. **B** type atoms from the matrix can move to **C** type sites in the twin in a direction parallel to the twinning plane, but the magnitude of the movement is not proportional to the distance form the twinning plane. **B** atoms from the twin could also move to **B** type sites in the twin. In this case, the magnitude of the movement is proportional to the distance from the twinning plane, but it is not parallel to the twinning plane. Again, these are equivalent from a structural point of view. Because the transformation of **B** atoms to either site cannot be accomplished by simple shear, the atom will move to whichever site is energetically favorable. For instance, note that above the twinning plane, the motion to **C** type sites would be in an opposite direction than the twinning shear, suggesting that such movement is energetically unfavorable [63]. In any event, given that **B** atoms can move to either site, stacking faults will form within the twin, and this is the origin of the faults seen in Figures 4.41 and 4.42. This stacking fault is defined as a partial stacking fault (PSF) because only half of the atom layers (**B** or **C**, not **A**) are displaced. The stacking sequence across the faulting plane is given as:

…**ABAB||ACAC**

This stacking sequence is identical to that given for the intrinsic I_1 fault, but the difference comes in the partial dislocation structure around the fault area [64]. In particular, there is no extra atomic plane involved in the PSF and little lattice disturbance in the vicinity of the faulted and unfaulted regions. More details of the PSF in HCP materials are given by Song and Gray [64].

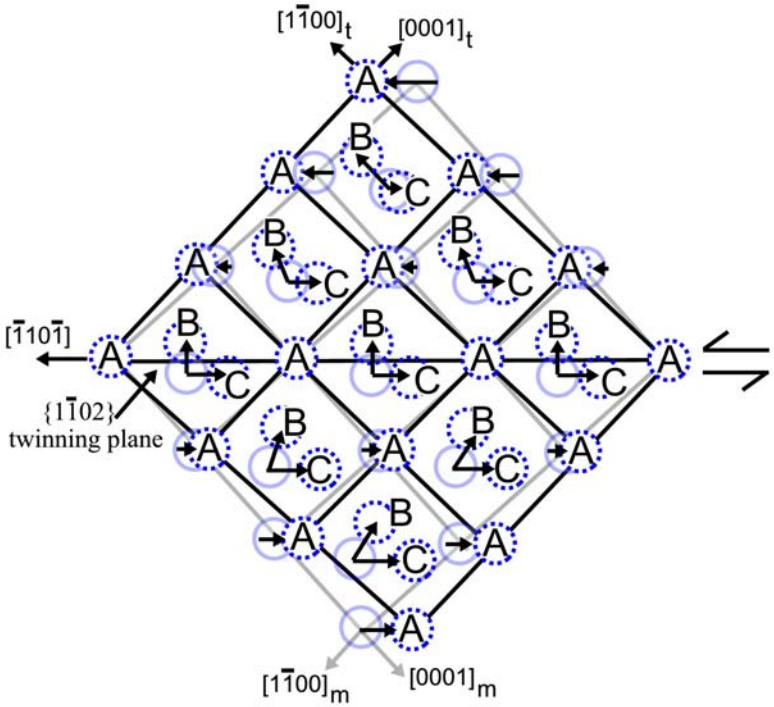

Figure 4.51: Schematic illustration of $\{1\bar{1}02\}$ twinning in HCP lattice of α-Ti projected onto $\{1\bar{2}10\}$ plane, after Song and Gray [52]. Ti atoms in *A*-type sites move to twinned position by simple shear. Ti atoms in *B* type sites move to either a *B*-type site or *C*-type site in the twin.

Figure 4.52, a computer generated CSL lattice by Song and Gray [52], shows a larger view of the lattice of the matrix and $\{1\bar{1}02\}$ twin projected onto the $\{1\bar{2}10\}$ plane. For α-titanium, the matrix and the twin are related by a rotation of approximately 85^o. The match planes, along which the lattice sites of the twin and matrix overlap, are indicated.

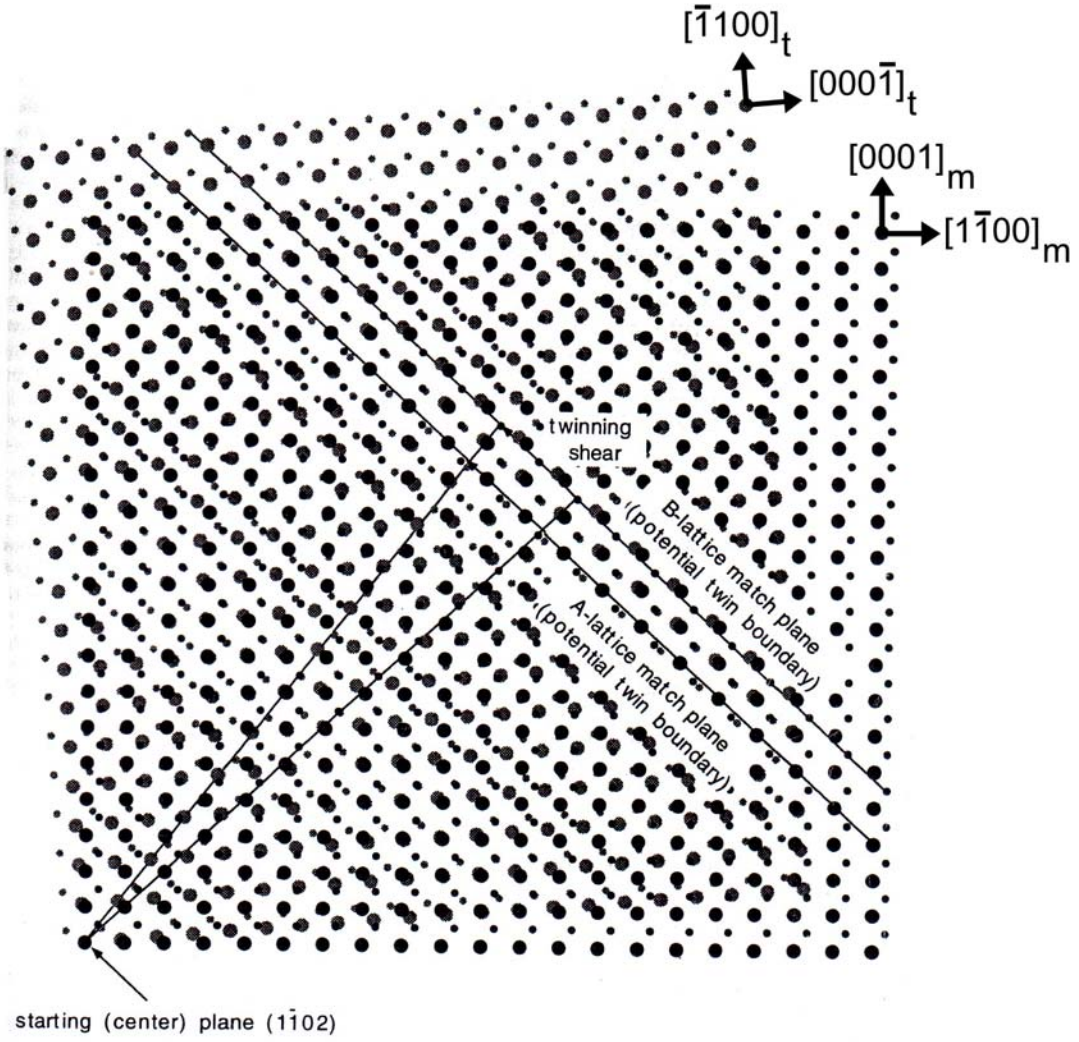

Figure 4.52: CSL lattice projection of the HCP lattice of α-Ti onto $(1\bar{1}02)$ plane showing overlap of untwinned and twinned lattices [52]. Untwinned matrix and twinned lattice are rotated by approximately 85° with respect to one another. Large dots represent positions of *A*-type atoms and small dots represent positions of *B*-type atom. Planes where the *A*-sites and *B*-sites of the untwinned matrix and twin lattices match are indicated. (Reprinted from *Acta Metall. Mater.*, Vol. 43, S.G. Song and G.T. Gray III, "Structural Interpretation of the Nucleation and Growth of Deformation Twins in Zr and Ti – I. Application of the Coincident Site Lattice (CSL) Theory to Twinning Problems in H.C.P. Structures," 2325-37, 1995, with permission from Elsevier)

The CSL analysis of this twin by Song and Gray [52] gives important information. First, unlike for cubic structures, there is no perfect match plane for the twinned and untwined lattices. There is a small strain due to this mismatch in the $\boldsymbol{\eta_1}$ direction. The ratio of the lattice mismatch, δ, is calculated to be 0.0216. This is not analogous to the misfit of coherent interfaces between lattices with different lattice constants. Rather, it is the relative shift of the respective lattices along the interface. Another important parameter revealed by the CSL analysis is the distance from the center plane to the first match plane. This distance is referred to as the unit step height of the advancing twin front. From the figure, there are 23 $\{1\bar{1}20\}$ type planes between the starting plane and the first match plane. This corresponds to a Σ value of 46 (23 planes on either side of the twin start plane) and a unit step height of 79.371 Å (23 planes multiplied by an interplanar spacing of approximately 3.44 Å). Note also that a good boundary match plane is found for **B**-atoms sites two rows past that of the **A**-match plane. Thus, a $\{1\bar{1}02\}$ twin may stop at the **B** match plane as well. If twin growth is then restarted, the homogeneous shearing lattice may be the **B**-lattice. If there is sufficient time before twin-growth is restarted and partial stacking faults can extend all the way to the boundary, **B** atoms in the match plane will move out of the coherent boundary in the region between two partial stacking faults. This region of the boundary will recede to the nearest **A** match plane because the previous boundary is no longer a match plane. Thus, resumed growth of the twin will involve the homogeneous shearing lattice alternating back and for the between **A-** and **B-** lattices when stacking faults are encountered along the boundary. A displacement with Burgers vector $\frac{1}{6}[20\bar{2}3]$ will characterize the region

of renewed twin growth. This Burgers vector leads to the formation of a partial dislocation on the $(11\bar{2}0)$ prism slip plane. Therefore, the stacking fault is on the prism plane that is normal to the partial stacking fault on the basal plane. The two stacking faults are connected at the twin boundary but extend on different planes that are 90^o from each other.

4.1.2.4.2 Stepwise Growth of $\{1\bar{1}02\}$ Twins

Song and Gray [52] propose that the nucleation and thickening of a twin occurs by the simultaneous motion of all the layers between the two match planes parallel to the initial twinning plane in the shear direction. The motion initiates at the twinning plane and does not stop until the first match plane is reached. A pause in this process would be unstable because of lattice distortion at the incoherent boundary. This is schematically illustrated in Figure 4.53. As the twin moves to each subsequent match plane, the twinned region shifts by a distance given by the Burgers vector of a lattice dislocation. The growth may stop at a match plane or continue to grow by a series of steps depending

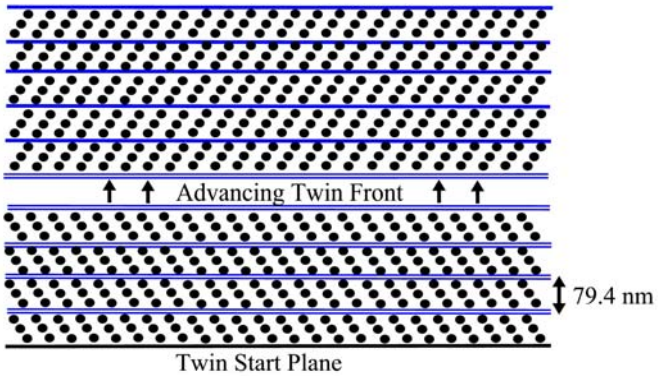

Figure 4.53: Schematic illustration of advancing twinning front in HCP lattice of α-Ti. Twin front advances by step-wise growth between match planes with a separation of 79.4 nm. Twinning occurs by coordinated movement of all the atoms between the match planes.

on the local stress. If the stress is sufficient, the twin could keep growing until it reaches the grain boundary.

The twin-matrix interface at the tip of the twin is incoherent, necessitating the minimization of this area so as to minimize interfacial energy. In the region of the twin tip, the displacement of the lattice in the twinned region is the distance between two adjacent lattice points on the match plane. The twin tip may not be able to accommodate such a large displacement, but given that the displacement is the sum of dislocations i.e. $a + a' + c$, it will likely dissociate into individual dislocations which are emitted from the twin tip or trapped in the twin interior. Further, dislocations of opposite sign in the matrix will likely be attracted to the area of the twin-matrix interface to neutralize the displacement given by the growth of the twin. Thus, the interfacial energy of the twin tip will be reduced by quite a bit.

The rate of twin propagation is determined by the local stress and is given by the jump distance (distance between match planes), and the time interval between consecutive jumps. Consider again the parameters given by the CSL analysis, the mismatch of the match planes (δ), the step height (h), the ratio of these $\left(\frac{\delta}{h}\right)$, and the twinning shear (γ). The step height of the $\{1\bar{1}02\}$ twin is larger than that of $\{1\bar{1}01\}$ or $\{1\bar{2}12\}$ type twins which are also observed in HCP materials. This implies that it would be easier to nucleate the latter type of twins. Indeed, $\{1\bar{1}01\}$ twins have been observed during ambient temperature deformation of titanium [65, 66], and are seen in Figure 4.36. However, the lattice mismatch and magnitude of the twinning shear must also be considered. The shear for $\{1\bar{1}02\}$ twins is significantly smaller than that of $\{1\bar{2}12\}$ and

$\{1\bar{1}01\}$ type twins. As such, $\{1\bar{1}02\}$ twins occur more frequently than these other types of twins. The mismatch ratio $\left(\frac{\delta}{h}\right)$ can affect the final thickness of the twin. The mismatch, δ, on the match plane accumulates with the increase of the twin thickness. Thus, twinning modes with smaller mismatch ratios will generally favor thicker twins. The smaller magnitude of shear and lattice mismatch of $\{1\bar{1}02\}$ suggests that they should be thicker than the other types of twins. A final implication of the twinning model described above is that twin formation will be very sensitive to the presence of interstitial atoms, as will be described in the subsequent sections.

4.1.2.5 Effect of Interstitial Atoms on Twinning of α-Titanium Alloys

Given the coordinated atomic movements associated with $\{1\bar{1}02\}$twinning in α titanium alloys, it is to be expected that the presence of interstitial atoms, particularly oxygen, could interfere with twin growth. Indeed, such a phenomenon has been observed. Paton, Williams, and Rauscher [67] compared the extent of twinning in α-titanium alloys containing 250 ppm and 2500 ppm oxygen, respectively. At room temperature, the alloy containing less oxygen showed nearly ten times more twins than the alloy with more oxygen. Similar results were obtained by Gray, *et al.* [68], when considering the shock loading of titanium alloys of differing oxygen content. In the α-Ti alloys in which time-dependent twinning has been observed during low temperature creep, oxygen is the only impurity present in significant concentration (approximately 0.07wt.%). It is worth noting here that in α-titanium, oxygen interstitials will reside in the octahedral lattice sites, as they are larger than tetrahedral sites. The octahedral sites

of HCP alloys were illustrated previously in Figure 3.9. Ankem, *et al* [23] were the first to suggest that the slow growth of deformation twins could be attributed to the interference of interstitial atoms such as oxygen in the lattice. However, the crystallographic models for twinning presented above do not consider the presence of interstitial atoms, only the host atoms. As such, in this investigation the existing crystallographic models for twinning in HCP α-Ti alloys are expanded to show clearly how the presence of impurity oxygen atoms residing in octahedral interstitial sites can be responsible for slow twin growth.

4.1.2.5.1 Crystallographic Model for the Effect of Octahedral Interstitial Atoms on $\{1\bar{1}02\}$ Twinning in Alpha-Titanium

Consider first the HCP lattice of α-titanium, including octahedral interstitial sites, projected onto two adjacent $\{11\bar{2}0\}$ type planes. This is shown in Figure 4.54. One plane will be considered to be in the plane of the projection, and the other will lie above or below by a distance of $\frac{a}{2}$ (see Figure 3.8). Figure 4.55 shows the $\{1\bar{1}02\}$ twinning shear about the $(10\bar{1}2)$ twinning plane, including the location of the octahedral interstitial sites after the shear. Only those Ti atoms residing in **A**-type sites in the plane of projection are sheared to the correct twin position, as those are the atoms that define the twinning plane. The other atoms are not sheared to a correct twinned position and require a subsequent shuffle. The arrows in Figure 4.56 show the shuffles that are required to move the Ti atoms from the sheared position to the correct twinned position. Recall that atoms in **B**-type sites can shuffle to one of two crystallographically equivalent sites, **B**-type sites or **C**-type sites in the twin [52]. This reorientation of the lattice would, however, eliminate

the volume where the interstitial atom could reside. Any interstitial atom residing in an octahedral site would impede the shuffle of the Ti atoms to the twinned position. These interstitial sites are called "unconserved" and are marked with an 'X' in Figure 4.56. An interstitial atom residing in an unconserved site must diffuse to an undisturbed part of the lattice. After the movements of the Ti atoms are completed, the octahedral interstitial sites will be reformed in new locations. At this point, interstitial atoms may diffuse back into the twinned part of the lattice. The completed $\{1\bar{1}02\}$ twin including the location of new octahedral interstitial sites is shown in Figure 4.57. The locations of **B** and **C**-type sites are shown, but only one of the two will be occupied.

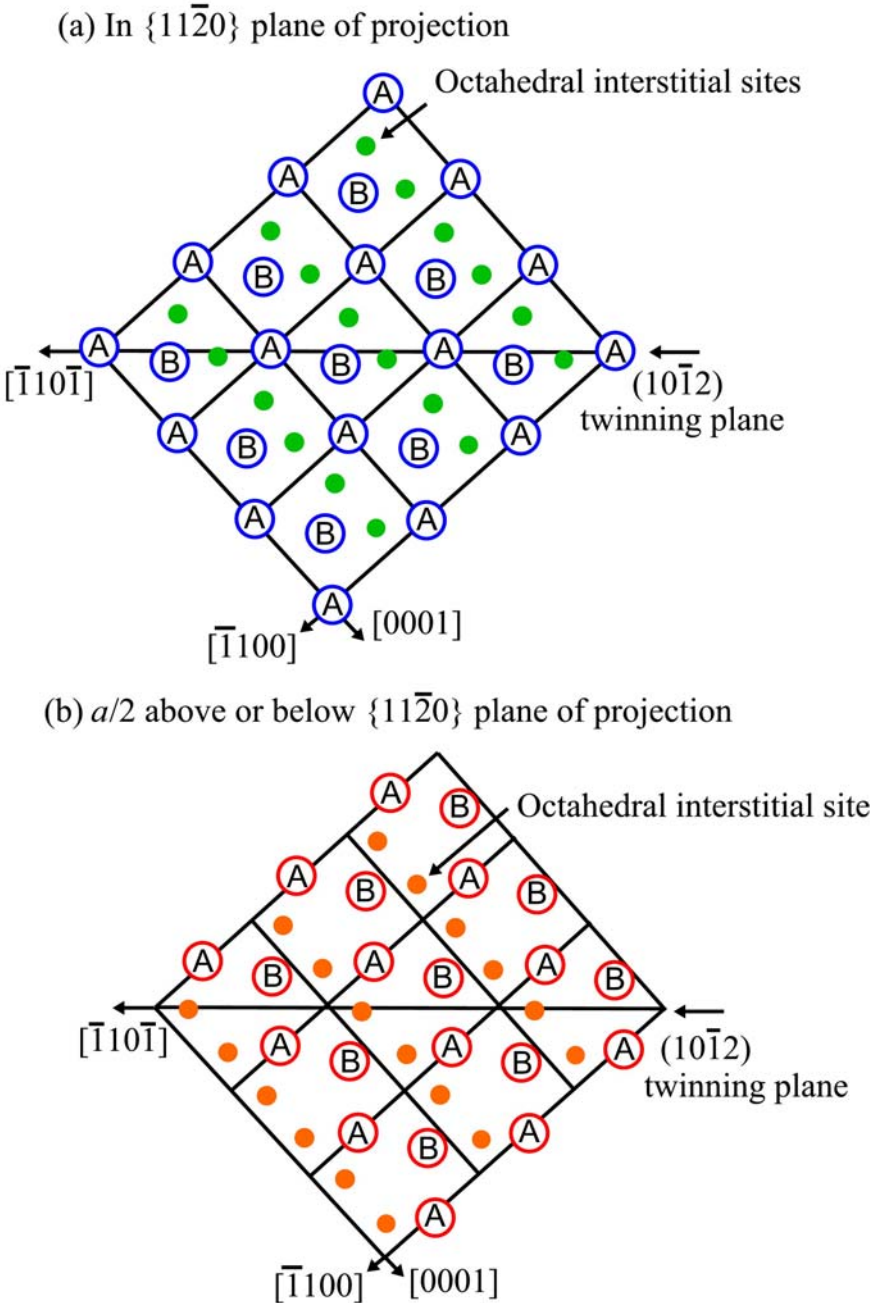

Figure 4.54: HCP lattice of α-Ti projected onto two adjacent $\{11\bar{2}0\}$ planes separated by a distance of $\frac{a}{2}$. (a) In the $\{11\bar{2}0\}$ plane of projection, including Ti atoms (blue) and octahedral interstitial sites (green). (b) $\{11\bar{2}0\}$ plane above or below the plane of projection including Ti atoms (red) and octahedral interstitial sites (orange).

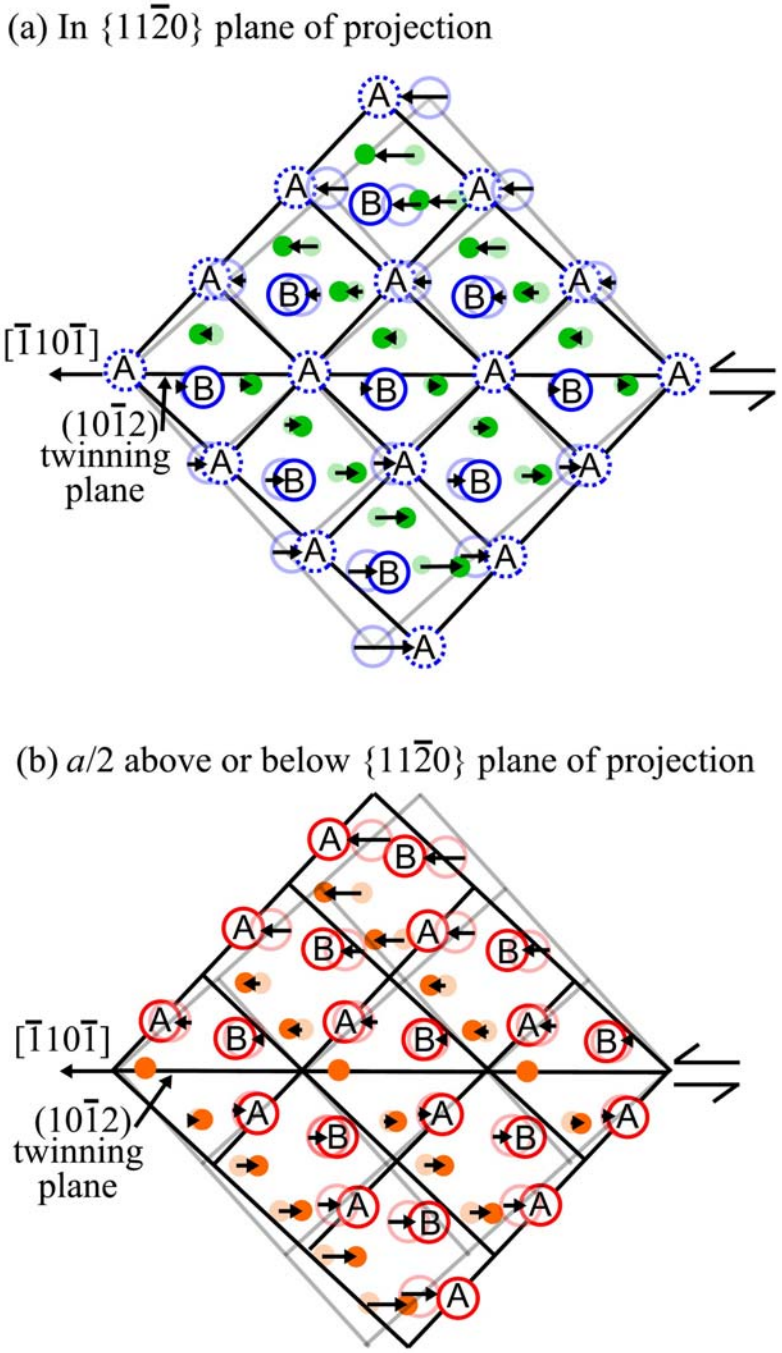

Figure 4.55: $\{1\bar{1}02\}$twinning shear of HCP lattice of α-Ti projected onto two adjacent $\{11\bar{2}0\}$ planes separated by a distance of $\frac{a}{2}$. (a) In the $\{11\bar{2}0\}$ plane of projection, including Ti atoms (blue) and octahedral interstitial sites (green). (b) $\{11\bar{2}0\}$plane above or below the plane of projection including Ti atoms (red) and octahedral interstitial sites (orange). *A*-type Ti atoms in plane of projection are homogeneously sheared to twinned position (dashed blue).

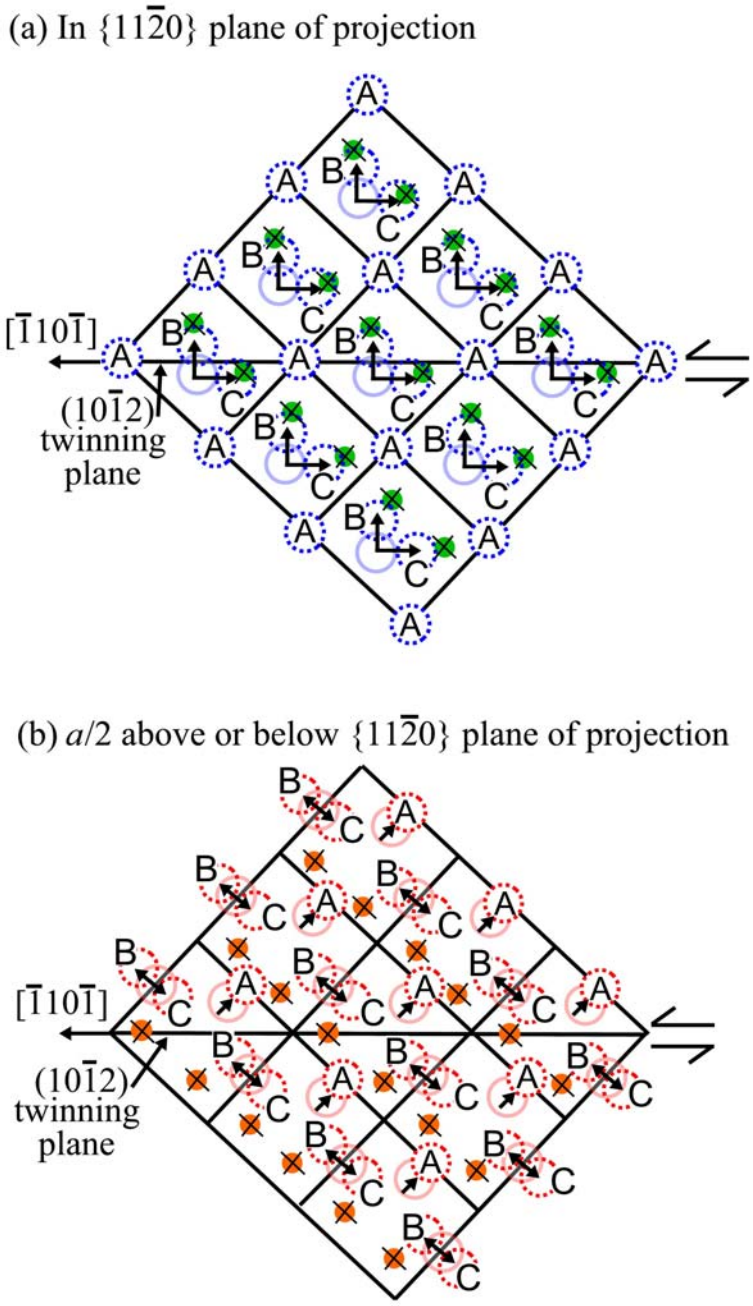

Figure 4.56: HCP lattice of α-Ti projected onto two adjacent $\{11\bar{2}0\}$ planes separated by a distance of $\frac{a}{2}$ with arrows illustrating shuffle required to move Ti atoms from sheared to proper $\{1\bar{1}02\}$ twinned position. Ti atoms shuffle to *A*-type sites and either *B* or *C*-type sites (dashed red). Atomic reorientation caused by shuffle eliminates octahedral interstitial sites which are marked with an 'X'.

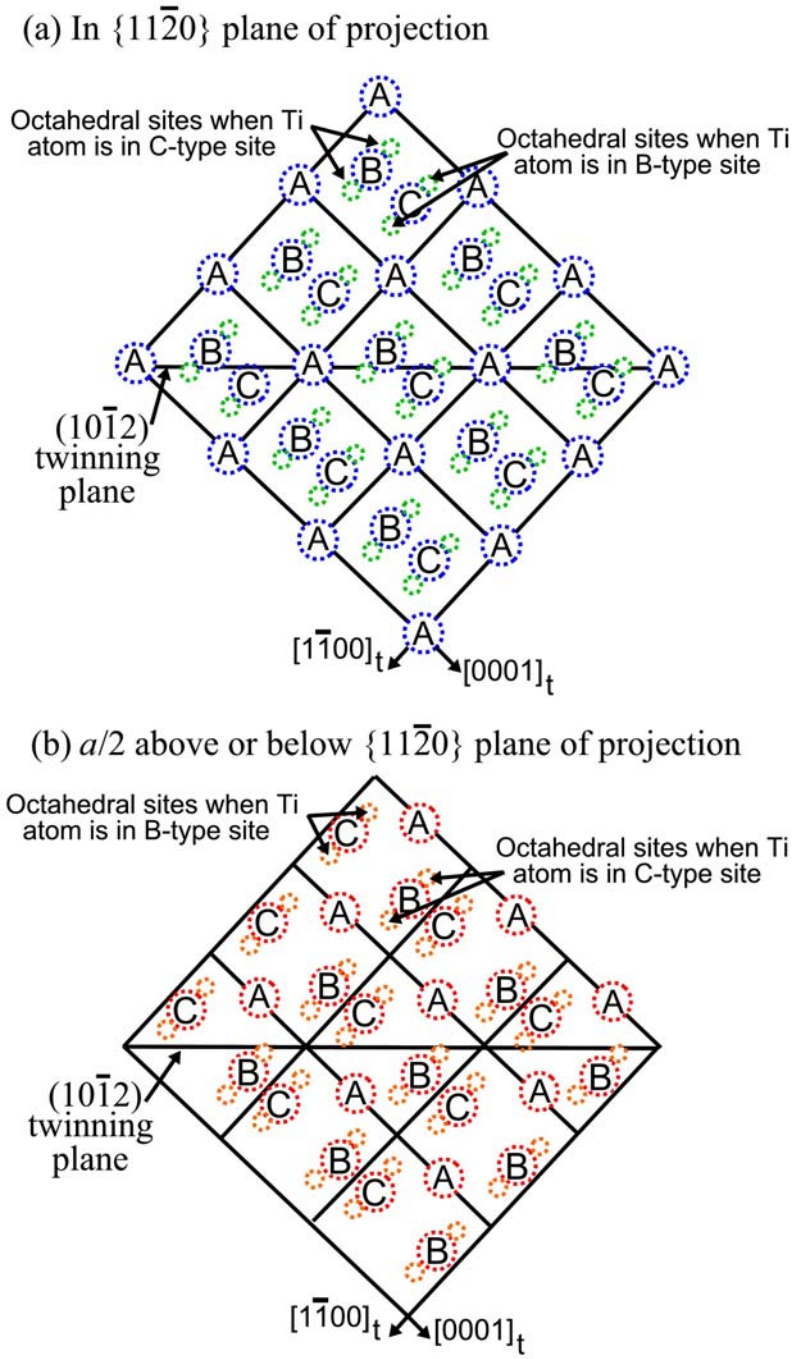

Figure 4.57: HCP lattice of α-Ti after $\{1\bar{1}02\}$ twinning, projected onto two adjacent $\{11\bar{2}0\}$ planes separated by a distance of $\frac{a}{2}$. (a) In the $\{11\bar{2}0\}$ plane of projection, Ti atoms may reside in one of two structurally equivalent sites, *B*-type or *C*-type, which are labeled. The location of the octahedral interstitial site will depend on whether the *B*-type or *C*-type site is occupied. (b) Similar to (a) for the $\{11\bar{2}0\}$ plane above or below the plane of projection.

4.1.2.5.2 Activation Energy for Time-Dependent Twin Growth in Alpha-Titanium Alloys

The model for time-dependent twin growth of $\{1\bar{1}02\}$ twins in α titanium alloys presented above suggests that twin-growth is rate limited by the diffusion of oxygen away from unconserved octahedral interstitial sites so that it will not impede the atomic movements associated with twinning. As such, the activation energy for time-dependent twinning based on the model should correspond with the experimentally measured value for the diffusivity of oxygen in α-titanium. Moreover, these values should also correspond with the experimentally measured activation energy for low temperature creep of an α-Ti alloy in the strain region where twinning is a predominant deformation mechanism.

For the purposes of this model, the advancing twin front accompanied by diffusion of oxygen atoms can be related to the diffusion of a species from the surface into the bulk of a sample, ie, carbon into a bulk sample of Fe. In such a case, the effective penetration distance is the point at which the concentration of the diffusing species has a value equal to the average of the initial concentration in the bulk and the surface concentration [69]. The effective penetration distance, x_{eff}, is given by the Equation 4-17:

$$x_{eff} = \sqrt{Dt} \tag{4-17}$$

where D is the diffusion constant and t is the time. In the case of twinning, the twinning start plane at the center of the lenticular twin is analogous to the surface of the specimen and the distance from the start plane to the twin-matrix interface is the effective penetration distance (see Figure 3.14).

Measurements of twin thickness from the SEM micrographs from interrupt creep testing of α-Ti-0.4 Mn [23, 37] and α-Ti-1.6V [26] (as seen in Figures 2.4 and 2.5) show that on average, the distance from the center of the twin to the twin-matrix interface increases by approximately 0.462 μm per hour within the first 10 to 17.7 hours of the test. It is assumed that the rate of twin growth is constant over this interval. Consider again the nature of the advancing twin front. It was proposed earlier that the twin thickens by the sequential jumping of the twin front from match plane to match plane. The step height between these planes has been calculated as 79.4 nm. The atoms in between the match planes undergo simultaneous, cooperative movement to the twin positions and any oxygen atoms between the match planes would need to diffuse away as the octahedral interstitial sites in which they reside are eliminated.

Now, using Equation 4-17 and the measurements taken from the SEM micrographs of interrupt creep tests, where x_{eff} is 0.462 μm and t is 1 hour, the value for D is calculated as 5.93×10^{-17} m^2/sec.

Interstitial diffusion in alloys is governed by an equation of the type given in Equation 4-18 [69]:

$$D = D_o * \exp\left(\frac{-Q}{RT}\right) \tag{4-18}$$

where D is the diffusivity, D_o is the pre-exponential diffusion constant, Q is the activation energy for diffusion, T is the temperature, and R is a constant. The value for the diffusivity of oxygen in α-Ti has been calculated in many investigations over the years, as reviewed by Liu and Welsch [70]. The diffusion constant, D_o, is a function of the number of available sites into which an interstitial atom can diffuse. For the case of

interstitial diffusion, the value of D_o has been shown to decrease with increasing oxygen concentration as fewer unoccupied interstitial sites are available [71]. At an oxygen content of approximately 0.07 wt.% (0.2 at.%), the α-Ti alloy will have about 1 out of every 286 octahedral interstitial sites occupied (in the HCP unit cell, there are 6 octahedral interstitial sites per host atom, i.e. Ti). At such a concentration, the value for D_o is approximately $1x10^{-4}$ [72]. Solving for Q by the equation:

$$Q = -RT \ln\left(\frac{D}{D_o}\right) \tag{4-19}$$

when D is $2.37x10^{-16}$ m^2/sec., D_o is $0.5x10^{-4}$ m^2/sec., and T is 298 K gives the theoretical activation energy for time-dependent twinning according to the model as 68.5 KJ/mol.

The theoretical activation energy for time-dependent twinning of 68.5 KJ/mol is close to the experimentally measured activation energy for the diffusion of oxygen in α-titanium. In the review by Liu and Welsch [70], this value is given in the range of 68 to 200 KJ/mol. Thus, it seems likely that the rate of twin growth is controlled by the diffusion oxygen atoms away from eliminated octahedral interstitial sites. Moreover, the value given for the model is close to the experimentally measured activation energy for creep of α-Ti-1.6V at higher strains, calculated in Section 4.1.3.2: 47 KJ/mol. As such, it is suggested that in the strain region where time-dependent twinning is the predominant creep deformation mechanism, the rate of twin growth, and hence the amount of creep strain is controlled by the diffusion oxygen atoms away from eliminated octahedral interstitial sites.

There are several important implications of the model presented above. First, given that the twin growth rate and hence, creep strain rate is controlled by the diffusion

of interstitial oxygen away from eliminated octahedral sites, the creep strain rate should decrease as the amount of oxygen in the alloy increases. As mentioned earlier, the value of the pre-exponential diffusion constant, D_o, decreases as the amount of oxygen increases and it will become more difficult for oxygen to diffuse away from eliminated sites because more of them are occupied. Thus, increasing the oxygen content will make the alloy more creep resistant, but it will also reduce ductility. Moreover, the twin-matrix interface is a known nucleation site for fatigue cracks so the extent of twinning can have a direct effect on the structural integrity of components. Second, the model should also be valid for other interstitial elements in α-Ti that reside in octahedral interstitial sites, such as nitrogen and carbon. Third, if interstitial atoms can interfere with the atomic movements associated with twinning, they should also impede other transformations, including the α to ω phase transformation (ω is a variant of the hexagonal phase). This has been experimentally observed [73]. Finally, as will be seen in the next part of this chapter, a similar model can be developed for a BCC material, suggesting that interstitial atoms can interfere with twinning in a variety of crystalline structures.

4.2 β-Titanium Alloys

Twinning has been identified as a deformation mechanism in low-stability β-titanium alloys [28-30]. At low temperatures (<0.25 T_m), β-Ti-14.8V has been shown to deform by the slow growth of twins, or time-dependent twinning [28] during creep. This is unusual as in crystalline metals, twins are expected to grow at the speed of sound. In the previous part of this chapter, it was proposed that the slow growth of twins in HCP α-Ti alloys is related to the diffusion of interstitial impurities in the material. In this part of the chapter, the crystallographic model is extended to the BCC lattice of β-Ti and it is shown how octahedral interstitial sites where oxygen atoms can reside are eliminated by the atomic movements of titanium atoms associated with $\{332\}\langle 113\rangle$ deformation twinning. Using this model, a theoretical activation energy for time-dependent twinning is calculated which correlates well with the experimentally measured value for the diffusion of oxygen in β-titanium. Moreover, the theoretical activation energy is close to the experimentally measured activation energy for creep deformation of β-Ti-14.8V in the strain region where twinning is the predominant deformation mechanism, as measured by Hudson and Ankem [35]. This section is an expanded version of a paper that was published by Ankem and Oberson in the journal *Physical Review Letters* [34].

4.2.1 Theoretical Background

Deformation twins have been observed in many BCC metals and their alloys including vanadium, niobium, tantalum, chromium, molybdenum, tungsten, and β-titanium [31]. The most common type twin identified in many of these alloys is the $\{112\}\langle 111\rangle$ twin, however, a less common $\{332\}\langle 113\rangle$ twinning mode has been observed during deformation of metastable β-Ti-V, Ti-Nb, and Ti-Mo alloys [28-30, 75-81]. $\{332\}\langle 113\rangle$ twins were first observed in Ti-11.6 wt.% Mo after quenching from the β-field and during extensive studies of the industrial alloy, βIII (Ti-11.5 Mo-6 Zr-4.5 Sn) [75]. Ankem and co-workers have identified these twins during ambient temperature creep deformation of β-Ti-14.8 wt.% V at stresses less than the yield stress [28, 30]. It is suggested that $\{332\}\langle 113\rangle$ twinning is responsible for the relatively low modulus and high plasticity of alloys which exhibit this mechanism as compared to β-Ti alloys which deform solely by slip [80]. The means by which $\{332\}\langle 113\rangle$ twins nucleate and grow has been described by a classical, shear mechanism and by a mechanism involving partial twinning dislocations. Crystallographic models for the respective mechanisms show that each has advantages and disadvantages and there is not a consensus on which is most likely. As such, both the shear mechanism and the twinning dislocation mechanism will be considered in this investigation. Whichever mechanism is responsible for twinning in β-Ti alloys, the presence of interstitial impurities has been shown to hinder twin growth, but they are not included in past crystallographic models for $\{332\}\langle 113\rangle$ twinning. In this part of the chapter, crystallographic models are presented for $\{332\}\langle 113\rangle$ twinning in the BCC lattice of β-Ti where it is shown how oxygen atoms which reside in octahedral

interstitial lattice sites can be responsible for the slow rate of twin growth as they must diffuse away from lattice sites that are eliminated by the atomic movements of Ti atoms associated with twinning. The activation energy for twin-growth based on the model will be compared with the experimentally measured activation energy for the diffusion of oxygen in β-Ti and for the activation energy for creep strain of β-Ti 14.8V when twinning is a predominant deformation mechanism.

4.2.2 Models for $\{332\}\langle 113\rangle$ Twinning in β-Titanium Alloys

In this section, reference will be made to the projections for the BCC lattice of β-Ti given in Section 3.8.1.2 (Figures 3.11-3.13).

4.2.2.1 The Classical Model for $\{332\}\langle 113\rangle$ Twinning in β Titanium Alloys

According to the classical model for twinning, twinning is the result of homogeneous shear on successive planes and this shear is not equal to a lattice vector [5]. In the simplest cases of twinning, the twinning shear will move all of the atoms from the untwinned lattice position to the correct lattice position in the twin such that there is a mirror reflection between the twin and the matrix across the interface and no additional shuffle is required. This is the case for $\{112\}\langle 111\rangle$ type twinning in BCC materials (see Figure 2.12). It is important to note, however, that this is not always the case, as was seen for the HCP structure described earlier. Similarly, in the $\{332\}\langle 113\rangle$ type twins identified in β titanium alloys, not all of the atoms can be translated to the twinned

position by a simple shear. As such, it is necessary to consider an additional atomic translation, or a shuffle, to bring a sheared atom to the correct twin position.

Such a mechanism for $\{332\}\langle 113\rangle$ twinning in BCC materials was first described by Crocker [82] and is illustrated in Figure 4.58. Figure 4.58(a) shows a projection of the BCC unit cell onto the $(1\,\bar{1}\,0)$ plane, with the $\mathbf{K_1}$ plane and $\boldsymbol{\eta_1}$ and $\boldsymbol{\eta_2}$ directions illustrated. Figure 4.58(b) shows the magnitude of the twinning shear is the difference between the $\boldsymbol{\eta_2}$ direction in the untwinned matrix and the $\boldsymbol{\eta_2}$ direction in the twin. However, only half of the atoms, those in the plane of the projection (blue), are sheared to the correct twin position (dashed blue) such that they are symmetric to a corresponding atom across the twin-matrix interface. The other half, those out of the plane of the projection (red), are not symmetric to a corresponding atom across the twin-matrix interface and must shuffle to the correct twinned position. The correct twinned sites (dashed red) lie on the same $\{33\bar{2}\}$ plane as the sheared atoms and at equal distances in the direction (to the left) and in the opposite direction (to the right) as the twinning shear. These atoms could shuffle to either site, but it is likely to be energetically difficult to shuffle in a direction opposite that of the twinning shear. The shuffles are indicated by arrows in Figure 4.58(c). The final twinned structure, after the shuffles, with mirror symmetry across the twin-matrix interface is shown in Figure 4.54(d). A similar description with slightly different shuffles has been proposed by Richman [83], but will not be illustrated here as it is largely similar to that shown in Figure 4.54.

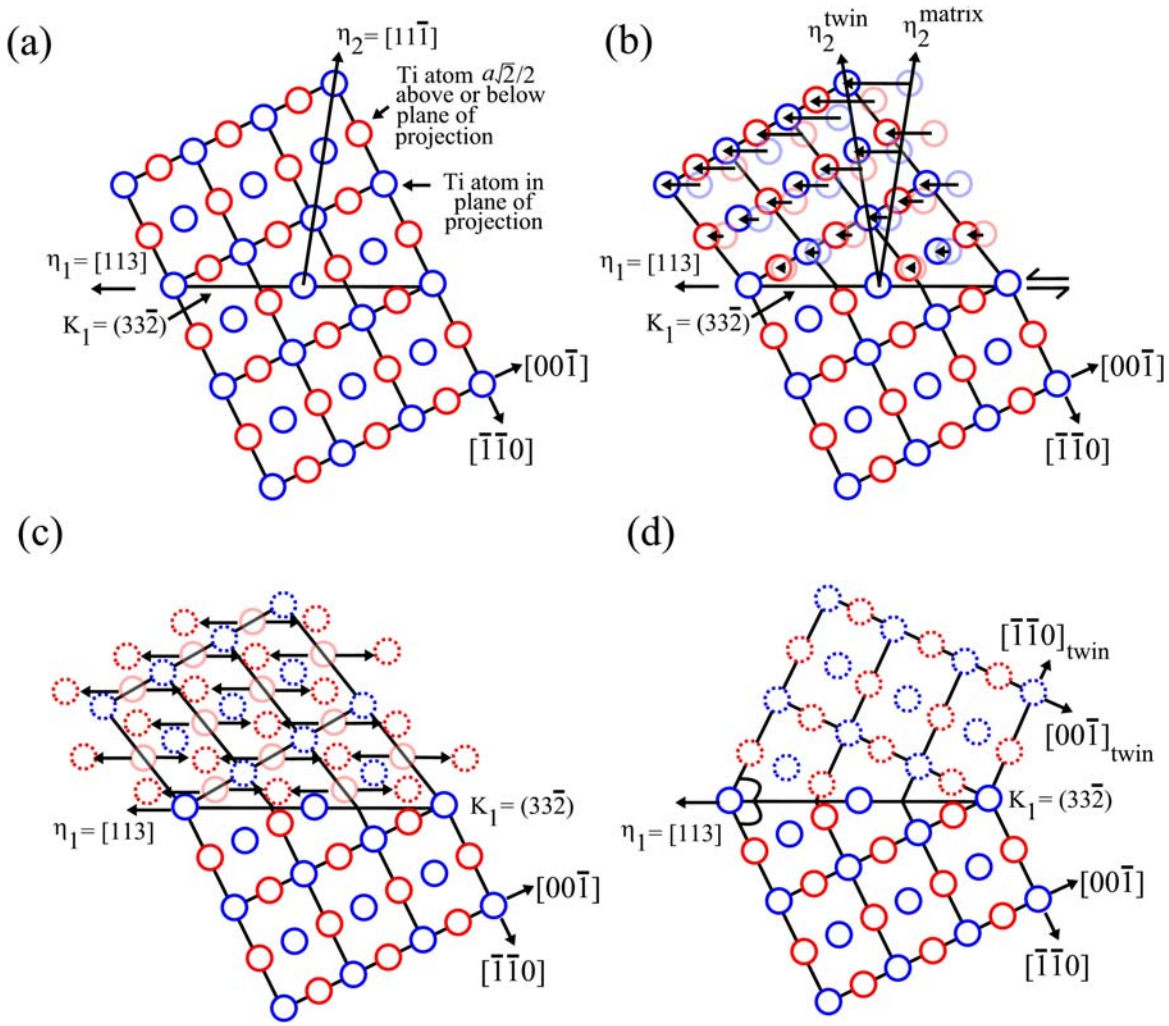

Figure 4.58: Classical shear mechanism for $\{332\}\langle 113\rangle$ twinning after Crocker [82]. (a) Untwinned BCC lattice projected onto $(1\bar{1}0)$ plane including atoms in (blue) and above/below (red) the plane of projection. (b) Shear of the lattice given by difference between η_2 directions in untwinned matrix and twinned lattice. Atoms in the plane of projection are sheared to correct twinned position (dashed blue). (c) Shuffles, indicated by arrows are required to move half of the atoms, those above or below the plane of projection), to the twinned position (dashed red). (d) Final twinned lattice.

Hanada, *et al* [76], have studied plastic deformation during tensile deformation of β-Ti-V alloys and note the presence of $\{332\}\langle 113\rangle$ type twins, particularly noting the effect of V content on deformation behavior. They note that the deformation mechanism varies depending on the V content. Above 22 wt.% V, slip is the predominant deformation mechanism and below 22wt.%V, $\{332\}\langle 113\rangle$ twinning is the deformation mechanism. Further, they note that in β-Ti alloys with similar V content, twinning is suppressed in alloys with higher interstitial oxygen content. These findings are interpreted to suggest that twinning occurs when the β-phase is very unstable and ready to transform into the ω-phase as this will make the shuffling of atoms described above easier. Indeed, it has been found [78] that the deformation mechanism corresponds to the ratio between interplanar spacings, $r = \frac{d^{\beta}_{(222)}}{d^{\omega}_{(0002)}}$ where $d^{\omega}_{(0002)}$ is the interplanar spacing in the lattice of the athermal ω-phase. In alloys with *r* close to the ideal value of 2/3, strain induced ω-phase is formed, whereas when *r* is slightly smaller or larger, $\{332\}\langle 113\rangle$ twinning will be the predominant deformation mechanism. It is to be noted, however, that high stability β-Ti-V alloys (V content greater than 20 wt. %) containing the ω-phase can deform solely by slip and $\{112\}\langle 111\rangle$ type twinning [84, 85] and conversely $\{332\}\langle 113\rangle$ twinning has been observed in β-Ti alloys with no athermal ω phase present [86, 87]. Moreover, Hanada, *et al* [76] propose that oxygen interstitial atoms interfere with lattice shearing and shuffling of the β-phase. Similar results have been observed in β-Ti-Mn [78] and β-Ti-Nb [77] alloys.

4.2.2.2 Dislocation Model for $\{332\}\langle 113\rangle$ Twinning in β-Titanium Alloys

The works of Hanada [76-78] were published in the early 1980's and for nearly 20 years, there were no studies published on the $\{332\}\langle 113\rangle$ twinning system. Recently, Litvinov and Rusakov [80], however, have identified a number of drawbacks to the classical model for $\{332\}\langle 113\rangle$ twinning. The analyses of Crocker [82] and Richman [83] consider atomic displacements on the basis of their initial and final positions without giving full consideration to the interatomic spacing requirements of a real lattice. For instance, examination of the twin-matrix interface according to the Crocker [82] and Richman [83] models reveals significant atomic superposition if the atoms are considered as rigid spheres. Such a symmetrical boundary would have high energy and would be unlikely without relaxation. A model should consider that twins are nucleated as thin interlayers consisting of two low-energy twin boundaries. Given the limitations of the classical shear mechanisms for $\{332\}\langle 113\rangle$ twinning in β-Ti alloys, Litvinov and Rusakov [80] propose dislocation mechanisms of twinning as described below.

4.2.2.2.1 Pole Dislocation Mechanism

The dislocation mechanism for twinning in BCC structures was first described by Cotrell and Bilby for the $\{112\}\langle 111\rangle$ twinning system [88], and is schematically illustrated in Figure 4.59. The plane-by-plane twin growth comes about as a result of the sequential glide of so-called "twinning dislocations" on a stack of twinning planes. The Burgers vector of the twinning dislocation is equal to the shear required to move the atoms of the

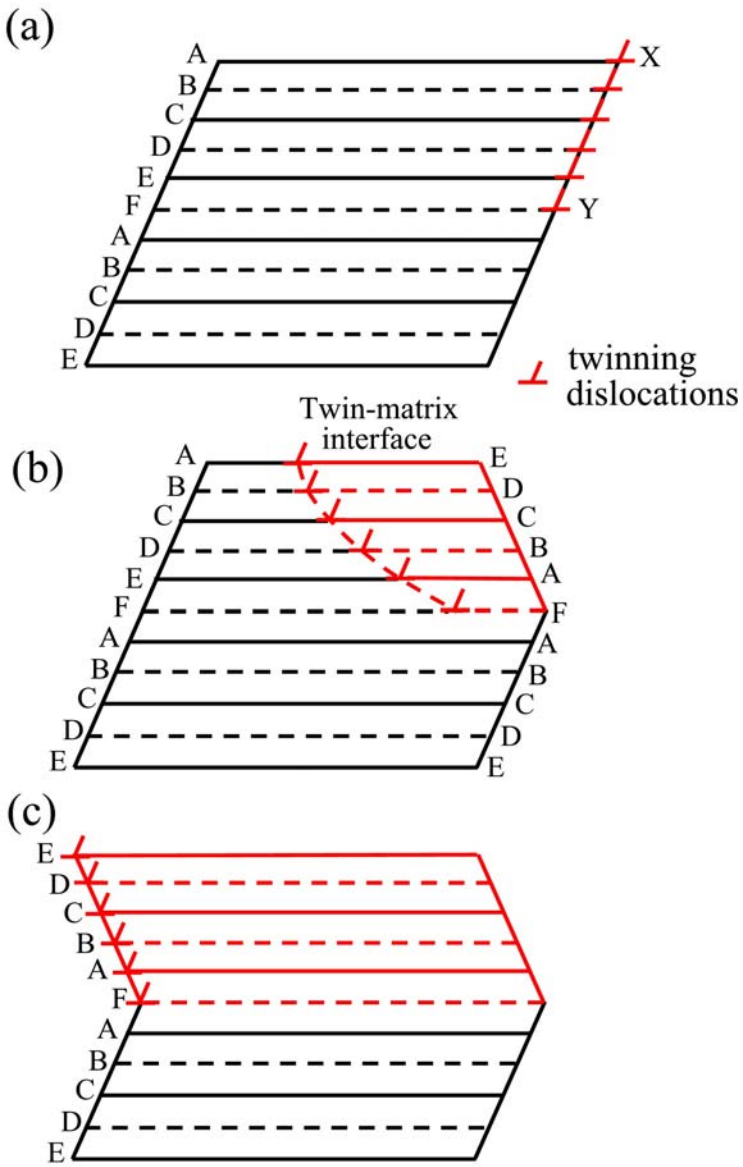

Figure 4.59: Illustration of dislocation mechanism for twinning in a BCC lattice. (a) Projection of a stack of twinning planes. *X*-*Y* is a row of twinning dislocations; one dislocation on each twinning plane. (b) The twinning dislocations have moved part of the way across the crystal to produce a twinned region. (c) Twinned crystal.

crystal from the untwinned to the twinned position. As the twinning dislocations lying along line **XY** in Figure 4.59 move from right to left, the volume swept out is twinned. The passage of twinning dislocations over each slip plane is attributed to the pole dislocation mechanism [89-91].

Consider a mobile dislocation that encounters a screw dislocation tree, or pole, that it cannot cut through as it moves through the crystal, after [60]. The dislocation may "swing" or coil itself around the pole as shown in Figure 4.60(a). The planes of atoms perpendicular to a screw dislocation are arranged in the form of a spiral ramp. The two arms of the mobile dislocation rotate around the pole in opposite directions, therefore one segment will spiral up and one segment will spiral down. The Burgers vector of the portion of the pole between the segments must change to a value, $\mathbf{b_3}$ equal to the sum or difference of $\mathbf{b_1}$ or $\mathbf{b_2}$. This is illustrated in Figure 4.60(b). A twin can be produced if a partial dislocation attached to a stacking fault crosses a pole dislocation whose Burgers vector has a component normal to the slip plane of the partial, seen in Figure 4.60(c). As the partial dislocation spirals around the pole, it produces a deformation twin, shown in Figure 4.60(d).

Cotrell and Bilby [87] propose the generation of a twinning partial dislocation by dissociation of a unit lattice dislocation. The twinning partial dislocation will then wind around the pole dislocation. The distance that it takes the twinning partial dislocation to complete its revolution around the pole is equal to the interplanar spacing of the twinning planes.

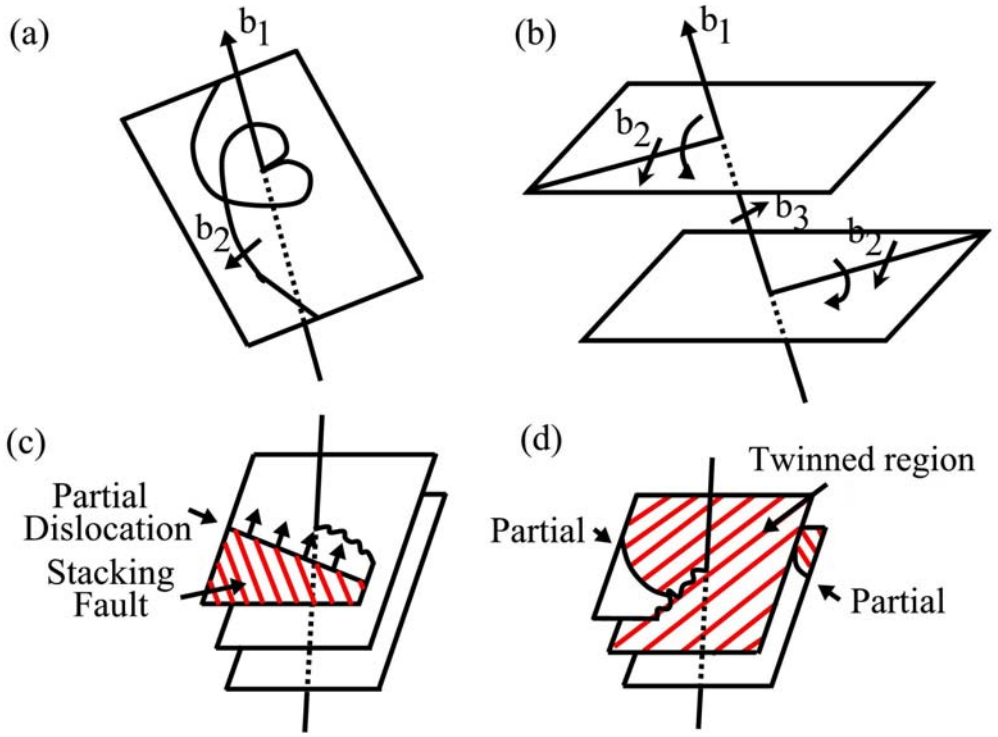

Figure 4.60: Pole dislocation mechanism, after [90]. (a) Mobile dislocation intersecting a screw dislocation that it cannot cut through. (b) The two arms of the dislocation spiral around the pole in opposite directions. (c) Partial dislocation attached to a stacking fault crosses a pole dislocation. (d) As the partial dislocation spirals around the pole, it produces a deformation twin.

There has been much controversy and many models to describe twinning by the pole dislocation mechanism, particularly regarding the nature of the pole dislocation, dislocation dissociation reactions, stacking fault energy [92]. In the case of BCC structures, almost all the models deal with the $\{112\}\langle 11\bar{1}\rangle$ twinning system, which is not the predominant twinning system in metastable β-Ti alloys. The first models for $\{332\}\langle 11\bar{3}\rangle$ twinning based on a pole dislocation mechanism were recently developed by Litvinov and Rusakov [80], and are described below.

4.2.2.2.2 Pole Dislocation Model for $\{332\}\langle 113\rangle$ Twinning

Litvinov and Rusakov [80] extend the theory of twinning by pole dislocations to the $\{332\}\langle 113\rangle$ system by considering the glide of $\frac{5a}{22}\left[\bar{1}\,\bar{1}\,3\right]$ twinning dislocations, which is schematically illustrated in Figure 4.61. In this case, the twinning shear is five times larger than that of $\{112\}\langle 111\rangle$ twinning. A shear of such magnitude is possible due to a large energy gain, i.e. a large degree of deformation, at the expense of the work done by the operative stresses.

The twinning partial dislocations are considered to arise out of a dissociation of the unit lattice dislocations by the reactions:

$$\frac{a}{2}\left[1\,\bar{1}\,1\right]\rightarrow\frac{5a}{22}\left[\bar{1}\,\bar{1}\,3\right]+\frac{a}{11}\left[8\bar{3}\bar{2}\right]$$

or

$$\frac{a}{2}\left[\bar{1}\,11\right]\rightarrow\frac{5a}{22}\left[\bar{1}\,\bar{1}\,3\right]+\frac{a}{11}\left[\bar{3}8\bar{2}\right]$$

Note that there is an energy gain associated with the above dislocation dissociation reactions, which must be supplied by the external stress. The gliding of the first $\frac{5a}{22}\left[\bar{1}\,\bar{1}\,3\right]$ dislocation will cause the formation of a stacking fault with significant atomic overlap due to the small (332) interplanar spacing, as shown in Figure 4.61(a). It is suggested that the degree of overlap at the twin-matrix interface may be relieved by a relative shear of the matrix and twinned lattices at an angle to the shear plane.

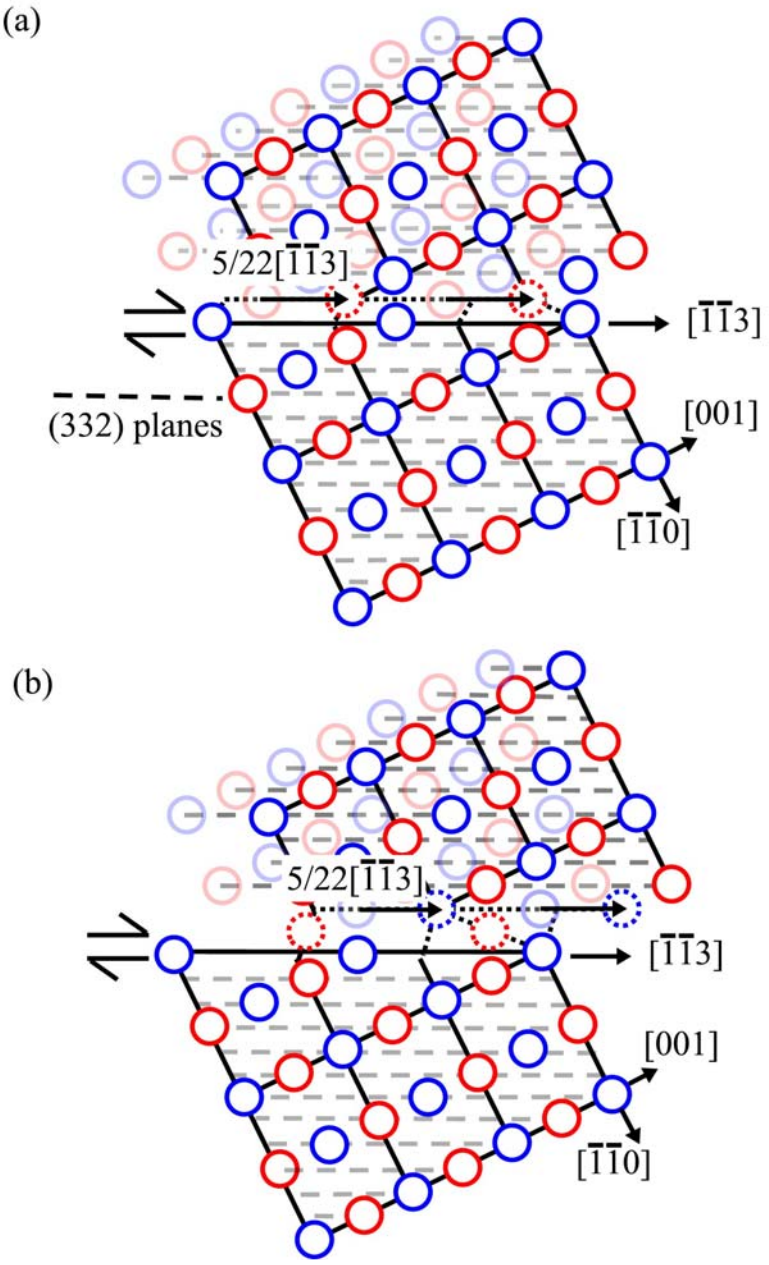

Figure 4.61: $\{332\}\langle 113\rangle$ **twinning by the dislocation mechanism of Litvinov and Rusakov [80]. (a) Stacking fault formed by the glide of the** $\frac{5a}{22}\left[\bar{1}\,\bar{1}\,3\right]$ **partial dislocation on the first {332} plane. (b) Glide of the** $\frac{5a}{22}\left[\bar{1}\,\bar{1}\,3\right]$ **dislocation on the second {332} plane. Twinning will proceed by the sequential glide of this dislocation on subsequent {332} planes.**

Litvinov and Rusakov [80] propose an alternative dislocation twinning mechanism based on the motion of $\frac{a}{22}[11\bar{3}]$ dislocations in the opposite direction of the dislocations described above. The twin growth occurs by the sequential glide of these dislocations of neighboring (332) planes concurrent with a shuffle of the atoms in these planes by $\pm\frac{a}{22}[332]$. This is illustrated in Figure 4.62. Motion of the dislocations without the shuffle would merely rearrange the cubic lattice to a monoclinic one. Thus, the dislocations may be referred to as zonal dislocations. This twinning shear is one-fifth of that given by $\frac{5a}{22}[\bar{1}\,\bar{1}\,3]$ dislocations. This twinning dislocation will arise out of the splitting of a unit lattice dislocation according to the reaction:

$$\frac{a}{2}[11\bar{1}] \rightarrow \frac{a}{11}[55\bar{4}] + \frac{a}{22}[11\bar{3}]$$

The movement of the first $\frac{a}{22}[11\bar{3}]$ twinning dislocation leads to the formation of a stacking fault with smaller overlap than that given by glide of $\frac{5a}{22}[\bar{1}\,\bar{1}\,3]$ dislocations, seen in Figure 4.62(a). The sessile partial dislocation $\frac{a}{11}[55\bar{4}]$ lies in the (332) plane and bounds the forming stacking fault. Though there is less atomic overlap, it is to be noted that the twin boundary is incoherent. While coherent twin-matrix boundaries fit well with the geometrical models for twin systems with a large interplanar spacing, i.e. $\{112\}\langle 111\rangle$ twins, the nature of the boundary is less well defined in $\{332\}\langle 113\rangle$ twins. In general, the crystal structures of the twin and matrix are related by a reflection in a plane

parallel to the boundary, but not coinciding with it. In order to reduce misfit energy, the "real" boundary can differ from the coherent one by a shear [93].

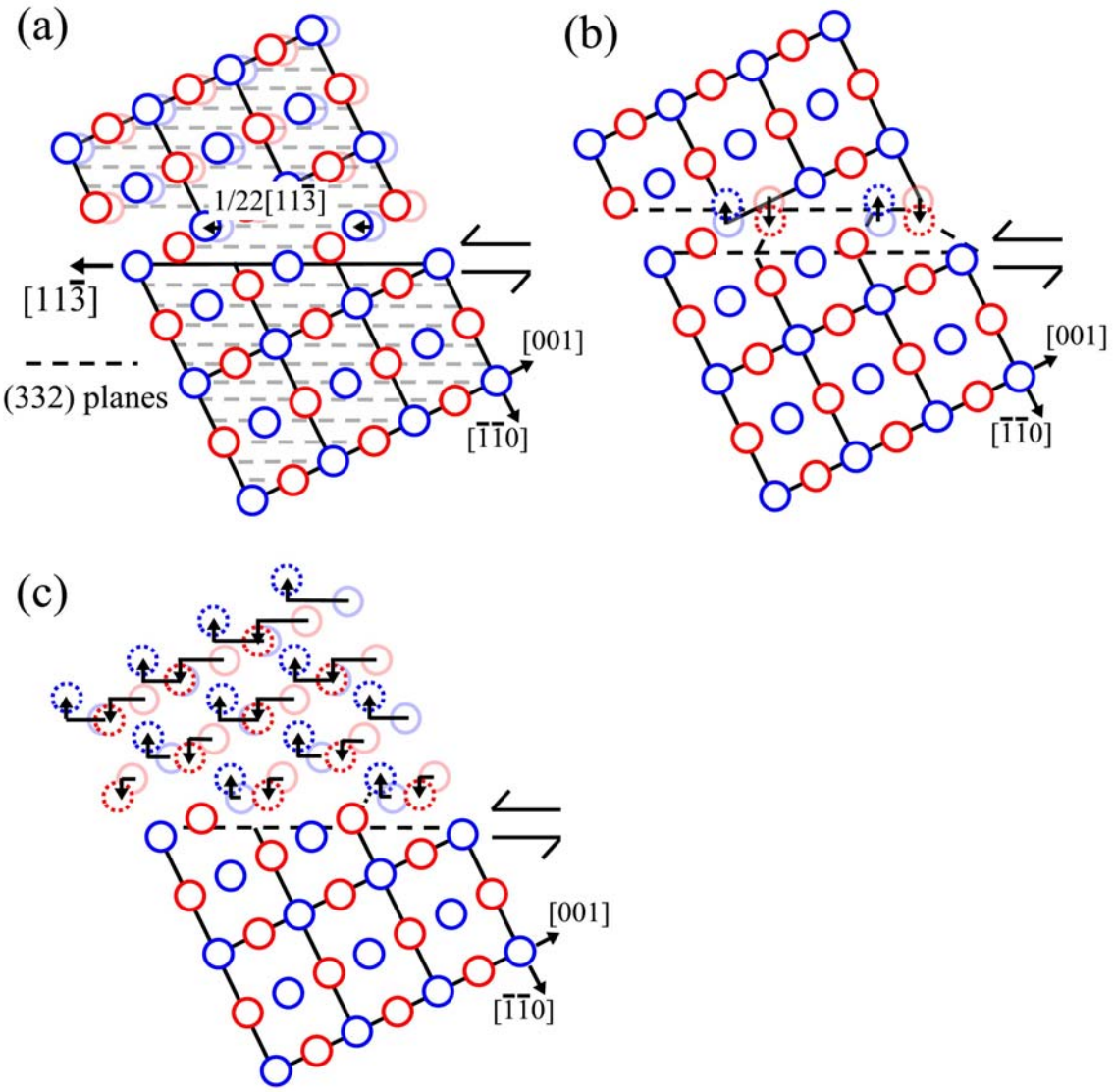

Figure 4.62: $\{332\}\langle 113\rangle$ twinning by the alternate dislocation mechanism of Litvinov and Rusakov [80]. (a) Glide of the $\frac{a}{22}[11\bar{3}]$ dislocation on the first {332} plane reorients the lattice and produces a stacking fault. (b) Arrows indicate shuffle of $\pm\frac{a}{22}[332]$ required to move atoms to twin position. (c) Scheme of glides and shuffles in the first several {332} planes.

As to whether the twin grows by $\frac{5a}{22}\left[\bar{1}\,\bar{1}\,3\right]$ dislocations or $\frac{a}{22}\left[11\bar{3}\right]$ dislocations, both mechanisms have advantages and disadvantages. In the case of $\frac{5a}{22}\left[\bar{1}\,\bar{1}\,3\right]$ dislocations, the large twinning shear would yield a significant amount of deformation at a small twin density. This large shear, however, would cause very high stresses at the twin tip. For the $\frac{a}{22}\left[11\bar{3}\right]$ dislocations, the Burgers vector is small, yet there is a necessary reshuffling which accompanies gliding.

4.2.2.3 Advantages and Disadvantages of the $\{332\}\langle 113\rangle$ Twinning Mechanisms

In the previous sections, two different twinning mechanisms were described which could be operative in β-Ti, the classical shear mechanism, and the partial twinning dislocation mechanism. It is beyond the scope of this investigation to definitively propose which is the preferred mechanism. This would involve an extensive TEM study to examine the nature of the twin-matrix interface, growing twin embryos, and dislocation arrays in the material. However, there is enough information to comment on the relative advantages and disadvantages.

The first issue that must be addressed is the speed of the growing twin. It has been well established that twins can grow at the speed of sound in bulk, polycrystalline materials. Twinning dislocations, however, move at speeds that are much lower than the speed of sound [52]. Thus, the question arises as to whether dislocations could be responsible for the high-speed twin growth in these materials. In the case of single crystalline Si, the velocity of twin growth accomplished by means of partial twinning

dislocations is on the order of 1mm/hour or less [84]. While the $\{332\}\langle 113\rangle$ twins grow very slowly during ambient temperature creep of β-Ti-14.8V, if the twinning mechanism is the same as that of rapid twinning at higher stresses, it is questionable whether twinning by dislocations could be possible given that the dislocations cannot move that quickly. This would seem to favor the classical mechanism, but recall that this mechanism requires large shuffles on planes with a small interplanar spacing, making this energetically difficult. Given the uncertainty regarding the twinning mechanism, in the following sections, both models will be used and as will be seen, provide similar results.

4.2.3 Effect of Interstitial Solute on Twinning in BCC Materials

As described in Section 2.3.2, time-dependent twinning has been identified as the predominant ambient temperature creep deformation mechanism in the coarse-grained β-Ti-14.8 V alloy. The SEM micrographs of Figures 2.8 and 2.9 were taken from an interrupt creep test of a coarse (350 μm) grain sized alloy [30]. The twin nucleates some time after the creep test starts, and slowly increases in thickness as the creep test proceeds. This behavior is unusual, in that twinning in alloys has long been expected to occur at speeds approaching that of the speed of sound. Also, as mentioned earlier, the presence of interstitial oxygen atoms has been shown to hinder $\{332\}\langle 113\rangle$ twin formation during the tensile deformation of β-Ti-V [76]. It was proposed that these interstitials interfere with lattice shearing and shuffling. Indeed, Christian and Mahajan [31] note that as the amount of interstitial solute in BCC metals and alloys increases the extent of twinning decreases and eventually is entirely terminated. Thus, the question

arises as to whether the presence of interstitial atoms, namely oxygen, could be responsible for time-dependent twinning in β-Ti alloys, as was the case for α-Ti alloys

The type of lattice site in which an interstitial atom will reside is based on the radii of the interstitial atom and that of host atom. The atomic radius of oxygen is 0.060 nm and that of titanium is 0.147 nm. This gives a ratio of:

$$\frac{0.060nm}{0.147nm} = 0.408$$

There are two possible types of interstitial sites in the BCC lattice, tetrahedral sites (bounded by four atoms) located at ¼, ½, 0-type positions and octahedral sites (bounded by six atoms) located at ½, 0, 0-type positions. In the BCC lattice, an interstitial-to-host atomic radius ratio of less than 0.291 is required for an interstitial to fit into a tetrahedral lattice site and less than 0.155 is required for an octahedral site. Given the ratio of 0.408, it would seem than an oxygen atom is too large to fit into either interstitial site. As is the case for carbon in BCC-iron, however, oxygen will reside in the octahedral interstitial sites of the β-titanium lattice [95]. The expansion of the lattice to accommodate the oxygen atom in a tetrahedral lattice site would require the displacement of four nearest-neighbor atoms, whereas only two must be displaced for the oxygen atom to reside in an octahedral lattice site. The BCC lattice with octahedral interstitial sites was shown in Figure 3.13.

The first crystallographic model to describe twinning in BCC materials, including interstitial atoms, was presented by Magee, *et al* [96], for $\{112\}\langle 111\rangle$ type twinning (see Figure 2.12) in α-iron containing interstitial carbon in octahedral lattice sites. This model is illustrated in Figure 4.63. In the case of this twin, all of the host atoms, i.e. Fe or Ti,

would be sheared to the proper twinned lattice site with no subsequent shuffle required. However, Magee, *et al* [96], note that this shear carries 2/3 of the potential octahedral interstitial lattice sites, those not lying in the plane of the projection, to improper positions. Such lattice sites are referred to as unconserved. As such, the presence of carbon increases the stress necessary for twinning in α-iron. This is the basis of the model for time-dependent $\{332\}\langle 113\rangle$ twin growth during ambient temperature creep of β-titanium alloys, which is presented below.

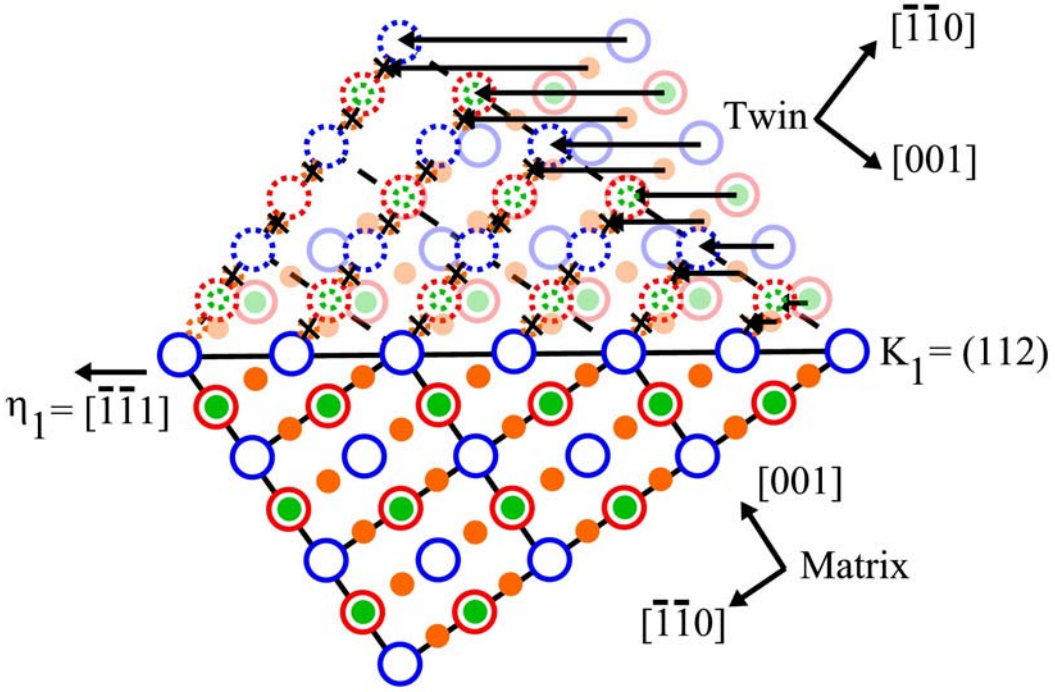

Figure 4.63: Crystallographic model for $\{112\}\langle 111\rangle$ twinning in the BCC lattice, after Magee, *et al* [96]. Twinning shear carries all of the host atoms (i.e. Ti) to the correct twin position. Only 1/3 of the octahedral interstitial sites, those in the plane of the projection (green) are sheared to the correct twinned position, or conserved. The other 2/3 of the octahedral sites, those not in the plane of the projection (orange), are sheared to incorrect positions. These are unconserved.

4.2.4 Classical Model for $\{332\}\langle 113\rangle$ Twinning Including Octahedral Interstitial Lattice Sites

This model is based on that described in Figure 4.58, but now including octahedral interstitial sites. Begin by considering the BCC lattice, including octahedral interstitial lattice sites projected onto the $(1\bar{1}0)$ plane, as shown in Figure 4.64. Figure 4.64(a) indicates the twinning plane $\mathbf{K_1} = (33\bar{2})$, and the shear direction $\eta_1 = [113]$. Figure 4.64(b) illustrates the twinning shear of the lattice. Recall that only the Ti atoms in the plane of the projection (blue) have been sheared to the correct twin position such that they are symmetrical to an atom on the other side of the twin-matrix interface. The Ti atoms above and below the plane of projection (red), and the octahedral interstitial lattice sites do not lie in correct twinned positions.

Given that the Ti atoms are not sheared to a correct twin position, they must shuffle to the proper lattice site, as described earlier. The models given by Crocker [82] and Richman [83] did not consider the fate of octahedral interstitial atoms. As the Ti atoms above and below the plane of the projection shuffle to their correct twin position, as seen in Figure 4.64(c), the lattice will be distorted and the octahedral interstitial lattice site in which the oxygen atom would reside will be destroyed. Any oxygen atom residing in such a site would impede the motion of the Ti atom to its correct twinned position. Such interstitial lattice sites are called unconserved. Thus, an oxygen atom would need to diffuse away from the advancing twin front to an undisturbed part of the lattice until new octahedral interstitial lattice sites are formed in the proper twin lattice shown in Figure 4.11(d). Note also that the Ti atoms adjacent to the twin-matrix interface are likely in

such close proximity that there will be no room for an oxygen atom to reside in an octahedral interstitial site in this region due to lattice distortion.

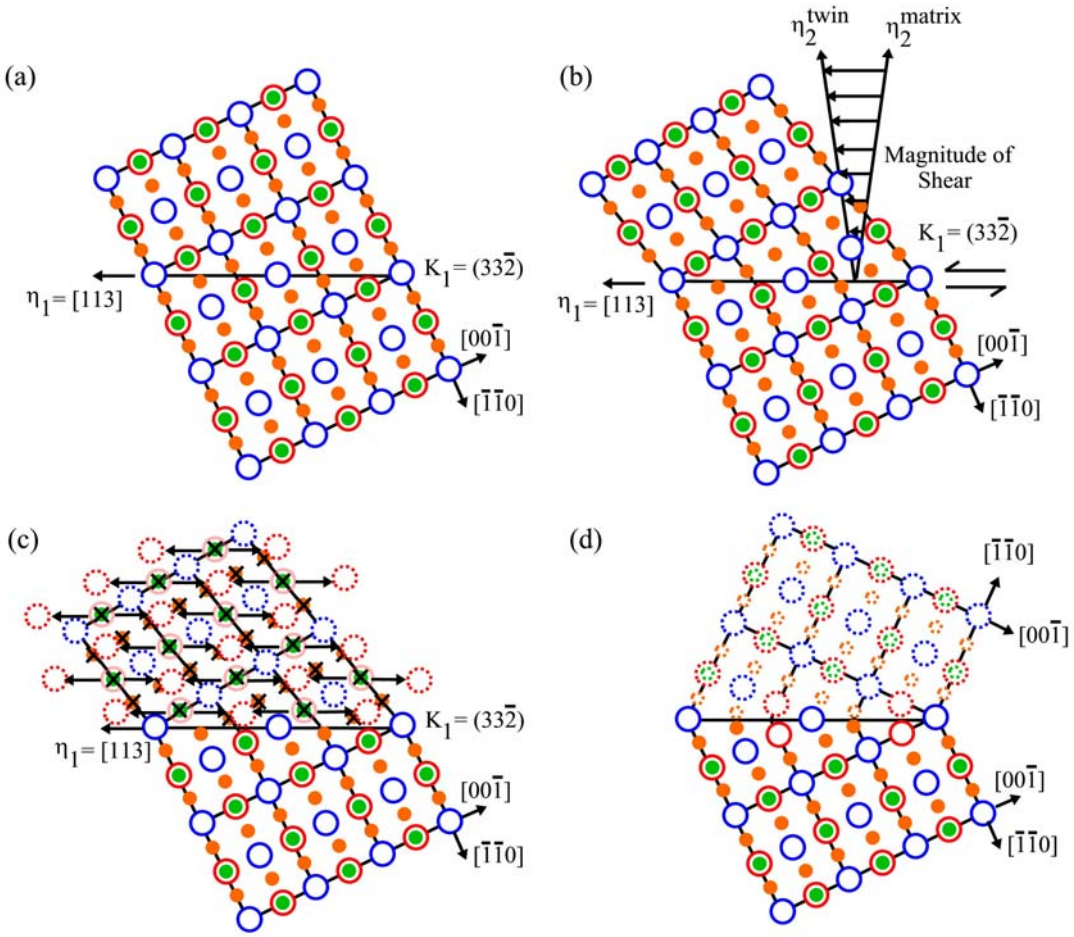

Figure 4.64: Crystallographic model for classical $\{332\}\langle 113\rangle$ twinning in the BCC lattice, including octahedral interstitial lattice sites. (a) Untwinned lattice with twinning plane, K_1 and shear direction η_1 indicated. (b) Shear of the lattice given by distance between η_2 direction in matrix and twin, respectively. (c) Arrows indicate shuffles required to move Ti atoms above and below plane of projection (red) to correct twinned site. Unconserved octahedral interstitial sites are marked with an 'X'. (d) Final twinned lattice with all atoms in correct twinned position.

4.2.5 Dislocation Models for $\{332\}\langle 113\rangle$ Twinning Including Octahedral Interstitial Sites

Consider now the case of $\{332\}\langle 113\rangle$ twinning caused by the glide of $\frac{5a}{22}[\bar{1}\,\bar{1}\,3]$ partial twinning dislocations. The model by Litvinov and Rusakov [80] which was previously discussed (illustrated in Figure 4.61) does not take into account the presence of interstitial atoms residing in octahedral lattice sites. Extending this model to include octahedral interstitial lattice sites as shown in Figure 4.65, however, reveals a similar pattern to that given by the classical shear model, namely the elimination of these lattice sites as the twin grows by each successive {332} plane. Figure 4.65(a) shows the stacking fault formed by the glide of the $\frac{5a}{22}[\bar{1}\,\bar{1}\,3]$ dislocation on the first (332) plane. Note that the octahedral interstitial lattice sites on the nearest {332} planes on either side of the twin-matrix interface are not conserved due to the close proximity of the Ti-atoms on these respective planes. Octahedral interstitial sites continue to be eliminated as subsequent {332} planes move to the twin position, as illustrated in Figure 4.65(b).

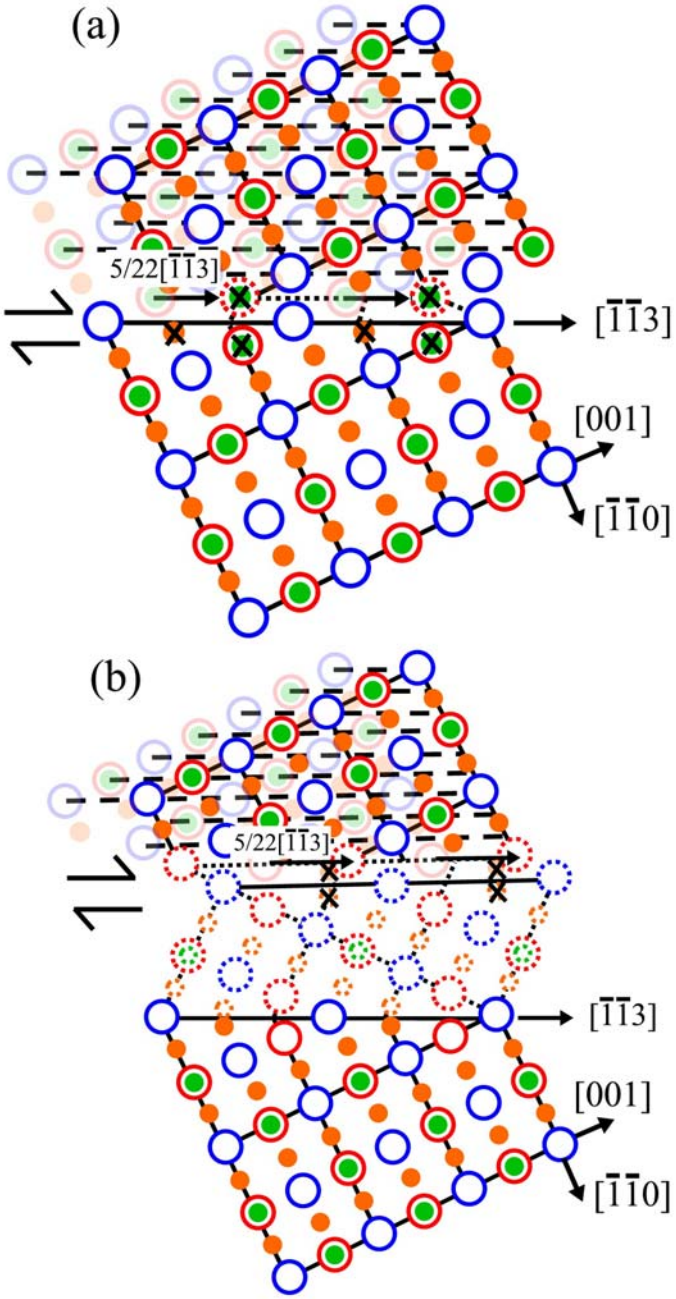

Figure 4.65: Crystallographic model for $\{332\}\langle 113\rangle$ twinning by the $\frac{5a}{22}[\bar{1}\,\bar{1}\,3]$ dislocation mechanism including octahedral interstitial sites, after Litvinov and Rusakov [80]. (a) Glide of $\frac{5a}{22}[\bar{1}\,\bar{1}\,3]$ dislocation on first {332} plane creates a stacking fault and eliminates the octahedral interstitial sites on either side of the twin-matrix interface, which are marked by an 'X'. (b) As dislocations glide on subsequent {332} planes to form the twin, octahedral interstitial sites continue to be eliminated.

For $\{332\}\langle 11\bar{3}\rangle$ twinning generated by glide of $\frac{a}{22}[11\bar{3}]$ and the reshuffle of $\pm\frac{a}{22}[332]$ (see Figure 4.62), a similar pattern emerges, as schematically shown in Figure 4.66. As the stacking fault is created by the glide of the dislocation on the first {332} plane, the octahedral interstitial sites nearest the twin-matrix interface are eliminated because of lattice distortion, seen in Figure 4.66(a). More interstitial sites are eliminated by the subsequent shuffle of $\pm\frac{a}{22}[332]$, as seen in Figure 4.66(b). Figure 4.66(c) illustrates that these sites will continue to be eliminated as the twin front advances by each {332} plane.

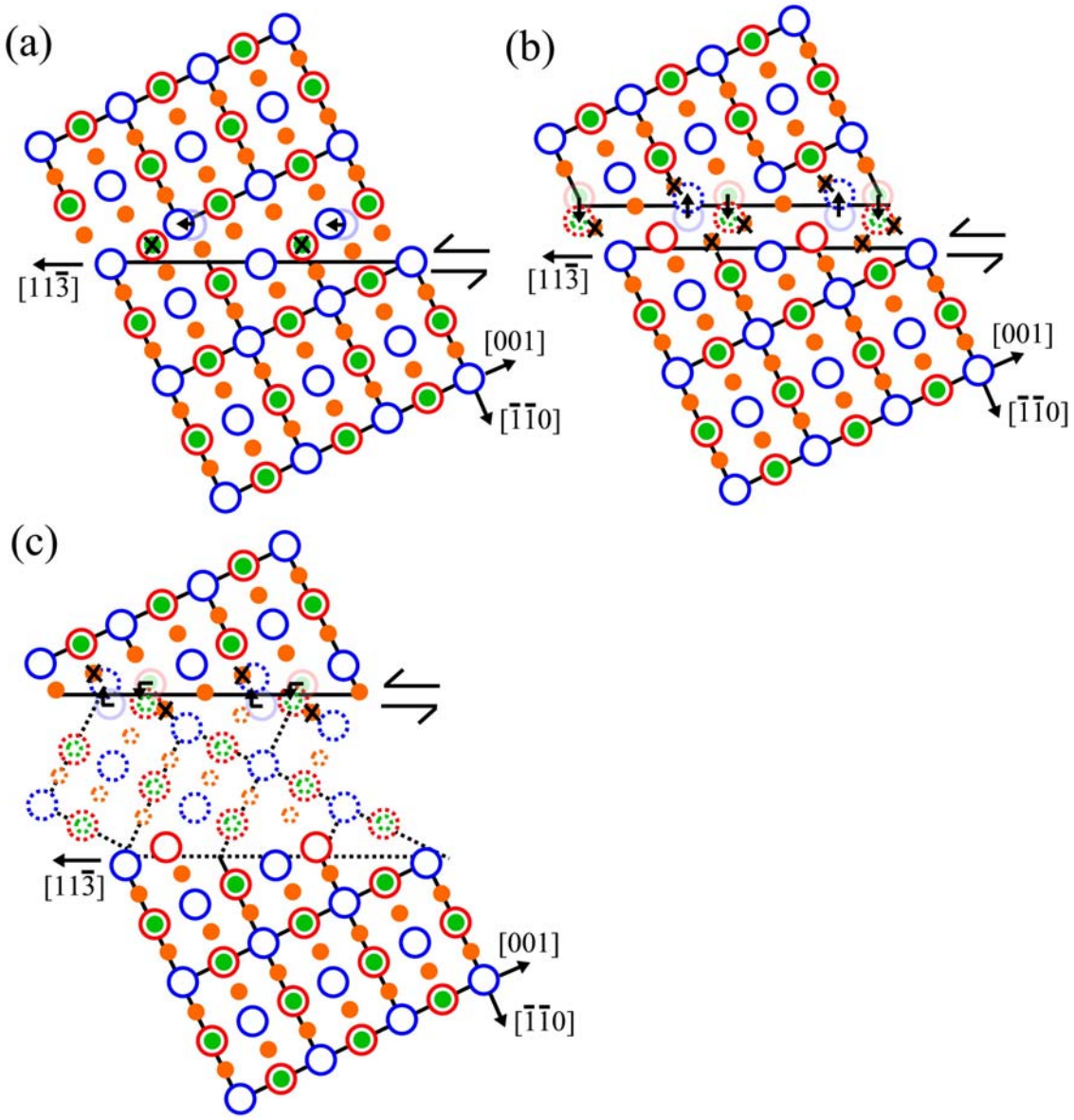

Figure 4.66: Crystallographic model for $\{332\}\langle 113\rangle$ twinning by the $\frac{a}{22}[11\bar{3}]$ dislocation mechanism including octahedral interstitial sites, after Litvinov and Rusakov [80]. (a) Glide of $\frac{a}{22}[11\bar{3}]$ dislocation on first {332} plane creates a stacking fault and eliminates the octahedral interstitial sites closest to the twin-matrix interface, which are marked by an 'X'. (b) Shuffle of $\pm\frac{a}{22}[332]$ eliminates more interstitial sites. (c) As dislocations glide on subsequent {332} planes to form the twin, octahedral interstitial sites continue to be eliminated.

4.2.6 Activation Energy for Time-Dependent Twin Growth in Beta-Titanium Alloys

The models of time-dependent $\{332\}\langle 113\rangle$ twin growth in β-Ti proposed above suggest that as is the case for α-Ti twinning is rate-limited by the diffusion of oxygen away from eliminated octahedral interstitial sites at the twin-matrix interface. Thus, the activation for twinning based on the model should be similar to the experimentally measured activation energy for diffusion of oxygen in β-titanium. Moreover, if the experimentally measured activation energy for ambient temperature creep of β-titanium in the strain region where twinning is the predominant deformation mechanism is close to these values, it is likely that the amount of creep strain is controlled by the rate of twin growth which is in turn controlled by the diffusion of oxygen in the material.

Measurements taken from the SEM micrographs such as those in Figures 2.8 and 2.9 [28, 30] show that the distance from the center plane of the twin to the twin-matrix increases by approximately 1.75 μm in a time period of 1.62 hr. Consider now the nature of the advancing twin front. Whether by classical shear and shuffles or by glide of partial twinning dislocations, the twin grows as {332} planes of Ti atoms sequentially move in a <113> direction from the untwinned to the twinned position. The interplanar spacing of the {332} planes is approximately 0.73 Å. Based on the models, as each {332} plane of Ti atoms moves to the twinned position, are any oxygen atoms residing in the interstitial sites in the vicinity of this plane must diffuse to a conserved interstitial site in the lattice due to lattice distortion.

As was the case for α-Ti, the advancing twin front accompanied by diffusion of oxygen atoms can be related to the diffusion of a species from the surface into the bulk of a sample. The effective penetration distance, x_{eff}, was given by Equation 4-17 [69]:

$$x_{eff} = \sqrt{Dt} \tag{4-17}$$

Where D is the diffusion constant and t is the time. Using this equation, a value for D is calculated given that the twin grows by a distance of 1.75 μm (x_{eff}) in a time period of 1.62 hr (t). Solving the equation for D, $D = 5.25\text{x}10^{-16}$ m^2/sec.

Interstitial diffusion in alloys is governed by an equation of the type that was given in Equation 4-18 [68]:

$$D = D_o * \exp\left(\frac{-Q}{RT}\right) \tag{4-18}$$

where D is the diffusivity, D_o is the pre-exponential diffusion constant, Q is the activation energy for diffusion, T is the temperature, and R is a constant. The value for the diffusivity of oxygen in β-Ti has been calculated in many investigations over the years, and is reviewed by Liu and Welsch [70]. A value for D_o is taken from an experiment where the oxygen concentration is close to that of the Ti-14.8 V alloy used as the basis for this investigation, namely 0.09 wt.% (approximately 1 of every 222 octahedral interstitial sites is occupied). The best match comes from Claisse and Koenig [97] where D_o is 0.083 m^2/sec. Now, solving for Q using Equation 4-18, when $D = 5.25\text{x}10^{-16}$ m^2/sec, $D_o = 0.083$ m^2/sec, and T = 298 K, gives $Q = 81.5$ KJ/mol. This calculated value is close to the measured activation energy for the diffusion of oxygen in β-Ti given by Liu and Welsch in the range of 98-155 KJ/mol. Thus, it seems likely that time-dependent twin growth in the β-titanium alloys may be attributed to the diffusion of oxygen from unconserved octahedral interstitial sites. Further confirmation of the validity of this model comes from the experimental work of Hudson and Ankem [35]. They have measured the activation energy for creep deformation of the β-Ti-14.8V alloy which was

the basis for this model. The activation energy varies from 39 KJ/mol at low strains to 112 KJ/mol at high strains, as seen in Figure 4.67. Time-dependent twinning has been shown to be the predominant deformation mechanism at the later stages of creep. Thus, the value of 112 KJ/mol corresponds to the strain region where twinning is the predominant deformation mechanism. This value is close to the theoretical activation energy for time-dependent twinning based on the model given above, and the experimentally measured activation energy for the diffusion of oxygen in β-titanium. Thus, it is reasonable to conclude that in the strain region where time-dependent twinning is the predominant, the amount of creep strain is controlled by the rate of twin growth which is in turn controlled by the diffusion of oxygen away from unconserved octahedral interstitial sites. This behavior is similar to that described for the HCP α-Ti alloys in the previous part of the chapter. This suggests that the model is applicable for a range of materials and crystal structures.

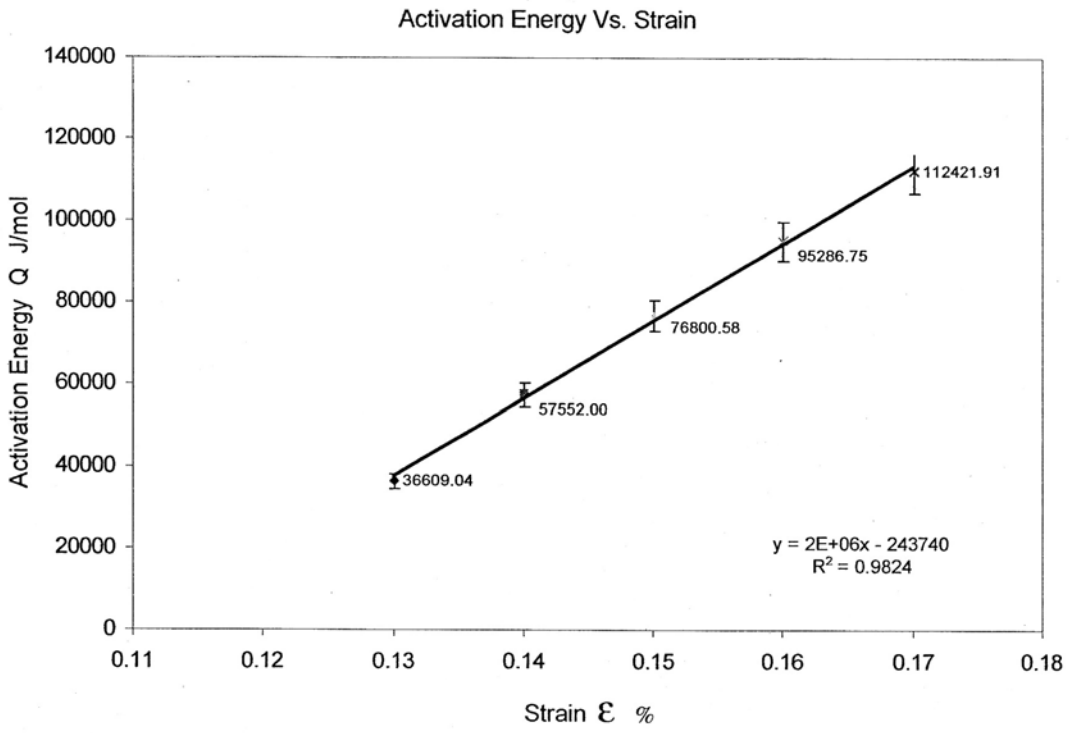

Figure 4.67: Activation energy as a function of creep strain for β-Ti-14.8V, as determined by Hudson and Ankem [35].

4.3 Summary

The first part of this chapter described an experimental investigation of the low temperature creep deformation mechanisms of α-titanium alloys, using α-Ti-1.6V as the model system. The first part of the investigation involved calculating the activation energy for creep of the α-Ti-1.6V alloy. In previous investigations, it was shown that α-Ti alloys can deform by slip and time-dependent twinning [23, 26]. Creep tests were performed at 95% YS at four temperatures, 338 K, 358 K, 378 K, and 478 K, and data was used from an earlier investigation where the alloy was creep tested at 298 K [26]. Optical and SEM micrographs of the same areas before and after creep testing indicate

that slip and twinning are creep deformation mechanisms for this alloy across the temperature range of this investigation. It was found that the creep strain rate increases as the test temperature increase. From the creep test data, the activation energy can be calculated using the equation:

$$Q(\varepsilon) = -R\left[\frac{\Delta \ln \dot{\varepsilon}(\varepsilon)}{\Delta(1/T)}\right]_{const.\sigma} \quad (4\text{-}4)$$

The activation energy for creep deformation was found to increase from approximately 37 KJ/mol at strains less than 2% to approximately 47 KJ/mol at strains greater than 4%. Previous investigators [38-41] have measured the activation energy for low temperature creep of α-Ti alloys which deform solely by slip to be in the range of 30-50 KJ/mol. This is the first time that the activation energy has been measured for creep of an α-Ti alloy that deforms by twinning. The change in activation energy as the creep strain increases, along with micrographs from interrupt creep tests [23, 26, 37], suggests that the deformation mechanism changes from slip at low strains to slip + twinning at higher strains.

A model was described to explain the change in deformation mechanism from slip to twinning as creep proceeds. The initial effect of the applied load is to initiate slip on those grains which are favorably oriented for slip. The dislocations will pile up at grain boundaries as they lack sufficient energy to cross the boundary onto grains which are not favorably oriented for slip. The stress concentration caused by this dislocation pile up is, however, sufficient to nucleate a twin in the neighboring grain. From this point forward, the rate of creep strain will be controlled by the rate of twin growth. Twinning is favored in large-grain alloys compared with fine-grained alloys and there is a critical size below which twinning will not occur and the extent of creep strain will be limited.

TEM specimens were prepared from the creep tested alloy to characterize the creep deformation products and examine the defect interactions in the material. Dislocations in the untwinned matrix were identified as *a*-type dislocations with a Burgers vector of the type $\frac{1}{3}\langle 11\bar{2}0\rangle$. It was shown that dislocation pileups can be found adjacent to twins growing from grain boundaries, suggesting that such pileups can generate the stress necessary for twin nucleation and growth. Twins of the types $\{1\,\bar{1}\,02\}$ and $\{1\,\bar{1}\,01\}$were identified by selected area diffraction, with $\{1\,\bar{1}\,02\}$ type twins being most common. *a* and *c*-type dislocations can aid in reducing the energy of the twin-matrix interface in the region of the twin tips. *c*-type dislocations with a Burgers vector of the type [0001] were identified inside the twins. The presence of these dislocations was explained by a model for twin growth by the sideways motion of semicoherent boundary ledges. Also identified inside the twins were unusual stacking faults that result from the atomic movements associated with twinning.

The second part of this chapter presented a theoretical model for the phenomenon of time-dependent twinning during low temperature creep of α-Ti alloys. This phenomenon is unusual because in bulk, polycrystalline metals, twins are expected to grow at the speed of sound. One aspect of twinning in HCP materials that was addressed was the concept of a shuffle. In the HCP lattice, a homogeneous shear, proportional to the distance from the twin-matrix interface, cannot move all of the atoms from the untwinned to the twinned position. As such, an additional translation, called a shuffle, is necessary. Early attempts to model the shears and shuffles associated with $\{1\,\bar{1}\,02\}$

twinning were presented, but such models were focused on the region close to the twin-matrix interface and failed to consider the macroscopic implications.

An alternative model for twinning in HCP materials was developed by Song and Gray [52] and is based on a Coincident Site Lattice (CSL) analysis. According to this model, in order to minimize interfacial energy, twin growth occurs by the stepwise jumping of the twin-matrix boundary between match planes for the untwinned and twinned lattice. All the atoms between the match planes move in a coordinated manner during twinning. Half the atoms, those residing in **A**-type sites are homogeneously sheared to the correct twinned position. The other half of the atoms, those residing in **B**-type sites must move by an additional shuffle to one of two crystallographically equivalent sites in the twin. This is the origin of the stacking faults observed in the TEM portion of the investigation.

Given the complicated, coordinated movements required for twinning in the HCP lattice of α-Ti, it is expected that interstitial atoms, particularly oxygen, will make twinning more difficult in these alloy, and this has been experimentally observed. Ankem, *et al* [23] were the first to recognize that the presence of interstitial oxygen could be responsible for the slow growth of deformation twins. The twinning model of Song and Gray [52] was modified to show the location of octahedral interstitial sites where atoms such as oxygen can reside. It was shown that the volume in which these interstitial atoms are located will be eliminated by the reorientation of the lattice during twinning. Any interstitial atom in such a site would impede twinning and must diffuse to an undisturbed part of the lattice before twinning can proceed. As such, twinning is rate-limited by the diffusion of oxygen atoms away from the advancing twinning front.

Given that the twin growth rate is controlled by the diffusion of oxygen, the activation energy for twinning based on the model should correspond with the experimentally measured activation energy for diffusion of oxygen in α-Ti, as well as the experimentally measured activation energy for creep of α-Ti in the strain region where twinning is a predominant deformation mechanism. For the purposes of the model, the advancing twinning front is analogous to the penetration of a species into a bulk material from the surface, i.e. C into Fe. Measurements of the twin growth rate were taken from micrographs from interrupt creep tests. Using this model, the activation energy for time-dependent twinning was calculated as 68.5 KJ/mol, close to the experimentally measured activation energy for the diffusion of oxygen in α-Ti, which is in the range of 68-200 KJ/mol [70]. Moreover, these values are close to the experimentally measured activation energy for low temperature creep of α-Ti in the strain region where twinning is seen to be common. In the first part of this chapter, the value was measured as approximately 47 KJ/mol. Given the fact that the rate of twin growth and hence, creep strain is controlled by the diffusion of oxygen away from eliminated interstitial sites, a small variation in the amount of interstitial impurity can have a significant effect on the extent of creep strain and structural reliability.

In the third part of this chapter, the crystallographic model for twinning in HCP materials is extended to the BCC lattice of β-titanium alloys. Deformation twins have been observed in a number of BCC alloys, including β-titanium alloys. In particular, time-dependent $\{332\}\langle 113\rangle$ type twins have been observed during the ambient temperature creep deformation of coarse-grained β-Ti-14.8wt.%V.

Two different twinning mechanisms are described in this section, the classical shear mechanism, and dislocation twinning mechanisms. The classical shear mechanism considers the atoms largely on the basis of their initial and final position. The twinning shear for $\{332\}\langle 113\rangle$ twinning will shear only half of the titanium atoms to their proper twin positions. The rest of the atoms will require an additional large shuffle to reach the twin position. As such, Litvinov and Rusakov [80] suggest an alternative twinning mechanism where by the twin grows by the glide of partial twinning dislocations on a stack of {332} planes.

Whether the twin grows by direct shear or by partial dislocations, it is to be noted that octahedral interstitial sites in the BCC lattice are eliminated by the reorientation of the lattice as the Ti atoms move from the untwinned to the twinned position. Furthermore, it has been observed in BCC alloys that the presence of interstitial atoms, particularly oxygen, hinders twin growth. Thus, a model for time-dependent twinning is presented which suggests that this phenomenon is due to the presence of oxygen impurities in the octahedral interstitial sites of the β titanium alloy. As the twin grows, lattice distortion will eliminate octahedral interstitial sites where oxygen impurities can reside. Twin growth is rate limited by the speed at which the oxygen atoms can diffuse to acceptable sites in the lattice. The calculated activation energy for twin growth based on this model, 81.5 KJ/mol, is close to the measured activation energy for oxygen diffusion in β-titanium, 98-155 KJ/mol [70], and to the measured activation energy for creep deformation of the β-Ti-14.8V alloy during the strain region where twinning is the predominant deformation mechanism, 112 KJ/mol [35]. The model is similar to that

which describes time-dependent twinning in HCP α-Ti suggesting that the model is valid across a range of crystal structures where deformation twinning is seen.

Chapter 5

Conclusions

1. A systematic study shows that the extent of twinning and hence, creep deformation, is higher in coarse-grained alloys (>200 μm) than in fine-grained alloys based on a model for twin nucleation by the stress concentration from dislocation pileups. The critical stress for twin nucleation is very high in fine-grained alloys and it will be difficult to generate dislocation pileups of sufficient length to generate this required stress, thus explaining the experimental findings of previous investigators
2. A crystallographic model was developed, including octahedral interstitial sites, to determine the activation energy for twinning in BCC β-Ti alloys, thereby explaining the unusual phenomenon of time-dependent twinning in β-Ti alloys where twin growth rate is much lower than the speed of sound.
3. Furthermore, in regard to β-Ti alloys, the theoretical activation energy for twinning is compared with, and found to be close to the experimentally measured activation energy for the diffusion of interstitial oxygen in β-Ti and to the experimentally measured activation energy for low temperature creep of a β-Ti alloy in the strain region where twinning is the predominant deformation mechanism. This suggests that the twin growth rate and, in turn, the creep strain rate is controlled by the diffusion of interstitial oxygen.
4. A crystallographic model was developed to determine the activation energy for twinning of HCP α-Ti alloys, which is similar to the model for twinning in BCC

β-Ti alloys, thereby explaining the unusual phenomenon of time-dependent twinning in α-Ti alloys where twin growth rate is much lower than the speed of sound.

5. The activation energy for low temperature creep of an α-Ti alloy that deforms by twinning, namely α-Ti-1.6wt.%V, is experimentally measured. This is the first time that the activation energy for low temperature creep has been measured for an α-Ti alloy that deforms by twinning.
6. In regard to the α-Ti alloy, the theoretical activation energy for twinning is compared with, and found to be close to the experimentally measured activation energy for the diffusion of interstitial oxygen in α-Ti and to the experimentally measured activation energy for low temperature creep of a α-Ti alloy in the strain region where twinning is the predominant deformation mechanism. Similar to the case for β-Ti alloys, the twin growth rate and, in turn, the creep strain rate is controlled by the diffusion of interstitial oxygen.
7. A systematic TEM study of the creep deformed α-Ti-1.6wt.%V specimens shows the proximity of dislocation pileups and growing twins, as well as the interaction between dislocations and growing twins. These findings support the models for twin nucleation and growth presented in this investigation.

Chapter 6

Suggestions for Future Work

1. Creep testing of α-Ti alloys with different oxygen contents. In this study, the α-Ti alloy had an oxygen content of approximately 0.69wt.%. Creep testing at different oxygen contents would reveal the effect of oxygen content on the twin growth rate, and hence creep strain rate. It is likely that increasing the oxygen content will slow the rate of twin growth and limit the amount of creep, but will also make the alloy more brittle.
2. Creep testing of α-Ti alloys with different impurity elements. In the alloys in this investigation, oxygen is the only impurity element in significant concentration. Other impurity elements such as nitrogen may also reside in the octahedral interstitial sites and should also slow the twin growth rate.
3. Perform in situ SEM creep testing of a very small α-Ti specimen to continuously record the twin growth rate. For instance, a small cantilever beam could be made from the Ti alloy which would be fixed at one end. A strong magnet would be fixed to the other end of the beam which would be used to pull the beam down toward a second magnet to generate a constant stress. The twin growth could be recorded on video, which would give a more accurate measurement of the twin growth rate than interrupt creep testing.
4. Extend the duration of the creep tests to months or years. Long-term predictions (hundreds or thousands of years) of creep behavior are currently based on

extrapolations from tests that are measured in the hundreds of hours. A small change in the shape of the creep curve in the duration of the test can become extremely significant when extended far beyond the measured data points.

5. Examine the creep-fatigue interaction in α-Ti alloys that deform by time-dependent twinning. Creep-fatigue testing involves alternating a static load with a cyclic load. In α-Ti alloys that deform by slip, it has been found that a static load at peak stress significantly reduces the number of cycles to failure due to damage accumulation at peak stress. No such studies have been performed on alloys which deform by twinning, though twins can act as crack nucleation sites.
6. In β-Ti alloys, perform a systematic TEM study to identify and characterize the creep deformation products. At the present, it is unclear whether the twinning mechanism involves shear/shuffles, or twinning by partial dislocations. An examination of the interaction of dislocations and twins in creep deformed β-Ti, similar to that performed in this investigation for α-Ti may reveal evidence that would favor one mechanism over the other.
7. Measure the activation energy for low temperature creep of an α–β two-phase Ti alloy. The activation energy for creep of the single-phase α (α-Ti-1.6V) and β (β-Ti-14.8 V) alloys whose chemistry is equivalent to that of the respective phases of α–β Ti-8.1V has been measured, and it is not known how that of the two-phase alloy compares with that of the individual phases.
8. Perform interrupt creep testing of two-phase α–β Ti-8.1V to see if twins grow slowly in the two-phase alloy, and if so, how the twin growth rate compares to that of the component single-phase alloys.

Appendix A

Titanium Etch Solutions

A-etch is used to etch grain boundaries. Etching times of 10-20 seconds should be used. **Only a small amount of A-etch should be prepared at one time. Do not store A-etch or A-etch waste. DES should be called immediately for waste pickup.**

A-etch	
Chemical	**Amount**
Hydrofluoric Acid – HF 50%	2.5 mL
Nitric Acid – HNO_3	2.5 mL
Glycerine	5.0 mL

Kroll's reagent is an alternative to the A-etch to reveal grain boundaries. Etching times of up to 30 seconds should be used. Kroll's reagent should be stored in a sealed polyethylene bottle.

Kroll's Reagent	
Chemical	**Amount**
Hydrofluoric Acid – HF 50%	2 mL
Nitric Acid – HNO_3	10 mL
Distilled Water – H_2O	88 mL

R-etch is a color etchant which lightly stains the surface of the specimen to give increased contrast for optical and SEM microscopy. Etching times of 5-10 seconds should be used. R-etch should be stored in a sealed polyethylene bottle.

R-etch	
Chemical	**Amount**
Hydrofluoric Acid – HF 50%	25 mL
Benzalkonium Chloride	18.5 g
Glycerine	40 mL
Ethanol	35 mL

Dilute titanium etch is used prior to depositing gold fiducial grid lines in order to facilitate the removal of photoresist.

Dilute Ti Etch	
Chemical	**Amount**
Hydrofluoric Acid – HF 50%	2 mL
Nitric Acid – HNO_3	4 mL
Water	194 mL

Appendix B

Instructions for Applied Test Systems (ATS) Series 2330 Creep Tester

1. Raise weight pan so that there is no load on the specimen.
2. Disconnect water in, water out, gas in, and gas out lines from the retort assembly.
3. Disconnect leads from LVC.
4. Unlatch and open split tube furnace door.
5. Swing retort assembly out and away from the brackets which attach the assembly to the lever arm tester. The nuts that are on the ends of the upper and lower pull rods may need to be adjusted so that the retort assembly will come loose.
6. Unscrew upper and lower retort mounting brackets. Use caution as the retort is now only resting on the bracket and would be free to fall if bumped.
7. Lift retort assembly up and out of brackets and place it on its sides on a flat surface, i.e. a table or workbench. Be careful as the retort assembly is very heavy (~60 lbs.).
8. Remove clamp and O-ring on upper end cap. Unscrew and remove upper end cap and set it aside.
9. Unscrew and remove stainless steel tube connecting water cooling ports on lower end of retort assembly.
10. Unscrew and remove clamp connecting retort tube to accessory chamber.
11. CAREFULLY slide retort tube up and off the pull rod assembly using caution not to damage upper and lower heat shields.

12. The test specimen and extensometer assembly are now visible. To remove specimen, unscrew screws connecting specimen to the extensometer assembly.
13. Unscrew top and bottom of specimen from couplings which connects specimen to pull rods.
14. Replace with new test specimen and connect the specimen to the upper and lower couplings.
15. Reattach extensometer crossheads to test specimen. Make sure they are tight enough that they will not slip when the test begins. Check the travel of the extensometer for freedom of movement.
16. Use the zero adjusting screw to adjust position of extensometer gaging platforms. This may be easier if the cap opposite the LVC connections is removed.
17. When specimen is mounted, carefully slide the retort tube back over the pull rod assembly and clamp to lower accessory chamber.
18. Reattach stainless steel tube connecting water cooling ports on lower end of retort assembly.
19. Screw upper cap onto pull rod and seal with O-ring and clamp. The retort is now reassembled.
20. Carry assembled retort back to creep tester and carefully rest on mounting brackets making sure that the assembly is balanced.
21. Screw upper and lower retort mounting brackets back together so that the retort assembly is mounted securely.

22. Swing retort assembly back into the brackets which connect the assembly to the lever arm. Make sure that the nuts on the pull rods are rest securely on the brackets.
23. Reattach the water in, water out, gas in, and gas out lines to the retort assembly.
24. Reconnect the LVC leads.

Appendix C

Operating Instructions for Electroscan Environmental Scanning Electron Microscope (ESEM)

1. Loading Specimen

1.1. Enter VACUUM menu and select VENT CHAMBER

1.2. After about 30 seconds, open chamber and remove stage.

1.3. Mount specimen on stage with grid lines facing up.

1.4. Replace the stage slowly and close the chamber door.

1.5. Enter VACUUM menu and select WET. The compressor requires about 90 seconds to create the vacuum in the chamber.

2. Obtaining an Image

2.1. When the message bar reads WET MODE, enter GUN menu.

2.2. Select HEAT FILAMENT. The filament requires about 4 minutes to stabilize.

2.3. While the filament is heating, go to the STAGE menu and select CALIBRATE. The stage will automatically position itself to the default position.

2.4. When the stage stops moving, turn on the chamber light.

2.5. Use the z-control switch next to the joystick to move the sample surface approximately 5 mm from the probe.

2.6. Push the SET button on the microscope and turn the water pressure dial clockwise until the readout is about 2.2. Push the SET button again.

2.7. Click the ON button for the voltage at the bottom left of the monitor.

2.8. Slowly increase the voltage to 20 kV with the arrows.

2.9. By looking into the chamber through the chamber window, use the joystick to position the grid surface directly below the probe.

2.10. Reduce the magnification below 100x and turn up the contrast until a white circle appears on the monitor.

2.11. Increase the magnification to over 500x. Press the P.F. button on the console.

2.12. Adjust the three silver knobs on top of the microscope by turning them one at a time and maximizing the height of the green line on the brightness monitor above the camera.

2.13. Press the P.F. button again to turn it off. Press the SOURCE button and decrease the magnification below 100x.

2.14. Open the left door below the console and adjust the left GUN BIAS know so the white circle on the monitor is as bright as possible.

2.15. Close the door. Press the SOURCE button again to turn it off and increase the magnification to over 500x.

2.16. Press the P.F. button on the console. Adjust the three silver knobs on top of the microscope by turning them one at a time and maximizing the brightness of the image.

2.17. Press the P.F. button again to turn it off. Press the ALIGN button.

2.18. Using the waveform on the oscilloscope as a guide, adjust the two aperture knobs on the chamber column so the green line is horizontal.

2.19. Press the ALIGN button again and turn it off. Press the P.F. button.

2.20. Adjust the three silver knobs on top of the microscope by turning them one at a time and maximizing the brightness of the image.

2.21. Press the P.F. button to turn it off.

2.22. Simultaneously increase the contrast and decrease the brightness until the brightness cannot be decreased.

2.23. Decrease the contrast so that the bottom of the green line touches the black horizontal line in the center of the oscilloscope.

2.24. Focus the image and adjust the X and Y stigmators properly to obtain a clear image.

3. Taking Pictures

3.1. Enter RECORD menu and select exposure time of 30 seconds.

3.2. Open Image Pro Plus software.

3.3. Click on icon of video camera (RECORD LIVE) to enable image capturing. Screen will show a live view of the magnified image.

3.4. Press P.F. button and focus image. Press P.F. button again.

3.5. Press PHOTO button to obtain an image.

3.6. In Image Pro program, use sliders to obtain desired brightness and contrast.

3.7. Press SNAP to take picture.

3.8. Save image to ZIP disk as a TIF file.

4. Turning off Microscope

4.1. When microscopy is complete, enter GUN menu and select COOL FILAMENT.

4.2. Turn VOLTAGE to 0 kV and click the ON button to turn voltage off.

4.3. Enter VACUUM menu and click VENT CHAMBER.

4.4. Remove the sample from chamber and close chamber door.

4.5. Select WET from VACUUM menu.

4.6. When the WET mode is achieved, select STANDBY from the VACUUM menu.

4.7. Turn off chamber light.

4.8. Press SET button and turn water pressure to 0.0.

4.9. Press SET button again.

4.10. If last microscope user of the day, turn CONSOLE POWER off.

Appendix C

Procedures for TEM Sample Preparation by Jet-Polishing

1. Gather supplies needed including: methanol, hydrochloric acid, sulfuric acid, dry ice (available at Chemistry Building loading dock), graduated measuring cylinders, polyethylene pipettes, gloves, eye protection, lab coat.

2. Electropolisher and glassware are located in the fumehood in the Sample Preparation Laboratory. Thoroughly wash all glassware to be used during the procedure.

3. In the fumehood: in large, round Pyrex dish, place 120 mL methanol.

4. **SLOWLY** add 4 mL sulfuric acid to the Pyrex dish and stir to mix.

5. **SLOWLY** add 4 mL hydrochloric acid to the Pyrex dish and stir to mix.

6. Pour methanol into rectangular Styrofoam container to depth of approximately 0.75".

7. Place Pyrex dish with electropolish solution into Styrofoam container using caution not to let the methanol bath come over the sides of the dish into the electropolish solution.

8. With insulated glove on, add small pieces of dry ice to methanol bath until methanol is cool enough that ice is no longer rapidly melting and bubbling has mostly stopped.

9. Unscrew the face of the specimen holder and mount specimen. Screw face back on.

10. Place electropolisher into the Pyrex dish such that the pumps are submerged.

11. Place the specimen holder into the electropolisher such that the specimen is in the path of the jets.

12. Connect the wire which supplies the current to the top of the specimen holder with the alligator clip.

13. Turn POWER and POLISH switches on.

14. Turn SPEED dial to approximately 6.

15. Turn POLISH dial to maximum of 10 to begin process.

16. When electropolishing is complete, there will be a tiny hole in the center of the specimen. To examine specimen for hole, every 30 seconds, turn power off and remove specimen holder from electropolisher. Hold up to light and look for hole. If

there is no hole, replace the specimen holder in the electropolisher, turn power back on and continue. If there is a hole, continue to next step.

17. Rinse specimen holder in water.

18. Unscrew face from specimen holder and carefully remove polished specimen with tweezers. If there are more specimens, place next one in holder and repeat process from above. If this is the last specimen, continue to next step.

19. Dispose of electropolish solution into properly labeled waste container.

20. Place electropolisher into water and run water through jets to flush out any acid that may corrode components.

21. Turn SPEED and POLISH dials to 0.

22. Turn POWER switch off.

Appendix E

Instructions for LabVIEW Software

LabVIEW programs are called virtual instruments (VIs). A VI and its components are analogous to programs and subroutines from text programming languages such as C and FORTRAN. VIs have a user interface called the front panel and a source code which is represented graphically by the block diagram. The front panel allows the user to run the VI and view the outputs. The block diagram consists of executable icons, or nodes, which are connected (wired) together.

LabVIEW 7.1 Student Edition was used to acquire the data from the creep tests in this investigation. As described in Chapter 2, the creep strain is measured with a linear voltage capacitator. This means that the actual output from the creep tester is a voltage which changes as a function of the strain of the specimen. A voltage change of 10V from the starting point corresponds to a strain of 0.5 inches. The voltage data is input to the computer with a USB Data Acquisition Unit, and it is recorded with the LabVIEW program. Each creep test is divided into six intervals with different data acquisition rates and durations. A separate VI was written for each interval. A sample VI is shown below in Figure E.1. The VI entails the following components:

1. ***For* Loop**: The *For* Loop executes its subdiagram *n* times, where *n* is the value wired to the count (**N**) terminal. The iteration terminal provides the current loop iteration count, which ranges from 0 to $n - 1$.
2. **Merge Signals**: The Merge Signals node merges two or more signals into a single output, in this case, the iteration count and the test data.

3. **DAQ Assistant**: This is the interface with the Data Acquisition Unit, which is receiving voltage data from the creep tester. If there were additional inputs, for instance temperature, resistance, current, etc., they would be added here. The DAQ Assistant settings for this investigation are shown below in Figure E.2.
4. **Waveform Chart**: Plots the data in real-time on the VI front panel.
5. **Write LabVIEW Measurement File**: Writes data to a spreadsheet file. The file name for the data is specified here.
6. **Time Delay**: Establishes time interval between data acquisition (0.1 sec, 1 sec, 1 hour, etc.)

For the respective intervals of the creep test which require a certain duration and data acquisition rate, the only items to be changed are the **N**-value (number of data points), the time delay (acquisition rate), and the file name. When the creep test is started, the first VI is launched. The data can be monitored with the Waveform Graph on the Front Panel as seen in the Figure E.3 below.

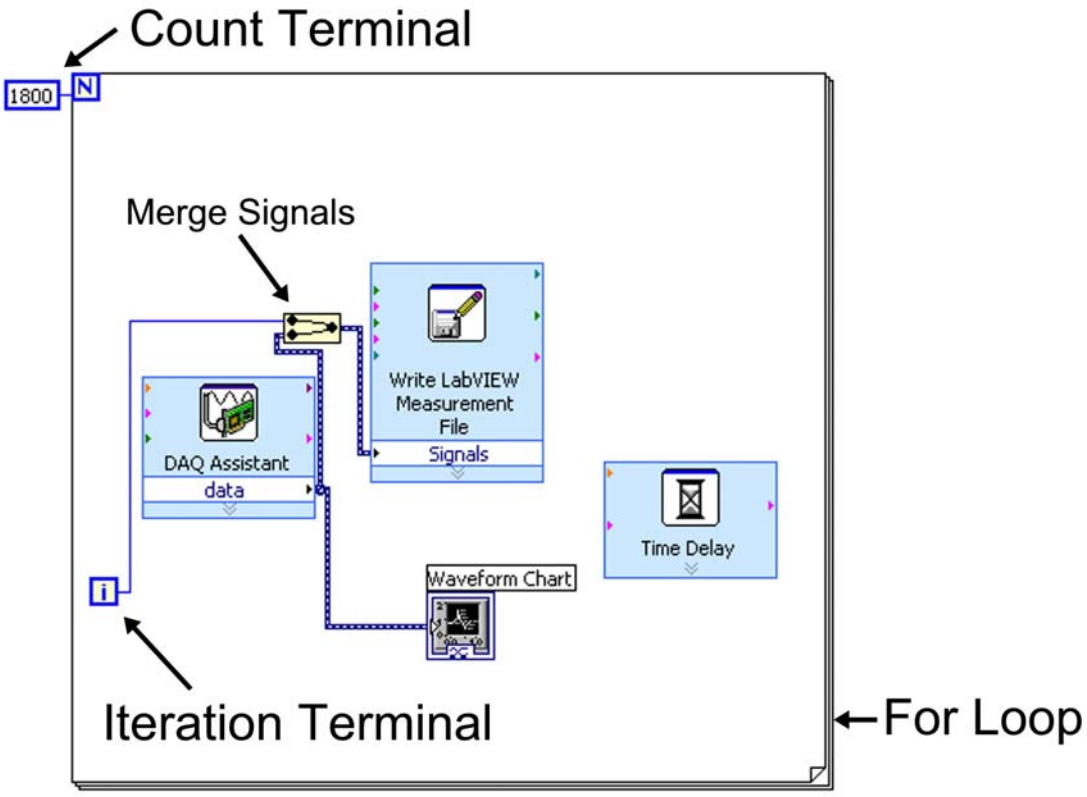

Figure E.4: LabVIEW Virtual Instrument (VI) block diagram for creep tests performed in this study.

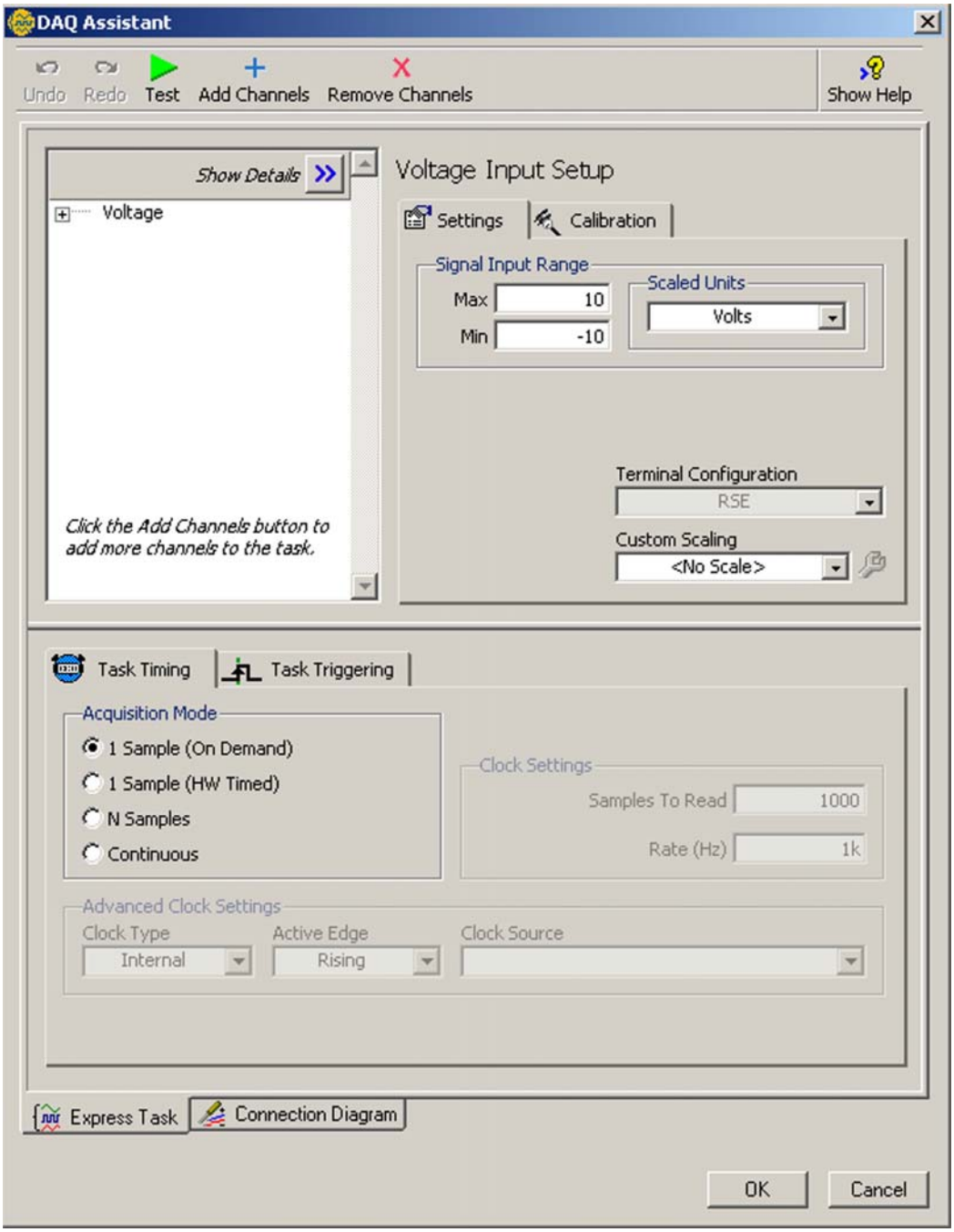

Figure E.5: Data Acquisition (DAQ) Assistant settings for this investigation.

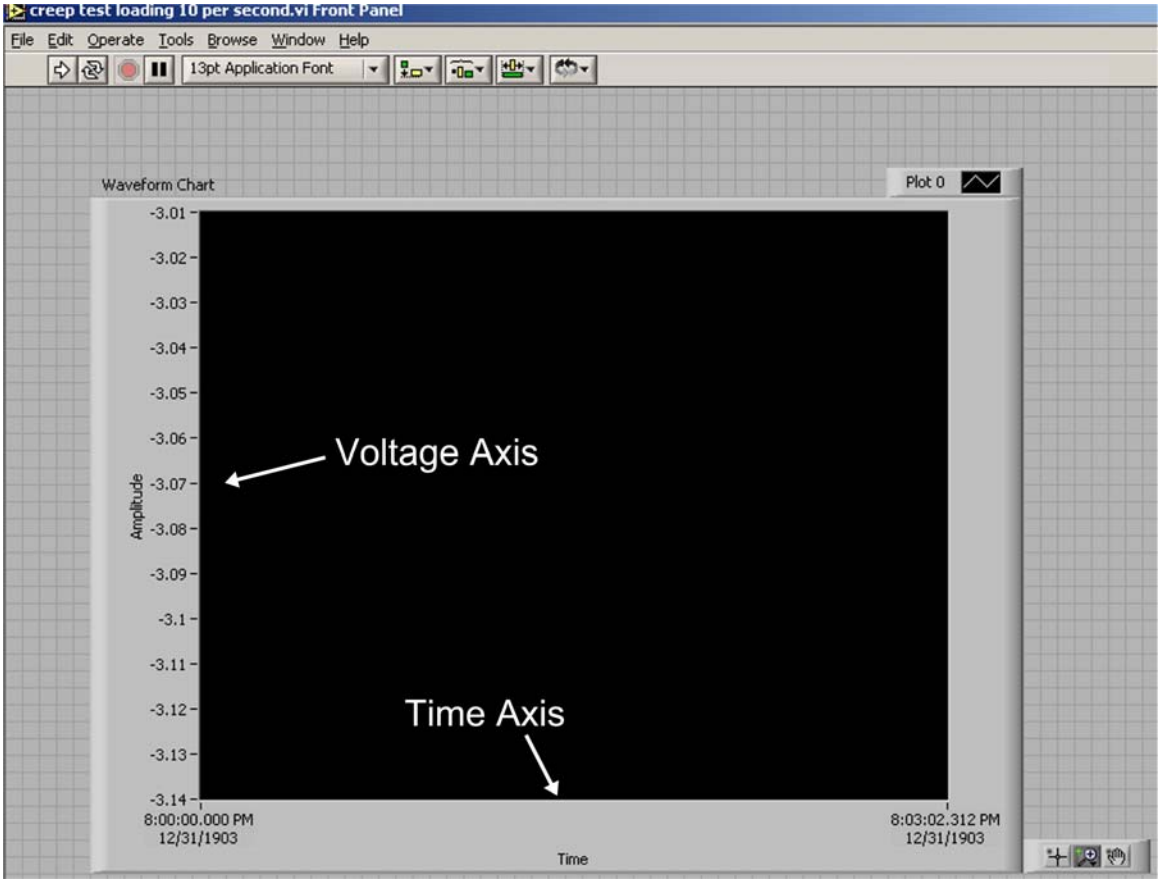

Figure E.3: Real-time voltage (strain) vs. time plot is shown on the front panel of the VI.

Appendix F

Operating Instructions for

JEOL 2100F Field Emission TEM

The following is a brief outline of the operating instructions for the JEOL 2100F Field Emission TEM. This instrument should NOT be operated without proper training and certification by NISP Laboratory management. This outline is not a substitute for the official TEM operating manual.

PRELIMINARY STEPS

1. Load specimen onto double tilt holder. Specimen retainer is held down by a small screw. Make sure specimen is secure and centered. Check O-rings on the holder for lint which may compromise the vacuum.
2. Fill cold-trap to the left of the column with liquid nitrogen.
3. Raise High-Voltage Control window on the computer. Under Auto HT & Emission, click on StartUp to begin accelerating voltage. The status bar will show the time until the accelerating voltage of 200 kV is reached.

INSERTING SPECIMEN HOLDER INTO COLUMN

4. Open Specimen Property window on computer. Select Double Tilt Holder from drop down menu. Click Apply.
5. Align the specimen holder guide pin with the guide groove on the microscope column. Push the holder into the goniometer until it stops and set the goniometer

PUMP/AIR switch to PUMP. The yellow light will turn on and the evacuation will begin. It will take about 10 minutes to pump down, until the green light on the goniometer goes on.

6. When the green light is on, turn the specimen holder clockwise and push the holder into the goniometer as far as it will go.
7. Turn holder fully clockwise and push in into the yellow light on the goniometer goes off.
8. Connect the cable from the end of the double tilt holder into the port above the specimen holder.

OBTAINING AN IMAGE

9. Press the BEAM VALVE button on the left side of the column to turn on the electron beam.
10. Press the LOW MAG button on the right side of the column and find the hole in the center of the specimen by using the sample translator trackball.
11. Turn BRIGHTNESS knob to increase or decrease the brightness of the beam and center beam using the SHIFT knobs.
12. Press STD FOCUS button to set the objective lens current to the reference value.
13. Microscope should now be aligned. The details of this procedure are too complex to include here. See operating manual for procedures.

TAKING A PICTURE

14. When ready to take a picture, press the PHOTO button on the right side of the column with the small screen placed in the electron beam path.
15. When the PHOTO button lights up, the film is at the photographing position. Press the PHOTO button again. The exposure time (when set to automatic exposure time) should be set using the small drop-down screen.

TURNING OFF THE MICROSCOPE

16. If specimen holder has been tilted, return tilt and azimuth to 0.
17. Decrease magnification to 5000x and press BEAM VALVE button to turn off the electron beam.
18. Go to Specimen Property window on the computer and click on Holder Exchange.
19. Specimen holder can now be removed from the column. Pull holder until it stops. Turn fully counterclockwise. Pull a little more. Turn fully counterclockwise again. Set PUMP/AIR switch to AIR and wait 30 seconds.
20. Remove holder from goniometer.
21. Raise High-Voltage Control window on the computer. Under Auto HT & Emission, click on Standby to decrease accelerating voltage.
22. Remove specimen from holder.

DEVELOPING MICROGRAPHS

23. Go to dark room and get empty film box and full film box from desiccator. Transport full film box in black bag and bring a second bag as well.

24. Turn off lights in microscope room. Open the door to the camera chamber by turning the handle clockwise until it stops. It will take about 5 minutes for the vacuum to be released and the door will pop open.
25. Slide magazine drawer out. Remove receiving magazine and place in film bag. Replace with an empty film box. Remove dispensing magazine and place in film bag. Replace with full film box.
26. Push magazine drawer back into chamber, close door, and turn handle counterclockwise.
27. Take film boxes back to dark room. Take negatives from receiving box one at a time and remove the negative from its frame. Place the negatives into the cradle being careful that they don't touch one another.
28. When all films are in cradle, place in developer and agitate. Developing should take about 1 minute or until numbers begin to appear at the scale bar. Be careful not to over or under develop the negatives.
29. After developing, rinse films in water for a couple minutes, then place cradle in fixer solution. The negatives must remain in the fixer for about 5-10 minutes.
30. While negatives are in fixer, refill the dispensing film box with new negatives. See the diagram in the dark-room for the correct way to place the pieces of film in the frames.
31. When dispensing film box is full, place it in the desiccator.
32. Remove negatives from fixer and rinse with water.
33. Place negatives in dryer for 30 minutes.

Appendix G

Diffraction Pattern Rotation Calibration for

JEOL 2100F Field Emission TEM

The image in a TEM rotates to various degrees depending on the magnification. In contrast, the diffraction pattern will remain at the same rotation regardless of which magnification or selected area aperture is used. In order to properly orient the diffraction pattern and the image, film recording selected area diffraction patterns must be rotated with respect to the image film. This calibration is essential for labeling crystallographic directions and identifying dislocation types. Below are the rotation angles of the diffraction pattern for common magnification settings on the JEOL 2100F Field Emission TEM. Rotation for magnifications between those measured can be extrapolated.

Magnification (x1000)	Rotation (^{o})
1	3 CCW
20	3 CCW
40	3 CCW
50	0
60	3 CW
80	2 CCW
100	2 CCW
≥ 120	28 CW

Note: There is no change in the rotation with a change in camera length.

References

1. F-22 Raptor Team Website – http://www.f22-raptor.com

2. B.W. Neuberger, C.A. Greene, G.D. Gute, "Creep Analyses of Titanium Drip Shield Subjected to Rockfall Static Loads in the Proposed Geologic Repository at Yucca Mountain," Mat. Res. Soc. Symp. Proc. **713**, JJ11.7.1 (2002).

3. E.W. Collings, *The Physical Metallurgy of Titanium Alloys*, Metals Park, OH, American Society for Metals, 1984.

4. P.J. Bania "Beta Titanium Alloys and Their Role in the Titanium Industry," in *Beta Titanium Alloys in the 1990's*, D. Eylon, R.R. Boyer, D.A. Koss, eds., TMS, Warrendale, PA, 1993, p. 3.

5. G.E. Dieter, *Mechanical Metallurgy – 3rd ed.*, McGraw-Hill, New York, 1986.

6. H. Adenstedt, "Creep of Titanium at Room Temperature," *Met. Prog.* **65**, 658 (1949).

7. W.R. Kiessel, M.J. Sinnot, "Creep Properties of Commercially Pure Titanium," *J. Met.* **5**, 331 (1953).

8. D.R. Luster, W.W. Wentz, D.W. Kaufmann, "Creep Properties of Titanium," *Mater. and Methods* **37**, 100 (1953).

9. A.J. Hatch, J.M. Partridge, R.G. Broadwell, "Room Temperature Creep and Fatigue Properties of Titanium Alloys," *J. Mater.* **2**, 111 (1967).

10. H.P. Chu, "Room Temperature Creep and Stress Relaxation of a Titanium Alloy," *J. Mater. JMLSA* **5**, 633 (1970).

11. W.H. Reimann, "Room Temperature Creep in Ti-6Al-4V," *J. Mater.* **6**, 926 (1971).

12. R.R. Zeyfang, R. Martin, H. Conrad, "Low Temperature Creep of Titanium," *Mater. Sci. Eng.* **8**, 134 (1971).

13. A.W. Thompson, B.C. Odegard, "The Influence of Microstructure on Low Temperature Creep of Ti-5Al-2.5Sn," *Metall. Trans.* **4**, 899 (1973).

14. B.C. Odegard, A.W. Thompson, "Low Temperature Creep of Ti-6Al-4V," *Metall. Trans.* **5**, 1207 (1974).

15. M.A. Imam, C.M. Gilmore, "Room Temperature Creep of Ti-6Al-4V," *Metall. Trans. A* **10A**, 419 (1979).

16. W.H. Miller, Jr., R.T. Chen, E.A. Starke, "Microstructure, Creep, and Tensile Deformation in Ti-6Al-2Nb-1Ta-0.8Mo," *Metall. Trans. A* **18A**, 1451 (1987).

17. G.Y. Gao, S.C. Dexter, "Effect of Hydrogen on Creep Behavior of Ti-6Al-4V Alloy at Room Temperature," *Metall. Trans. A* **18A**, 1125 (1987).

18. T. Neeraj, D.-H. Hou, G.S. Daehn, M.J. Mills, "Phenomenological and Microstructural Analysis of Room Temperature Creep in Titanium Alloys," *Acta Mater.* **48**, 1225 (2000).

19. T. Neeraj, M.J. Mills, "Short-Range Order (SRO) and its Effect on the Primary Creep Behavior of a Ti-6wt.%Al Alloy," *Mater. Sci. Eng. A* **319-321**, 415 (2001).

20. M.F. Savage, T. Neeraj, M.J. Mills, "Observations of Room-Temperature Creep Recovery in Titanium Alloys," *Metall. and Mater. Trans. A* **33A**, 891 (2002).

21. V. Hasija, S. Ghosh, M.J. Mills, D.S. Joseph, "Deformation and Creep Modeling in Polycrystalline Ti-6Al Alloys," *Acta Mater.* **51**, 4533 (2003).

22. T. Neeraj, M.F. Savage, J. Tatalovich, L. Kavarik, R.W. Hayes, M.J. Mills, "Observation of Tension-Compression Asymmetry in α and α/β Titanium Alloys," *Phil. Mag.* **85**, 279 (2005).

23. S. Ankem, C.A. Greene, S. Singh, "Time-Dependent Twinning during Ambient Temperature Creep of α-Ti-Mn Alloy," *Scripta Metall. Mater.* **15**, 803 (1994).

24. S. Ankem, C.A. Greene, A.K. Aiyangar, "Recent Developments in Growth Kinetics of Deformation Twins in Bulk Metallic Materials," in: *Advances in Twinning. Proceedings of the 1999 TMS Annual Meeting.* S. Ankem, C.S. Pande, Eds. TMS, Warrendale, PA (1999).

25. C.A. Hultgren, C.A. Greene, S. Ankem, "Time-Dependent Twinning During Ambient Temperature Compression Creep of Alpha-Ti-0.4Mn Alloy," *Metall. Mater. Trans. A* **30A** 1675 (1999).

26. A.K. Aiyangar, B.W. Neuberger, P.G. Oberson, S. Ankem, "The Effects of Stress Level and Grain Size on the Ambient Temperature Creep Deformation Behavior of an Alpha-Ti-1.6wt.%V Alloy," *Metall. Mater. Trans. A* **36A**, 673 (2005).

27. R. Reed-Hill, R. Abbaschian, *Physical Metallurgy Principles – 3rd ed.,* PWS-Kent, Boston, 1992.

28. A. Ramesh, S. Ankem, "The Effect of Grain Size on the Ambient Temperature Creep Deformation Behavior of a Beta Ti-14.8V Alloy," *Metall. Mater. Trans. A* **33A**, 1137 (2002).

29. D. Doraiswamy, S. Ankem, "The Effect of Grain Size and Stability on Ambient Temperature Tensile and Creep Deformation in Metastable Beta Titanium Alloys," *Acta Mater.* **51**, 1607 (2003).

30. A. Ramesh, *Effect of Stability and Grain Size on Ambient Temperature Tensile and Creep Behavior of Beta Titanium Alloys*. Master's Thesis, University of Maryland, College Park, 1998.

31. J.W. Christian, S. Mahajan, "Deformation Twinning," *Prog. Mater. Sci.* **94**, 1 (1995).

32. D.G Attwood, P.M. Hazzledine, "A Fiducial Grid for High-Resolution Metallography," *Metallography* **9**, 483 (1976).

33. Applied Test Systems Series 3210 Split Tube Furnace and Accessories, Instruction Manual, 2002.

34. P.G. Oberson, S. Ankem, "Why Twins Do Not Grow at the Speed of Sound All the Time," *Phys. Rev. Lett.* **95**, 165501 (2005).

35. C.M. Hudson, *Investigation of the Low Temperature Creep Behavior of a Metastable Beta-Ti-14.8wt.% Vanadium Alloy.* PhD Dissertation, University of Maryland, College Park, 2004.

36. P.G. Partridge, "The Crystallography and Deformation Modes of Hexagonal Close-Packed Metals," *Metall. Rev.* **118**, 169 (1968).

37. C.A. Greene, *Fundamental Studies on Ambient Temperature Creep Deformation Behavior of Alpha and Alpha-Beta Titanium Alloys.* PhD Dissertation, University of Maryland, College Park, 1994.

38. H. Conrad, "Rate Controlling Mechanism During Yielding and Flow of Alpha-Titanium at Temperatures Below 0.4 T_m," *Acta Metall.* **14**, 1631 (1966).

39. P.P. Tung, A.W. Sommer, "Dislocation Energetics in Alpha Titanium," *Metall. Trans.* **1**, 947 (1970).

40. H. Conrad, M. Doner, B. de Meester, "Critical Review – Deformation and Fracture," in: *Titanium Science and Technology, Vol. 2,* R.I. Jaffee, H.M. Burte, Eds. New York, Plenum Press, 1973, p. 1049.

41. L. Yongning, Z. Jinhau, Z. Huijiu, "The Plastic Deformation of an α-Ti Alloy and its Thermal Activation Process vs. Effective Stress," *Metall. Trans. A* **23A**, 335 (1992).

42. M.A. Meyers, O. Vöhringer, V.A. Lubarda, "The Onset of Twinning in Metals: A Constitutive Description," *Acta Mater.* **49**, 4025 (2001).

43. S.G. Song, G.T. Gray, III, "Influence of Temperature and Strain Rate on Slip and Twinning Behavior of Zr," *Metall. Mater. Trans. A* **26A**, 2665 (1995).

44. A.A. Salem, S.R. Kalidindi, R.D. Doherty, "Strain Hardening of Titanium: Role of Deformation Twinning," *Acta Mater.* **51**, 4225 (2003).

45. W.G. Johnston, J.J. Gilman, "Dislocation Velocities, Dislocation Densities, and Plastic Flow in Lithium Fluoride Crystals," *J. App. Phys.* **30**, 129 (1959).

46. J.D. Eshelby, "The Determination of the Elastic Field of an Ellipsoidal Inclusion, and Related Problems," *Proc. Roy. Soc. A* **241A**, 376 (1957).

47. J.D. Eshelby, F.C. Frank, F.R.N. Nabarro, "The Equilibrium of Linear Arrays of Dislocations," *Phil. Mag.* **42**, 351 (1951).

48. R.W. Armstrong, P.J. Worthington, "A Constitutive Relation for Deformation Twinning in Body Centered Cubic Metals," in: *Metallurgical Effects at High Strain Rates,* R.W. Rodhe, B.M. Butcher, J.R. Holland, C.H. Karnes, Eds. New York, Plenum Press, 1973, p. 401.

49. K. Okazaki, H. Conrad, "Effects of Interstitial Content and Grain-Size on Strength of Titanium at Low Temperatures," *Acta Metall.* **21**, 1117 (1973).

50. G.T. Gray, III, "Influence of Strain Rate and Temperature on the Structure – Property Behavior of High-Purity Titanium," *J. Phys. IV* **7**, 423 (1997).

51. F.J. Zerilli, R.W. Armstrong, "Deformation Twinning and Grain Size Aspects of Numerical Simulations of Plastic Flow," in: *Grain Size and Mechanical Properties – Fundamentals and Applications. MRS Symposium Proceedings*, M.A. Otooni, R.W. Armstrong, N.J. Grant, K. Ishizaki, Eds. Pittsburgh, PA, MRS, 1995, p. 149.

52. S.G. Song, G.T. Gray III, "Structural Interpretation of the Nucleation and Growth of Deformation Twins in Zr and Ti – I. Application of the Coincident Site Lattice (CSL) Theory to Twinning Problems in H.C.P. Structures," *Acta Metall. Mater.* **43**, 2325 (1995).

53. S.G. Song, G.T. Gray III, "Structural Interpretation of the Nucleation and Growth of Deformation Twins in Zr and Ti – II. TEM Study of Twin Morphology and Defect Reactions During Twinning," *Acta Metall. Mater.* **43**, 2339 (1995).

54. S. Mendelson, *Mater. Sci. Eng.* **4**, 231 (1964).

55. A. Akhtar, "Basal Slip and Twinning in α-Titanium Single Crystals," *Metall. Trans. A* **6A**, 1105 (1975).

56. D.R. Thornburg, H.R. Piehler, "An Analysis of Constrained Deformation by Slip and Twinning in Hexagonal Close Packed Metals and Alloys," *Metall. Trans A* **6A**, 1511 (1975).

57. M.H. Yoo, "Slip, Twinning, and Fracture in Hexagonal Close-Packed Metals," *Metall. Trans. A* **12A**, 409 (1981).

58. M.H. Yoo, J.K. Lee, "Deformation Twinning in HCP Metals and Alloys," *Phil. Mag. A* **63**, 987 (1991).

59. N. Thompson, D.J. Millard, "Twin Formation in Cadmium," *Phil. Mag.* **43**, 422 (1952).

60. B.A. Bilby, A.G. Crocker, "The Theory of the Crystallography of Deformation Twinning," *Proc. Roy. Soc A* **A288**, 240 (1965).

61. A.G. Crocker , M. Bevis, in *The Science, Technology, and Application of Titanium*, R. Jaffee, N. Promisel, Eds. Oxford, Plenum Press, 1970, p. 453.

62. M.L. Kronberg, "A Structural Mechanism for the Twinning Process on $\{10\bar{1}2\}$ in Hexagonal Close Packed Metals," *Acta Metall.* **16**, 29 (1968).

63. W. Bollmann, *Crystal Defects and Crystalline Interfaces.* Berlin, Springer, 1970.

64. S.G. Song, G.T. Gray, III, "Transmission Electron Microscopy Examination and Analysis of an Anomalous Stacking Fault in HCP Metals," *Phil. Mag. A* **71**, 263 (1995).

65. A. Jaworski, Jr., S. Ankem, "Influence of the Second Phase on the Room Temperature Tensile and Creep Deformation Mechanisms of α-β Titanium Alloys Part I: Tensile Deformation," *Metall. Mater. Trans. A* **37A**, (2006).

66. A. Jaworski, Jr., S. Ankem, "Influence of the Second Phase on the Room Temperature Tensile and Creep Deformation Mechanisms of α-β Titanium Alloys Part II: Creep Deformation," *Metall. Mater. Trans. A* **37A**, (2006).

67. N.E. Paton, J.C. Williams, G.P. Rauscher, "The Deformation of α-Phase Titanium," in: *Titanium Science and Technology, Vol. 2,* R.I. Jaffee, H.M. Burte, Eds. New York, Plenum Press, 1973, p. 1049.

68. G.T. Gray, III, G.C. Kaschner, T.A. Mason, P.J. Maudlin, S.R. Chen, "The Influence of Interstitial Content, Temperature, and Strain Rate on Deformation Twin Formation," in: *Advances in Twinning,* S. Ankem, C.S. Pande, Eds. Warrendale, PA, TMS, 1999, p. 157.

69. D.A. Porter, K.E. Easterling, *Phase Transformations in Metals and Alloys, 2nd ed.* London, Chapman and Hall, 1992.

70. Z. Liu, G. Welsch, "Literature Survey on Diffusivities of Oxygen, Aluminum, and Vanadium in Alpha Titanium, Beta Titanium, and Rutile," *Metall. Trans. A* **19A**, 1121 (1988).

71. Y. Nakamura, H. Nakajima, S. Ishioka, M. Koiwa, "Effect of Oxygen on Diffusion of Manganese in Alpha-Titanium," *Acta Metall.* **36**, 2787 (1988).

72. D.R. Miller, "Internal Friction of Titanium and its Alloys," *Trans. AIME* **224**, 275 (1962).

73. R.G. Hennig, D.R. Trinkle, J. Bouchet, S.G.Srinivasan, R.C. Albers, J.W. Wilkins, "Impurities Block the α to ω Martensitic Transformation in Titanium," *Nature Materials* **4**, 129 (2005).

74. P.G. Oberson, S. Ankem, "Why Twins Do Not Grow at the Speed of Sound All the Time," *Phys. Rev. Lett.* **95**, 165501 (2005).

75. M.J. Blackburn, J.C. Williams, "Phase Transformation in Ti-Mo and Ti-V Alloys," *Trans. Metall. Soc. AIME* **242**, 2461 (1968).

76. S. Hanada, A. Takemura, O. Izumi, "The Mode of Plastic Deformation of β Ti-V Alloys," *Trans. JIM* **23**, 507 (1982).

77. S. Hanada, M. Ozeki, O. Izumi, "Deformation Characteristics in β Phase Ti-Nb Alloys," *Metall. Trans. A* **16A**, 789 (1985).

78. S. Hanada, O. Izumi, "Correlation of Tensile Properties, Deformation Modes, and Phase Stability in Commercial β-Phase Titanium Alloys," *Metall. Trans. A* **18A**, 265 (1987).

79. H. Ohyama, T. Nishimura, "Effects of Alloying Elements on Deformation Mode in Ti-V Based β Titanium Alloy System," *ISIJ Int'l.* **35**, 927 (1995).

80. V.S. Litvinov, G.M. Rusakov, "Twinning on the $\{332\}\langle 11\bar{3}\rangle$ System in Unstable β Titanium Alloys," *Phys. Met. Metall.* **90**, S96 (2000).

81. A.V. Litvinov, A.G. Illarionov, G.M. Rusakov, V.S. Litvinov, "Structure and Properties of a Metastable β Alloy Aged after Plastic Deformation," *Phys. Met. Metall.* **98**, 624 (2004).

82. A.G. Crocker, "Twinned Martensite," *Acta Metall.* **10**, 113 (1962).

83. R.H. Richman, "The Diversity of Twinning in Body-Centered Cubic Structures," in: *Deformation Twinning,* R.E. Reed-Hill, J.P. Hirth, H.C Rogers, Eds. Gordon and Breach, New York, 1964, p. 237.

84. F.-W. Ling, E.A. Starke, Jr., B.G. LeFevre, "Deformation Behavior and Texture Development in Beta Ti-V Alloys," *Metall. Trans.* **5**, 179 (1974).

85. H.G. Paris, B.G. LeFevre, E.A. Starke, Jr., "Deformation Behavior in Quenched and Aged Beta Ti-V Alloys," *Metall. Trans. A* **7A**, 279 (1976).

86. M. Oka, Y. Taniguchi, "{332} Deformation Twins in a Ti-15.5 pct. V Alloy," *Metall. Trans. A* **10A**, 651 (1979).

87. A.A. Popov, A.V. Litvinov, A.G. Illarionov, "Structure of Twins of a Ti-Al-Mo-V-Cr Alloy of the Transition Class," *Phys. Met. Metall.* **88**, 478 (1999).

88. A.H. Cottrell, B.A. Bilby, "A Mechanism for the Growth of Deformation Twins in Crystals," *Phil. Mag.* **42**, 573 (1951).

89. D. Hull, B.J. Bacon, *Introduction to Dislocations, 4th ed.* Boston, Butterworth-Heinemann, 2001.

90. J. Weertman, J.R. Weertman, *Elementary Dislocation Theory.* New York, Oxford University Press, 1992.

91. J.P. Hirth, J. Lothe, *Theory of Dislocations, 2nd ed.* New York, Wiley, 1982.

92. S.G. Song, G.T. Gray, III, "Double Dislocation Pole Model for Deformation Twinning in FCC Lattice," *Phil. Mag. A* **71A**, 661 (1995).

93. H. Gleiter, B. Chalmers, *Progress in Materials Science, Vol. 16. High-Angle Grain Boundaries.* New York, Pergamon, 1972.

94. K. Yasutake, S. Shimizu, M. Umeno, H. Kawabe, "Velocity of Twinning Partial Dislocations in Silicon," *J. Appl. Phys.* **61**, 940 (1987).

95. S.K. Wu, A.G. Khachaturyan, C.M Wayman, "Superstructure of Interstitial Ordering of Oxygen in TiNi Alloys," *Acta Metall.* **36**, 2065 (1988).

96. C.L. Magee, D.W. Hoffman, R.G. Davies, "The Effect of Interstitial Solutes on the Twinning Stress of B.C.C. Metals," *Phil. Mag.* **23**, 1531 (1971).

97. F. Claisse, H.P. Koenig, "Thermal and Forced Diffusion of Oxygen in β-Titanium," *Acta Metall.* **4**, 650 (1956).